frontiers | Research Topics

# Advances in sustainable mine tailings management

**Edited by**
Lijie Guo, Valerio Funari and Miao Li

**Published in**
Frontiers in Earth Science

ISSN 1664-8714
ISBN 978-2-8325-3497-7
DOI 10.3389/978-2-8325-3497-7

## About Frontiers

Frontiers is more than just an open access publisher of scholarly articles: it is a pioneering approach to the world of academia, radically improving the way scholarly research is managed. The grand vision of Frontiers is a world where all people have an equal opportunity to seek, share and generate knowledge. Frontiers provides immediate and permanent online open access to all its publications, but this alone is not enough to realize our grand goals.

## Frontiers journal series

The Frontiers journal series is a multi-tier and interdisciplinary set of open-access, online journals, promising a paradigm shift from the current review, selection and dissemination processes in academic publishing. All Frontiers journals are driven by researchers for researchers; therefore, they constitute a service to the scholarly community. At the same time, the *Frontiers journal series* operates on a revolutionary invention, the tiered publishing system, initially addressing specific communities of scholars, and gradually climbing up to broader public understanding, thus serving the interests of the lay society, too.

## Dedication to quality

Each Frontiers article is a landmark of the highest quality, thanks to genuinely collaborative interactions between authors and review editors, who include some of the world's best academicians. Research must be certified by peers before entering a stream of knowledge that may eventually reach the public - and shape society; therefore, Frontiers only applies the most rigorous and unbiased reviews. Frontiers revolutionizes research publishing by freely delivering the most outstanding research, evaluated with no bias from both the academic and social point of view. By applying the most advanced information technologies, Frontiers is catapulting scholarly publishing into a new generation.

## What are Frontiers Research Topics?

Frontiers Research Topics are very popular trademarks of the *Frontiers journals series*: they are collections of at least ten articles, all centered on a particular subject. With their unique mix of varied contributions from Original Research to Review Articles, Frontiers Research Topics unify the most influential researchers, the latest key findings and historical advances in a hot research area.

Find out more on how to host your own Frontiers Research Topic or contribute to one as an author by contacting the Frontiers editorial office: frontiersin.org/about/contact

# Advances in sustainable mine tailings management

**Topic editors**

Lijie Guo — Beijing Mining and Metallurgy Technology Group Co., Ltd., China
Valerio Funari — National Research Council (CNR), Italy
Miao Li — Charles Sturt University, Australia

**Citation**

Guo, L., Funari, V., Li, M., eds. (2023). *Advances in sustainable mine tailings management*. Lausanne: Frontiers Media SA. doi: 10.3389/978-2-8325-3497-7

# Table of contents

frontiers | Frontiers in Earth Science

TYPE Editorial
PUBLISHED 01 September 2023
DOI 10.3389/feart.2023.1269955



OPEN ACCESS

EDITED AND REVIEWED BY
Ben van der Pluijm,
University of Michigan, United States

*CORRESPONDENCE
Lijie Guo,
guolijie@bgrimm.com

RECEIVED 31 July 2023
ACCEPTED 16 August 2023
PUBLISHED 01 September 2023

CITATION
Guo L, Funari V and Li M (2023), Editorial: Advances in sustainable mine tailings management.
*Front. Earth Sci.* 11:1269955.
doi: 10.3389/feart.2023.1269955



# Editorial: Advances in sustainable mine tailings management

Lijie Guo[1,2]*, Valerio Funari[3] and Miao Li[4]

[1]BGRIMM Technology Group, Beijing, China, [2]National Centre for International Research on Green Metal Mining, Beijing, China, [3]National Research Council (CNR), Rome, Italy, [4]School of Computing, Mathematics and Engineering, Faculty of Business, Justice and Behavioural Sciences, Charles Sturt University, Bathurst, NSW, Australia

KEYWORDS

**sustainable mining, mine tailings, waste disposal and management, tailings storage facilities (TSFs), mine backfill**

Editorial on the Research Topic
Advances in sustainable mine tailings management

This Research Topic focuses on progress and achievements of research in sustainable mine tailings (MTs) management. MTs are byproducts generated from mechanical and chemical processes to extract valuable elements from ore deposits. Typically, MTs are stored within tailings storage facilities (TSFs) or in the form of dry stacks. This causes a series of social, environmental, and economic problems, such as acid mine drainage and failure of TSFs. Backfill technology has been a reliable solution for sustainable MTs management. However, only a partial amount of MTs has been returned to underground voids (stopes), leaving still large amounts of MTs on the ground surface. A more worrying fact is that advanced technologies increase production from lower-grade ores in mines, yielding a higher tonnage of MTs. Sustainable recycling and reuse of MTs has become one of the major challenges in mining engineering.

To combat this challenge, interdisciplinary collaborations from fields of chemistry, physics, and material science are needed. Therefore, we called for a Research Topic on frontiers and advances in sustainable MTs management, with a view to bringing together expertise, knowledge and insights from multiple disciplines to achieve sustainable MTs disposal.

In the present Research Topic of Frontiers in Earth Science, a total of 16 manuscripts were received and 12 were accepted and published. These works cover aspects ranging from physicochemical properties of MTs, new technologies for MTs disposal, risk and stability analysis of TSFs, MTs backfill and underground environmental protection, to hydration and microstructure formation of green cementitious materials for MTs disposal.

For physicochemical properties of MTs, Chen et al. performed consolidated drained triaxial shear tests to investigate the non-linear mechanical characteristics of tailings under high pressure from high tailing ponds. They observed a linear increase in the breakage index value as the shear strength increased, suggesting that the dense region in the deeper section of the tailings dam is susceptible to particle crushing, which adversely impacts the stability of the large-scale high dam. Wang et al. conducted a comparative triaxial shear test on both pure unclassified tailings and concentrated unclassified tailings at various curing ages. They examined how the curing materials affected the shear strength of unclassified tailings and uncovered the evolution of shear strength in concentrated unclassified tailings with different curing durations.

For new technologies for MTs disposal, Wang et al. investigated the physical and chemical properties, grindability, and fundamental characteristics of ultra-fine particle iron ore tailings (IOTs), laying the groundwork for the comprehensive utilization of these IOTs in construction materials. Yuan et al. formulated a composite modifier named CMSFR, which consists of silicon calcium slag, fly ash, and reservoir sediment, to enhance the chemical and mineral composition of steel slag. Through their research, it was observed that high-temperature modification using CMSFR led to an improvement in the content of cementitious phases (C3S, C2S, C3A) and the glass phase in steel slag. The study focused on developing environmentally friendly applications of steel slag and coal-based solid waste in cement concrete. Bao et al. utilized vanadium-titanium iron ore tailings (VTIOTs) to produce high-strength fired water permeable brick (HSFWPB), and investigated the fundamental characteristics and firing process of HSFWPB incorporating VTIOTs. Additionally, an economic assessment was performed on the investment related to HSFWPB containing VTIOTs. This study holds promise in enhancing the utilization of VTIOTs and presents a novel avenue for widespread applications of VTIOTs.

For risk and stability analysis of TSFs, Chen et al. developed a predictive model for the evolution of reinforced tailings breach, incorporating an erosion model derived from the reinforced tailings erosion test and a stability analysis of the reinforced slope. Mei et al. improved the algorithm for two combined strategies involving lowering the cover plate of tailing ponds and installing additional drainage pumps. The objective was to suggest supplementary drainage measures for tailing ponds in anticipation of forecasted rainfalls. Correspondingly, they presented prediction and calculation methods utilizing fundamental data from the water level-reservoir capacity curve of tailing ponds, forecasted rainfall parameters, and flood discharge system parameters.

For MTs backfill and underground environmental protection, Han et al. conducted a study on heavy metal pollution in mine tailings, soils, and groundwater based on a database of 27 abandoned lead–zinc mine tailing sites in China. The investigation revealed a positive correlation between the content of heavy metals in soil, groundwater, and mine tailings, indicating the primary pollution source and transport pathways. The research is expected to assess the pollution levels in lead-zinc mining regions and guide remediation efforts for specific sites, thereby contributing to environmental management initiatives concerning MTs in China.

For hydration and microstructure formation of green cementitious materials used for MTs disposal, Wang et al. used steel slag, vanadium-titanium slag and vanadium-titanium iron ore tailings as the main raw materials to produce the mine cemented paste backfill material (CPBM). The composition, properties, and hydration mechanism of the new cementitious materials were analyzed. They found that the 28-day flexural strength and compressive strength of CPBM reached 4.25 and 9.41 MPa when certain conditions were met. Zhang et al. used steel slag, granulated blast furnace slag, and flue gas desulfurization gypsum after mechanical activation to prepare building foundation pit backfilling materials (BFPBM) with the coordination of iron ore tailings. They found that 28-day compressive strength and the mixture slump of BFPBM could meet the index requirements of Chinese National Standard T/CECS 1037–2022 Technical Standard for backfilling projects using premixed fluidized solidified soil.

In the paper by Guo et al., the variable head method was employed to conduct saturation permeation tests on ionic rare earth under various leaching conditions. This study revealed the impact of type, concentration, and leaching path on the saturation permeability coefficient. In the paper by Yin et al., they analyzed the correlation between indicators identifying unsafe psychological states among coal mine workers.

We believe this Research Topic builds up the understanding and knowledge of all researchers and practitioners who have interests in the recent developments and advancements in sustainable MTs management. This Research Topic informs future research on the sustainable utilization of MTs, and contributes to green mining.

## Author contributions

LG: Writing–original draft, Writing–review and editing. VF: Writing–review and editing. ML: Writing–original draft, Writing–review and editing.

## Acknowledgments

The authors thank all experts and scholars for contributing quality papers to this Research Topic, and the reviewers for providing constructive comments.

## Conflict of interest

LG was employed by BGRIMM Technology Group.

The remaining authors declare that the research was conducted in the absence of any commercial or financial relationships that could be construed as a potential conflict of interest.

## Publisher's note

frontiers | Frontiers in Earth Science

TYPE Original Research
PUBLISHED 30 January 2023
DOI 10.3389/feart.2022.1075588



OPEN ACCESS

EDITED BY
Lijie Guo,
Beijing Mining and Metallurgy Technology Group Co., Ltd., China

REVIEWED BY
Guangjin Wang,
Kunming University of Science and Technology, China
Zhihong Zhang,
Beijing University of Technology, China

*CORRESPONDENCE
Xiaofei Jing,
xfjing@cqust.edu.cn

SPECIALTY SECTION
This article was submitted to Geoscience and Society, a section of the journal Frontiers in Earth Science

RECEIVED 20 October 2022
ACCEPTED 02 December 2022
PUBLISHED 30 January 2023

CITATION
Chen M, Jing X, Xie D, Li X, Zhang Y and Liu X (2023), Prediction model investigations of the reinforced fine-grained tailings dam overtopping failure. *Front. Earth Sci.* 10:1075588. doi: 10.3389/feart.2022.1075588



# Prediction model investigations of the reinforced fine-grained tailings dam overtopping failure

Meibao Chen[1], Xiaofei Jing[2]*, Dongxu Xie[3], Xiaoshuang Li[4], Yuanzhen Zhang[2] and Xiaohua Liu[2]

[1]Chongqing Safety Science and Technology Co., Ltd., Chongqing University of Science and Technology, Chongqing, China, [2]School of Safety Engineering, Chongqing University of Science and Technology, Chongqing, China, [3]Chongqing 107 Municipal Construction Engineering Co., Ltd., Chongqing, China, [4]School of Civil Engineering, Shaoxing University, Shaoxing, China

Overtopping dam break is a frequent accident in tailings reservoirs. However, little attention has been paid to the study of overtopping hydraulic erosion damage characteristics of tailings dam after adding reinforcement. Nowadays, there were few people have researched the prediction of the overtopping failure process of the reinforced tailings dam. It is important significance to establish a prediction model for the overtopping of reinforced tailings dam which aims at the problem of overtopping erosion of reinforced tailings. For the anti-erosion and anti-collapse effects of the reinforced tailings dam, a mathematical model for the development of the overtopping breach of the reinforced tailings dam is established. The formula of reinforced erosion rate derived from water flow shear stress theory, simulation of breach erosion development by time iteration method in the mathematical model. Secondly, the limit equilibrium method is used to analyze the stability of the reinforced breach slope. Then, the physical test is used to reproduce the dam failure process of the tailings dam. In addition, the development process of the breach and discharge are monitored. Ultimately, the maximum depth and width of the breach are in brilliant agreement with the calculated values.

KEYWORDS

**reinforced tailings dam, overtopping failure, erosion, prediction model, model experiment**

## 1 Introduction

The failure of the tailings dam poses a threat to the safety of downstream residents and the natural environment, making it a crucial topic of research for the prevention of accidents involving tailings dam (Sun et al., 2012; Clarkson et al., 2021). Numerous variables impact geotechnical properties, resulting in tailings dam failure (Li et al., 2022). The following failure modes have been identified for tailings dam reservoirs: foundation destruction (Psarropoulos et al., 2008; Meng et al., 2021), pipe surge (Van Niekerk et al., 2005), overtopping failure (Zhang et al., 2016), seepage (Mittal, 1976; Lottermoser et al., 2005), earthquake (Villavicencio et al., 2014; Agurto-Detzel et al., 2015), and slope instability (Silva et al., 2008). In 2000, strong rains and snowmelt caused the tailings dam

at the Baiaborsa gold mine in Romania to burst, discharging 100,000 $m^3$ of tailings into Tisa River tributaries, causing aquatic heavy metal toxicity and broad ecological degradation (Michnea et al., 2001). The Fundo dam failure in Brazil was severe, with 806 buildings in 10 districts of five cities directly affected by tailings, along with 21.1 km of country roads, 12 bridges, and a minor hydroelectric facility. The tailings clog the Doce River downstream, spreading 548 km to the Atlantic Ocean, impacting forty communities downstream, and denying hundreds of thousands of people access to clean water (Carmo et al., 2017).

In the 1960's, European and American researchers began studying the overtopping failure prediction model, which was based on the overtopping failure mechanism and utilized hydraulics and sediment transport theory. This model was a rather complex mathematical model for overtopping failure with speedy computation features. Cristofano (1973) developed the first mathematical model of homogeneous dam overtopping based on sediment erosion in 1965. Later, researchers presented a set of mathematical models to simulate dam overtopping. Fread (1981) developed the NWS BREACH model considering the collapse effect. At present, this kind of model is also applied in the tailings reservoir. Wu and Qin (2018) used the proposed river embankment stability analysis method in the simplified overtopping failure model. Petkovek et al. (2021) proposed that tailings slurry exhibits a stratification phenomenon, whereby the upper layer is the flow, the lower layer is the tailings bed load, and the erosion of tailings slurry is distinct from that of clear water. Consequently, this double-layer fluid erosion model was utilized to incorporate and modify the DAMBRK (Mohamed et al., 2002) overtopping failure model, and a new calculation model of tailings overtopping failure was developed. This model uses different flow calculation formulas and erosion formulas to simulate the erosion of dam materials by assuming the shape of the breach, as well as other simulation methods to analyze the longitudinal undercutting and lateral expansion of the breach.

The majority of prediction models simulate the overtopping failure process using the numerical calculation methodology of time step iteration, which can provide the overtopping failure parameters for each time step (such as flow rate, size, reservoir water level, etc.). In recent years, with the improvement of computer performance and the advancement of sedimentology and computational fluid dynamics, there have been a number of exemplary calculation models (Kesserwani et al., 2014; Abderrezzak et al., 2015; Marsooli et al., 2015; Cantero-Chinchilla et al., 2016; Di Cristo et al., 2018), which were based on the continuous flow equation, momentum equation and energy equation, coupled with the process of sediment motion equation. The governing equations were resolved using finite volume and other numerical simulation techniques. This model was capable of producing an accurate simulation of the overtopping failure process. The model introduced above has the advantage of quick analysis and wide applicability.

The selected tailings particles become finer and finer as mineral processing technology advances, and the secondary reinforcement belt is widely used in fine-grained tailings as a reinforcement material. This resulted in an increase in the storage height of fine-grained tailings dams and a steady rise in the number of reinforced high-pile fine-grained tailings dams. However, most overtopping failure prediction models do not consider the influence of the reinforcement belt, resulting in the inaccurate prediction of the consequences of the overtopping failure disaster and unnecessary economic losses (Jing et al., 2019). Therefore, based on the mechanism of overtopping failure, the prediction model of overtopping breach development of reinforced tailings is established, which provides particular guiding significance for the risk prediction of overtopping failure of reinforced tailings.

## 2 Prediction model of overtopping burst development of reinforced tailings dam

It was found in the overtopping dam failure test of reinforced fine-grained tailings that the reinforcement belt has a significant positive effect on the collapse constraints on both sides, a contributor to a smaller degree of collapse, and the reinforcement can improve the anti-erosion effect of tailings. Therefore, with reference to the improved water flow model of Chen et al. (2015, 2019), the reinforced erosion rate, start-up conditions, and reinforced slope stability calculation are introduced to establish the reinforced fine-grained tailings dam burst development prediction model.

### 2.1 Water flow model

The hydraulic characteristics of the dam crest cross-section of the gully are similar to the broad crest weir flow after the flow overtopping. Therefore, the burst of the cross-section of the dam crest can be regarded as the broad-crested weir section, and the overflow flow from the dam crest can be calculated by the broad-crested weir formula (Chen et al., 2019). The formula is as follows:

$$Q_{out} = CB(z_w - z_b)^{3/2} = C_1C_2\sqrt{2g}B(z_w - z_b)^{3/2} \quad (1)$$

$Q_{out}$ is the burst flow; $C$ is the comprehensive flow coefficient, and the general value is 1.7; $C_1$ is the discharge coefficient; $C_2$ is the contraction coefficient; $B$ is the burst width; $z_w$ is the dam water level elevation; $z_b$ is burst bottom elevation.

Fread et al. (1981) considered the flow at the burst to be uniform and constant, with a water depth of h after the flow passes through the dam crest burst; Chen et al. (2015) adopted

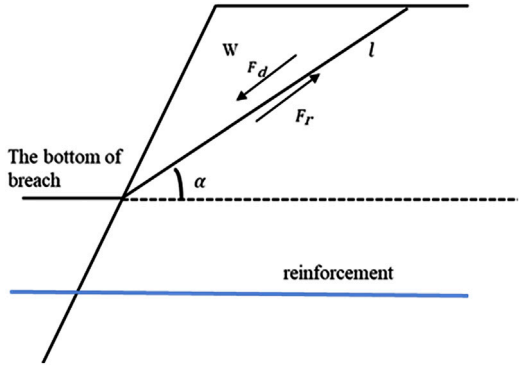


FIGURE 1
Schematic diagram of reinforcement not yet eroded.

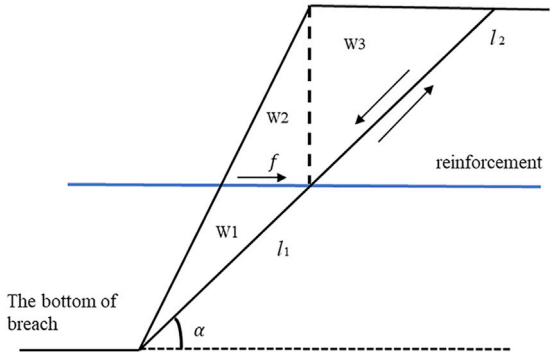


FIGURE 2
Schematic diagram of erosion to reinforcement.

a simplified treatment scheme, assuming a drop coefficient m to calculate the water depth of the burst, the $m$ is 0.6–0.8, as follows:

$$h = m(z_w - z_b) \tag{2}$$

The instantaneous flow velocity $V$ of the burst section can be determined by:

$$\begin{aligned} V &= \frac{Q_{\text{out}}}{Bh}, \\ &= C\frac{(z_w - z_b)^{3/2}}{h}, \\ &= Cm^{-1}\sqrt{(z_w - z_b)} \end{aligned} \tag{3}$$

Among them, through parameter sensitivity analysis, the $m$ impact on the peak flow rate is small, and the assumed drop coefficient of 0.8–0.6 empirical value can be used to simplify the model calculation.

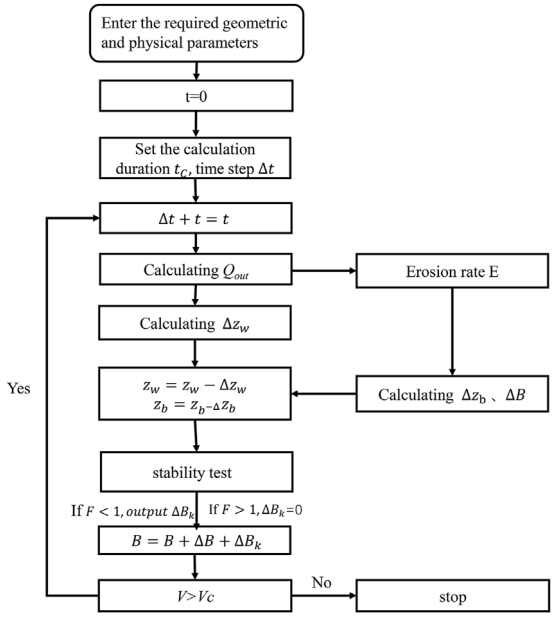


FIGURE 3
Calculation flow chart.

$$A_s\frac{dz_w}{dt} = Q_{in} - Q_{\text{out}} \tag{4}$$

$Q_{\text{out}}$ is the outflow, $Q_{in}$ is the inflow, and $A_s$ is water surface area in the reservoir.

## 2.2 Reinforced erosion models

The incorporation of reinforcement can effectively enhance the mechanical occlusion between the tailings particles, thereby enhancing the anti-erosion performance of tailings and increasing their water shear strength. Chen et al. (2021) carried out the erosion test of reinforced tailings. The test results show that the addition of reinforcement can enhance the erosion resistance of particles, but with the increase of the spacing of reinforcement, the critical velocity of tailings erosion decreases, and the erosion rate will gradually increase. Since the conventional non-reinforced erosion equation can no longer reasonably show the erosion results. Referring to other overtopping dam burst development prediction models, assuming that the overall erosion resistance of the burst at the top of the tailings dam is the same, the erosion equation summarized by the tailings erosion test with different reinforcement spacing is adopted. The equation is as follows:

The resulting critical start rate $V_c'$, such as Eq. 5.

$$V_c' = \left(1 + e^{(-d/0.73)}\right) \cdot V_c \tag{5}$$

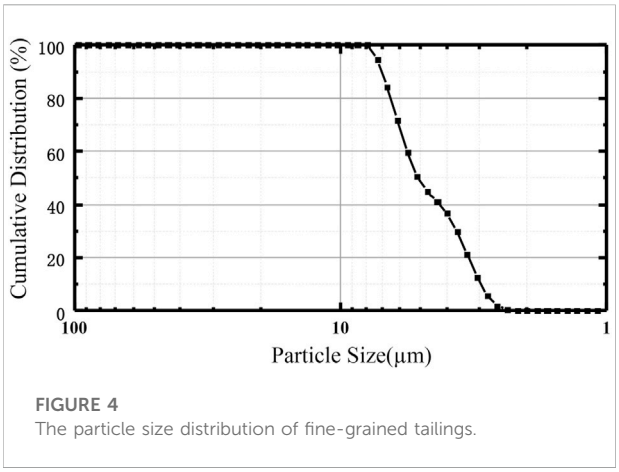


FIGURE 4
The particle size distribution of fine-grained tailings.

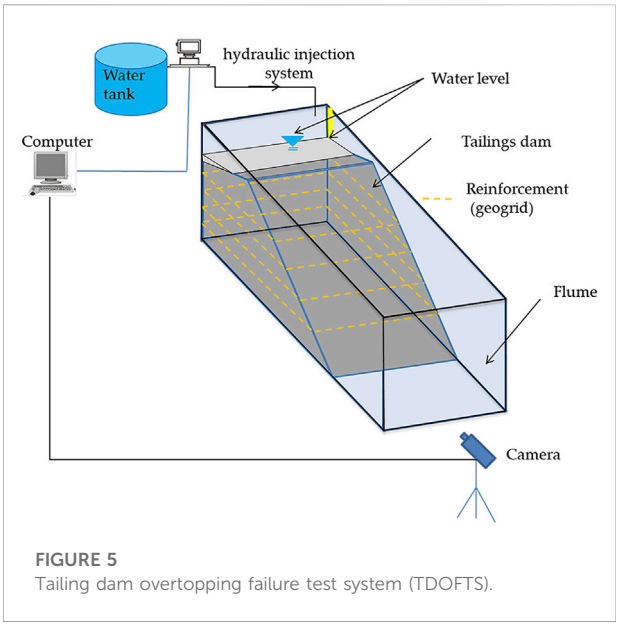


FIGURE 5
Tailing dam overtopping failure test system (TDOFTS).

$V_c$ is the starting flow rate. Where $d$ is the reinforcement spacing, as shown in $V_c$ Eq. 6, as follows:

$$\frac{V_c}{\sqrt{\frac{(\gamma_s-\gamma)gD}{\gamma}}\left(\frac{R}{D}\right)^{\frac{1}{6}}} = 0.0035\left(\frac{NR^{\frac{1}{6}}}{\sqrt{g}\,nRe_{vd}}\right)^2 + 1.5 \tag{6}$$

Among them, $n$ the Manning coefficient is the Reynolds number $Re_{vd}$, $N$ is the number of reinforcement layers, and $R$ is the hydraulic radius.

When the water flow velocity is greater $V_c'$, the particles begin to erode, and the erosion rate $E$ is:

$$E = 0.056\left(\frac{U^2}{V_c{}'^2} - 1\right)^{0.503} \tag{7}$$

$U$ is the flow velocity.

In the stop condition of dam burst erosion, one part adopts a time setting to calculate the rock stratum at the bottom of the dam, and the other part adopts a particle starting condition. When the water flow shear force is less than the particle starting shear force, the erosion stops. Due to the large capacity of the dam, the dam body is easy to erode the rock layer at the bottom of the dam, which can be calculated by setting time. However, for the small capacity of the dam, it is easy to produce incomplete dam break and not easy to erode to the bottom of the dam. The preset fixed time is not practical, so the shear force starting method is more suitable. When the water flow rate is less than $V_c'$, stop erosion.

## 2.3 Reinforced fender lateral extension model

With the continuous scour of the water flow, high-risk slopes are formed on both sides of the burst, and it is known from the test that the lateral expansion of the burst is largely from the burst collapse. The behavior of burst collapse has certain randomness, and it is difficult to express the collapse behavior through pure empirical formula. Zhong et al. (2016) and Singh et al. (1988) used the wedge analysis method to simulate the lateral expansion of the burst caused by the sudden collapse of the bank slope. However, it is found through experiments that the reinforcement belt can curb the collapse of the bank slopes on both sides of the burst. Therefore, in order to describe the lateral expansion of the burst of the reinforced tailings overtopping dam, based on the limit equilibrium method, the lateral expansion model of the reinforced burst is established as shown in Figures 1, 2. When the erosion of the burst does not develop to the reinforcement belt, the limit equilibrium calculation is adopted, and the tension of the reinforcement belt is added on this basis.

The pressure on the reinforced overtopping slope is analyzed and deformed by limit balance, and the safety factor obtained is:

$$F_i = \frac{W\ \tan\varphi + cl/\cos\alpha + NT_i}{W\ \tan\alpha} \tag{8}$$

$W$-gravity, $c$-cohesion, $\varphi$-internal friction angle, and $\alpha$-sliding surface angle. The distribution of the rib tension $T_i$ is more complicated, in order to simplify the calculation, at present, when domestic and foreign scholars calculate the stability of the reinforced slope, the reinforcement tension is regarded as a uniform distribution, and the reinforcement tension in the extreme equilibrium state is regarded as the limit pull of the reinforcement. $N$ is the number of reinforcement layers.

The distance of the dam is $x$, if it has not eroded into the reinforcement:

$$z_0 - z_b < x,\ N = 0 \tag{9}$$

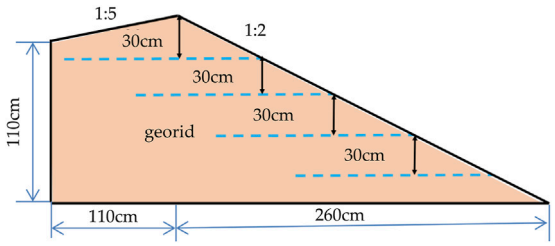


FIGURE 6
The schematic diagram of the geogrid.

Erosion to a layer of reinforcement:

$$x < z_0 - z_b < x + \alpha,\ N = 1 \tag{10}$$

Further erosion, then:

$$z_0 - z_b > x + d,\ N = \frac{z_0 - z_b - x}{d} \tag{11}$$

$N$ takes the integer.

## 2.4 Calculation process

**Step 1:** the first step is to set the initial parameters: the initial breach depth and width, dam height, inner slope ratio, etc., and the passage Eqs 1, 2, the parameters such as instantaneous discharge and water depth of the initial breach section are calculated.

**Step 2:** the flow velocity and the change of water level in the reservoir are calculated by the instantaneous flow rate of the breach outflow calculated in the previous step $\Delta z_w$, and the erosion rate is calculated by the reinforced erosion model, and the erosion depth of the next unit time is calculated according to the unit time $\Delta z_b$.

$$\Delta z_b = E\Delta t \tag{12}$$

Depending on the erosion depth, the lateral erosion width can be calculated $\Delta B$.

$$\Delta B = k\Delta z_b \tag{13}$$

$k$ is the empirical coefficient, generally 0.5–3.0 (Singh et al., 1988).

**Step 3:** through the calculation value of the second step, the new water level elevation and dam bottom elevation of the next time unit are obtained.

$$\begin{aligned} z_w &= z_w - \Delta z_w, \\ z_b &= z_b - \Delta z_b \end{aligned} \tag{14}$$

**Step 4:** Calculate the new breach depth $H$: based on the new water level elevation $z_w$ and the dam bottom elevation $z_b$.

$$H = z_w - z_b \tag{15}$$

Stability tests are performed according to $H$, if the safety factor $F_i$ is greater than or equal to 1, $\Delta B_k = 0$.

Output collapse width:

$$B = B + \Delta B \tag{16}$$

If $F_i$ it is greater than 1.0, it is calculated $\Delta B_k$, that is, the distance between the sliding surface and the breach.

$$B = B + \Delta B + \Delta B_k \tag{17}$$

Finally, the first step is repeated, and the calculation is repeated until the erosion damage stops, the flow velocity is less than the reinforced start-up velocity. The above calculation process is shown in Figure 3.

# 3 Model validation

Due to further verify the reliability of the model, the above theory is verified by physical experiments (Coleman et al., 2002; Hanson et al., 2013). Cause the overtopping accident of tailings dam has certain suddenness and high risk, there are few field observation data, and reinforced overtopping cases are scarce. As a result that the overtopping test of the reinforced tailings dam is carried out to obtain the depth, width, and discharge flow of the breach, which is compared with the model calculation results.

## 3.1 Physical model experiment

### 3.1.1 Test scheme

The test material is red mud, taken from a red mud tailings dam in Chongqing, which is a fine-grained tailing. The fundamental properties of fine-grained tailings were examined independently by following the "Geotechnical Test Method Standard" (GB/T50123-2019, the Natural Standard of China). The physical properties of the tailings material were measured as follows: *in-situ* moisture content at 23% and dry density at 1.61 g/cm$^3$. The particle size distribution of fine-grained tailings is shown in Figure 4. The test water supply is tap water for Chongqing city, China.

The experimental equipment adopts the self-made overtopping dam break system of the tailings dam, which is composed of a test tank, water supply system, and monitoring system. The test tank is used to store the tailings dam model and is the test site for physical model stacking and molding. The second water injection system is mainly composed of a water storage system, water pump, frequency converter, and water supply pipeline, which is used to simulate the upstream

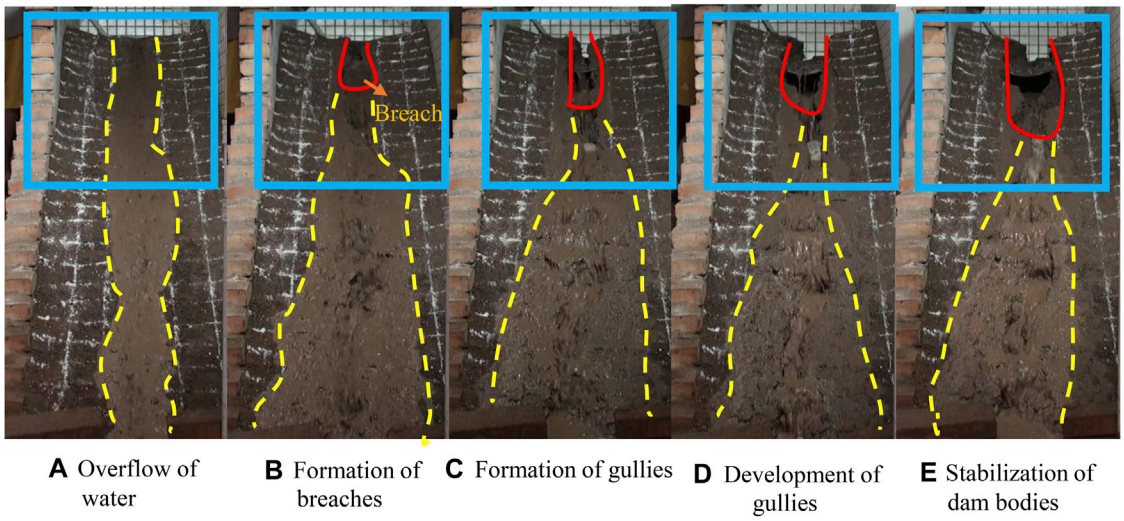


FIGURE 7
The overtopping process of reinforced tailings. **(A)** Overflow of water; **(B)** Formation of breaches; **(C)** Formation of gullies; **(D)** Development of gullies; **(E)** Stabilization of dam bodies.

**TABLE 1 Tailings reservoir characteristic parameter setting table.**

| Tailings reservoir characteristics | Back slope ratio/λ | Water level elevation/$z_w$ | Initial collapse bottom elevation/$z_b$ | Initial ulcer width/$B$ | Ribbing resistance/$F_i$ |
|---|---|---|---|---|---|
| Enter a value | 1:5 | 130 cm | 2 cm | 2 cm | 1.5 kN/m |

**TABLE 2 Hydraulic parameter setting table.**

| Hydraulic parameters | Inbound traffic/$Q_{in}$ | Water flow density/$\rho$ | Drop factor/$m$ |
|---|---|---|---|
| Enter a value | 0.5 L/s | 1,000 kg/m$^3$ | 0.6 |

**TABLE 3 Tailings parameter setting table.**

| Tailings parameters | Cohesion/ $C$ | Reinforcement spacing/d | Internal friction angle/$\varphi$ | Average particle size/D | Soil density/$\rho_s$ |
|---|---|---|---|---|---|
| Enter a value | 11 kPa | 30 cm | 17 | 0.005 mm | 1800 kg/m$^3$ |

confluence flow of the tailings dam. The water storage system is composed of a glass transparent water tank as the water supply tank. The water pump is connected to the frequency converter, and the speed of the water pump is controlled by adjusting the frequency of the frequency converter to achieve the purpose of controlling the flow rate. Finally, the water supply pipeline is connected to the dam of the pump and the tailings dam model, and the confluence in the dam is simulated by the pipeline injection flow. During this process, the water supply pool remains filled to prevent the water pressure change of the water supply pool from affecting the pump. The recording camera (provided by SONY in settings of the resolution of 1,920 × 1,080 and 50 frames per second, Beijing city, the People's Republic of China) was selected as the visual recording equipment for this dam damage monitoring system (DDMS). The vertical and horizontal dimensions of the modeled tailing dam with specific locations of pre-embedded reinforcements in geogrid are schematically depicted in Figure 5.

The slope monitoring of the tailings dam is used to monitor the change of gully caused by overtopping

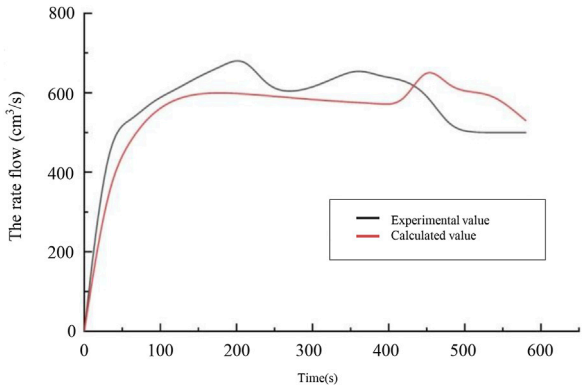


FIGURE 8
Comparison of flow rate.

overflow and record the whole process of overtopping dam break. The breach change monitoring is to measure the breach change of the dam section, which is measured by inserting the vertical steel wire into the gully surface, and the length of the measured steel wire is the gully depth. The size of the test model is length × width × height (260 cm × 60 cm × 140 cm), and reinforcement spacing is 30 cm, as shown in Figure 6.

### 3.1.2 Procedure of test

1. The original tailings are crushed into powder by a crusher, and the water content is 20% according to the "Geotechnical Test Method Standard" (GB/T50123-2019, the Natural Standard of China), and the polyethylene film is sealed and treated for 24 h leading to the water content of the material is evenly distributed.
2. Tailings dam model length × width × height: 260 cm × 60 cm × 140 cm, in the stacking model using the layered compaction method, the use of compaction hammer layered compaction, in order to ensure that the degree of compaction is more uniform, in the soil above the board to make the compaction force uniform. After each layer of compaction is completed should also be for the surface of the roughening, to prevent the model stratification.
3. In the process of piling up, according to the designed test scheme, the reinforcement belt is laid horizontally inside the tailings dam. The method of laying the reinforcement belt is as follows: First, the compacted soil is cut in with a ring knife, and the mass of the ring knife is weighed after it is taken out. If the mass is close, it is subjected to roughening treatment, and then the reinforcement belt is placed horizontally. After the reinforcement belt is laid, a thin layer of soil is added to the upper layer of the reinforcement belt, and then compaction and roughening are performed to prevent the influence of stratification.
4. After the completion of the heap, set the water level mark in the reservoir, and install the high-resolution camera, respectively, to monitor and record the water level changes and the erosion process of the tailings dam surface.
5. After the installation and commissioning of the monitoring equipment are completed, it is assumed that the drainage system in the reservoir fails, and the water injection system is opened to inject water into the reservoir.
6. After the end of the test, repeat the above operation for the next set of tests.

As shown in Figure 7, after the water flow overflows the dam crest, a rectangular-like erosion surface is formed on the slope, and then a breach is formed, and the downstream erosion surface gradually increases in a fan shape. As the water flow continues to scour, the breach gradually develops, forming gullies in the upper and lower reaches until the water flow no longer erodes and the breach no longer develops, it is considered that the overtopping failure is over.

According to the results of the overtopping test of reinforced tailings in each group, the test results did not cause erosion to the dam foundation, which was an incomplete dam break. This was because the water capacity in the tailings dam was small, and no erosion occurred after scouring to a certain position, that is, the overtopping stopped. According to the test phenomenon, the overtopping dam-break process of tailings under the condition of reinforcement-soil-water coupling is divided into five stages: water overflow stage, breach formation stage, gully formation stage, breach development stage, and dam stability stage. In the water overflow stage, the water injection system continues to inject water into the reservoir, resulting in a continuous rise in the water level. When the water level in the reservoir is higher than the dam crest, the water flow will begin to overflow from the dam crest. The water flow scours downstream along the dam's surface. At this stage, the scour surface of each group of tests is basically close to a long strip, and no strong erosion damage is carried out.

**TABLE 4 Comparison of calculated values.**

| Name of parameter | The model calculates the value | Test values | Error |
|---|---|---|---|
| Final breach depth/*cm* | 38 | 36 | 5.5% |
| Final breach width/*cm* | 20.35 | 20 | 1.75% |
| Discharge flow $m^3/s$ | 0.00078 | 0.00066 | 18% |

### 3.2 Model validation

The input test parameters are shown below in Tables 1, 2, 3.

Using Python scientific calculation, through time iteration calculation, the flow calculation is shown in Figure 8. The curve first indicates a rapid increase trend and then slowly decreases. When the analysis collapses, the flow rate increases instantaneously and then decreases rapidly, and finally tends to be flat and close to the inflow flow. The overall trend is similar to the test flow trend.

Calculated the final width of the diffuse roof breach dam is 20.52 cm, the last breach depth is 38 cm, and the maximum peak flow rate is 0.00078 $m^3/s$. As shown in Table 4, the maximum breach depth and width calculation are more consistent, and the error is 5.5% and 1.75%, respectively, and the calculated peak discharge flow rate and the test value error are 18%.

The computational model fits well with the experimental values, but the discharge flow error is significant. The model assumption regards the reinforced tailings dam as a uniform whole, ignoring the blocking movement of the reinforcement belt and the water flow, which needs further improvement.

## 4 Conclusion

The findings of this paper provided insights for the overtopping erosion of the reinforced fine-grained tailings dam overtopping failure. A prediction model for reinforced tailings breach development was established by inserting the erosion model derived from the reinforced tailings erosion test and the reinforced slope stability analysis. The erosion rate, breach depth, and width could all be predicted using the created formulas. The research presented in this paper resulted in the following findings:

1. The mathematical model of the breach development predicting of the reinforced fine-grained tailings dam overtopping is established. In the model, the formula of supported erosion rate is obtained by using the principle of water flow shear stress, the development of breach erosion is simulated by the time iterative calculation method, and the stability of reinforced breach slope is analyzed by the limit equilibrium method.
2. A physical model is established to simulate the breach development process of the reinforced tailings dam, and the final breach depth, width, and discharge flow are obtained. Comparing the data measured by the reinforced tailings physical model test with the calculated values by the mathematical model, the depth and width errors are 5.5% and 1.75% respectively, and the calculated peak discharge flow rate and the test value error are 18%. The mathematical model had a good prediction effect on the evolution of the breach.
3. The model still has significant uncertainty, and it is essential to consider the heterogeneity of dam materials. There is an urgent need for field cases to verify the existing models further.

## Data availability statement

The original contributions presented in the study are included in the article/Supplementary Material, further inquiries can be directed to the corresponding author.

## Author contributions

Conceptualization, MC and XL; methodology, XJ and XL; validation, MC; supervision, MC; writing—original draft preparation, XJ and DX; writing—review and editing, YZ, XL, and DX.

## Funding

This research is funded by the National Natural Science Foundation of China (No. 51974051), China Occupational Safety and Health Association (CXCY-2021-19), the Self-made Equipment Foundation of Chongqing University of Science and Technology (No. ZZSB2019013), the Graduate Innovation Program Project of Chongqing University of Science and Technology (Grants No. YKJCX2120702, YKJCX2120719, and YKJCX2120721).

## Conflict of interest

Author MC was employed by the company Chongqing Safety Science and Technology Co., Ltd., and Author DX was employed by the company Chongqing 107 Municipal Construction Engineering Co., Ltd.

The remaining authors declare that the research was conducted in the absence of any commercial or financial relationships that could be construed as a potential conflict of interest.

## Publisher's note

# References

Abderrezzak, K. E. K., Moran, A. D., Tassi, P., Ata, R., and Hervouet, J. M. (2016). Modelling river bank erosion using a 2D depth-averaged numerical model of flow and non-cohesive, non-uniform sediment transport. *Adv. Water Resour.* 93, 75–88. doi:10.1016/j.advwatres.2015.11.004

Agurto-Detzel, H., Bianchi, M., Assumpção, M., Schimmel, M., Collaco, B., Ciardelli, C., et al. (2016). The tailings dam failure of 5 November 2015 in SE Brazil and its preceding seismic sequence. *Geophys. Res. Lett.* 43 (10), 4929–4936. doi:10.1002/2016gl069257

Cantero-Chinchilla, F. N., Castro-Orgaz, O., Dey, S., and Ayuso-Muñoz, J. L. (2016). Nonhydrostatic dam break flows. II: One-dimensional depth-averaged modeling for movable bed flows. *J. Hydraul. Eng.* 142 (12), 04016069. doi:10.1061/(asce)hy.1943-7900.0001206

Carmo, F. F. D., Kamino, L. H. Y., Junior, R. T., de Campos, I. C., do Carmo, F. F., Silvino, G., et al. (2017). Fundão tailings dam failures: The environment tragedy of the largest technological disaster of Brazilian mining in global context. *Perspect. Ecol. Conserv.* 15, 145–151. doi:10.1016/j.pecon.2017.06.002

Chen, X., Jing, X., Cai, H., Wang, Y., and Ye, L. (2021). Hydraulic erosion rate of reinforced tailings: Laboratory investigation and prediction model. *Adv. Mater. Sci. Eng.* 2021, 1–13. doi:10.1155/2021/8764862

Chen, Z. Y., Chen, S., Wang, L., and Zhang, Q. (2019). Analysis of Earth-rock dam break flood: Theory and calculation program. *Hydro Sci. Cold Zone Eng.* 2 (2), 12–19.

Chen, Z. Y., Ma, L., Yu, S., Chen, S., Zhou, X., Sun, P., et al. (2015). Back analysis of the draining process of the Tangjiashan barrier lake. *J. Hydraul. Eng.* 141, 05014011. doi:10.1061/(asce)hy.1943-7900.0000965

Clarkson, L., and Williams, D. (2021). An overview of conventional tailings dam geotechnical failure mechanisms. *Min. Metallurgy Explor.* 38 (3), 1305–1328. doi:10.1007/s42461-021-00381-3

Coleman, S. E., Andrews, D. P., and Webby, M. G. (2002). Overtopping breaching of non-cohesive homogeneous embankments. *J. Hydraul. Eng.* 128 (9), 829–838. doi:10.1061/(asce)0733-9429(2002)128:9(829)

Cristofano, E. A. (1973). *Method of computing erosion rate for failure of earthfill dams*. Denver: US Department of the Interior, Bureau of Reclamation, Engineering and Research Center.

Di Cristo, C., Evangelista, S., Greco, M., Iervolino, M., Leopardi, A., and Vacca, A. (2018). Dam-break waves over an erodible embankment: Experiments and simulations. *J. Hydraulic Res.* 56 (2), 196–210. doi:10.1080/00221686.2017.1313322

Fread, D. L. (1981). *The NWS simplified dam-break flood forecasting model*. Silver Spring, Maryland: National Weather Service, 164–197.

Hanson, G. J., Cook, K. R., and Hunt, S. L. (2005). Physical modeling of overtopping erosion and breach formation of cohesive embankments. *Trans. ASAE* 48 (5), 1783–1794. doi:10.13031/2013.20012

Jing, X. F., Chen, Y. L., Williams, D. J., Serna, M. L., and Zheng, H. (2019). Overtopping failure of a reinforced tailings dam: Laboratory investigation and forecasting model of dam failure. *Water* 11, 315. doi:10.3390/w11020315

Kesserwani, G., Shamkhalchian, A., and Zadeh, M. J. (2014). Fully coupled discontinuous Galerkin modeling of dam-break flows over movable bed with sediment transport. *J. Hydraul. Eng.* 140 (4). doi:10.1061/(asce)hy.1943-7900.0000860

Li, X. S., Peng, J., Xie, Y. L., Li, Q., Zhou, T., Wang, J., et al. (2022). Influence of high-temperature treatment on strength and failure behaviors of a quartz-rich sandstone under true triaxial condition. *Lithosphere* 2022, 3086647. doi:10.2113/2022/3086647

Lottermoser, B. G., and Ashley, P. M. (2005). Tailings dam seepage at the rehabilitated Mary Kathleen uranium mine, Australia. *J. Geochem. Explor.* 85 (3), 119–137. doi:10.1016/j.gexplo.2005.01.001

Marsooli, R., and Wu, W. (2015). Three-dimensional numerical modeling of dam-break flows with sediment transport over movable beds. *J. Hydraul. Eng.* 10, 1061. doi:10.1061/(asce)hy.1943-7900.0000947

Meng, Q. X., Wang, J., Tao, Z., Ren, D., Zhang, G., Li, X., et al. (2021). 3D nonlinear analysis of stilling basin in complex fractured dam foundation. *Lithosphere* 2021, 2738130. doi:10.2113/2022/2738130

Michnea, A., and Gherhes, I. (2001). Impact of metals on the environment due to technical accident at Aurul Baia Mare, Romania. *Int. J. Occup. Med. Environ. Health* 14 (3), 255–259.

Mittal, H. K., and Morgenstern, N. R. (1976). Seepage control in tailings dams. *Can. Geotech. J.* 13 (3), 277–293. doi:10.1139/t76-030

Mohamed, M. A., Samuels, P. G., Morris, M. W., and Ghataora, G. S. (2002). Improving the accuracy of prediction of breach formation through embankment dams and flood embankments. Proceedings of the River Flow 2002 - International Conference on Fluvial Hydraulics September 2002, Ottignies-Louvain-la-Neuve, Belgium.

Petkovšek, G., Hassan, M. A. A. M., Lumbroso, D., and Roca Collell, M. (2021). A two-fluid simulation of tailings dam breaching. *Mine Water Environ.* 40 (1), 151–165. doi:10.1007/s10230-020-00717-3

Psarropoulos, P. N., and Tsompanakis, Y. (2008). Stability of tailings dams under static and seismic loading. *Can. Geotech. J.* 45 (5), 663–675. doi:10.1139/t08-014

Silva, F., Lambe, T. W., and Marr, W. A. (2008). Probability and risk of slope failure. *J. Geotech. Geoenviron. Eng.* 34 (12), 1691–1699. doi:10.1061/(asce)1090-0241(2008)134:12(1691)

Singh, V. P., Scarlatos, P. D., Collins, J. G., and Jourdan, M. R. (1988). Breach erosion of Earth fill dams (BEED) model. *Nat. Hazards (Dordr).* 1 (2), 161–180. doi:10.1007/bf00126613

Sun, E. J., Zhang, X. K., Li, Z. X., and Wang, Y. H. (2012). Tailings dam flood overtopping failure evolution pattern. *Procedia Eng.* 28, 356–362. doi:10.1016/j.proeng.2012.01.733

Van Niekerk, H. J., and Viljoen, M. J. (2005). Causes and consequences of the Merriespruit and other tailings-dam failures. *Land Degrad. Dev.* 16 (2), 201–212. doi:10.1002/ldr.681

Villavicencio, G., Espinace, R., Palma, J., Fourie, A., and Valenzuela, P. (2014). Failures of sand tailings dams in a highly seismic country. *Can. Geotech. J.* 51 (4), 449–464. doi:10.1139/cgj-2013-0142

Wu, T., and Qin, J. (2018). Experimental study of a tailings impoundment dam failure due to overtopping. *Mine Water Environ.* 37 (2), 272–280. doi:10.1007/s10230-018-0529-x

Zhang, L., Peng, M., Chang, D., and Xu, Y. (2016). *Dam failure mechanism sand risk assessment*. 1st. Singapore: John Wiley & Sons.

Zhong, Q., Wu, W., Chen, S., and Wang, M. (2016). Comparison of simplified physically based dam breach models. *Nat. Hazards (Dordr).* 84 (2), 1385–1418. doi:10.1007/s11069-016-2492-9

frontiers | Frontiers in Earth Science

TYPE Original Research
PUBLISHED 20 March 2023
DOI 10.3389/feart.2023.1154791



OPEN ACCESS

EDITED BY
Lijie Guo,
Beijing Mining and Metallurgy Technology Group Co., Ltd., China

REVIEWED BY
Guangjin Wang,
Kunming University of Science and Technology, China
Qing-Fa Chen,
Guangxi University, China

*CORRESPONDENCE
Chao Zhang,
20172001004@cqu.edu.cn

SPECIALTY SECTION
This article was submitted to Geoscience and Society, a section of the journal Frontiers in Earth Science

RECEIVED 31 January 2023
ACCEPTED 03 March 2023
PUBLISHED 20 March 2023

CITATION
Chen Q, Li Z, Zhang C, Dai Z, Wang X and Zhang X (2023), Non-linear mechanical characteristics of tailings in large-scale high tailings dams.
*Front. Earth Sci.* 11:1154791.
doi: 10.3389/feart.2023.1154791



# Non-linear mechanical characteristics of tailings in large-scale high tailings dams

Qinglin Chen[1], Zugui Li[1], Chao Zhang[2]*, Zeyu Dai[1], Xiaojun Wang[1] and Xuepeng Zhang[1]

[1]School of Resources and Environmental Engineering, Jiangxi University of Science and Technology, Ganzhou, Jiangxi, China, [2]State Key Laboratory of Geomechanics and Geotechnical Engineering, Institute of Rock and Soil Mechanics, Chinese Academy of Sciences, Wuhan, Hubei, China

The non-linear mechanical characteristics of tailings under high pressure are the research foundation of large-scale high tailings dams. Considering the high stress caused by high tailing ponds, consolidated drained triaxial shear tests were carried out. The deterioration mechanism of non-linear mechanics was revealed by particle crushing. The test results show that sample density has a great influence on volumetric strain under low pressure. However, volumetric strain is not related to sample density under high pressure. The shear strength of the tailings is significantly non-linear. The internal friction angle under low pressure can still be obtained by the traditional linear Mohr–Coulomb criterion and the internal friction angle under high pressure by the power function of the Mohr criterion. The particle crushing of tailings occurs not only at high pressure but also at low pressure. The value of the breakage index increases with sample density. The non-linear mechanics of shear strength are affected by particle breakage. The breakage index value increases linearly with increasing shear strength, indicating that the high density of the deep part of the tailings dam is prone to particle crushing, which affects the stability of the large-scale high dam.

KEYWORDS

**tailings, high pressure, non-linear mechanics, particle crushing, breakage index**

## 1 Introduction

Tailings are the lower-grade tailings residue after ore has been sorted and the tailings disposed of by manually constructing a tailings pond (Wu et al., 2020; Chen et al., 2023). More than 1.4 billion tons of tailings are disposed of in tailings ponds every year in China, and a total of 14.6 billion tons had been deposited in tailings ponds by 2014 (Zhou et al., 2020). Tailings dams are being piled higher and higher due to the numerous demands for mineral resources and the restricted use of land resources. At present, there are at least 26 tailings dams with a height greater than 100 m and at least 10 tailings dams with a storage capacity over 100 million $m^3$. The highest tailings dam in the world is the Wanniangou tailings dam in Sichuan Province, China, with a total dam height of 325 m and a total storage capacity of 326 million $m^3$ (Wang, 2014). The largest tailings dam in Asia is the Dexing No. 4 tailings dam, with a total dam height of 208 m and a storage capacity of 890 million $m^3$. Stress in the deep regions of high tailings ponds has reached 4 MPa (Wu et al., 2017). Potential safety threats to the stability of the dam are becoming more prominent because the stress level in the dam increases with its height.

Catastrophic accidents caused by the collapse of high tailings dams occur frequently (Rico et al., 2008). Deaths from tailings dam instability are not uncommon. For example, on

18 October 2000, a tailings pond collapsed in Nandan County, Guangxi Province, leading to 28 deaths and 56 injuries (Guo, 2010). In 2008, a tailings pond collapsed in Xianfen County, Shanxi Province, causing a tailings discharge of 268,000 $m^3$, covering an area of 30.2 ha, and resulting in 276 deaths and 34 injuries (Guo and Wu, 2009). On 5 November 2015, the collapse of a tailings pond in the state of Minas Gerais, Brazil led to 19 deaths and is considered the worst environmental disaster. On 25 January 2019, a tailings pond collapsed in Brumadinho, Brazil, leading to 58 deaths and 305 missing people (Zhang et al., 2020).

The statistical analysis of many tailings pond accidents reveals many reasons for tailings pond accidents, including rainstorms, overtopping, earthquake liquefaction, seepage failure, dam foundation instability, dam structure failure, and load increase. The final cause of dam instability, which mainly refers to changes in the stress fields and seepage fields of tailings dams caused by the aforementioned factors (Wang et al., 2021), is discussed. It is worth noting that the instability characteristics of tailings ponds are completely different at high stress and low stress, so it is necessary to study them. The mechanical characteristics of the soil are significantly different under high pressure than under low pressure. The strength of the soil under high pressure varies non-linearly and is accompanied by particle crushing. Slope stability prediction for large-scale high slopes is a complex, non-linear system problem (Wang G. G. et al., 2020; Wang J. X. et al., 2020). The compression and strength characteristics of tailings sand under high pressure were studied by Zhang (1995), who believed the shear strength envelope to be related to the saturation of tailings sand and drainage consolidation conditions. The shear strength parameter of tailings is significantly less in the deep zone than in the shallow zone (Zhang et al., 2010). To study the strength characteristics of tailings materials under high pressure, numerous triaxial tests were carried out under high pressure, as well as a power function Mohr strength criterion, as established by Liu et al. (2012). Wang et al. (2023) simulated the tailings pond accumulation process using soil tests and indoor physical model tests and found that the saturation line increased with increasing dam height in the physical model. The triaxial compression tests were carried out using a high-pressure triaxial apparatus by Zhang et al. (2020) and revealed that the tailings exhibit strain softening under low confining pressure and strain hardening under high confining pressure. Chen et al. (2022) conducted consolidated undrained axial shear tests with a high-pressure triaxial apparatus to study the mechanical behavior of sandwich tailings under high confining pressure and compared the results against tests under low confining pressure. The triaxial compression and triaxial elongation of Cambria sand under high pressure were carried out by Lade and Bopp (2005) and revealed that the internal friction angle of Cambria sand is larger in triaxial compression than in triaxial elongation.

In reality, the deposition structure of high tailings dams is very complex. Consolidated drained tests of tailings under high stress caused by high dam tailings ponds were carried out. The mechanical properties of three sets of tailings specimens with different initial densities were investigated. The deterioration mechanism of non-linear mechanics was explained by particle breakage.

## 2 Specimen materials and methods

### 2.1 Test instrument

Strain-controlled high-pressure triaxial equipment mainly includes four major components: a pressure testing machine, a high-pressure triaxial pressure chamber, a pressure volume controller, and a data acquisition system. The triaxial pressure chamber is made of stainless steel, with a wall thickness of 12 mm, and the perimeter pressure connection pipe is made of copper, with a maximum perimeter pressure of 5 MPa and a counterpressure of 1 MPa. The maximum travel of the motor is 80 mm. The maximum load of the axial load sensor is 60 kN, the maximum measurement range of the axial displacement sensor is 20 mm, and the volume variation capacity of the pressure volume controller is 200 mL. Three types of tests can be performed: unconsolidated undrained shear (UU shear), consolidated

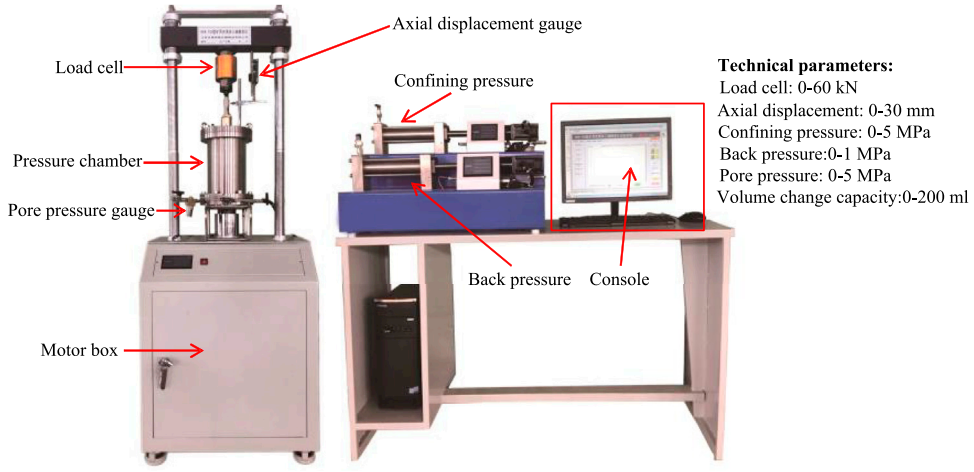


FIGURE 1
Strain-controlled high-pressure triaxial apparatus.

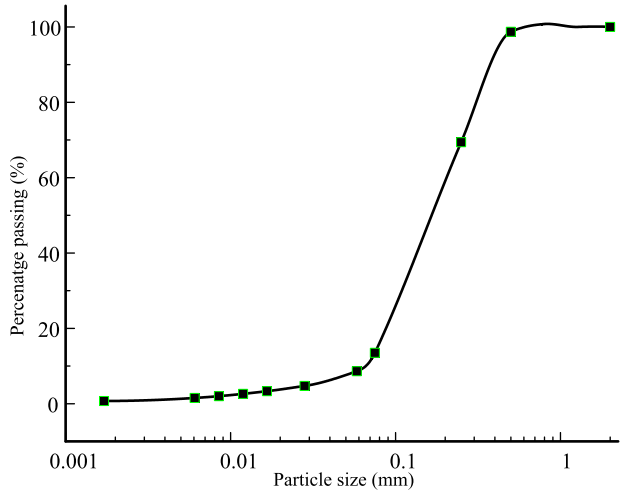


FIGURE 2
Particle size distribution of tailings.

undrained shear (CU shear), and consolidated drained shear (CD shear). The high-pressure triaxial testing machine is shown in Figure 1.

## 2.2 Tailings specimen

The tailings samples were taken from the No. 4 tailings dam in the Dexing copper mine in Jiangxi Province (Wu et al., 2017), the largest tailings dam in Asia, with a maximum design height of 208 m. The undisturbed tailings are gray and non-cohesive, with a particle-specific gravity of 2.7, an average particle size of 0.65 mm, and an inhomogeneity factor of 3.4. The tailings contain 1.4% cohesive particles, 12.1% powder particles, and 86.5% sand particles. The particle size distribution curve is shown in Figure 2 and the physical property indexes are shown in Table 1.

The German Bruker AXSD8-Focus X-ray diffractometer was used to analyze the mineral composition of the tailings, and the results are shown in Table 1. The tailings are mainly composed of quartz sand, with a content of 53.61%; the other mineral components are illite, plagioclase, dolomite, and calcite, in descending order of content. Microscopic SEM images of the tailing samples are shown in Figure 3. The tailings particles exist in granular form, and their surface morphology is uneven and angular. Some of the particles have sharp edges, and the particles do not have a uniform profile.

## 2.3 Specimen preparation and test plan

According to test regulations (GB/T50123, 1999), the size diameter of the tailings sample in the triaxial test was 39.1 mm and the height was 80 mm. Specimen preparation was performed using the wet sample preparation method (Wood et al., 2008). The moisture content of the samples was 10%. To ensure homogeneity, the specimens were prepared by the layered tamped method: the prepared samples were poured into the sampler three times and were then tamped with a tamping rod. The contact surface of each layer was shaved.

To study the mechanical properties of tailings under high pressure, three densities of specimens were set to 1.4 g/cm3, 1.6 g/cm3, and 1.8 g/cm3, representing loose, medium, and dense

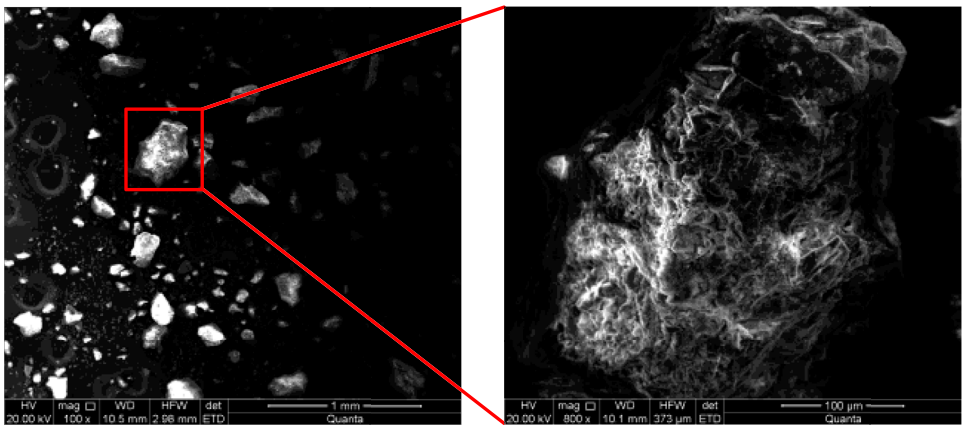

FIGURE 3
Shape topography of tailing particles.

**TABLE 1 Mineral composition of tailings.**

| Name of the mineral | Quartz sand | Illite | Oblique chlorite | Dolomite | Calcite |
|---|---|---|---|---|---|
| Accounted for (%) | 53.61 | 31.64 | 8.09 | 4.21 | 2.45 |

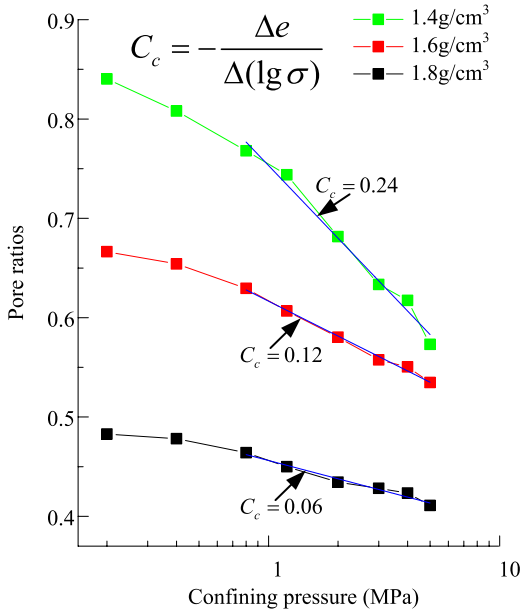


FIGURE 4
Consolidation curves of specimens with different densities.

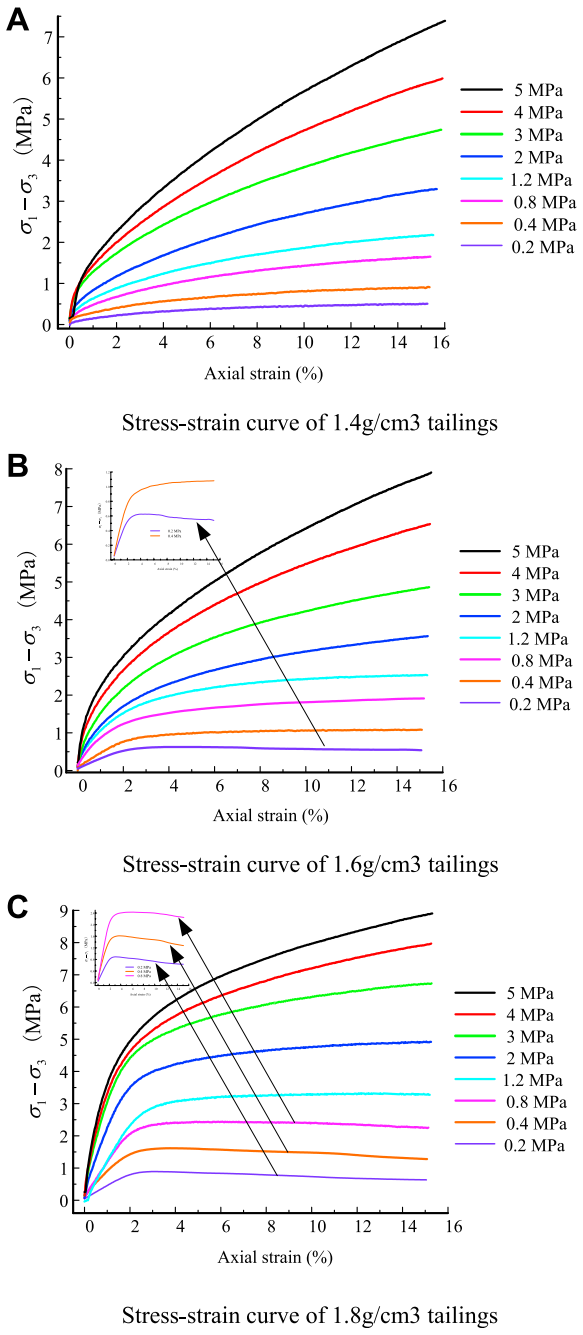


FIGURE 5
Stress–strain relationships of tailings for different densities. **(A)** Stress–strain curve for 1.4 g/cm$^3$ tailings. **(B)** Stress–strain curve for 1.6 g/cm$^3$ tailings. **(C)** Stress–strain curve for 1.8 g/cm$^3$ tailings.

tailings specimens. The test confining pressure was 0.2 MPa, 0.4 MPa, 0.8 MPa, 1.2 MPa, 2 MPa, 3 MPa, 4 MPa, and 5 MPa in this test. Less than 0.8 MPa is low confining pressure, and more than 0.8 MPa is high confining pressure. Because the accumulation rate of a tailings dam is slower than that of pore pressure dissipation during dam construction, the consolidated drained test method was adopted in this test. To prevent the rubber membrane being broken during the test, a reasonable thickness of the rubber membrane should be selected for different confining pressures. Based on the literature (Henkel and Gilbert, 1952; Ren, 2018), a rubber film with a thickness of 0.38 mm was chosen for specimens with confining pressures of less than 0.8 MPa. For specimens with confining pressures greater than 0.8 MPa and less than 2 MPa, a rubber film with a thickness of 0.5 mm was chosen. For specimens with a confining pressure greater than 2 MPa, a 1-mm rubber film was used. When a prepared tailings specimen is installed directly in the triaxial pressure chamber, the specimens are easily disturbed and damaged. Therefore, the freezing method was used before installing the specimen: the specimen was installed in the triaxial pressure chamber after freezing, then saturated using the head saturation method while the confining pressure was slowly applied. The shear rate was 0.074 mm/min, and the test was stopped when the axial strain reached 15% (GB/T50123 1999).

# 3 Non-linear mechanical properties of tailings

## 3.1 Isotropic consolidation compression

Isotropic compression tests were conducted on three tailings specimens with different densities under confining pressures of 0–5 MPa. The consolidation volume change in the test was measured by the drainpipe. After the consolidation time reached 4 h, the specimen pore pressure dropped to zero and the drainage volume was kept constant. Therefore, the specimen consolidation was close to stability after 4 h. The isotropic consolidation curves of tailings specimens with different densities could be obtained and are shown in Figure 4.

The pore ratio of the specimens of three different densities decreased with increased confining pressure. The pore ratio for the

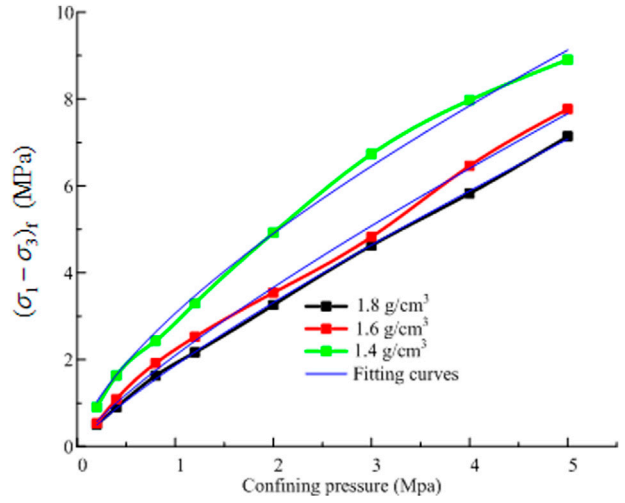


FIGURE 6
Relationship between shear strength and confining pressure.

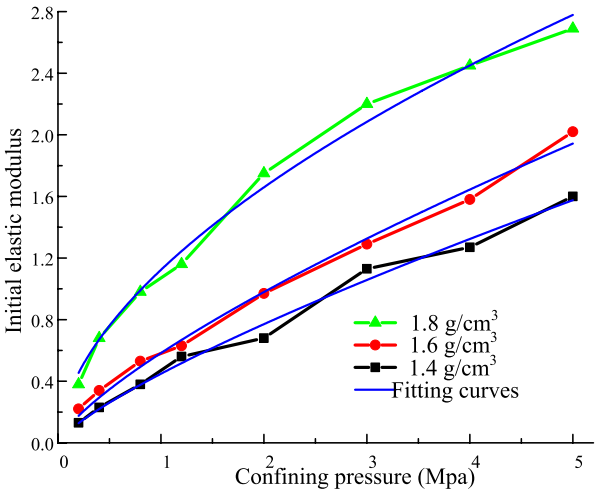


FIGURE 7
Relationship between initial elastic modulus and confining pressure.

three groups of specimens did not approach a fixed value in the pressure range of 5 MPa. The pore ratio for specimens with densities of 1.4 g/cm$^3$ and 1.6 g/cm$^3$ gradually approached 0.55. The pore ratio of the specimen with density of 1.8 g/cm$^3$ still had a large deviation from the other two groups of specimens. The consolidation curves for three groups of specimens were curvilinear under low confining pressure and a straight line under high confining pressure. In the range of high confining pressure, the linear fitting method was used to obtain a straight-line segment; the slope of the straight-line segment could be expressed by the compression index $C_c$, defined as

$$C_c = -\frac{\Delta e}{\Delta(\lg \sigma)}. \quad (1)$$

In the formula, $\Delta e$ is the amount of pore ratio reduction under the lateral limiting condition and $\Delta(\lg \sigma)$ is the effective stress increase under the confined condition. The compression index $C_c$ decreases with increasing specimen density. The compression index $C_c$ of the specimen with a density of 1.8 g/cm$^3$ is 0.06. The compression index $C_c$ of the specimen with a density of 1.6 g/cm$^3$ is 0.12. The compression index $C_c$ of the specimen with a density of 1.4 g/cm$^3$ is 0.24.

## 3.2 Stress–strain curves

Figure 5 presents the stress–strain curves of the tailings for specimens at the three different densities. For the specimens with densities of 1.4 g/cm$^3$, the stress–strain curves are all strain-hardened. The stress increases with increasing axial strain, the strain-elastic phase is not obvious, and the specimens show mainly strain-plastic behavior.

For the specimens with a density of 1.6 g/cm$^3$, the stress–strain curve is only strain-softening at 0.2 MPa confining pressure and is strain-hardening at other confining pressures. At an axial strain of 0%–2%, the specimens mainly exhibit strain–elastic behavior with a rapid increase in stress. When the axial strain is greater than 2%, the specimen mainly exhibits strain–plastic behavior with a slow increase in stress.

**TABLE 2 Fitting parameters of shear strength.**

| Density of (g/cm$^3$) | $a$ | $b$ | $R^2$ |
|---|---|---|---|
| 1.4 | 1.9 | 0.83 | 0.999 |
| 1.6 | 2.1 | 0.81 | 0.997 |
| 1.8 | 3.1 | 0.68 | 0.996 |

For the specimens with a density of 1.8 g/cm$^3$, the stress–strain curves under 0.2 MPa, 0.4 MPa, and 0.8 MPa confining pressure are of the strain-softening type. The stress increases rapidly and reaches a peak rapidly, then drops after the peak. The peak corresponds to an axial strain of 3%. Other stress–strain curves exhibit hardening types. The stress increases rapidly and then slowly with increasing axial strain.

In summary, the stress–strain curves of the specimens at high confining pressure ($\sigma_3$>0.8 MPa) exhibit a strain-hardening type regardless of whether they are loose or dense specimens. The hardening behavior of the specimens increases with increasing confining pressure, which means that the specimens' strain type at high pressure is independent of their density. At low pressures ($\sigma_3$<0.8 MPa), the strain-softening behavior of the specimen is more likely to be present with increasing density. Dense specimens are prone to softening behavior under low pressure.

Figure 6 presents the relationship between the peak strength and confining pressure of different-density specimens. The higher the density of the specimen, the higher the peak strength. The difference between the peak strengths of the specimens increases with increased confining pressure. The peak strength shows a

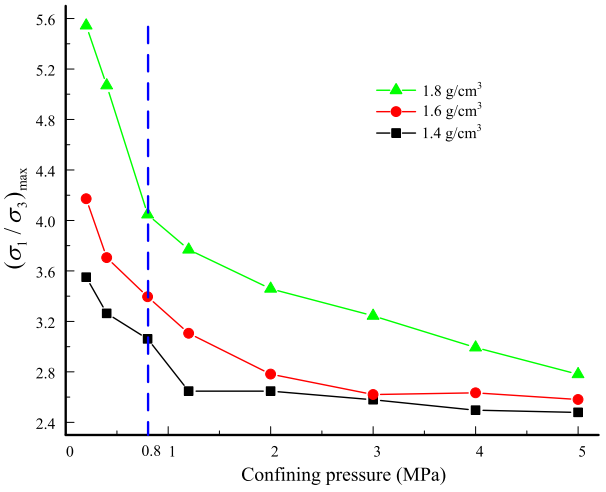


FIGURE 8
Maximum stress ratio of tailings for three different densities.

**TABLE 3 Fitting parameters of the initial elastic modulus.**

| Density of (g/cm$^3$) | *c* | *d* | $R^2$ |
|---|---|---|---|
| 1.4 | 0.45 | 0.78 | 0.989 |
| 1.6 | 0.58 | 0.75 | 0.992 |
| 1.8 | 1.12 | 0.56 | 0.99 |

downward deflection, which indicates an obvious non-linear strength behavior of the tailings; this means that the strength parameter of the tailings is variable under high pressure and can be explained by the Mohr–Coulomb criterion. The criterion is expressed in Eq. 2:

$$(\sigma_1 - \sigma_3)_f = \frac{2}{1 - \sin\varphi}(c\cos\varphi + \sigma_3 \sin\varphi). \quad (2)$$

Only when the strength parameter is a constant value is the relationship between the peak strength $(\sigma_1-\sigma_3)_f$ and the confining pressure $\sigma_3$ linear, according to Eq. 2. An obvious non-linear strength behavior occurred in the test. Therefore, the strength parameter in Eq. 2 is variable. The internal friction angle is gradually decreasing because the strength is deteriorated by particle crushing under high pressure.

The relationship between the peak strength $(\sigma_1-\sigma_3)_f$ and the confining pressure under high pressures can be represented by the non-linear strength mathematical model proposed by Yin et al. (1980). It is defined as

$$(\sigma_1 - \sigma_3)_f = a\sigma^b, \quad (3)$$

where *a* and *b* are test constants.

The parameters *a* and *b* can be obtained by Eq. 3. The fitting results are shown in Table 2. The fitted curves are in good agreement with the peak strength. The parameter *a*, which increases with increasing specimen density, represents the linear growth rate of the peak strength. The parameter *b* decreases with increasing specimen density and represents the

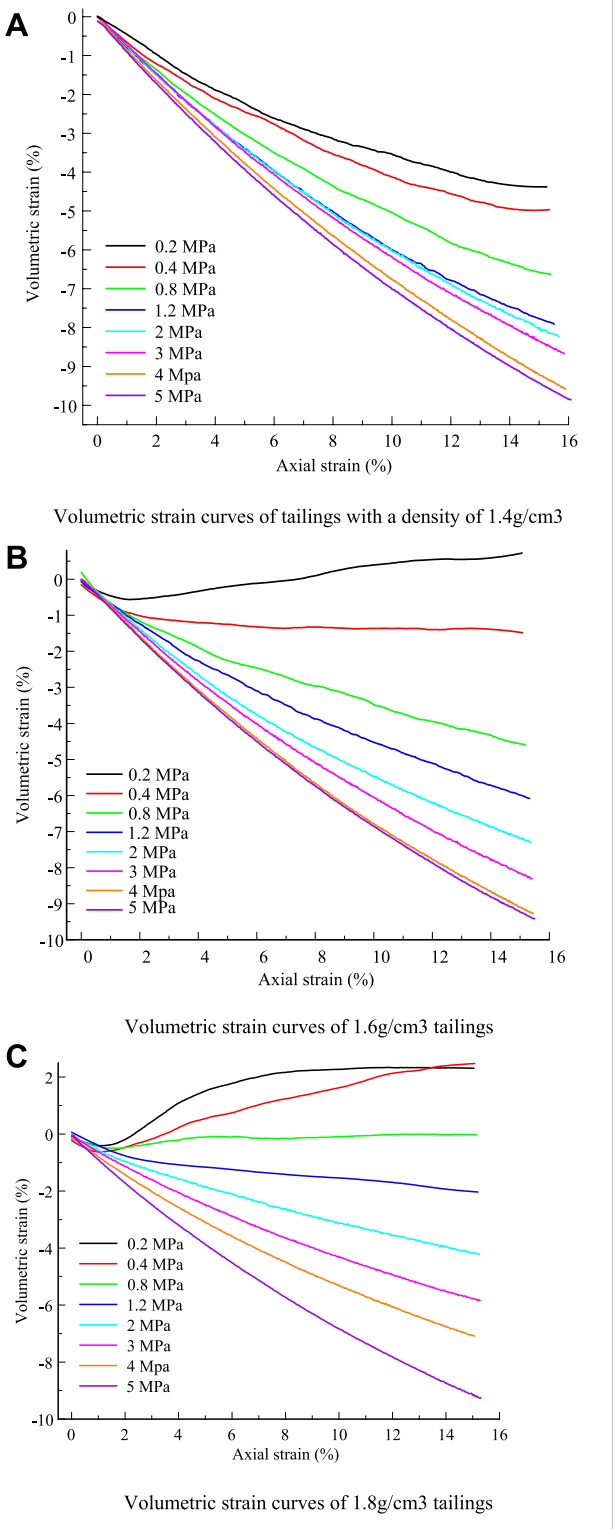


FIGURE 9
Volumetric strain of tailings for different densities. **(A)** Volumetric strain curves of tailings with a density of 1.4 g/cm$^3$. **(B)** Volumetric strain curves of 1.6-g/cm$^3$ tailings. **(C)** Volumetric strain curves of 1.8-g/cm$^3$ tailings.

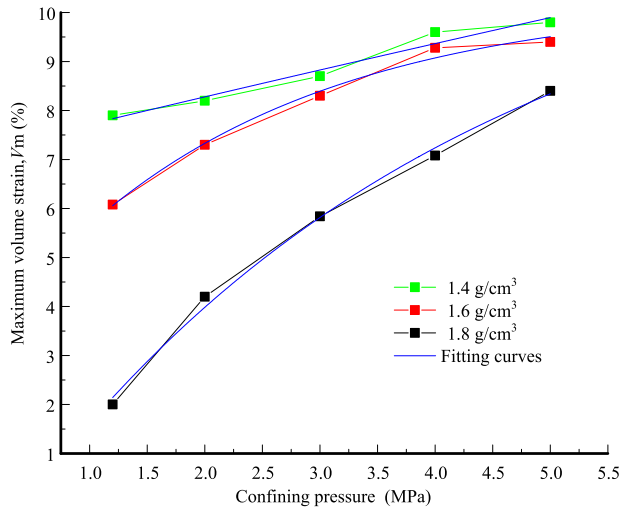


FIGURE 10
Maximum volume strain under different confining pressures.

non-linear growth rate of the peak strength; it indicates that there are obvious non-linear strength behaviors for tailings specimens under high pressure.

Figure 7 presents the relationship between the initial elastic modulus and the confining pressure for different-density specimens. The initial elastic modulus is the slope of the stress–strain curve at the initial stage. The evolution law of the initial elastic modulus is similar to the peak strength. The initial modulus increases with confining pressure. The between the initial elastic modulus and the confining pressure is non-linear. It can be expressed by Eq. 4:

$$E_e = c\sigma^d, \tag{4}$$

where $c$ and $d$ are the test constants.

The parameters $c$ and $d$ can be obtained by Eq. 4. The fitting results are shown in Table 3. The fitted curve is in good agreement with the initial elastic modulus. The parameters $c$ and $d$ have the same variation as the parameters $a$ and $b$. The parameter $c$ increases as the density of the specimen increases, which represents the linear growth rate of the initial elastic modulus. The constant $d$, which decreases with increasing specimen density, represents the non-linear growth rate of the initial elastic modulus.

## 3.3 Maximum stress ratio

Figure 8 presents the maximum stress ratio of tailings with three different densities. The maximum stress ratio increases with the density of the specimen. The maximum stress ratio for the tailings of three different densities is significantly affected by the confining pressure and decreases with increasing confining pressure; the decreasing rate of the curve decreases with increasing confining pressure. When the confining pressure is 5 MPa, the maximum stress ratios of the tailings with three different densities are generally around 2.8. When the confining pressure is less than 0.8 MPa, the maximum stress ratio of tailings with three different densities decreases rapidly with increasing confining pressure. When the confining pressure is greater than 0.8 MPa, the maximum stress ratio of tailings with three different densities decreases slowly with increasing confining pressure. The Mohr–Coulomb criterion was rewritten by the stress ratio. It is expressed as

$$\left(\frac{\sigma_1}{\sigma_3}\right)_{\max} = \frac{1+\sin\varphi}{1-\sin\varphi} + \frac{2c\cos\varphi}{1-\sin\varphi}\cdot\frac{1}{\sigma_3}. \tag{5}$$

When the strength parameter is constant, the relationship between the maximum stress ratio and the confining pressure is hyperbolic. When the confining pressure is low, the maximum stress ratio is caused by the confining pressure because the strength parameter is constant. When the confining pressure is high, the strength parameter is variable due to particle breakage. The maximum stress ratio is caused by both confining pressure and particle breakage. Therefore, the relationship between the maximum stress ratio of the tailings and confining pressure under high confining pressure is not hyperbolic.

## 3.4 Volumetric strain

Figure 9 presents the volumetric strain of tailings with three different densities. For specimens with a density of 1.4 g/cm$^3$, volumetric strain decreases with increasing axial strain. Shear shrinkage occurred for all specimens. The volumetric strain of the specimen increases with confining pressure. For the specimen with a density of 1.6 g/cm$^3$, when the confining pressure was 0.2 MPa, the volumetric strain of the specimen decreased until the axial strain reached 2% and then increased with increasing axial strain. Shear dilation occurred. For the specimen under confining pressure of less than 0.2 MPa, the volumetric strain of the specimen decreased with increasing axial strain. Shear shrinkage occurred. For the specimen with a density of 1.8 g/cm$^3$, when the confining pressure was less than 0.8 MPa, the volumetric strain of the specimen decreased until the axial strain reached 1% and then increased with increasing axial strain. Shear dilation occurred. When the confining pressure was more than 0.8 MPa, the volumetric strain of the specimen decreased with increasing axial strain. Shear dilation occurred.

In summary, the density of the specimen has a great effect on volumetric strain under low pressure (a confining pressure of less than 0.8 MPa). There are two types of volumetric strain: 1) the volumetric strain of the sample decreasing with increasing axial strain and 2) the volumetric strain of the sample decreasing until it reaches a certain strain, and then increasing with increasing axial strain. These curves can be divided into three phases. 1) In the volumetric strain decrease stage, the particle pores are filled by tailings particles under axial pressure and confining pressure. The volume of the sample decreases until the volume reaches a minimum value, which is the expansion point. 2) In the volumetric strain increase stage, the particle pores increase due to the shear expansion effect. The volume of the sample increases. 3) In the volumetric strain-invariant stage, when the axial strain reaches a certain value, the volume of the specimen remains at a certain value, which is called the critical state. For the samples under confining pressure greater than 0.8 MPa, the volumetric strain of the specimen is

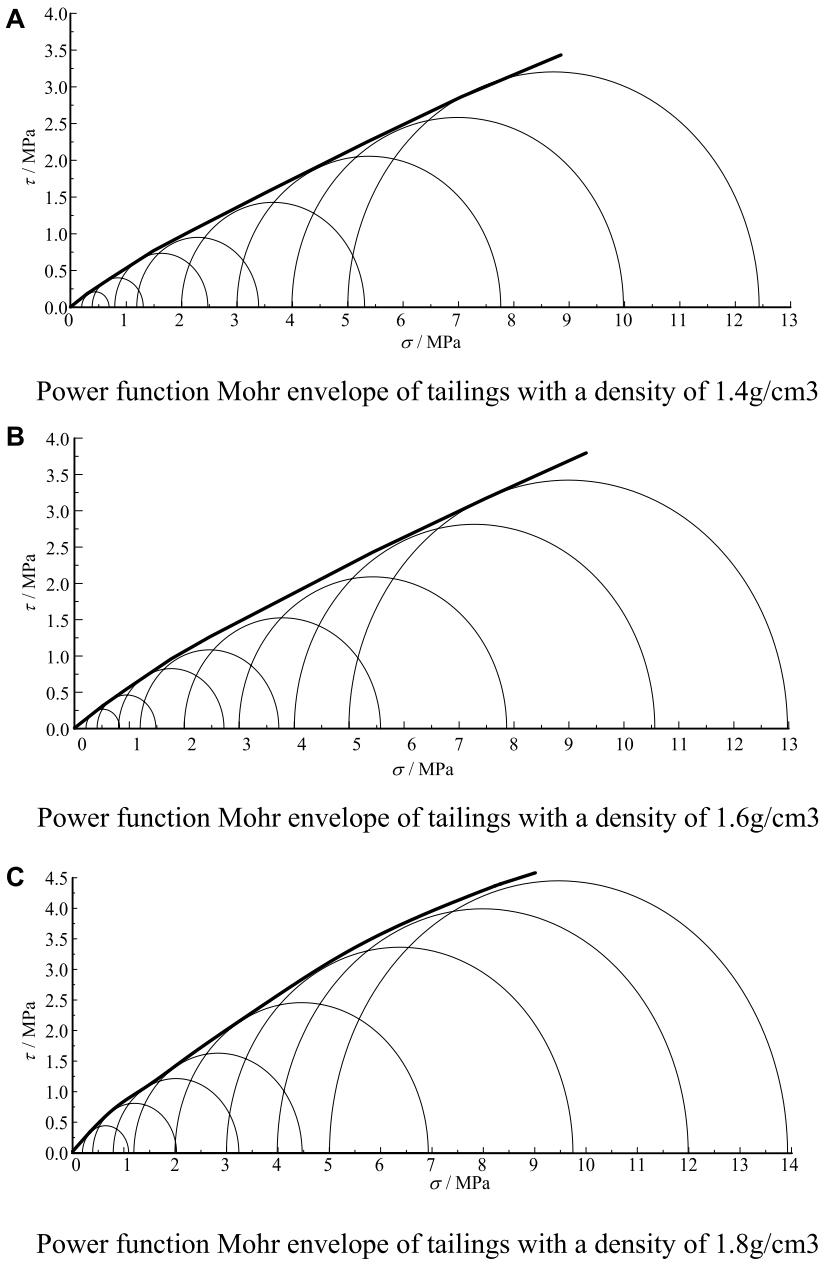


FIGURE 11
Power function Mohr envelope of tailings. **(A)** Power function Mohr envelope of tailings with a density of 1.4 g/cm$^3$. **(B)** Power function Mohr envelope of tailings with a density of 1.6 g/cm$^3$. **(C)** Power function Mohr envelope of tailings with a density of 1.8 g/cm$^3$.

negligibly affected by the density. The volumetric strain of all samples decreases with increasing axial strain, which can be explained by the mechanism of particle motion during shearing.

For dense specimens under low pressure, the motion of particles is mainly in the form of rotation and slip. The tailings particles are rearranged during the shear test. The pores between the particles of the dense specimen expand, resulting in an increase in the pores. The volume of the specimen increases.

For loose specimens under low pressure, the pores of the particles continue to be filled by the particles during the shearing process because the initial pores of the tailings are large. The volume of the specimen is decreased.

For specimens under high pressure, particle rotation and sliding are limited. The movement of particles is mainly particle breakage. The fine particle fragments continue to fill the particle pores, reducing the volume of the specimen. The specimen becomes more and more dense.

The volumetric strain curve of all specimens under high pressure decreases with increasing axial strain. To investigate the relationship between density and maximum volumetric strain of the specimen under

**TABLE 4 Internal friction angle of tailings for different densities.**

| | Confining pressure (MPa) | 0.2 | 0.4 | 0.8 | 1.2 | 2 | 3 | 4 | 5 |
|---|---|---|---|---|---|---|---|---|---|
| Density of 1.4 g/cm3 | Internal friction angle calculated using Eq. 8 (°) | 30.64 | 28.63 | 26.70 | 25.69 | 24.39 | 23.36 | 22.67 | 22.13 |
| | Internal friction angle calculated by linear Mohr–Coulomb (°) | 29.19 | 29.19 | 29.19 | — | — | — | — | — |
| | deviation (°) | 1.45 | −1.27 | −2.49 | — | — | — | — | — |
| | Recommended internal friction angle (°) | 29.19 | 29.19 | 29.19 | 25.69 | 24.39 | 23.36 | 22.67 | 22.13 |
| Density of 1.6 g/cm3 | Internal friction angle calculated using Eq. 8 (°) | 33.15 | 30.49 | 27.91 | 26.56 | 24.92 | 23.63 | 22.69 | 21.98 |
| | Internal friction angle calculated by linear Mohr–Coulomb (°) | 30.1 | 30.1 | 30.1 | — | — | — | — | — |
| | deviation (°) | 3.05 | 0.39 | −2.19 | — | — | — | — | — |
| | Recommended internal friction angle (°) | 30.1 | 30.1 | 30.1 | 26.56 | 24.92 | 23.63 | 22.69 | 21.98 |
| Density of 1.8 g/cm3 | Internal friction angle calculated using Eq. 8 (°) | 38.46 | 34.8 | 31.74 | 29.88 | 27.6 | 25.89 | 24.82 | 24.03 |
| | Internal friction angle calculated by linear Mohr–Coulomb (°) | 33.72 | 33.72 | 33.72 | — | — | — | — | — |
| | deviation (°) | 4.74 | 1.08 | −1.98 | — | — | — | — | — |
| | Recommended internal friction angle (°) | 33.72 | 33.72 | 33.72 | 29.88 | 27.6 | 25.89 | 24.82 | 24.03 |

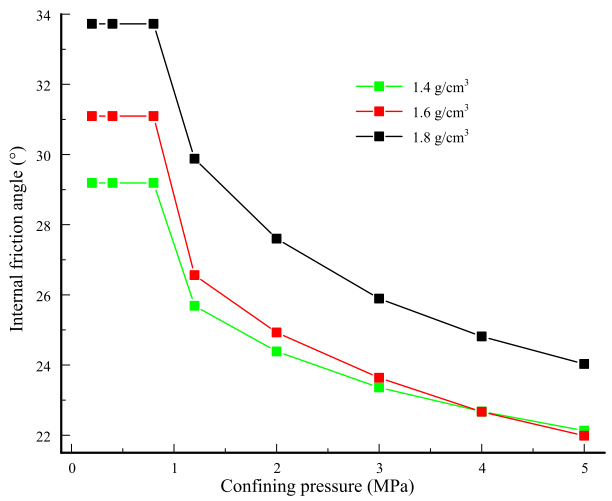


FIGURE 12
Relationship between the recommended internal friction angle and confining pressure of samples for different densities.

high pressure, the relationship between maximum volumetric strain and confining pressure was drawn. Figure 10 presents the maximum volumetric strain under different confining pressures. The relationship between maximum volumetric strain and confining pressure was fitted, and the fitting coefficients of each curve were all greater than 0.9. The fitting function of each curve is shown as, respectively,

$$\left.\begin{array}{ll} V_m = -5.08\exp\left(-\sigma_3/6.54\right) + 12.23 & \left(1.4\mathrm{g/cm^3}\right) \\ V_m = -7.22\exp\left(-\sigma_3/2.23\right) + 10.27 & \left(1.6\mathrm{g/cm^3}\right) \\ V_m = -13.12\exp\left(-\sigma_3/3.39\right) + 11.29 & \left(1.8\mathrm{g/cm^3}\right) \end{array}\right\}. \quad (6)$$

The maximum volumetric strain of the tailing specimen increases exponentially in relation to the confining pressure. The increase rate decreases with increasing confining pressure. When the confining pressure is 5 MPa, the maximum volumetric strain is almost close to the certain value. A more interesting finding is that the maximum volume strain for different-density specimens will converge to the same value when the confining pressure $\sigma_3$ tends to infinity. This means that the volumetric strain of the sample is greatly affected by density under low pressure and that the volume strain of the sample is independent of sample density under high pressure.

## 3.5 Strength envelope line

Numerous tests have shown that the linear Mohr–Coulomb strength theory is no longer applicable to high-stress-level conditions. To describe the strength characteristics under high stress, many non-linear strength criteria have been proposed. However, some disadvantages exist for these criteria. Because the shear stress index parameter is constant. The parabolic Mohr strength criterion causes limited adjustment of the bending degree of the curve, resulting in test data that do not fit well. For the hyperbolic Mohr strength criterion, a characteristic of the hyperbolic curve is that it has an asymptote; this causes the shear stress to vary approximately linearly with normal stress under high-stress conditions and to deviate from the experimental data. Charles and Watts (1980) proposed a power function Mohr strength criterion to overcome the shortcomings of the parabolic and hyperbolic Mohr strength criterion. Therefore, the power function Mohr strength criterion was used to describe the strength characteristics of tailings under high confining pressure in this paper. The power function Mohr strength criterion is expressed as

$$\tau = m\sigma^n + l, \quad (7)$$

where $m$, $n$, and $l$ are constant values.

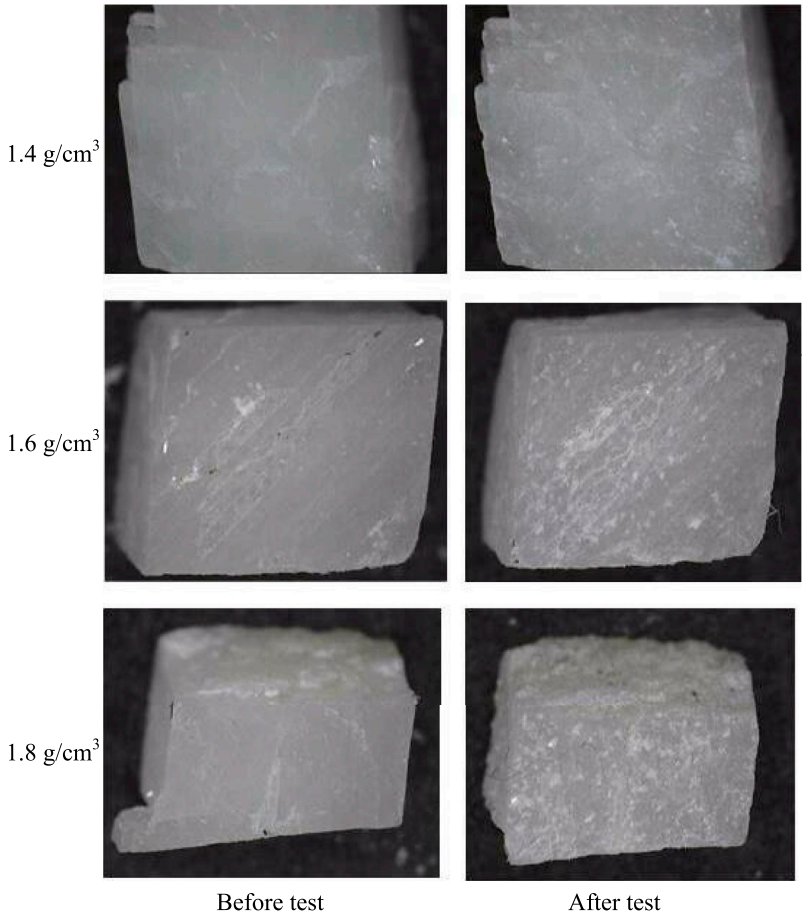


FIGURE 13
Morphological changes of calcite particles before and after testing for different densities.

The data were fitted by Eq. 7 using an iterative method. The detailed iterative steps are referred to in Liu et al. (2012). Figure 11 presents the power function Mohr envelope of the tailings with three different densities under high pressure. The fitting coefficients were all greater than 0.95, and the fitting formulas were as follows:

$$\left.\begin{array}{ll} \tau = 0.5879\sigma^{0.8793} & (1.4\mathrm{g/cm^3}) \\ \tau = 0.6548\sigma^{0.8439} & (1.6\mathrm{g/cm^3}) \\ \tau = 0.8132\sigma^{0.8088} & (1.8\mathrm{g/cm^3}) \end{array}\right\}. \quad (8)$$

The strength characteristics of the tailings under high pressure are well-represented by the power function Mohr strength criterion. The linear growth rate of the strength envelope increases with increasing sample density, and the non-linear growth rate of the strength envelope decreases. The deviation between the internal friction angles calculated using Eq. 8 and those calculated by the conventional linear Mohr–Coulomb criterion under low confining pressure. Deviation increases with the increase of density and confining pressure, which is consistent with the conclusions obtained by Liu et al. (2012). It is recommended that the conventional linear Mohr–Coulomb criterion be used to obtain the internal friction angle under low confining pressures and that the power function Mohr strength criterion be used to obtain the internal friction angle under high confining pressures. The formula is calculated as

$$\varphi = \begin{cases} \arctan\left(\dfrac{\tau - c}{\sigma}\right) & \sigma_3 \le 0.8\mathrm{MPa}, \\ \arctan\left(mn\sigma^{n-1}\right) & \sigma_3 > 0.8\mathrm{MPa}, \end{cases} \quad (9)$$

where φ is the internal friction angle, $\sigma_3$ is the effective normal stress, $c$ is the cohesion, and $\tau$ is the shear force.

The recommended internal friction angles of tailings at low and high pressures can be calculated by Eq. 9. The recommended values of the internal friction angle are shown in Table 4.

Figure 12 presents the relationship between the recommended internal friction angle and the confining pressure of samples of different densities. The internal friction angle of samples under high pressure is significantly lower than that of samples under low pressure. All three groups of specimens with different densities showed a large decrease in the internal friction angle, with a decrease of 7.06° for the loose specimen (1.4 g/cm$^3$), 8.12° for the medium dense specimen (1.6 g/cm$^3$), and 9.69° for the dense specimen (1.8 g/cm$^3$). The internal friction angles of specimens with densities of 1.4 g/cm$^3$ and 1.6 g/cm$^3$ coincide when the confining pressure reaches 4 MPa. The internal friction angle of the specimen with density 1.8 g/cm$^3$ also gradually approaches that of the other two groups of specimens. The significant reduction in the internal friction angle of the tailings under high pressure is very likely to

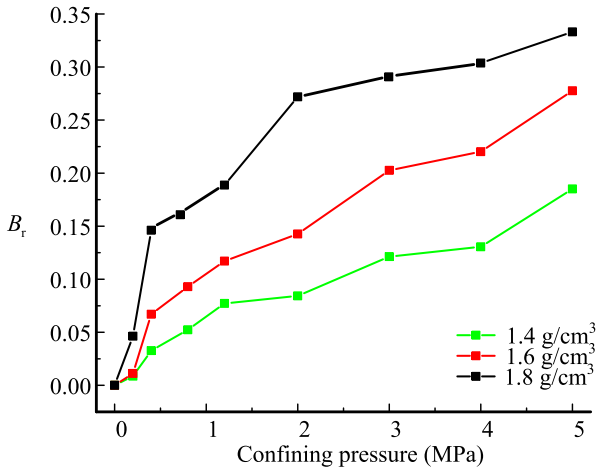


FIGURE 14
Relationship between the particle breakage index and confining pressure.

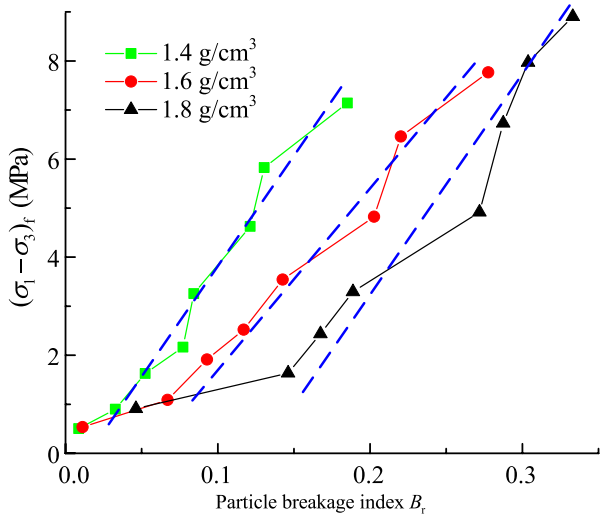


FIGURE 15
Relationship between the particle breakage index and shear strength.

destabilize the high-pile tailings dam. If strength parameters obtained under low pressure are used in the analysis of the stability of the high-pile tailings dam, the calculation results will undoubtedly be undesirable. Therefore, it is necessary that the test results be obtained under high pressure. For high-dam stability analysis, zoning assignment calculation is recommended.

## 4 Deterioration mechanism of non-linear mechanics

The mechanical behavior of geotechnical material is obviously affected by particle crushing. Therefore, the engineering structure will have less stability when particle breakage takes place. The deterioration mechanism of non-linear mechanics can be explained by particle breakage. To study the particle crushing of soil particles, Hyodo et al. (2002) and Nakata et al. (1999) both obtained information related to particle crushing using the marked particle method. The marked particle method, by which some particles are identified, was used in this study. Calcite was used as the marked particle because its hardness (Mohs hardness 3) is lower than that of quartz, which is the main mineral in the tailings. The surface of calcite particles is smooth and flat. It is easy to compare morphological changes before and after the test. The size of the marked particles was 5 mm, and the marker particles were placed in the middle of the specimen so that they would be in similar stress environments.

To compare the effect of density on particle crushing, the marked particles before and after the test, under confining pressure of 4 MPa, were compared; Figure 13 presents the morphological changes in the marked particles before and after the test. There were large differences in the surfaces of the marked particles before and after the test. The number of indentations at the marked particles increased with the density of the specimen, indicating that particle crushing is more prone to occur in dense samples.

The degree of particle breakage can be defined by the breakage index. Several methods have been proposed to quantify the amount of particle breakage. These methods are empirical in nature. Some are based on a single particle size, while others are based on aggregate changes in the overall grain size distribution. The most widely accurate particle breakage indices were developed by Einav (2007), who modified the definition of Hardin's breakage index. The improved relative breakage index $B_r$ proposed by Einav overcomes the disadvantage of the breakage index proposed by Hardin, which requires the artificial setting of an arbitrary cut-off value.

The Hardin's breakage index is defined as

$$Br = Bt/Bp, \tag{10}$$

where $B_r$ is the breakage index, $B_t$ is total breakage, and $B_p$ is breakage potential.

The improved relative breakage index is defined as

$$B_r = (F_t - F_0)/(F_u - F_0), \tag{11}$$

where $B_r$ is the breakage index. $F_0$, $F_t$, and $F_u$ are the cumulative areas of particle size distributions before testing, after testing under current confining pressure, and after testing under ultimate confining pressure, respectively.

The improved relative breakage index $B_r$ has a range of 0–1. $B_r$=0 means that particle crushing does not occur, and $B_r$=1 means that the particles are completely crushed. In this paper, the improved relative breakage index $B_r$ was used to quantify the particle crushing of tailings under high pressure. Figure 14 presents the relationship between the particle breakage index and confining pressure.

The value of $B_r$ increases with increasing confining pressure, and the growth rate decreases with increasing confining pressure. The particle crushing of tailings occurs not only under high pressure but also under low pressure. For different-density specimens, the larger the density of the tailing specimen, the greater the particle crushing. This indicates that when the height of the tailings dam is large, the mechanical properties of the tailings will continue to deteriorate under high pressure, which is detrimental to the stability of the high dam.

To explain the finding of the non-linear mechanics of shear strength under high confining pressure, the relationship between the particle breakage index and shear strength was drawn, as shown in Figure 15. The blue dashed lines represent the fitting trend lines. For tailings with three different densities, the value of $B_r$ increases linearly with increasing shear strength. The fitting trend lines are roughly parallel, which indicates that the non-linear mechanics of shear strength is affected by particle breakage. The degree of particle breakage can be explained by non-linear mechanical behavior.

## 5 Conclusion

For the high stress caused by large high-dam tailings ponds, consolidated drained tests of tailings under high stress were carried out. Isotropic consolidation compression and stress–strain curves of tailings specimens were obtained for three different densities under high stress, and particle crushing was studied. The main conclusions are as follows.

(1) The compression index $C_c$ decreases with increasing specimen density under isotropic consolidation. All stress–strain curves of the specimens exhibit strain hardening under high pressure. The dense specimens are prone to softening behavior under low pressure. The volumetric strain of the sample is greatly affected by density under low pressure, and the volumetric strain of the sample is independent of its density under high pressure.
(2) The strength and initial modulus of the tailing specimen increase with increasing confining pressure. The shear strength of the tailings is significantly non-linear. The internal friction angle under low pressure can be obtained by the linear Mohr–Coulomb criterion, and the internal friction angle under high pressure can be obtained by the power function Mohr strength criterion.
(3) The marked particle method was used to qualitatively study particle crushing during tailings shearing. The number of indentations at the marked particles increases with the density of the specimen. Particle crushing is more prone to occur with dense samples.
(4) The value of $B_r$ increases with increasing confining pressure, and the growth rate decreases with increasing confining pressure. The value of $B_r$ increases linearly with increasing shear strength. The non-linear mechanics of shear strength is affected by particle breakage. The degree of particle breakage can be explained by non-linear mechanical behavior.

## Data availability statement

The original contributions presented in the study are included in the article/Supplementary Material; further inquiries can be directed to the corresponding author.

## Author contributions

Conceptualization, CQ and LZ; methodology, ZC; validation, CQ; supervision, CQ; writing—original draft preparation, ZD, ZX and LZ; writing—review and editing, ZD, LZ, ZX and WX.

## Funding

The research was supported by the National Natural Science Foundation of China (No. 52104085).

## Conflict of interest

The authors declare that the research was conducted in the absence of any commercial or financial relationships that could be construed as a potential conflict of interest.

## Publisher's note

All claims expressed in this article are solely those of the authors and do not necessarily represent those of their affiliated organizations, or those of the publisher, the editors, and the reviewers. Any product that may be evaluated in this article, or claim that may be made by its manufacturer, is not guaranteed or endorsed by the publisher.

## References

Charles, J. A., and Watts, K. S. (1980). The influence of confining pressure on the shear strength of compacted rockfill. *J. Géotech.* 30 (4), 353–367. doi:10.1680/geot.1980.30.4.353

Chen, Q. L., Li, Z. G., Dai, Z. Y., Wang, X. J., and Zhang, C. (2022). Mechanical properties of tailings with dipping interlayers under high confining pressure. *J. Geomech. Eng.* 31 (6), 557–571. doi:10.12989/gae.2022.31.6.000

Chen, M., Jing, X., Xie, D., Li, X., Zhang, Y., and Liu, X. (2023). Prediction modelinvestigations of the reinforced finegrained tailings dam overtopping failure. *Front. Earth Sci.* 1-9. doi:10.3389/feart.2022.1075588

Einav, I. (2007). Breakage mechanics—part I: Theory. *J. J. Mech. Phys. Solids* 55 (6), 1274–1297. doi:10.1016/j.jmps.2006.11.003

GB/T50123 (1999). *Standard for soil test method, Chinese*. Beijing: aqsiq.

Guo, Z. S., and Wu, Y. Q. (2009). Soil and water loss prediction and treatment of tailings dam. *J. J. Soil Water Conserv.* 23 (4), 59–63.

Guo, Z. S. (2010). *The stability analysis of high tailings dam and the research on key consolidation technique*. Xi'an University of Technology.

Henkel, D. J., and Gilbert, G. D. (1952). The effect measured of the rubber membrane on the triaxial compression strength of clay samples. *J. Géotech.* 3 (1), 20–29. doi:10.1680/geot.1952.3.1.20

Hyodo, M., Hyde, A. F., Aramaki, N., and Nakata, Y. (2002). Undrained monotonic and cyclic shear behaviour of sand under low and high confining stresses. *J. Soils Found.* 42 (3), 63–76. doi:10.3208/sandf.42.3_63

Lade, P. V., and Bopp, P. A. (2005). Relative density effects on drained sand behavior at high pressures. *J. J. Jpn. Geotech. Soc. soils Found.* 45 (1), 1–13. doi:10.3208/sandf.45.1_1

Liu, H. M., Yang, C. H., Zhang, C., Mao, H. J., and Cao, J. (2012). Study of characteristics of power function Mohr strength criterion for tailings material under high pressures. *J. Rock Soil Mech.* 33 (7), 1986–1992. doi:10.16285/j.rsm.2012.07.037

Nakata, A. F. L., Hyde, H., Hyodo, M., and Murata (1999). A probabilistic approach to sand particle crushing in the triaxial test. *J. Geotech.* 49 (5), 567–583. doi:10.1680/geot.1999.49.5.567

Ren, J. (2018). *The mechanical properties of Fujian standard sand in high pressure triaxial test*. Northeast Electric Power University.

Rico, M., Benito, G., Salgueiro, A. R., D&iacuteez-Herrero, A., and Pereira, H. G. (2008). Reported tailings dam failures: A review of the European incidents in the worldwide context. *J. J. Hazard. Mater.* 152 (2), 846–852. doi:10.1016/j.jhazmat.2007.07.050

Wang, G. J., Hu, B., Tian, S., Ai, M., Liu, W. L., and Kong, X. Y. (2021). Seepage field characteristic and stability analysis of tailings dam under action of chemical solution. *J. Sci. Rep.* 11 (1), 4073–4111. doi:10.1038/s41598-021-83671-6

Wang, G. J., Zhao, B., Wu, B. S., Zhang, C., and Liu, W. L. (2023). Intelligent prediction of slope stability based on visual exploratory data analysis of 77 *in situ* cases. *J. Int. J. Min. Sci. Technol.* 33 (1), 47–59. doi:10.1016/j.ijmst.2022.07.002

Wang, G. G., Tian, S., Hu, B., Kong, X. Y., and Chen, J. (2020). An experimental study on tailings deposition characteristics and variation of tailings dam saturation line. *J. Geomech. Eng.* 23 (1), 85–92. doi:10.16058/j.issn.1005-0930.2020.01.014

Wang, J. X., Chen, S. L., and Dong, J. H. (2020). Elastic-plastic constitutive model and program implementation based on the generalized Double$\tau^2$ strength theory. *J. J. Basic Sci. Eng.* 28 (01), 160–173. doi:10.16265/j.cnki.issn1003-3033.2020.04.025

Wang, Y. W. (2014). Application of enhanced blind drain in Wan Nian Gou tailing pond. *J. Eng. Constr.* 46 (05), 31–33+43.

Wood, F. M., Yamamuro, J. A., and Lade, P. V. (2008). Effect of depositional method on the undrained response of silty sand. *J. Can. Geotech. J.* 45 (11), 1525–1537. doi:10.1139/t08-079

Wu, S., Yang, C., Zhang, C., Zhang, X., and Wang, G. (2017). The effects of silt content on the mechanical properties of tailings. *J. Chin. J. Rock Mech. Eng.* 36 (8), 2007–2017. doi:10.13722/j.cnki.jrme.2016.1456

Wu, L. G., Xiao, L. X., Liu, X. F., Yao, C., Jiang, Q. H., and Zhou, C. B. (2020). Influence of particle size on overtopping dam break of tailings dam. *J. China Saf. Sci. J.* 30 (4), 160–165.

Yin, J. Y., Lai, A. N., and Jiang, P. (1980). Strength and deformation characteristics of tailings under high pressure. *J. Chin. J. Geotech. Eng.* 2 (2), 1–10.

Zhang, Y. X., He, J. G., and Guo, Z. S. (2010). Study on tailing accumulation characteristics of high tailings dam. *J. Chin. Molybdenum Ind.* 34 (5), 8–12. doi:10.13384/j.cnki.cmi.1006-2602.2010.05.001

Zhang, C., Chen, Q. L., Pan, Z. K., and Ma, C. K. (2020). Mechanical behavior and particle breakage of tailings under high confining pressure. *J. Eng. Geol.* 265, 105419–105511. doi:10.1016/j.enggeo.2019.105419

Zhang, J. L. (1995). Dynamic characteristics of tailing ore under periodic load. *J. Northwest Water Resour. Water Proj.* 6 (1), 66–72.

Zhou, X. Y., Liu, Y. H., Wang, Z. Y., Xiong, W. Y., Yu, X. M., Zhao, K., et al. (2020). Genetic diversity of bacteria in bioremediation system of iron mine tailing by Robinia pseudoacacia-Ryegrass-Trifolium repens. *IOP Conf. Ser. Earth Environ. Sci.* 467 (1), 012145. doi:10.1088/1755-1315/467/1/012145

frontiers | Frontiers in Earth Science

TYPE Original Research
PUBLISHED 14 April 2023
DOI 10.3389/feart.2023.1181952



OPEN ACCESS

EDITED BY
Lijie Guo,
Beijing Mining and Metallurgy Technology Group Co., Ltd., China

REVIEWED BY
Liang Cui,
Lakehead University, Canada
Erol Yilmaz,
Recep Tayyip Erdoğan University, Türkiye

*CORRESPONDENCE
Yongxiang Zhou,
zhouyx@bjut.edu.cn

RECEIVED 08 March 2023
ACCEPTED 06 April 2023
PUBLISHED 14 April 2023

CITATION
Wang C, Qi Y, Jing J, Ma J, Zhou Y, Ping H, Zheng Y, Zhai Y and Liu F (2023), Properties and microstructure of total tailings cemented paste backfill material containing mining and metallurgical solid waste.
*Front. Earth Sci.* 11:1181952.
doi: 10.3389/feart.2023.1181952



# Properties and microstructure of total tailings cemented paste backfill material containing mining and metallurgical solid waste

Changlong Wang[1], Yang Qi[1], Jianlin Jing[1], Jintao Ma[1], Yongxiang Zhou[2]*, Haoyan Ping[1], Yongchao Zheng[3], Yuxin Zhai[4] and Feng Liu[5]

[1]Collaborative Innovation Center for Intelligent Regulation and Integrated Management of Water Resources Jointly Built by Provinces and Ministries, School of Civil Engineering, Hebei University of Engineering, Handan, China, [2]Faculty of Architecture, Civil, and Transportation Engineering, Beijing University of Technology, Beijing, China, [3]State Key Laboratory of Solid Waste Reuse for Building Materials, Beijing Building Materials Academy of Science Research, Beijing, China, [4]Technical Center, China Railway Construction Group Co., Ltd., Beijing, China, [5]Construction Development Co., Ltd., China Railway Construction Group, Baoding, China

**Introduction:** In order to improve the utilization efficiency of industrial waste discharged in the process of iron and steel metallurgy, a kind of material that can replace cement for mine filling is sought. In the test, steel slag (SS) and vanadium-titanium slag (VTS) were used as the primary raw materials to prepare cementing agents (CA). Then, combine it with vanadium-titanium iron ore tailings (VTIOTs) to make mine cemented paste backfill material (CPBM).

**Methods:** The composition, properties and hydration mechanism of CPBM are studied through various tests, in-cluding mechanical property test, hydration heat test, X-ray diffraction (XRD), scanning electronic mi-croscopy (SEM), and fourier transform-infrared spectroscopy (FT-IR).

**Results:** The results show that when the following conditions are met, the slump is 216 mm, and the 28-day flexural strength and compressive strength of CPBM reach 4.25 and 9.41 MPa, respectively, which meets the requirements of Chinese National Standard GB/T 39489-2020 Technical specification for the total tailings paste backfill: the mass percentage SS: VTS: phosphogypsum (PG): dicyandiamide waste slag (DWS) = 31:59:6:4; the content of compound phosphoric acid (CPA) accounts for 4% of the dry material; the cement sand ratio of CPBM is 1:4; the paste mass concentration (PMC) is 80%; and the content of water reducing agent (WRA) is 0.18%.

**Discussion:** Mechanism studies show that the hydration product of the CA is mainly ettringite (AFt) and C-S-H gel. The addition of CPA promotes the hydration of active minerals in SS and VTS. The existence of PG pro-motes the formation of AFt, and the formation of AFt further promotes the fracture of $[AlO_4]^{5-}$ and $[SiO_4]^{4-}$ along the bridge oxygen in VTS and SS.

KEYWORDS

**steel slag (SS), vanadium-titanium slag (VTS), cementing agent (CA), cemented paste backfill material (CPBM), ettringite**

# 1 Introduction

With the rapid growth of the world's demand for mineral resources, people's requirements for environmental mining protection are increasing day by day, and mining equipment and technical level and gelling agent technical level are greatly improved (Wang F et al., 2020). Cemented paste backfill material (CPBM) is becoming a modern technology with high efficiency, strength, and recovery (Ghirian and Fall, 2016; Deng et al., 2017). Total-tailings CPBM, as a new mining technology, can return environmentally hazardous tailings to underground tunnels or stopes, which maximizes the safety and productivity of mining process operations. This is of great significance to solving the safety risks and environmental problems caused by a large accumulation of tailings (Su and Zhang, 2013; Yilmaz et al., 2014). Traditional CPBMs mostly use Portland cement as the cementing agent (Yılmaz et al., 2014; Ke et al., 2015; Yilmaz et al., 2015; Li and Fall, 2016). According to statistics, the cost of CPBM generally accounts for 25%–40% of the total mining cost, and the cost of cementing agent accounts for about 70%–80% of the filling cost (Li et al., 2011; Peyronnard and Benzaazoua, 2012). Therefore, how to develop suitable materials based on local conditions and local materials to replace cement materials is an important subject. It can reduce filling costs and determine the application prospect of filling mining technology.

At present, a lot of practical work has been carried out in China and abroad to find a substitute for cement materials. Metallurgical slag, as a kind of industrial solid waste, has certain cementitious properties and pozzolanic activity. Therefore, it has a great potential to prepare filling materials through mechanical milling and chemical activation, such as steel slag (SS) (Zhang et al., 2016), granulated blast furnace slag (GBFS) (Cihangir and Akyol, 2018), lead-zinc slag (Li et al., 2018) and copper-nickel slag (Zhang et al., 2020; Wu et al., 2018). Vanadium-titanium slag (VTS) and SS, as industrial residues during iron and steel metallurgy, have good potential activity after the activation of desulfurized gypsum 17–21 (Cho and Choi, 2016; Zhao et al., 2016; Ashrit et al., 2017; Duan et al., 2018; Jiang et al., 2018). Therefore, based on the studies on cementing materials of cement concrete, some researchers have begun to explore the use of SS and VTS to replace or partially replace cement in the preparation of cementing agent (CA) for CPBM (Zhang et al., 2016; Zhang et al., 2019a; Zhang et al.). In order to improve the performance of the system, so that the CPBM can be better used in practice, the experimenter selected solid waste powder different from the previous study, such as: SS, VTS, dicyandiamide waste slag (DWS), phosphogypsum (PG), and compound phosphoric acid (CPA). In this system, the experiment provided a large amount of $SO_4^{2-}$ for the formation of C-S-H gels and ettringite by adding PG. On the one hand, the hydration of DWS could provide an alkaline environment for the reaction of the system; on the other hand, it could react with PG to convert harmful phosphorus and fluorine impurities into inert insoluble salts. On this basis, in order to improve the early strength characteristics of the material, CPA was used to modify the system. The addition of CPA promoted the consumption of $Ca(OH)_2$, the activity of mineral powder and steel slag powder was further stimulated, and the hydration products increased in the early stage of the system. Then, vanadium-titanium iron ore tailings (VTIOTs) are added to make total-tailings CPBM. The produced CPBM meets the conveying and strength requirements of backfill materials, and it has the characteristics of early strength, which can improve the filling mining efficiency.

All the materials used in the CPBM were solid wastes, which can greatly reduce the production cost of filling materials and improve the resource utilization of bulk industrial solid wastes such as SS, VTS, and VTIOTs. In this study, activated metallurgical slag was adopted as the main raw material to make CPBM. Then, various tests, including mechanical property test, X-ray diffraction (XRD), scanning electronic microscopy (SEM), and flourier transform-infrared spectroscopy (FT-IR), are conducted to explore its raw material composition and properties, and the effect of the amount of its raw materials and activators on the working performance and mechanical properties of CPBM. Besides, the hydration products of the CA are also studied.

# 2 Test materials and methods

## 2.1 Test materials

The test materials include SS, VTS, DWS, PG, CPA, and VTIOTs. Their chemical compositions are shown in Table 1.

### 2.1.1 SS

The SS used is the converter steel slag (without overheating treatment) with the chemical composition of f-CaO as 1.42% and f-MgO as 0.93%. The alkalinity value can reflect the activity of SS to a certain extent, and it is calculated through the Mason's method (Mason, 1944).

According to the alkalinity value, SS is classified as: low-alkalinity SS (<1.8), medium-alkalinity SS (1.8–2.5), and high-alkalinity SS (>2.5). The alkalinity value of the SS used in the test is 2.48 and it is medium-alkalinity SS. Moreover, the f-CaO content and alkalinity value of the SS meet the requirements of Chinese National Standard GB/T 20491-2017 Steel Slag Powder Used for Cement and Concrete, that is, f-CaO content ≤3% and alkalinity value ≥1.8. The particle size distribution analysis of the SS shows that 82.03% of the SS particles have the diameter between 0.3 mm and 9.5 mm. Thus, the SS should be broken before grinding. The major mineral phases of SS are $C_3S$, $C_2S$, RO phase (Figure 1A). According to BSE image analysis (Huo et al., 2021a), the used SS contains 18.78% glass phase by volume, 20.68% RO phase by volume, 58.14% silicate phase by volume and 2.40% $SiO_2$, MgO, and other phases.

### 2.1.2 VTS

As can be seen from Table 1, the chemical composition of VTS is similar to that of ordinary GBFS. The main chemical components are $SiO_2$, CaO, MgO, and $Al_2O_3$. The content of CaO is low while that of $TiO_2$ is high, reaching 14.56%. The main mineral components are perovskite and merwinite (Figure 1B).

### 2.1.3 DWS

The dry base size of DWS is 0–0.1 mm, and the CaO content is 59.54%. The main mineral components are $Ca(OH)_2$(CH) and $CaCO_3$ (see Figure 1C). The residue on the sieve with 0.08 mm square holes accounts for 12.8%.

**TABLE 1** Chemical composition of raw materials (wt.%).

| Materials | $SiO_2$ | $Al_2O_3$ | $Fe_2O_3$ | FeO | MgO | CaO | $Na_2O$ | $K_2O$ | $SO_2$ | $TiO_2$ | LOI |
|---|---|---|---|---|---|---|---|---|---|---|---|
| SS | 15.71 | 5.86 | 13.58 | 6.22 | 8.59 | 43.69 | 0.10 | 0.06 | 0.64 | — | 1.67 |
| VTS | 23.47 | 11.12 | 2.48 | 0.02 | 12.20 | 33.05 | 0.52 | 0.40 | 0.99 | 14.56 | 1.11 |
| DWS | 3.45 | 1.94 | 0.078 | 0.29 | — | 59.54 | 0.28 | 0.001 | 3.55 | — | 30.11 |
| PG | 3.16 | 1.35 | 0.47 | 0.09 | 7.49 | 33.38 | 0.13 | 0.18 | 36.56 | 0.13 | 8.28 |
| VTIOT | 44.47 | 7.39 | 9.78 | 0.92 | 11.21 | 21.62 | 0.55 | 0.23 | 0.09 | 0.04 | 2.04 |

### 2.1.4 PG

PG is derived from Hubei Huangmailing Phosphoric Chemical Co., Ltd., which is gray powder with the particle size as 5–150 μm and the relative density as 2.31 g $cm^{-3}$. The major components are $CaSO_4{\cdot}2H_2O$ and $CaSO_4{\cdot}1/2H_2O$ (Figure 1D).

### 2.1.5 VTIOTs

For the VTIOTs with the mass fraction of about 77.4%, the particle size is between 0.08 and 0.32 mm. The particles with more than 0.32 mm account for 14.5%, and those with less than 0.08 mm account for 8.1% (Table 2). The main mineral components are augite and hornblende, while the secondary mineral components are biotite, chlorite and ilmenite (Figure 1E). It can be seen from Figure 2 that the particle size of VTIOTs is mainly concentrated in the range of 0.3–1.18 mm, accounting for 64.43% (Figure 2).

### 2.1.6 Other materials

In the test, phosphoric acid (PA) is an analytical reagent, and the concentration is 85.0 wt.%. Anhydrous alcohol (AA) is also an analytical reagent and the concentration is no less than 99.5%. PA and AA are combined to prepare 80 wt.% CPA modified solution. The superplasticizer is polycarboxylates high performance water-reducing admixture (PC), and P·O 42.5 ordinary Portland cement (OPC) is used in the contrast test.

## 2.2 Test methods

Firstly, SS was broken into 1–3 mm particles by jaw crusher, and then the broken SS, VTS, DWS, PG were placed in the oven at 105°C for 24 h to make moisture content less than 1%, respectively. Secondly, they were milled with the SM φ 500 mm × 500 mm laboratory ball mill at the speed of 48 r $min^{-1}$ to yield specific surface area (SSA) after milling were 510, 540, 455, and 390 $m^2$ $kg^{-1}$, respectively. The grinding media consists of several steel balls and a steel forging. The loading mass of the grinding media should be 100 kg. The steel balls add up to 40 kg, in which the Φ70 mm ball takes up 19.7%, the Φ60 mm ball takes up 33.1%, the Φ50 mm ball takes up 29.6%, and Φ40 mm ball takes up 17.6%; the Φ25 mm ×30 mm steel forging weighs 40 kg.

When the pulverized raw materials were mixed evenly in proportion, some 80 wt.% CPA modified solution was dripped into the cement mortar mixer with the raw materials at the speed of 125 ± 10 r $min^{-1}$ for 8–15 min. After stirring for 2 h, the materials were put in an oven at 105°C for 2 h and the CA was obtained. Then, the CA was mixed with VTIOTs according to a certain cement sand ratio, and some water was added. And we stirred the materials until a certain paste mass concentration (PMC) was reached. After stirring, the slurry was put into the cement mortar triple testing mold (40 mm × 40 mm × 160 mm) and it was vibrated on the cement mortar vibration platform. After 24 h, it was demoulded and put into a standard curing box with the temperature of (20 ± 1)°C and humidity of more than 90%. Finally, the mechanical properties of the test blocks at different ages were determined. By measuring the mechanical properties of the sample fillers, we obtained a set of the optimal ratio of the CA. XRD, FT-IR and SEM were used to analyze the CA paste hydration process.

## 2.3 Property characterization

Based on Chinese National Standard YB/T 140-2009 Methods of Chemical Analysis for Steel Slag, the f-CaO of SS was determined by EDTA complexometric titration with ethylene glycol as the extractant. According to Chinese national standard GB/T 19077-2016 Particle size analysis—Laser diffraction methods, we chose ethanol as the dispersant and analyzed the particle size distribution of ground steel slag by MASTER SIZER 2000 (a laser particle size analyzer with the analysis range between 0.02 and 2,000 μm). The SSA was measured using SSA-3200 dynamic specific surface area analyzer. For the test blocks at different ages, we tested their compressive strength according to Chinese National Standard GB/T 17671-2022 Method of testing cements—Determination of strength. The mechanical properties were tested by YES-300 digital hydraulic pressure testing machine. Its loading rate was (2.0 ± 0.5) kN/s and the maximum load was 300 KN. The slurry slump in the test was determined by referring to Chinese National Standard GB/T 50080-2016 Standard for Test Method of Performance on Ordinary Fresh Concrete.

For XRD analysis, Japan's neo-confucianism Rigaku D/MAX-RC 12 KW rotating anode diffractometer with Cu target was adopted whose working current was 150 mA and working voltage was 40 kV. It could generate rays with the wavelength of 1.5406 nm. The exothermic rate of hydration and the total heat of hydration were measured by Calmetrix isothermal calorimeter. The SEM observation was performed to analyze the hydration products of the CA samples using a Zeiss SUPRATM55 scanning electron microscope coupled with a Be4-U92 energy spectrum. The functional group's vibration of CA samples was qualitatively analyzed by NEXUS70 Fourier transform infrared (FT-IR, test range 350–4,000 $cm^{-1}$).

10.3389/feart.2023.1181952

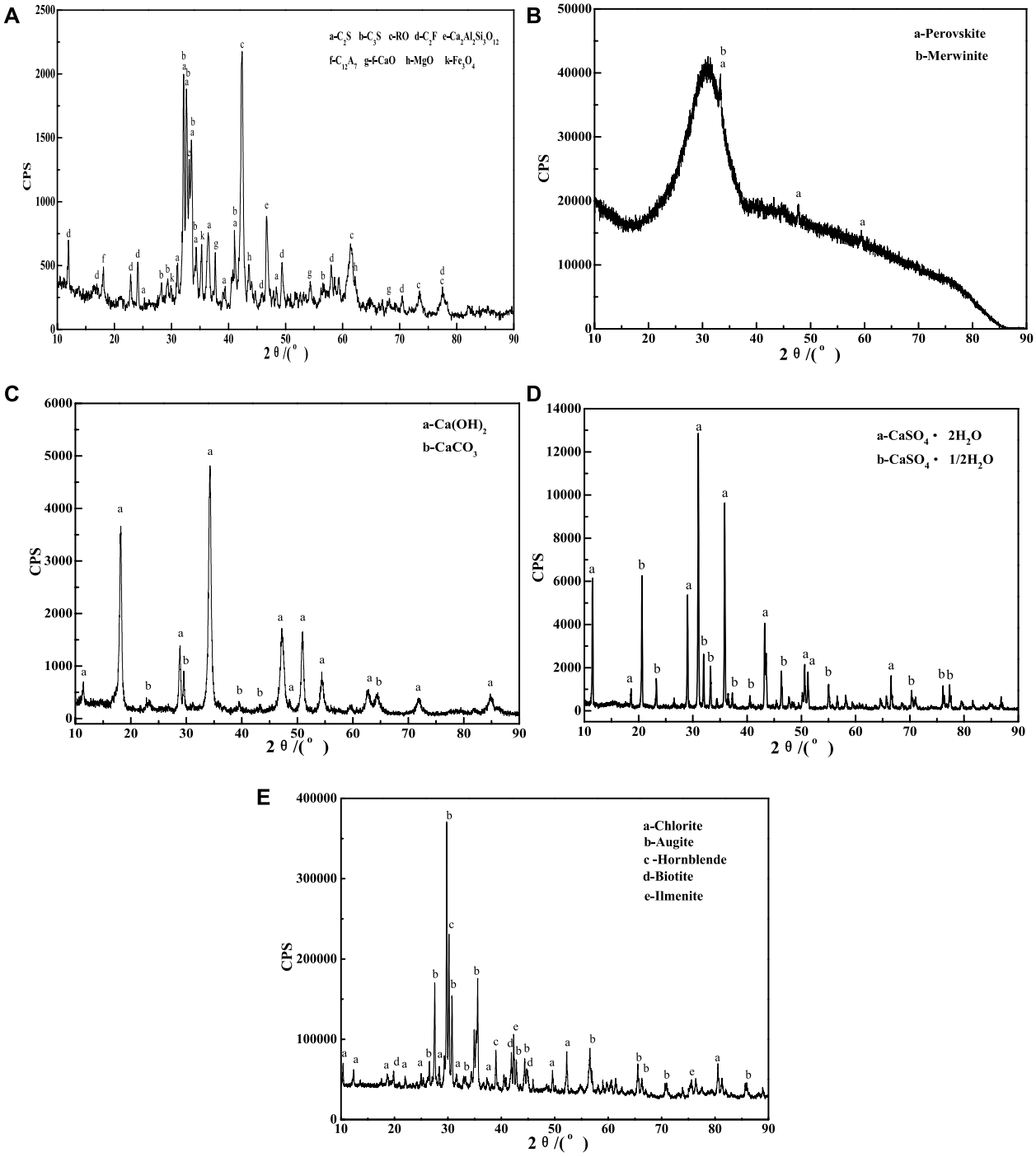


FIGURE 1
XRD patterns of raw materials. **(A)** SS; **(B)** VTS; **(C)** DWS; **(D)** PG; **(E)** VTIOTs.

**TABLE 2 Particle size distribution of VTIOTs.**

| Sieve size/mm | +1.25 | −1.25 +0.63 | −0.63 +0.32 | −0.32 +0.16 | −0.16 +0.08 | −0.08 |
|---|---|---|---|---|---|---|
| Meter sieve/% | 1.7 | 6.1 | 6.7 | 36.1 | 41.3 | 8.1 |
| Cumulative sieve/% | 1.7 | 7.8 | 14.5 | 50.6 | 91.9 | 100 |

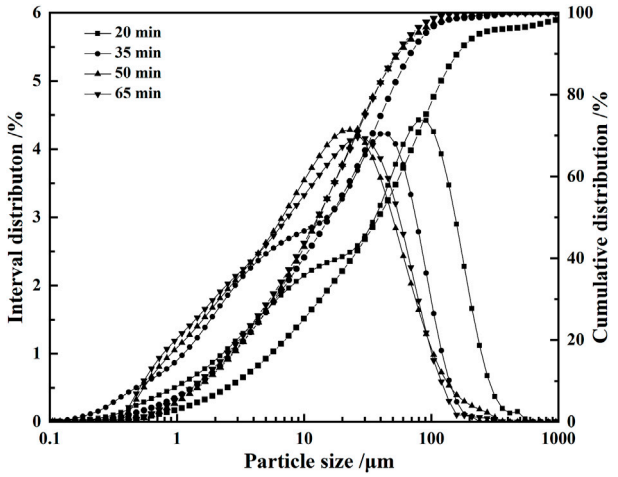


FIGURE 2
Cumulative distribution and interval distribution curves of VTIOTs at different grinding time.

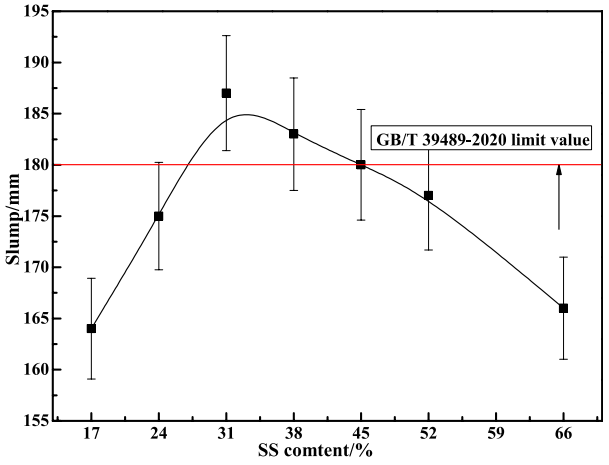


FIGURE 3
Effect of SS content on slump of CPBM.

**TABLE 3 Mix proportion of total-tailings CPBM.**

| Number | Composition of CA | | | | Cement sand ratio | PMC/% |
|---|---|---|---|---|---|---|
| | SS% | VTS/% | DNS/% | PG/% | | |
| C-1 | 17 | 77 | 1 | 9 | 1:4 | 79 |
| C-2 | 24 | 66 | 3 | 7 | | |
| C-3 | 31 | 59 | 4 | 6 | | |
| C-4 | 38 | 52 | 5 | 5 | | |
| C-5 | 45 | 45 | 6 | 4 | | |
| C-6 | 52 | 38 | 8 | 2 | | |
| C-7 | 66 | 24 | 9 | 1 | | |

Note: PMC = solid mass/(solid mass + liquid mass) × 100%.

# 3 Results and discussion

## 3.1 Effect of SS content on the properties of CPBM

SS contains a certain amount of $C_3S$ and $C_2S$, and has certain gelling activity. Besides, VTS has a certain glass phase. Thus, SS and VTS can be used as cementing materials at the same time. With the activator, SS and VTS can activate each other. Therefore, the total content of SS, VTS, PG and DWS is 100% in the initial ratio tentatively. DWS belongs to the alkali activator while PG is the sulfate activator. Only when the two activators are added according to a reasonable proportion, can SS and VTS produce the best excitation effect. Based on our previous studies (Zhang et al., 2019a; Zhang et al., 2019b; Wang C et al., 2020; Wang et al., 2021), the total mass percentage of SS and VTS in the CA is set as 90% while that of PG and DWS is 10%. The SSA of SS and VTS after grinding are 510 and 540 $m^2 kg^{-1}$, respectively. The cement sand ratio is 1:4. The paste mass concentration (PMC) is 79%. The test ratio is shown in Table 3.

Figure 3 shows the influence of different SS contents on the slump value of CPBM. As seen in Figure 3, slurry fluidity first increases and then decreases with the increase of SS content. Slump value reaches 180 mm when SS content is 31%, 38%, and 45%. Figure 4 represents the influence of SS content on the compressive strength of the CPBM. It can be seen that the compressive strength of sample blocks at each age first increases and decreases then with the increase of SS content. The compressive strength reaches the maximum when the SS content is 31%.

The compressive strength of the CPBM samples at 3 d, 7 d and 28 d are 0.80, 2.58, and 5.96 MPa, respectively, and the slump reaches 187 mm, which meets the following requirements of Chinese national standard GB/T 39489-2020 Technical specification for the total tailings paste backfill: 180 mm ≤ slump value ≤260 mm; 0.2 MPa ≤uniaxial compressive strength ≤5 MPa.

In this case, using metallurgical solid waste SS and VTS as the CA can generate environmental and ecological benefits which are in line with the national industrial policy. Therefore, C-3 was selected as the optimal formulation in the subsequent studies.

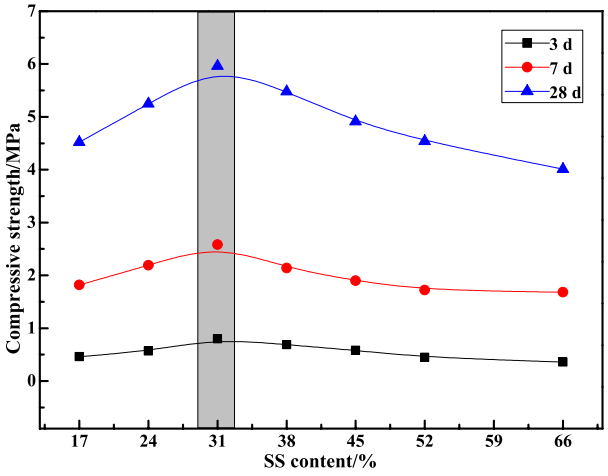


FIGURE 4
Effect of SS content on compressive strength of CPBM.

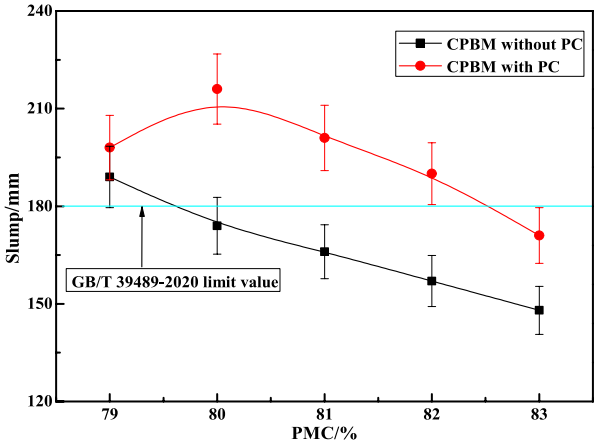


FIGURE 6
Effect of PMC on slump of CPBM.

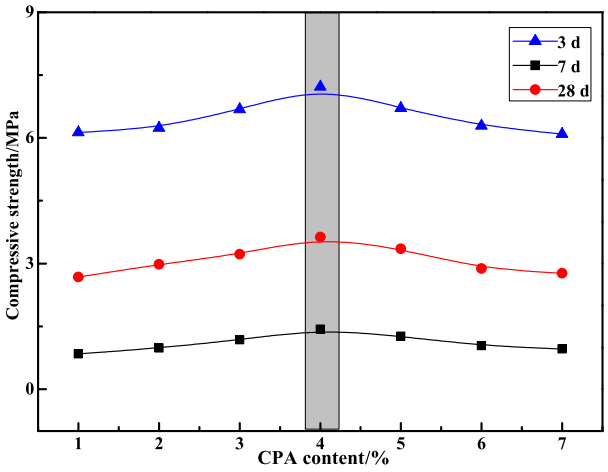


FIGURE 5
Effect of CPA content on compressive strength of CPBM.

## 3.2 Effect of CPA content on the properties of CPBM

From Section 3.1, we can find that the cementitious activities of SS and VTS can be stimulated to a certain extent after being activated by mechanical force. However, the activation effect is limited, and the strength of the prepared CPBM is low. Therefore, CPA was selected as the auxiliary activator in this study, and its appropriate dosage was determined through experiments. Based on the mix proportion of C-3, the ratio of SS, VTS, DWS and PG in the CA was determined. Then, the CPA content was set from 1% to 7% of the CA, so as to investigate the influence of the CPA content on the properties of the CPBM. The results are shown in Figure 5.

It can be seen from Figure 5 that the compressive strength of CPBM reaches the highest value at 3 d, 7 d, and 28 d when the CPA content is 4%. When the mass fractions of SS, VTS, PG and DWS in the CA are 31%, 59%, 6%, and 4%, respectively, the cement sand ratio is 1:4 and the PMC is 79%, the compressive strength of the CPBM is 1.43, 3.63, and 7.22 MPa at 3 d, 7 d, and 28 d, respectively. The compressive strength of the CPBM mixed with 4% CPA is increased by 78.8%, 40.7%, and 21.1% compared with that of the CPBM with no CPA at 3 d, 7 d, and 28 d, respectively. This is mainly because SS and VTS, as the products after high-temperature calcination, have dense connections among their mineral crystals (Fisher and Barron, 2019). After milling, the hydration of SS and VTS is slow, producing fewer hydration products. Therefore, the early activity of CA and the strength of CPBM are lower.

According to Huo et al. (2020) and Huo et al. (2021b), the surface roughness of SS and VTS modified by CPA, increases the SSA and porosity of the powder, which makes it easier for the surface of the powder to absorb water molecules. Meanwhile, water molecules can enter the interior of the powder particles through pore channels, which enables the active minerals in SS and VTS to have more contact with water molecules. As a result, they can participate in the hydration reaction and generate more hydration products. However, excessive CPA will delay the hydration process of active minerals in SS and VTS, decreasing the mechanical properties of CPBM.

## 3.3 Effect of PMC on the properties of CPBM

Usually, the PMC is 75%–88%. If the PMC is too large, the fluidity of the paste will become poor. If it is too small, the paste filling body will become layered and separated. Therefore, the PMC was set between 79% and 83%, and the mix proportion of optimized CA was SS: VTS: PG: DWS = 31:59:6:4. The cement sand ratio was 1: 4. Then, CPA (4% of the CA) and PC (0.18% of the CA) were added to determine the mechanic strength and slump of the CPBM. The test results are compared with the samples without PC (Figures 6, 7).

As can be seen from Figure 6, when the PMC is between 79% and 83%, the slump of the CPBM with PC is significantly higher than that without PC. Only when the PMC is 79% can the slump of the

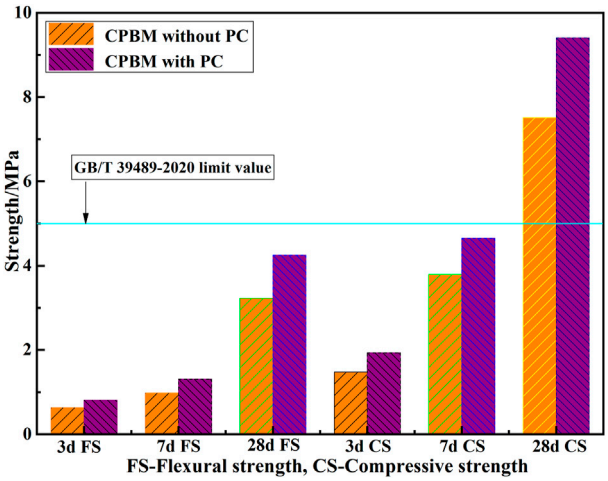


FIGURE 7
Mechanical properties of CPBM at 80% PMC.

latter one meet the slump index (189 mm) in Chinese National Standard GB/T 39489-2020 Technical Specification for the Total Tailings Paste Backfill. After adding PC, the slump of the CPBM increases significantly. When the PMC is between 79% and 82%, the slump value of the CPBM system is always higher than the lowest slump (180 mm) in GB/T 39489-2020. The maximum slump reaches 216 mm when the PMC is 80%.

With the increase of PMC, the slump decreases. The addition of PC is beneficial to improve the mechanical properties of the CPBM system. Figure 7 shows the mechanical properties of CPBM with the PMC of 80%. The 3 d, 7 d, and 28 d flexural strength and compressive strength of CPBM with PC are obviously better than those without PC.

The flexural strength of the CPBM samples with PC reaches 0.81, 1.31, and 4.25 MPa at 3 d, 7 d, and 28 d, respectively, increased by 28.6%, 33.7%, and 31.6% compared with those without PC at the same age. Meanwhile, the compressive strength reaches 1.93, 4.65, and 9.41 MPa at 3 d, 7 d, and 28 d, respectively, increased by 30.4%, 22.7%, and 25.3%. The flexural strength and compressive strength of the CPBM meet the strength index in Chinese National Standard GB/T 39489-2020 Technical Specification for the Total Tailings Paste Backfill. Compared with the filling requirements of most mines, the strength of CPBM in this study is higher. In application, the water-binder ratio and slump can be selected and adjusted according to the specific requirements of the mine for strength and pumping conditions.

## 3.4 Mechanism analysis

### 3.4.1 Hydration heat analysis

Figure 8 shows the hydration exothermic rate curve of cement slurry (W/b = 0.50) and CA (W/b = 0.50) measured by a TAM air 8-channel isothermal calorimeter (a precise temperature control within ±0.02°C). In the test, the mix proportion of the optimized CA is SS: VTS: PG: DWS = 31:59:6:4 and the content of CPA accounts for 4% of the CA. During the test, they are placed in the room at 25°C. By comparing the hydration exothermic process of the CA paste and the cement paste, it can be seen that the early hydration exothermic process of the CA can be divided into five stages: the CA dissolves rapidly in contact with water and releases much heat rapidly, thus forming the first exothermic peak, 24–26 mW $g^{-1}$ $h^{-1}$ (Figure 8B). In order to make the curve clearer in the later stage, the maximum value of the vertical coordinate in Figure 8A is set to 8 mW $g^{-1}$ $h^{-1}$.

This stage is called the early induction stage. The exothermic peak is formed mainly due to the release of surface energy when the powder is in contact with water. Only when the concentrations of $Ca^{2+}$ and $OH^-$ reach a critical value do the hydration products CH and C-S-H gel begin to crystallize from the solution. Therefore, after the first stage, the hydration is relatively inactive, which is called the induction phase.

Then comes the hydration acceleration phase. During this phase, the hydration reactions are most concentrated and intense, and CH and C-S-H gel are formed in large quantities. The hydration exothermic power of the CA reaches the second peak.

With the decrease of active substances in hydration, it enters the deceleration stage and the hydration exothermic power of the sample slowly decreases. C-S-H gel forms the wrapping layer around the paste particles as the hydration continues. The increasing thickness of the wrapping layer will make it harder for the water to pass through the layer and arrive at the remaining paste particles. Thus, the hydration becomes much slower, which is called the stable phase. During this phase, the hydration of $C_2S$ and $C_3S$ is controlled by the diffusion rate and becomes stable.

As can be seen from Figures 8C, D and Table 4, the exothermic rate of CA is significantly lower than that of pure cement during hydration. It is decreased by 68.56%, 78.16%, 65.02%, 47.21%, and 41.84% at the age of 12, 24, 36, 48, and 60 h, respectively. The main reason is that the hydration activity of CA is less than that of pure cement. Although PG, DWS and CPA are activated, the overall hydration activity is still lower than that of pure cement. When the hydration continues for 60 h, the maximum hydration heat release of the CA is only 58.16% of that of pure cement.

### 3.4.2 XRD analysis

Figure 9 shows the XRD pattern of the hydration products of the CA paste samples with the curing age of 3 d, 7 d, and 28 d, respectively. These samples are prepared according to the optimized CA content ratio and the water-binder ratio is 0.5.

In the above XRD patterns of the CA paste samples at 3 d, 7 d, and 28 d of standard curing, we can find ettringite (AFt), $Ca(OH)_2$, RO phase, $CaSO_4$, $C_2F$, $Ca_3(PO_4)_2$, $CaCO_3$, and unhydrated $C_3S$ and $C_2S$. SS is similar to cement clinker, in which active minerals $C_3S$ and $C_2S$ undergo hydration reaction to produce C-S-H gel and CH, and the reaction formula is shown as Eq. 1. In Figure 9, there is an obvious "bulging" at 25°–35°, indicating that the system contains a large number of C-S-H gel and amorphous substances with low crystallinity (Bensted and Barnes, 2002; Wang et al., 2016; Wang et al., 2018). C-S-H gel is continuously deposited with the extension of curing age, which gradually thickens and hardens the slurry, thus rapidly increasing its macroscopic strength (Cui et al., 2017).

$$C_3S/C_2S + H_2O \rightarrow C - S - H + CH \quad (1)$$

$$(CaO)_m\,(SiO_2)_n\,(Al_2O_3)_k + CH + H_2O \rightarrow C - (A) - S - H \quad (2)$$

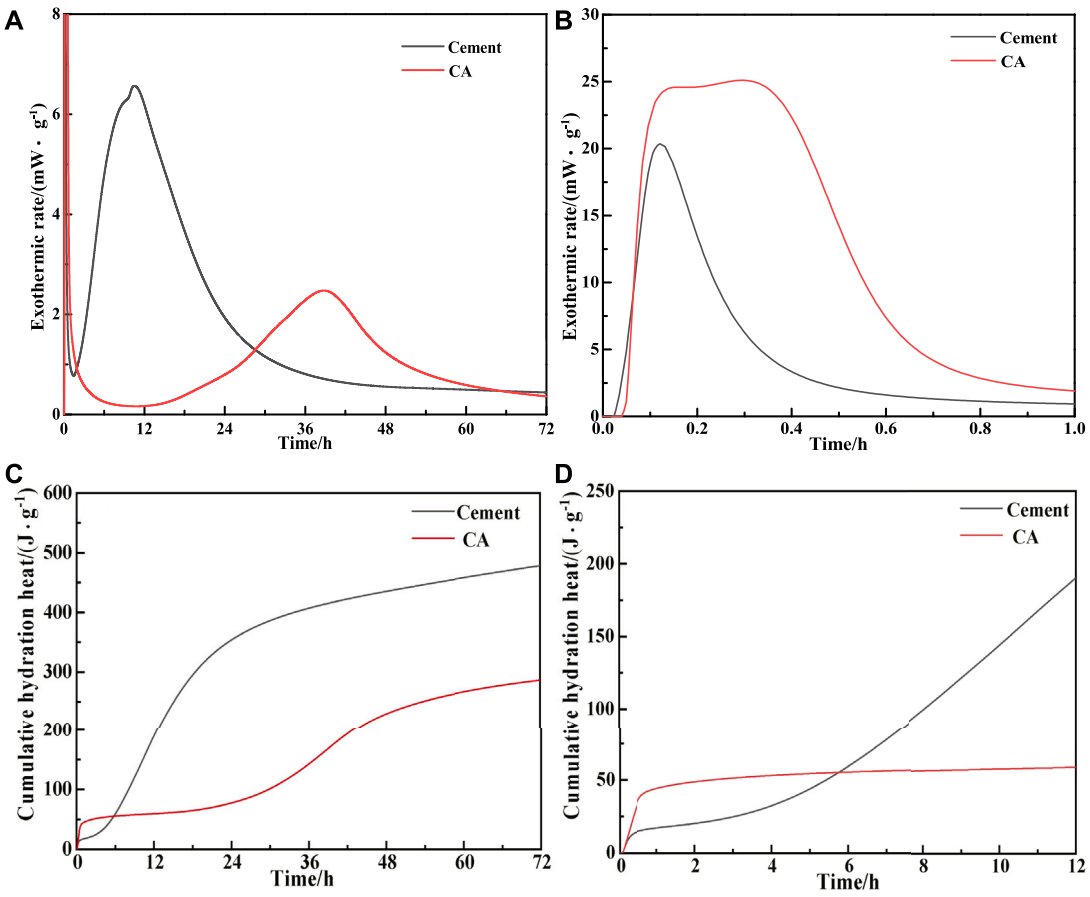


FIGURE 8
Calorimetry curves of the cement paste and CA paste. **(A)** and **(B)** heat flow; **(C)** and **(D)** cumulative heat.

**TABLE 4 Hydration rate and total exothermic of hydration at different hydration times.**

| Hydration time/h | | 12 | 24 | 36 | 48 | 60 |
|---|---|---|---|---|---|---|
| Cement | hydration rate/(mW $g^{-1}$) | 6.21 | 1.94 | 0.81 | 0.56 | 0.50 |
| | total exothermic/(J $g^{-1}$) | 188.98 | 354.21 | 407.30 | 435.41 | 458.03 |
| CA | hydration rate/(mW $g^{-1}$) | 0.17 | 0.80 | 2.28 | 1.24 | 0.59 |
| | total exothermic/(J $g^{-1}$) | 59.41 | 77.37 | 142.48 | 229.86 | 266.40 |

It is worth noting that amorphous vitreous $[(CaO)_m\ (SiO_2)_n\ (Al_2O_3)_k]$ also exists in SS and VTS, which is proved by the steamed bun peaks between 25° and 40° (Figures 1A, B). Vitreous has volcanic activity (Mejdi et al., 2019). The reaction formula is shown in Eq. 2. Therefore, CH generated by the hydration of $C_3S$ and $C_2S$ in SS and CH in DWS will consume the glass phase of SS and VTS. As a result, the diffraction summit of $C_3S$ and $C_2S$ in Figure 9 will gradually weaken with the extension of curing age.

In Figure 9, AFt diffraction peaks appear at 2θ of 15.7°, 19.0°, 23.1°, and 32.3°, and the peaks gradually strengthen with the extension of curing age. Since the generation of AFt consumes the $CaSO_4$ in PG, the diffraction summit of $CaSO_4$ in hydration products weakens with the extension of curing age (Li et al., 2017; Wu et al., 2019). Activated by gypsum sulfate and CPA, VTS are continuously hydrated. The cations such as $Ca^{2+}$ and $Mg^{2+}$ on the surface of VTS vitreous body first dissolve into the solution, and the charge imbalance between $[SiO_4]^{4-}$ and $[AlO_4]^{5-}$ intensifies, resulting in the break of Al-O bond of $[AlO_4]^{5-}$ and dissolving out $AlO^{2-}$ from the vitreous surface. And a dissolution balance tends to occur between the vitreous surface and the solution. AFt is produced in the participation of free gypsum, improving the strength of the gel system.

With the continuous formation of AFt, the dissolution balance of $AlO^{2-}$ between the VTS vitreous surface and the solution is

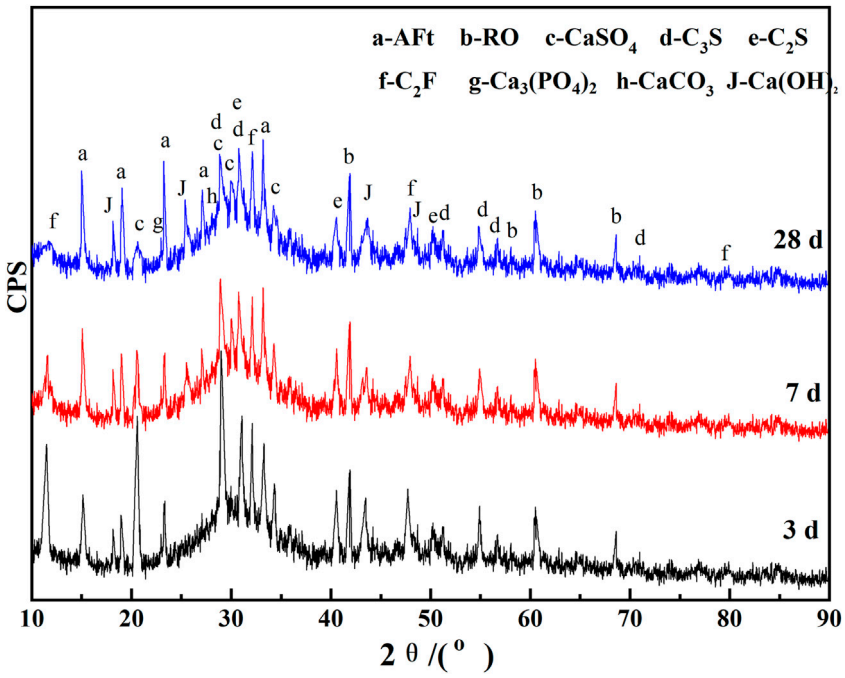


FIGURE 9
XRD pattern of CA paste samples at different ages.

constantly broken, which promotes the continuous migration of $[AlO_4]^{5-}$ from the VTS vitreous surface, so as to maintain the slag secondary hydration. The migration of $[AlO_4]^{5-}$ from the slag vitreous surface destroys the connection between $[SiO_4]^{4-}$ and $[AlO_4]^{5-}$. It results in a rapid decline in the polymerization degree of silicon (aluminum) oxygen tetrahedron on the VTS vitreous surface, and a significant increase in the activity of residual $[SiO_4]^{4-}$ and $[AlO_4]^{5-}$. C-S-H gel is continuously formed in CA solution with rich $Ca^{2+}$ and they are continuously deposited, which gradually thickness and hardens the slurry, thus rapidly increasing the macroscopic strength. The sample used in the test has been enclosed in the centrifugal tube since it is formed. So, there is no $CaCO_3$ produced by carbonization. The mineral phase of $CaCO_3$ in Figure 9 is the mineral residue in DWS. RO phase basically does not participate in the hydration reaction of the system, so there is RO phase in the hardened slurry. After CPA is added to the CA system, the hydration of minerals in SS and VTS is accelerated. Thus, the mineral phase of $Ca_3(PO_4)_2$ appears in the hydration products.

### 3.4.3 SEM analysis

SEM was used to observe the morphological structure and distribution characteristics of hydration products of CA paste samples with different curing ages. The observation results are shown in Figure 10. It can be seen that with the increase in curing age, more hydration products are generated. After 28 d of hydration, it is observed that the grain of ettringite gradually becomes coarser, the crystallinity increases, and the structure is rod-like. AFt and C-S-H gels interlace with each other to improve the compactness of the matrix, which is shown as a significant increase in flexural and compressive strength. Figure 10A shows the SEM images of the CA with 3 d age. Hydration products have been produced in net paste samples at 3 d age. Under low magnification, dense C-S-H gel is found. However, there are still large, unhydrated particles exposed out of the C-S-H gel. Figure 10B indicates that there are fibrous AFt crystals and crystal sparse C-S-H gel grown across the gaps of the CA. Figures 10C, D show that at the 7 d age, there are flaky C-S-H gel and the acicular AFt crystals filling their internal pores. Figure 10E reveals the flocculent C–S–H gel at the 28 d age. Loose small particles have disappeared, and acicular AFt crystals exist in the cracks and crevices of the gel (Li F et al., 2020). As shown in Figure 10F, AFt crystals overgrow in the large cavity. With the continuous formation of the C-S-H gel and AFt crystals, the network structure is consolidated, increasing the CA filling material's macroscopic strength.

### 3.4.4 FI-IR analysis

In order to verify that the added material participated in the hydration reaction and generated the hydration products mainly composed of C-S-H gels and ettringite, FT-IR was used to infer the diffraction peaks of the hydration products. FT-IR analysis of CA paste samples is given in Figure 11. As can be seen from the figure, C-S-H gels and AFt stably existed after the material underwent hydration reaction. With the increase in curing time, hydration products increased, which was conducive to improving the mechanical properties of the cementing material. It can be seen that there is no significant difference in the FT-IR spectra of the CA samples at 3 d, 7 d, and 28 d of hydration, except for a slight decrease in transmittance near the wave number of 3,425, 1,090, 990, and 459 $cm^{-1}$. The absorption band at 3,425 $cm^{-1}$ indicates the asymmetric stretching vibration

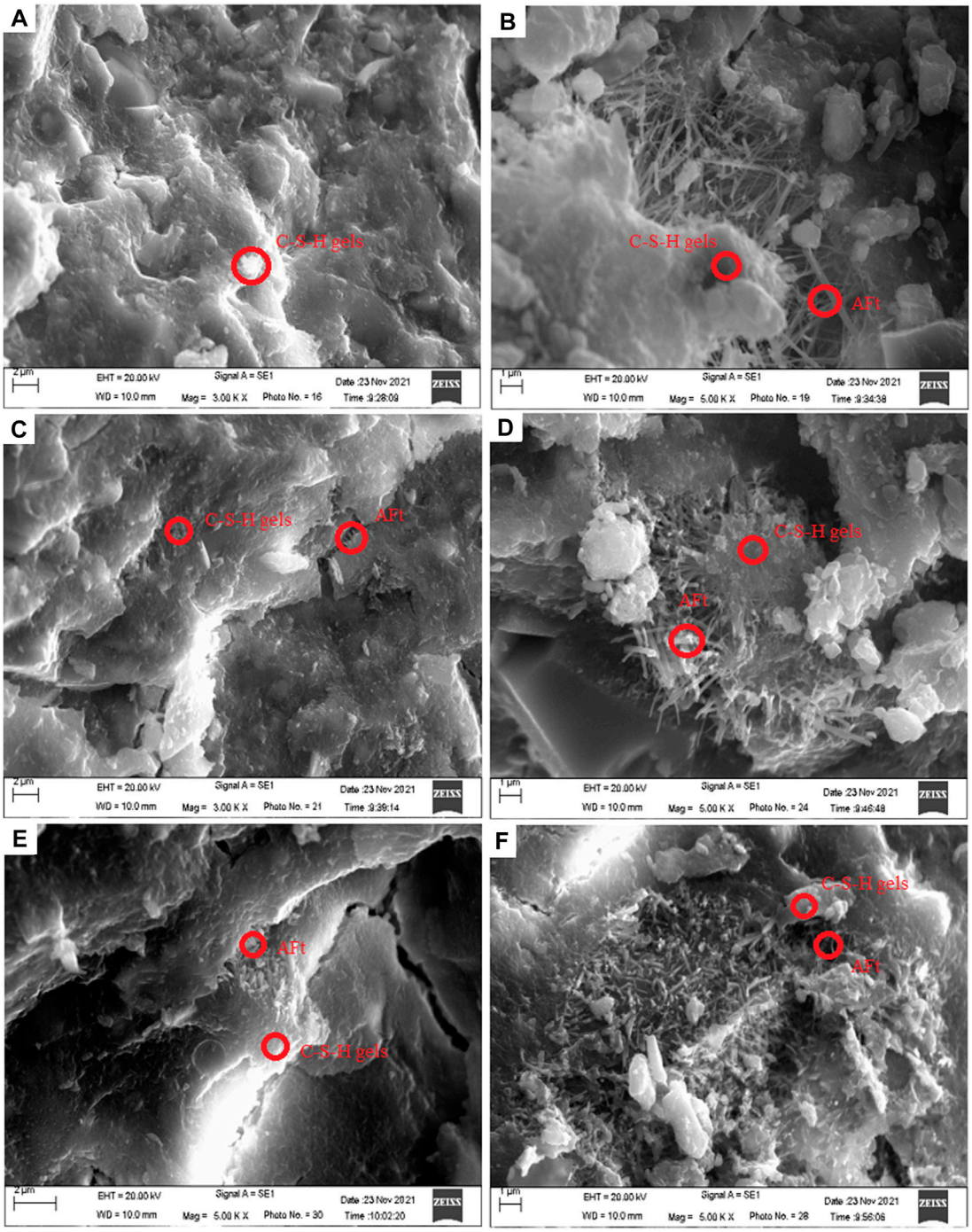


FIGURE 10
SEM images of CA paste samples at different ages. **(A)** and **(B)** 3 d; **(C)** and **(D)** 7 d; **(E)** and **(F)** 28 d.

of $OH^-$ (Figure 11A), while the band at 1,645 $cm^{-1}$ represents the flexural vibration of $OH^-$, which are the absorption characteristics of internal vibration of crystal water (Li Y et al., 2020; Liang et al., 2021; Li et al., 2022). This indicates that the hydration reaction of CA produces a lot of gel or substances with crystal water. However, as the reaction progresses, the transmittance of the $OH^-$ absorption band decreases, proving the gradual increase of hydrous substances.

The vibration peaks at 990, 518, and 450 $cm^{-1}$ represent the asymmetric stretching vibration of Si-O(Al), and the out-of-plane and in-plane flexural vibrations of Si-O, respectively. According to Clayden et al. (1999), Lecomte et al. (2006), and Hanna et al. (1995), the vibration frequency of $SiQ^n$ is: $SiQ^4$, 1,200 $cm^{-1}$; $SiQ^3$, 1,100 $cm^{-1}$; $SiQ^2$, 950 $cm^{-1}$; $SiQ^1$, 900 $cm^{-1}$; $SiQ^0$, 850 $cm^{-1}$. Q indicates the silicon-oxygen tetrahedra, and n refers to the number of bridge oxygen connecting each silicon-oxygen tetrahedra and other Si atoms.

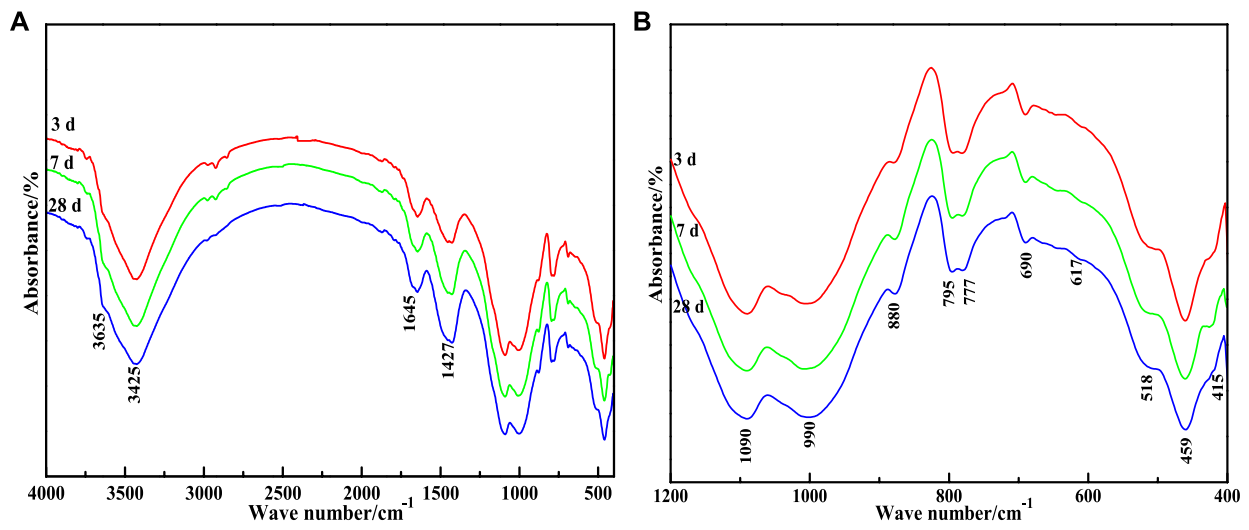


FIGURE 11
FT-IR patterns of CA paste samples at different ages. **(A)** 400–4000 $cm^{-1}$; **(B)** 400–1200 $cm^{-1}$

The displacement of absorption peak shifts to lower wave numbers when the Si atoms in the silico-oxygen tetrahedra are replaced by the Al atoms in the sub adjacent coordination. Combined with Figure 11B, it can be concluded that the weak absorption peak of 880 $cm^{-1}$ on the FT-IR map is attributed to $SiQ^0$, which is the signal peak of insulated silicate in unhydrated SS and VTS. The strong absorption band near 990 $cm^{-1}$ is attributed to the superposition of the chain silicate $SiQ^2$ phyllosilicate and $SiQ^3$ (mAl); The absorption peak near 1,090 $cm^{-1}$ is attributed to the phyllosilicate $SiQ^4$ (mAl).

Figure 11B shows the amplification of the fingerprint region of CA paste samples FT-IR atlas (400–1,200 $cm^{-1}$). According to the report of Moon et al. (2012), it is speculated that most absorption peaks in the interval are characteristic absorption peaks of AFt. At 617 and 415 $cm^{-1}$ is the flexural vibration of $[SO_4^{2-}]$; At 518 $cm^{-1}$ is the absorption band of $[AlO_6]$ octahedron; The absorption band at 795 $cm^{-1}$ is caused by the solid solution of AFt crystal with other elements which may be Fe, Si, and other elements.

## 4 Conclusion

In this paper, steel slag (SS), vanadium-titanium slag (VTS) and vanadium-titanium iron ore tailings (VTIOTs) were used as the main raw materials to make the mine cemented paste backfill material (CPBM). Through the research on its composition, properties, and hydration mechanism, it can be concluded that:

(1) When the specific surface areas of SS and VTS are both 510 $m^2\ kg^{-1}$, the CA composed of DWS, PG, and CPA can be used as the mine filling agent. Using the metallurgical waste SS and VTS as the cementing agent costs less than cement, and its environmental and ecological benefits are in line with national industrial policies.
(2) The optimal mix proportion of CA is SS: VTS: PG: DWS = 31:59:6:4. Then, add into CPA which accounts for 4% of the mass of CA. Further, prepare the filling materials with the cement sand ratio as 1:4, the PMC as 80%, and PC as 0.18% of the total CA. The slump value is 216 mm, and the 28 d flexural strength and compressive strength of CPBM reach 4.25 and 9.41 MPa, respectively, which meets the requirements of Chinese National Standard GB/T 39489-2020 Technical specification for the total tailings paste backfill.
(3) Through the analysis of hydration heat, XRD, SEM and FT-IR, it is found that the heat release of the CA with the hydration of 60 h is less than 60% of the cement. The hydration products of the CA are mainly AFt crystals and C-S-H gel. The addition of CPA promotes the hydration of active minerals in SS and VTS. The $SO_4^{2-}$ of PG accelerates the formation of AFt which further facilitates the fracture of $[AlO_4]^{5-}$ and $[SiO_4]^{4-}$ along the bridge oxygen in VTS and SS. Therefore, C-S-H gel is formed and deposited in the slurry solution with rich $Ca^{2+}$, gradually thickening and hardening the slurry.

## Data availability statement

The raw data supporting the conclusion of this article will be made available by the authors, without undue reservation.

## Author contributions

QY proposes method and writes manuscript; WC and ZhoY propose and participates in design research and reviews paper; JJ, MJ, PH, ZheY, ZhaY, and LF participate in design research and reviews paper. All the authors approved the final version of the manuscript.

## Funding

The authors gratefully acknowledge financial support by the National Key Research and Development Program of China (No.

2021YFC1910605), the Natural Science Foundation of Hebei Province (E2020402079), State Key Laboratory of Solid Waste Resource Utilization and Energy Conservation (SWR-2023-007), Science and Technology Research and Development Plan of China Railway Construction Group Co., Ltd. (No. 22-11b, 22-14b), Handan Science and Technology Research and Development Program (21422111260). The funder was not involved in the study design, collection, analysis, interpretation of data, the writing of this article or the decision to submit it for publication.

## Conflict of interest

Author YuZ and FL were employed by China Railway Construction Group Co., Ltd.

The remaining authors declare that the research was conducted in the absence of any commercial or financial relationships that could be construed as a potential conflict of interest.

## Publisher's note

All claims expressed in this article are solely those of the authors and do not necessarily represent those of their affiliated organizations, or those of the publisher, the editors and the reviewers. Any product that may be evaluated in this article, or claim that may be made by its manufacturer, is not guaranteed or endorsed by the publisher.

## Supplementary material

The Supplementary Material for this article can be found online at: https://www.frontiersin.org/articles/10.3389/feart.2023.1181952/full#supplementary-material

## References

Ashrit, S., Chatti, R. V., and Udpa, K. N. (2017). An infrared and Raman spectroscopic study of yellow gypsum synthesized from LD slag fines. *MOJ Min. Metall.* 1 (1), 1–4.

Bensted, J., and Barnes, P. (2002). *Structure and performance of cements*. New York: Spon Press.

Cho, B., and Choi, H. (2016). Physical and chemical properties of concrete using GGBFS-KR slag-gypsum binder. *Constr. Build. Mat.* 123, 436–443. doi:10.1016/j.conbuildmat.2016.07.023

Cihangir, F., and Akyol, Y. (2018). Mechanical, hydrological and microstructural assessment of the durability of cemented paste backfill containing alkali-activated slag. *Int. J. Min. Reclam. Env.* 32 (2), 123–143. doi:10.1080/17480930.2016.1242183

Clayden, N. J., Esposito, S., Aronne, A., and Pernice, P. (1999). Solid state 27Al NMR and FTIR study of lanthanum aluminosilicate glasses. *J. Non-Cryst. solids* 258 (1-3), 11–19. doi:10.1016/s0022-3093(99)00555-4(99)00555-4

Cui, X., Ni, W., and Ren, C. (2017). Hydration mechanism of all solid waste cementitious materials based on steel slag and blast furnace slag. *Chin. J. Mat. Res.* 31 (9), 687–694. doi:10.11901/1005.3093.2016.741

Deng, D., Liu, L., Yao, Z., Song, K., and Lao, D. (2017). A practice of ultra-fine tailings disposal as filling material in a gold mine. *J. Environ. Manage.* 196, 100–109. doi:10.1016/j.jenvman.2017.02.056

Duan, S., Liao, H., Cheng, F., Song, H., and Yang, H. (2018). Investigation into the synergistic effects in hydrated gelling systems containing fly ash, desulfurization gypsum and steel slag. *Constr. Build. Mat.* 187, 1113–1120. doi:10.1016/j.conbuildmat.2018.07.241

Fisher, L. V., and Barron, A. R. (2019). The recycling and reuse of steelmaking slags-A review. *Resour. Conserv. Recy.* 146, 244–255. doi:10.1016/j.resconrec.2019.03.010

Ghirian, A., and Fall, M. (2016). Strength evolution and deformation behaviour of cemented paste backfill at early ages: Effect of curing stress, filling strategy and drainage. *Int. J. Min. Sci. Technol.* 26 (5), 809–817. doi:10.1016/j.ijmst.2016.05.039

Hanna, R. A., Barrie, P. J., Cheeseman, C. R., Hills, C. D., Buchler, P. M., and Perry, R. (1995). Solid state 29Si and 27Al NMR and FTIR study of cement pastes containing industrial wastes and organics. *Cem. Concr. Res.* 25 (7), 1435–1444. doi:10.1016/0008-8846(95)00138-3

Huo, B., Li, B., Chen, C., and Zhang, Y. (2021a). Mechanism and properties of glacial acetic acid modified steel slag powder via dry chemical modification method. *J. Chin. Ceram. Soc.* 49 (5), 948–954. doi:10.1016/j.jclepro.2018.01.172

Huo, B., Li, B., Chen, C., Zhang, Y., and Wang, D. (2021b). Morphological and mineralogical insights into acetic acid modifying and hydraulic process on steel slag for enhanced reactivity. *Constr. Build. Mat.* 307, 125004. doi:10.1016/j.conbuildmat.2021.125004

Huo, B., Li, B., Huang, S., Chen, C., Zhang, Y., and Banthia, N. (2020). Hydration and soundness properties of phosphoric acid modified steel slag powder. *Constr. Build. Mat.* 254, 119319. doi:10.1016/j.conbuildmat.2020.119319

Jiang, L., Li, C., Wang, C., Xu, N., and Chu, H. (2018). Utilization of flue gas desulfurization gypsum as an activation agent for high-volume slag concrete. *J. Clean. Prod.* 205, 589–598. doi:10.1016/j.jclepro.2018.09.145

Ke, X., Hou, H., Zhou, M., Yang, Y., and Zhou, X. (2015). Effect of particle gradation on properties of fresh and hardened cemented paste backfill. *Constr. Build. Mat.* 96, 378–382. doi:10.1016/j.conbuildmat.2015.08.057

Lecomte, I., Henrist, C., Liégeois, M., Masen, F., Rulmont, A., and Cloots, R. (2006). (Micro)-structural comparison between geopolymers, alkali-activated slag cement and Portland cement. *J. Eur. Ceram. Soc.* 26 (16), 3789–3797. doi:10.1016/j.jeurceramsoc.2005.12.021

Li, F., Liu, L., Liu, K., Zheng, A., and Liu, J. (2020). Investigation on waterproof mechanism and micro-structure of cement mortar incorporated with silicane. *Constr. Build. Mat.* 239, 117865. doi:10.1016/j.conbuildmat.2019.117865

Li, H., Liu, Y., Xu, C., Guan, X., Zou, D., and Jing, G. (2022). Synergy effect of synthetic ettringite modified by citric acid on the properties of ultrafine sulfoaluminat cement-based materials. *Cem. Concr. Compos.* 125, 104312. doi:10.1016/j.cemconcomp.2021.104312

Li, N., Farzadnia, N., and Shi, C. (2017). Microstructural changes in alkali-activated slag mortars induced by accelerated carbonation. *Cem. Concr. Res.* 100, 214–226. doi:10.1016/j.cemconres.2017.07.008

Li, W., and Fall, M. (2016). Sulphate effect on the early age strength and self-desiccation of cemented paste backfill. *Constr. Build. Mat.* 106, 296–304. doi:10.1016/j.conbuildmat.2015.12.124

Li, W., Zhou, X., Liao, M., and Lin, Q. (2011). Research and practice on replacement materials for cementing backfilling. *Min. Eng.* 11 (3), 19–23. doi:10.13828/j.cnki.ckjs.2011.03.025

Li Y, Y., Qiao, C., and Ni, W. (2020). Green concrete with ground granulated blast-furnace slag activated by desulfurization gypsum and electric arc furnace reducing slag. *J. Clean. Prod.* 269, 122212. doi:10.1016/j.jclepro.2020.122212

Li, Y., Min, X., Ke, Y., Chai, L., Shi, M., Tang, C., et al. (2018). Utilization of red mud and Pb/Zn smelter waste for the synthesis of a red mud-based cementitious material. *J. Hazard. Mat.* 34, 343–349. doi:10.1016/j.jhazmat.2017.10.046

Liang, G., Ni, D., Li, H., Dong, B., and Yang, Z. (2021). Synergistic effect of EVA, TEA and C-S-Hs-PCE on the hydration process and mechanical properties of Portland cement paste at early age. *Constr. Build. Mat.* 272, 121891. doi:10.1016/j.conbuildmat.2020.121891

Mason, B. (1944). The constitution of some open-heart slag. *J. Iron Steel Res. Int.* 179 (11), 69.

Mejdi, M., Wilson, W., Saillio, M., Chaussadent, T., Divet, L., and Tagnit-Hamou, A. (2019). Investigating the pozzolanic reaction of post-consumption glass powder and the role of portlandite in the formation of sodium-rich C-S-H. *Cem. Concr. Res.* 123, 105790. doi:10.1016/j.cemconres.2019.105790

Moon, J., Oh, J. E., Balonis, M., Glasser, F. P., Clark, S. M., and Monterro, P. J. M. (2012). High pressure study of low compressibility tetracalcium aluminum carbonate hydrates $3CaO{\cdot}Al_2O_3{\cdot}CaCO_3{\cdot}11H_2O$. *Cem. Concr. Res.* 42 (1), 105–110. doi:10.1016/j.cemconres.2011.08.004

Peyronnard, O., and Benzaazoua, M. (2012). Alternative by-product based binders for cemented mine backfill: Recipes optimisation using Taguchi method. *Min. Eng.* 29, 28–38. doi:10.1016/j.mineng.2011.12.010

Su, L., and Zhang, X. (2013). Coordinated development between mineral resource exploitation and environmental protection with backfill technology. *Min. Metall. Eng.* 33 (3), 117–121. doi:10.3969/j.issn.0253-6099.2013.03.032

Wang, C., Ni, W., Zhang, S., Wang, S., Gai, G., and Wang, W. (2016). Preparation and properties of autoclaved aerated concrete using coal gangue and iron ore tailings. *Constr. Build. Mat.* 104, 109–115. doi:10.1016/j.conbuildmat.2015.12.041

Wang, C., Ren, Z., Huo, Z., Zheng, Y., Tian, X., Zhang, K., et al. (2021). Properties and hydration characteristics of mine cemented paste backfill material containing secondary smelting water-granulated nickel slag. *Alex. Eng. J.* 60 (6), 4961–4971. doi:10.1016/j.aej.2020.12.058

Wang, C., Zhang, K., Zuo, W., Ye, P., Zhao, G., Ren, Z., et al. (2020). Preparation and properties of autoclaved aerated concrete using coal gangue and fly ash. *Mat. Rep.* 34 (12), 24034–24039. doi:10.13225/j.cnki.jccs.2013.0551

Wang, F., Zheng, Q., Zhang, G., Wang, C., Cheng, F., and Lin, G. (2020). Preparation and hydration mechanism of mine cemented paste backfill material for secondary smelting water-granulated nickel slag. *J. New Mat. Electr. Sys.* 23 (1), 51–59. doi:10.14447/jnmes.v23i1.a10

Wang, S., Wang, C., Wang, Q., Liu, Z., Qian, W., Jin, C., et al. (2018). Study on cementitious properties and hydration characteristics of steel slag. *Pol. J. Environ. Stud.* 27 (1), 357–364. doi:10.15244/pjoes/74133

Wu, M., Zhang, Y., Jia, Y., Sha, W., Liu, G., Yang, Z., et al. (2019). Effects of sodium sulfate on the hydration and properties of lime-based low carbon cementitious materials. *J. Clean. Prod.* 220, 677–687. doi:10.1016/j.jclepro.2019.02.186

Wu, Q., Wu, Y., Tong, W., and Ma, H. (2018). Utilization of nickel slag as raw material in the production of Portland cement for road construction. *Constr. Build. Mat.* 193, 426–434. doi:10.1016/j.conbuildmat.2018.10.109

Yilmaz, E., Belem, T., and Benzaazoua, M. (2014). Effects of curing and stress conditions on hydromechanical, geotechnical and geochemical properties of cemented paste backfill. *Eng. Geol.* 168, 23–37. doi:10.1016/j.enggeo.2013.10.024

Yilmaz, E., Belem, T., Bussière, B., Mbonimpa, M., and Benzaazoua, M. (2015). Curing time effect on consolidation behaviour of cemented paste backfill containing different cement types and contents. *Constr. Build. Mat.* 75, 99–111. doi:10.1016/j.conbuildmat.2014.11.008

Yılmaz, T., Ercikdi, B., Karaman, K., and Külekçi, G. (2014). Assessment of strength properties of cemented paste backfill by ultrasonic pulse velocity test. *Ultrasonics* 54 (5), 1386–1394. doi:10.1016/j.ultras.2014.02.012

Zhang, G., Wu, P., and Gao, S. (2019a). Properties and microstructure of low-carbon whole-tailings cemented paste backfill material containing steel slag, granulated blast furnace slag and flue gas desulphurization gypsum. *Acta Microsc.* 28 (4), 770–780.

Zhang, G., Wu, P., Gao, S., Zhang, K., Wang, C., Huo, Z., et al. (2019b). Preparation of environmentally friendly low autogenous shrinkage whole-tailings cemented paste backfill material from steel slag. *Acta Microsc.* 28 (5), 961–971.

Zhang, J., He, W., Ni, W., Hu, W., Chen, J., Zhu, T., et al. (2016). Research on the fluidity and hydration mechanism of mine backfilling material prepared in steel slag gel system. *Chem. Eng. Trans.* 51, 1039–1046. doi:10.11817/j.issn.1672-7347.2016.10.005

Zhang, Q., Ji, T., Yang, Z., Wang, C., and Wu, H. (2020). Influence of different activators on microstructure and strength of alkali-activated nickel slag cementitious materials. *Constr. Build. Mat.* 235, 117449. doi:10.1016/j.conbuildmat.2019.117449

Zhao, J., Wang, D., Yan, P., Zhang, D., and Wang, H. (2016). Self-cementitious property of steel slag powder blended with gypsum. *Constr. Build. Mat.* 113, 835–842. doi:10.1016/j.conbuildmat.2016.03.102

frontiers | Frontiers in Earth Science

TYPE Original Research
PUBLISHED 18 April 2023
DOI 10.3389/feart.2023.1181974



OPEN ACCESS

EDITED BY
Lijie Guo,
Beijing Mining and Metallurgy Technology Group Co., Ltd., China

REVIEWED BY
Shuhua Liu,
Wuhan University, China
Zengqi Zhang,
University of Science and Technology Beijing, China

*CORRESPONDENCE
Changlong Wang,
baistuwong@139.com
Yongxiang Zhou,
zhouyx@bjut.edu.cn

RECEIVED 08 March 2023
ACCEPTED 03 April 2023
PUBLISHED 18 April 2023

CITATION
Zhang H, Qi Y, Jing J, Wang C, Zhou Y, Zhang K, Zheng Y, Zhai Y and Liu F (2023), Properties and environmental impact of building foundation pit backfilling materials containing iron and steel solid waste.
*Front. Earth Sci.* 11:1181974.
doi: 10.3389/feart.2023.1181974



# Properties and environmental impact of building foundation pit backfilling materials containing iron and steel solid waste

Hongze Zhang[1], Yang Qi[2], Jianlin Jing[2], Changlong Wang[2]*, Yongxiang Zhou[3]*, Kaifan Zhang[2], Yongchao Zheng[4], Yuxin Zhai[5] and Feng Liu[6]

[1]School of Earth Science and Surveying and Mapping, China University of Mining and Technology (Beijing), Beijing, China, [2]Collaborative Innovation Center for Intelligent Regulation and Integrated Management of Water Resources Jointly Built by Provinces and Ministries, School of Civil Engineering, Hebei University of Engineering, Handan, China, [3]Faculty of Architecture, Civil and Transportation Engineering, Beijing University of Technology, Beijing, China, [4]State Key Laboratory of Solid Waste Reuse for Building Materials, Beijing Building Materials Academy of Science Research, Beijing, China, [5]Technical Center, China Railway Construction Group Co., Ltd., Beijing, China, [6]Construction Development Co., Ltd., China Railway Construction Group, Baoding, China

**Introduction:** In order to promote the comprehensive utilization of iron and steel solid waste, steel slag (SS), granulated blast furnace slag (GBFS), and flue gas desulfurization gypsum (FGDG) were used as raw materials to replace cement to prepare the full solid waste premixed solidified agent (PSA). Then PSA, iron ore tailings (IOTs), and water were mixed to prepare building foundation pit backfilling materials (BFPBM).

**Methods:** Various tests were conducted to investigate the effects of SS fineness, SS content and mixing ratio of PSA on the properties of PFPBM, including mechanical property test, X-ray diffraction (XRD), scanning electronic microscopy (SEM), energy dispersive spectrometry (EDS) and synthetic precipitation leaching procedure (SPLP). The stability of the BFPBM was tested and the hydration mechanism of the PSA was analyzed.

**Results:** The results show that when the specific surface area (SSA) of SS is 457 $m^2 \cdot kg^{-1}$, the paste mass concentration (PMC) is 79%, the mixing ratio of PSA is 20%, and the mix proportion of PSA is SS: FGDG: GBFS = 58:10:32. In this case, water-reducing agent (WRA) accounting for 0.18% of the total amount of PSA is added. The 28d compressive strength of BFPBM is greater than 0.40 MPa with the maximum value of 6.22 MPa, and the mixture slump of BFPBM is greater than 215 mm, which meets the index requirements of Chinese National Standard T/CECS 1037-2022 *Technical Standard for Backfilling Project by Using Premixed Fluidized Solidified Soil*.

**Discussion:** According to the mechanism study, the mineral phases of the PSA after hydration are: $C_2S$, $C_3S$, Ca $(OH)_2$, ettringite (AFT), C-S-H gel, and RO phase. $C_2S$, $C_3S$, $CaSO_4$ and other substances gradually disappeared with the hydration, while the content of AFt and C-S-H gel substances increased. BFPBM prepared from iron and steel waste has high strength and environmental friendliness, making it have good application prospects in foundation pit backfilling and mine filling.

KEYWORDS

**iron and steel solid waste, steel slag (SS), granulated blast furnace slag (GBFS), premixed solidified agent (PSA), building foundation pit backfilling materials (BFPBM), mixture slump, ettringite (AFt)**

# 1 Introduction

With the acceleration of urban construction, building foundation pit backfilling materials (BFPBM) prepared via premixed solidified agent (PSA) which mainly contains cement or lime are widely used in filling projects (Ning and Huang, 2006; Abdi et al., 2021; Sun et al., 2021). In China, cement production is a traditional industry with high emissions and energy consumption. The annual $CO_2$ emissions account for 5%–8% of global emissions (Turner and Collins, 2013; Mo et al., 2017). Therefore, to achieve low-carbon and high-quality development, it is urgent to develop new materials to replace cement-based PSA in the current infrastructure industry. Although China has a huge stock of industrial solid waste, such as coal gangue, red mud, tailings, smelting slag, phosphogypsum, electrolytic manganese slag, fly ash, coal gasification slag, and so on. But the comprehensive utilization rate is only 62.3%, lower than that of western countries.

Steel slag (SS) is the main metallurgical slag of the Chinese iron and steel industry. The SS emission is roughly 12–20% of crude steel output (Shi, 2004; Guo et al., 2018; Dhoble and Ahmed, 2018). In China, the annual production of SS is about 80 million tons, and the cumulative storage is around 800 million tons (Zhuang and Wang, 2021; Zhang et al., 2022; Zhao et al., 2022). However, less than 30% of SS has been utilized comprehensively (Alanyali et al., 2009; Li et al., 2011; Wang et al., 2018). In terms of chemical composition, SS mainly consists of CaO, $SiO_2$, $Fe_2O_3$, and MgO, plus a small amount of $Al_2O_3$, $P_2O_5$, and MnO (Roslan et al., 2016; Peng and Huang, 2010; Shi, 2002). The main minerals in SS include $C_2S$ ($2CaO{\cdot}SiO_2$), $C_3S$ ($3CaO{\cdot}SiO_2$), $C_2F$ ($2CaO{\cdot}Fe_2O_3$), RO phase (a continuous solid solution composed of divalent metal oxides like FeO, MgO, MnO, and CaO), Fe, and free CaO (f-CaO) (Yan et al., 2014; Yüksel, 2017; Humbert and Castro-Gomes, 2019; Liu et al., 2020; Liu et al., 2020; Gencel et al., 2021). Overall, SS has similar chemical and mineral compositions as cement. At present, SS is mainly used in subgrade engineering (Gu et al., 2018; Aldeeky and Hattamleh, 2017; Wang et al., 2020), mine filling (Li et al., 2021; Zhang et al., 2022; Zhao et al., 2022), and asphalt concrete aggregate production (Hasita et al., 2020; Hasita et al., 2020; Jiao et al., 2020). The $C_2S$ and $C_3S$ in SS can react with water to generate many hydration products, such as C-S-H gel ($3CaO{\cdot}2SiO_2{\cdot}3H_2O$), C-A-H crystal ($CaO{\cdot}Al_2O_3{\cdot}10H_2O$), $Ca(OH)_2$, and C-A-S-H gel ($CaO{\cdot}Al_2O_3{\cdot}4SiO_2{\cdot}5H_2O$). SS provides a promising auxiliary cementitious material, which could reduce resource waste and protect the environment (Palankar et al., 2016; Zhao et al., 2016; Zhuang and Wang, 2021). Thus, replacing cement and lime with metallurgical wastes is feasible to prepare new curing agents (Huang et al., 2020; Wang et al., 2021).

In recent years, scholars at home and abroad have carried out research on the preparation of BFPBM with PSA of steel waste. Yu et al. (2021) concluded that clay minerals have a great effect on soil engineering characteristics when using carbonized SS to prepare PSA and stabilize soil filling. Shen et al. (2018) used flue gas desulfurization gypsum (FGDG), SS, and clinker-free cement to prepare PSA to solidify the soft soil. When the mixing ratio of PSA is 5% higher than that of P·O 42.5R, the curing effect is similar. Deng et al. (2018) solidified the soft soil with PSA containing 20% SS, and the 28d compressive strength of the solidified soft soil could reach 1.2 MPa; Wang and Wang (2022) used industrial waste slags such as granulated blast furnace slag (GBFS)and calcium carbide slag to solidify soil with cement. It was found that the production of erosion products was related to the CaO content of waste slag. Sun et al. (2021) concluded that with the dosage of 10% PSA, the 7d unconfined compressive strength of the prepared material was 3.46 MPa, meeting the requirements of all levels of highway pavement base with light traffic load. However, in the preparation of PSA from metallurgical slag, cement and metallurgical slag are used as raw materials, and the dosage of metallurgical slag is generally low. In the existing studies on PSA mixed with SS, most focus on accelerating the hydration process of SS and activating cementitious activity, while only a few studies are conducted to synergistically activate the physical and chemical activation of SS. The SS activated by mechanical force and mixed with GBFS and FGDG can ensure the soundness of the cementitious system and promote the generation of hydration products in the later stage. Adding and dissolving FGDG can provide conditions for the formation of ettringite (Xu et al., 2019; You et al., 2020; Zhang et al., 2020; Zhuang and Wang, 2021).

In this paper, steel waste (SS, GBFS, iron ore tailings (IOTs), FGDG) was used as raw materials to prepare full solid waste PSA and BFPBM to completely replace cement. Besides, the influences of SS fineness and content, and the mixing ratio of PSA on the performance of BFPBM were studied through various tests, including mechanical property test, X-ray diffraction (XRD), and energy dispersive spectrometry (EDS). In addition, the PSA stability and hydration mechanism were tested. Finally, synthetic precipitation leaching procedure (SPLP) was adopted to test the leaching of heavy metals from the solidified body. This paper provides theoretical and technical support for the application of iron and steel metallurgical wastes in construction and mine engineering.

# 2 Materials and methods

## 2.1 Experimental materials

(1) SS. The SS used is the converter steel slag with the content of f-CaO as 2.85% and of f-MgO as 2.29%. The active coefficient and alkalinity value can reflect the activity of SS to a certain extent. The active coefficient is the ratio of active ingredients to inert ingredients, HAI=0.38. The alkalinity value is calculated through the Mason's method (Mason, 1944). According to the alkalinity value, SS can be classified as low-alkalinity SS (<1.8), medium-alkalinity SS (1.8–2.5), and high-alkalinity SS (>2.5). The alkalinity value of the used SS is 3.175, indicating that it has high-alkalinity. The particle size distribution analysis shows that 86.12% of the SS particles have the diameter between 0.3mm and 9.5 mm. Thus, the SS should be broken before grinding. The chemical composition of SS is listed in Table 1 and the major chemical components are CaO, $Fe_2O_3$ and $SiO_2$. Mineral phases of SS are $C_3S$, $C_2S$, and RO phases (FeO, MnO, and solid solution of MgO) (See Figure 1A).

(2) IOTs. The density of IOTs used in the test is 3.20 g $cm^{-3}$. The major components are inorganic constituents, such as $SiO_2$, CaO, MgO, $Fe_2O_3$, and $Al_2O_3$. As the content of $SiO_2$ in IOTs is 73.15% (>60%), the IOTs belong to high silica mineral materials. As can be seen from Figure 2, most of the IOTs particles are between 0.3 and 1.18 mm in size, accounting for 64.43%.

**TABLE 1** Chemical composition of raw materials (mass fraction, %).

| Materials | CaO | $SiO_2$ | $Fe_2O_3$ | MgO | $Al_2O_3$ | $TiO_2$ | $Na_2O$ | $K_2O$ | $SO_3$ | Others |
|---|---|---|---|---|---|---|---|---|---|---|
| SS | 33.56 | 9.10 | 27.31 | 7.96 | 4.32 | 0.12 | 0.11 | 0.06 | 0.36 | 10.91 |
| GBFS | 38.14 | 29.94 | 0.48 | 9.82 | 16.90 | 1.35 | 0.23 | 0.38 | 1.66 | 1.10 |
| FGDG | 37.98 | 0.56 | 0.45 | 0.08 | 1.13 | 0.02 | 0.03 | 0.06 | 51.27 | 8.55 |
| IOTs | 3.19 | 73.15 | 7.41 | 3.42 | 6.28 | 0.09 | 0.65 | 2.05 | 0.59 | 2.01 |

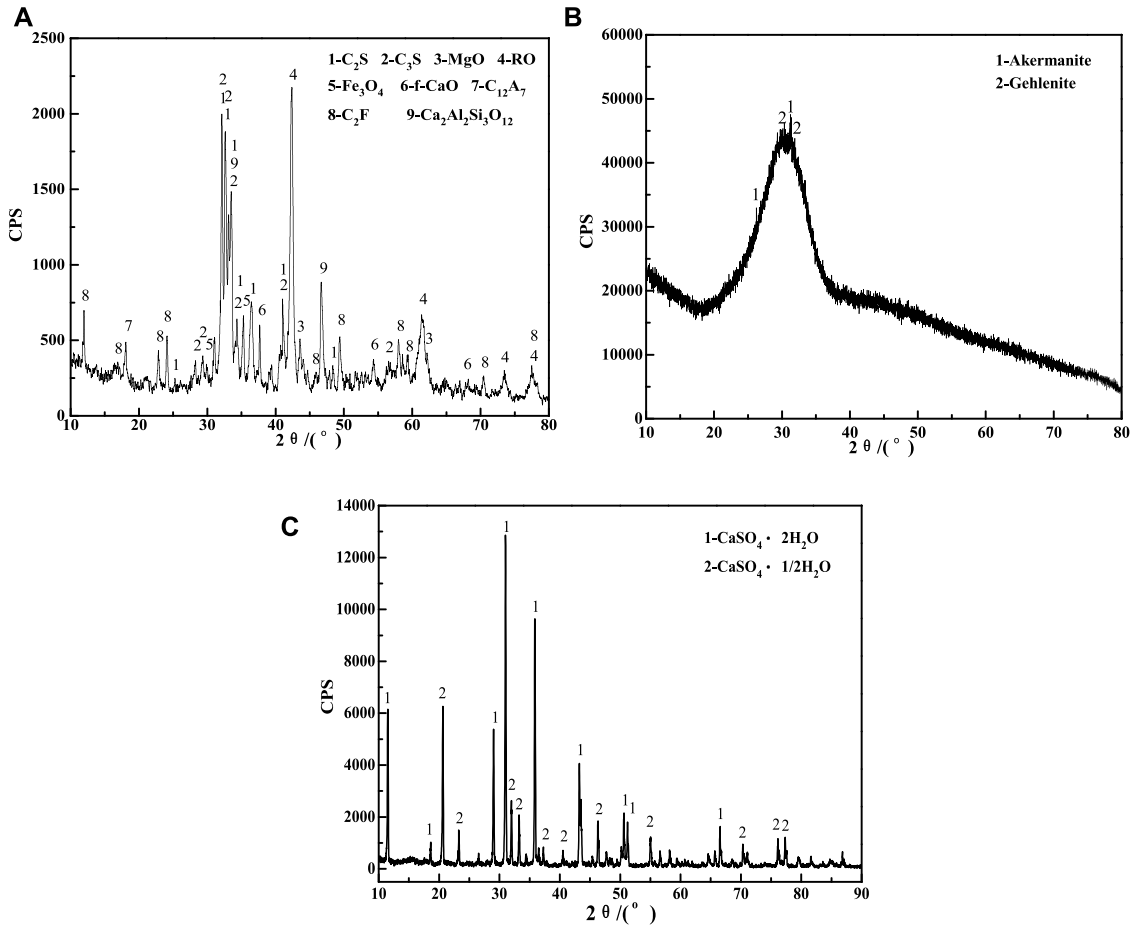


FIGURE 1
XRD patterns of raw materials. **(A)** SS; **(B)** GBFS; **(C)** FGDG.

(3) GBFS. The particle size of GBFS is 0.2–6 mm, and the apparent density is 2.86 × $10^3$ kg·$m^3$. According to the chemical composition of the used GBFS, the alkalinity value is 1.024 and it belongs to alkaline GBFS. The quality coefficient K is 2.058 (>1.2) and the larger the K value, the better. The active coefficient $M_a$ is 0.564 (>0.3), indicating that it belongs to highly-active GBFS. Figure 1B shows the XRD patterns. It can be seen that there is an obvious peak at 25–35°, which is indicating that GBFS belongs to vitreous substance.

(4) FGDG. The chemical composition of FGDG is listed in Table 1. The major components are $CaSO_4$·$2H_2O$ and $CaSO_4$·$1/2H_2O$ (Figure 1C).

(5) Other materials. In the test, the water-reducing agent (WRA) is polycarboxylates high performance water-reducing admixture (PC) whose water-reducing rate is 25%. P·O 42.5 ordinary Portland cement (OPC) is used in the contrast test.

## 2.2 Experimental method

(1) PSA preparation. Firstly, SS (ground into 1–3 mm particles with a jaw crusher), GBFS, and FGDG were put in the oven at 105°C for 24 h. Then, they were milled separately with the SMΦ 500 mm × 500 mm laboratory ball mill. Finally, the

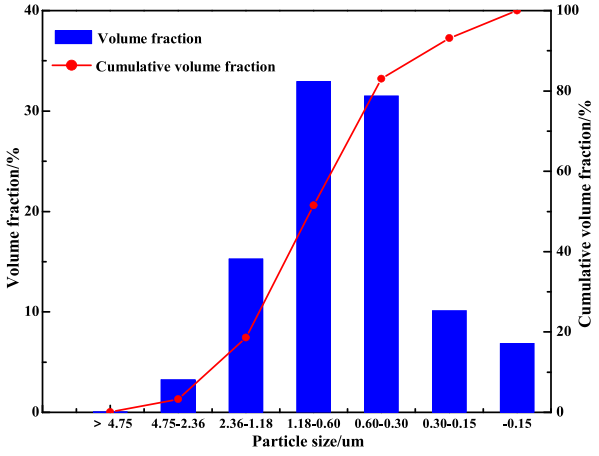


FIGURE 2
Particle size distribution of IOTs.

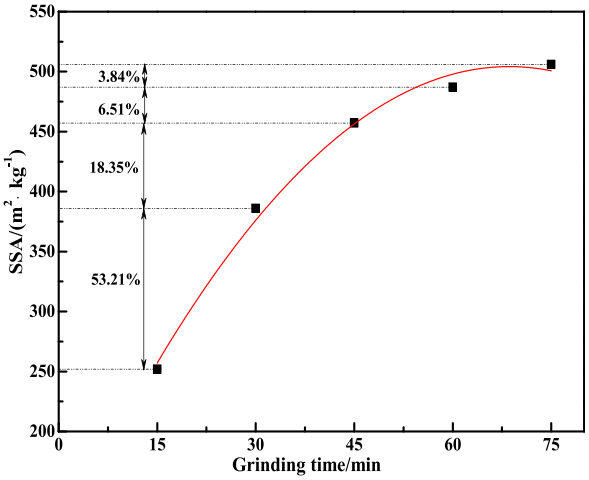


FIGURE 3
Fitting curve of SSA of SS at different grinding times.

pulverized raw materials were mixed according to the optimal ratio, thus obtaining the PSA.

(2) Preparation and testing of paste samples. The water requirement of normal consistency of PSA was determined according to GB/T 1346–2011 *Test methods for water requirement of normal consistency, setting time and soundness of the Portland cement*, and its setting time and stability were tested. Then, we added water and stirred well according to the water requirement of normal consistency. Next, we injected the mixture into the mold of 30 mm × 30 mm × 50 mm, and vibrated it. After 24 h, it was demoulded and put into a standard curing box with the temperature of (20 ± 1) °C and the humidity of more than 95%. The striding length ($L_0$) was measured by ISO-160 comparator with an accuracy of 0.001 mm. Then, the standard curing was continued until the set age. After that, the length ($l_i$) and its mechanical properties were determined. The central part of the test block was taken for phase composition and structure test.

(3) Preparation and testing of GFPBM. The PSA and IOTs were mixed according to a certain cement sand ratio. Then we added some water, stirred the GFPBM, and then put it into the cement mortar triple testing mold (40 mm × 40 mm × 160 mm). And it vibrated on the cement mortar vibration platform. After 24 h, it was demoulded and put into a standard curing box with the temperature of (20 ± 1) °C and the humidity of more than 95%. Finally, the mechanical properties of the test block at different ages were determined.

## 2.3 Property characterization

The f-CaO content of SS was determined by EDTA complexometric titration according to Methods of Chemical Analysis of SS (YB/T 140-2009) with ethylene glycol as extractant. The f-MgO content was measured by using ammonium nitrate-ethanol as extractant. The SSA of materials was obtained with SSA-3200 (a dynamic specific surface area analyzer). The compressive strength test was conducted on the samples based on the Chinese National Standard GB/T 17671-2021 *Method of testing cement-determination of strength*. The strength was measured by YES-300 (a hydraulic pressure testing machine) whose maximum load was 300 KN and the loading rate was 2.0 ± 0.5 kN/s. The value of mixture fluidity and slump were determined in accordance with GB/T 50,080–2016 *Standard for test method of performance on ordinary fresh concrete*.

The XRD spectras were obtained by a D/Max-RC diffractometer (Japan) with Cu-Kα radiation whose working voltage was 40 kV and working current was 150 mA. Its 2 θ scanning ranged between 10° and 90°, and it could generate rays with the wavelength of 1.5406 nm. Through the Zeiss SUPRA™55 scanning electron microscope coupled with a Be4-U92 energy spectrum, SEM observation was performed to analyse the mineral phase and the hydration products of the paste samples.

SPLP is a method used to evaluate the impact of BFPBM metal-leaching behavior. In this test, sulfuric acid or salpeter solution with the mass fraction of 60%/40% was added to adjust the pH to 4.20 ± 0.05, thus obtaining the leach liquor (Li and Chi, 2017). Then, the solidified powder of BFPBM with the particle size as 0.075 mm was mixed with the leach liquor according to the ratio of 1:20 (100 g of BFPBM solids/2,000 g leach liquor) and vibrated on a rotary agitator for 18 h. After that, the BFPBM slurry was filtered through a 0.45 μm filter, and the concentrations of Cr, Ni, Cu, Cd, Pb, Zn, As, and Hg were determined via the inductively coupled plasma optical emission spectrometer (ICP-OES) (Zhu et al.,2017).

# 3 Results and discussion

## 3.1 Effect of SS fineness on the mechanical properties of BFPBM

SS was ground for 15, 30, 45, 60, and 75 min, and the obtained specific surface areas (SSA) were 252 $m^2 kg^{-1}$, 386 $m^2 kg^{-1}$, 457 $m^2 kg^{-1}$, 487 $m^2 kg^{-1}$, and 506 $m^2 kg^{-1}$, respectively (see Figure 3). With the increase in grinding time, the SSA of SS presents an overall trend of

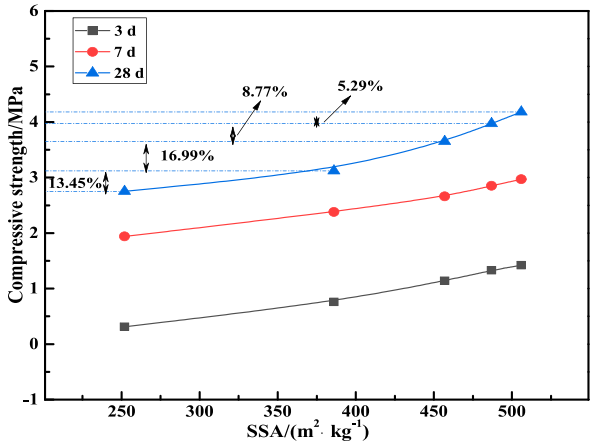


FIGURE 4
Effect of SS fineness on the mechanical properties of BFPBM at different curing ages.

increasing. In particular, the SSA of SS increases rapidly when the grinding time is less than 45 min. When the grinding time continues from 15 min to 30 min and 45 min, the SSA increases by 53.21% and 18.35%, respectively. Then, the increasing speed slows down, and the SSA of SS increases by 6.51% and 3.84% at 60 min and 75 min respectively. After 45 min grinding, the SSA of the SS is 457 $m^2 \cdot kg^{-1}$. After the preliminary exploration experiment, the mix proportion of optimized PSA was SS: FGDG: GBFS=50:12:38, and the SSAs of FGDG and GBFS after grinding were 390 $m^2 \cdot kg^{-1}$ and 480 $m^2 \cdot kg^{-1}$, respectively. The mixing ratio of PSA was 1:5, and the paste mass concentration (PMC) was set as 70%. The influence of SS fineness on BFPBM under different grinding times was studied, as shown in Figure 4.

As can be seen from Figure 4, with the increase of the SSA of SS, the compressive strengths of BFPBM at 3 d, 7 d and 28 d all show an increasing trend. Similar to the conclusion of SSA in Figure 3, when the SSA of SS is within 457 $m^2 \cdot kg^{-1}$, the compressive strength of BFPBM at each curing age will grow rapidly. Later, as the SSA continues to increase, the strength grows slowly. Therefore, the 28 d compressive strength of BFPBM is taken as an example. As the SSA of SS is increased from 252 $m^2 \cdot kg^{-1}$–386 $m^2 \cdot kg^{-1}$, and then increased to 457 $m^2 \cdot kg^{-1}$. The compressive strength of BFPBM is increased by 13.45% and 16.99%, respectively. Subsequently, the increasing rate of the compressive strength of BFPBM slows down to 8.77% and 5.29%. Therefore, when the SSA of SS is 457 $m^2 \cdot kg^{-1}$, the BFPBM has the compressive strength of 1.14, 2.66 MPa and 3.65 MPa at 3 d, 7 d and 28 d, respectively. It can be seen that when the grinding time of SS is greater than 45 min, the SSA of SS and the compressive strength of BFPBM prepared is increased slowly. Considering the grinding efficiency and cost, the optimal grinding time of SS is 45 min, at which the SSA of SS is 457 $m^2 \cdot kg^{-1}$ and BFPBM has high compressive strength.

## 3.2 Effect of SS content on the mechanical properties of BFPBM

Considering the soundness of SS, the mixing amount of SS was tested, and the mix proportion was shown in Table 2. The FGDG content was 10%. The SSAs of FGDG and GBFS after grinding were 390 $m^2 \cdot kg^{-1}$ and 480 $m^2 \cdot kg^{-1}$. The mixing ratio of PSA was 1:5, and the PMC was 79%. Then, the obtained sample was determined at the specified age (3 d, 7 d, and 28 d) to obtain the compressive strength. The experimental results are shown in Figure 5.

With the fixed mixing ratio of PSA and the content of FGDG, as the SS content decreases, the compressive strength of BFPBM in each age increases first and then decreases. When the SS content decreases from 68% to 58%, the 28d compressive strength is higher than the initial value (G1-28 d compressive strength) of 48.44%. With the further reduction of the SS content, the 28d compressive strength of BFPBM decreases, and the 28 d compressive strength of G7 decreases by 35.50% compared with that of G3. Compared with the 28d compressive strength of the BFPBM, the variation trends of the compressive strengths at 3 d and 7 d are the same as that of the 28 d compressive strength. When the SS content is 58%, the compressive strength of BFBPM is the maximum, and the experimental result of G3 is the best. That is, the PSA mix proportion is SS: GBFS: FGDG=58:32:10, the cement sand ratio is 1:5, and PMC is 79%. At this time, the 3 d, 7 d and 28 d compressive strengths of the BFPBM are 1.87 MPa, 3.26 MPa, 5.24 MPa, respectively. It meets the requirement of 0.4 MPa strength in Chinese National Standard T/CECS 1037–2022 *Technical Standard for backfilling project by using premixed fluid solidifying soil.*

## 3.3 Effect of WRA dosage on the properties of BFPBM

The water-reducing agent (WRA) is a kind of concrete admixture applied in the field of building materials. The mechanism of WRA contains: dispersion, lubrication, steric hindrance, and sustained release. WRA can reduce the mixing water consumption with the slump of concrete basically unchanged. It can be used to disperse the mixture, improve its working property, reduce unit water consumption, enhance the fluidity of the mixture, and reduce unit cementitious material consumption.

In this study, the material mix proportion determined in Section 3.2 was adopted. The PMC was 79%, and polycarboxylate superplasticizer (PC) was selected as the WRA. The dosages of PC accounted for 0.14%, 0.15%, 0.16%, 0.17%, 0.18%, 0.19%, and 0.20% of the weight of PSA, respectively. The corresponding experimental numbers were W1, W2, W3, W4, W5, W6, and W7. The effect of PC dosage on the property of BFPBM is shown in Figures 6, 7.

As can be seen from Figure 6, when the PMC is 79%, the slump of the BFPBM with PC is significantly higher than that without PC, which meets the slump requirement (150 mm<slump<240 mm) in Chinese National Standard T/CECS 1037–2022 *Technical Standard for backfilling project by using premixed fluid solidifying soil.*

With the same PMC, the slump of BFBPM increases significantly after adding PC, which is higher than that without adding PC (175 mm). With the increase of PC content, the slump increases first and then decrease. When the content of PC is 0.18%, the maximum slump reaches 215 mm. The addition of PC is beneficial to improve the mechanical properties of the BFPBM system.

**TABLE 2 Mix proportion of BFPBM.**

| Number | Composition of PSA/% | | | Cement sand ratio | PMC/% |
|---|---|---|---|---|---|
| | SS | FGDG | GBFS | | |
| G1 | 68 | 10 | 22 | 1:5 | 79 |
| G2 | 63 | 10 | 27 | 1:5 | 79 |
| G3 | 58 | 10 | 32 | 1:5 | 79 |
| G4 | 53 | 10 | 37 | 1:5 | 79 |
| G5 | 48 | 10 | 42 | 1:5 | 79 |
| G6 | 43 | 10 | 47 | 1:5 | 79 |
| G7 | 38 | 10 | 52 | 1:5 | 79 |

Note: PMC, solid mass/(solid mass +liquid mass) ×100%.

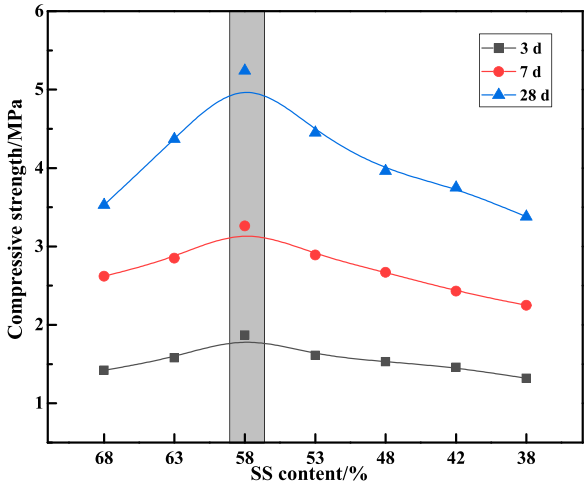


FIGURE 5
Effect of content of SS on the mechanical properties of BFPBM at different curing ages.

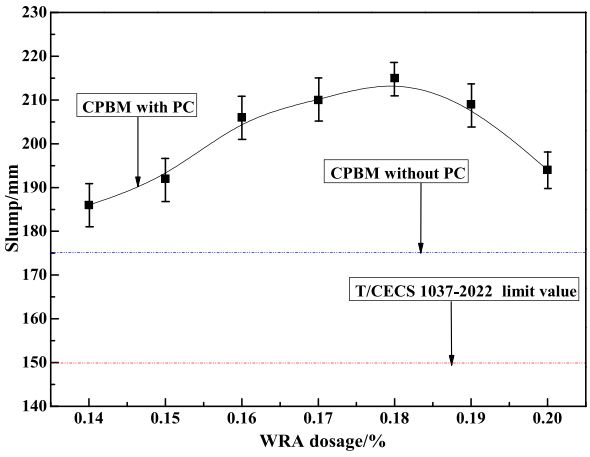


FIGURE 6
Effect of WRA dosage on the working properties of BFPBM.

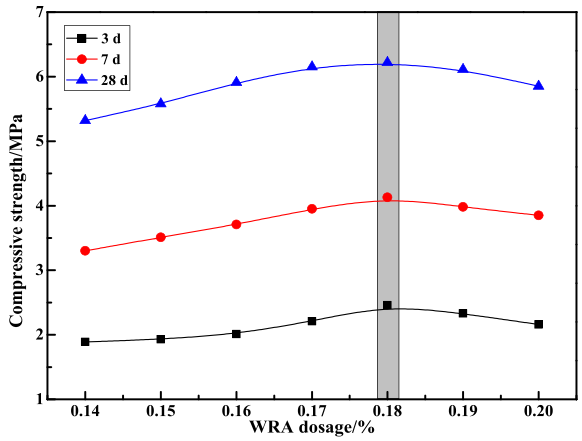


FIGURE 7
Effect of WRA dosage on the mechanical properties of BFPBM at different curing ages.

Figure 7 shows the trend diagram of the mechanical properties of the BFPBM when the PMC is 79%. The bending strengths and compressive strengths of the BFPBM sample with PC at 3 d, 7 d, and 28 d are obviously better than those without PC in Figure 5. The compressive strengths of the BFPBM samples with 0.18% PC at 3 d, 7 d, and 28 d increased by 31.56%, 26.69% and 18.70%, respectively, compared with the samples without PC at the same age.

The compressive strengths of the BFPBM mixed with 0.18% PC reach 2.46 MPa, 4.13 MPa, and 6.22 MPa at 3 d, 7 d and 28 d, respectively. They all meet the strength index (>0.4 MPa) in Chinese National Standard T/CECS 1037-2022. Compared with most building foundation pit backfilling requirements, the strength of the BFPBM is relatively higher. In application, the water-binder ratio and slump can be selected and adjusted more reasonably according to the specific requirements of BFPBM for strength and pumping conditions.

## 3.4 Soundness analysis of BFPBM

From Section 3.3, the full solid waste PSA with the mix proportion of SS: GBFS: FGDG=58:32:10 was prepared into paste

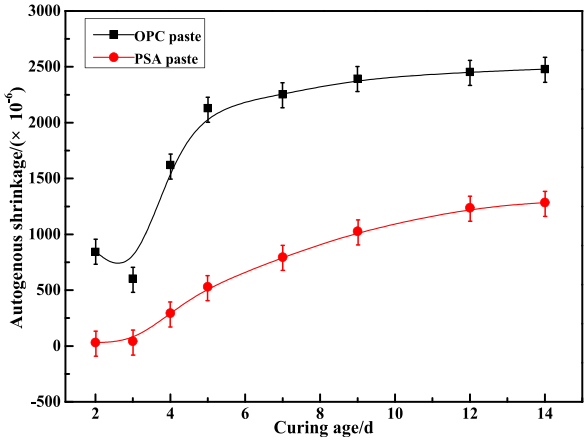


FIGURE 8
Volume soundness comparison of OPC and PSA paste samples.

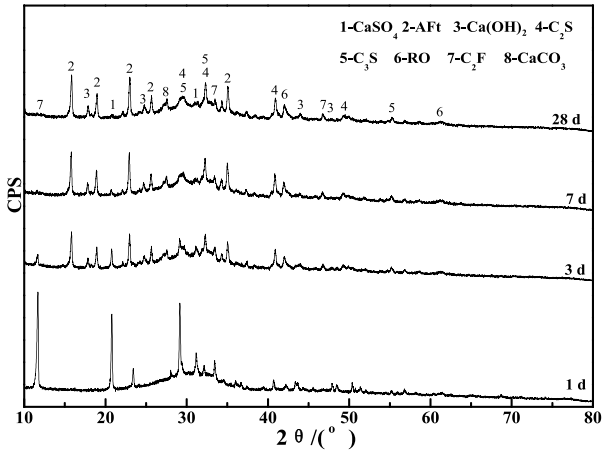


FIGURE 9
XRD patterns of hydration products of PSA paste at different ages.

according to the water-cement ratio of 1:2 Then, initial setting, final setting and fluidity tests were conducted, and no water seepage phenomenon was found in the PSA paste, proving its good water-retaining properties. The initial setting time of PSA was 162 min and the final setting time was 246 min, which could not only ensure the conveying and backfilling of BFPBM, but also facilitate solidification and improve the backfilling efficiency. The fluidity of the PSA paste was 136 mm, which also meets the fluidity requirement of the PSA for fertilizer tank backfilling (>100 mm) specified in Chinese National Standard T/CECS 1037-2022.

Since the BFPBM contains SS, it has soundness problems. It is necessary to test the volume soundness. In our test, the volume expansion values of two groups of samples were measured by the Le Chatelier Needles, and the results were 2.2 mm and 2.5 mm, respectively. This proved that the soundness was qualified. With OPC as the control group, we measured the changes in the volume soundness of the paste samples prepared by PSA at different ages, as shown in Figure 8.

It is reflected in Figure 8 that both paste samples present shrinkage characteristics under the standard condition, but their shrinkage degrees are obviously different: the shrinkage degree of the latter is smaller. At 14 d, the shrinkage values of the two samples were $2480\times10^{-6}$ and $1285\times10^{-6}$, respectively. The shrinkage values of the PSA samples with SS at 14 d were 48.2% lower than that of OPC at the same age. The volume soundness of the newly prepared PSA was better than that of the ordinary Portland cement. In summary, it can be seen that the optimal proportion of PSA is determined through the test, and its working performance and soundness meet the standard requirements, making it suitable for the next practical engineering.

## 3.5 Hydration mechanism analysis of PSA

### 3.5.1 XRD analysis

The PSA paste sample with the water-binder ratio of 0.5 was prepared according to the optimized mix proportion. The hydration products of the paste sample were cured for 1 d, 3 d, 7 d and 28 d, as shown in Figure 9. As can be seen from their XRD patterns, the following substances are observed, including ettringite (AFt), $Ca(OH)_2$, RO phase, $CaSO_4$, $C_2F$, $CaCO_3$, and unhydrated $C_3S$ and $C_2S$. SS is similar to cement clinker, in which active minerals $C_3S$ and $C_2S$ undergo hydration reaction to form C-S-H gel and $Ca(OH)_2$. There is an obvious "bulge" at 25–35 °, indicating that the system contains a large number of C-S-H gels and amorphous substances with low crystallinity (Bensted and Barnes, 2002; Wang et al., 2016; Wang et al., 2019). With the extension of the curing age, C-S-H gels are continuously deposited, gradually thickening and hardening the paste, and rapidly increasing its macroscopic strength (Cui et al., 2017). There is the amorphous vitreous body ($((CaO)_m(SiO_2)_n(Al_2O_3)_k$) in SS and GBFS, which can be illustrated by the steamed bread peaks between 25° ~ 35° (Figures 1A, B). Since the vitreous body has volcanic activity (Mejdi et al., 2019), the $Ca(OH)_2$ generated by the hydration of $C_3S$ and $C_2S$ in SS will consume the glass phase of SS and GBFS. Therefore, the diffraction summit of $C_3S$ and $C_2S$ in Figure 9 will gradually weaken with the extension of curing time. AFt diffraction peaks appear at 2θ of 15.7°, 19.0°, 23.1° and 32.3°, and the AFt diffraction peaks gradually increase with the extension of curing age. Since the generation of AFt consumes $CaSO_4$ in FGDG, the diffraction summit of $CaSO_4$ in hydration products decreases with the extension of age (Li et al., 2017; Wu et al., 2019).

In our test, after curing 1-day paste sample, hydration products did not change greatly and mainly contained more $C_3S$, $C_2S$ and $CaSO_4{\cdot}2H_2O$. The contents of $Ca(OH)_2$ and AFt increased significantly with the curing age increasing to 3 d, which was because the $Ca(OH)_2$ generated by the hydration of $C_3S$ and $C_2S$ in SS created an alkaline environment for the system. Therefore, more $Ca^{2+}$ and $Al^{3+}$ ions were dissociated from the GBFS vitreous body to generate C-S-H gels, and they reacted with $SO_4^{2-}$ provided by FGDG to form AFt (see Eq. 1), making the diffraction peaks of $C_3S$, $C_2S$ and $CaSO_4{\cdot}2H_2O$ in Figure 9 drop significantly. The contents of $Ca(OH)_2$ and AFt in the system continued to increase when the curing age reached 7 d, and the reaction continued. When the age increased 28 d, the content of $CaSO_4{\cdot}2H_2O$ in the system was basically exhausted, and the

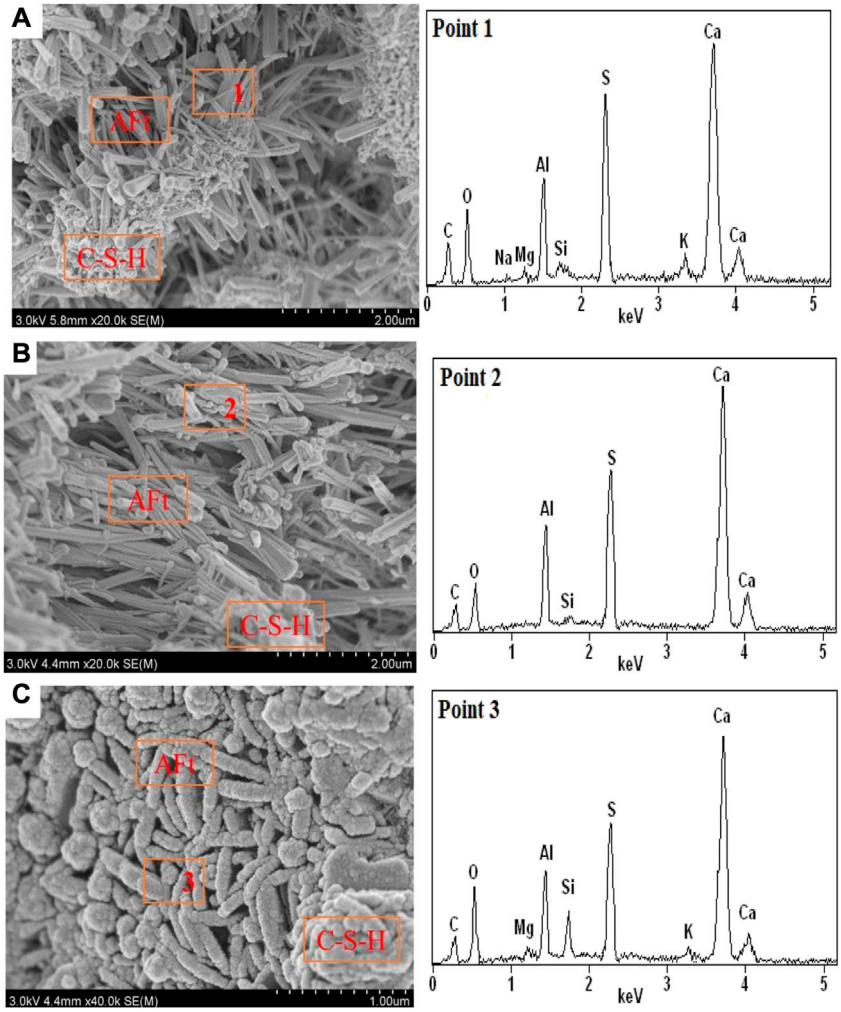


FIGURE 10
SEM-EDS images of hydration products of PSA paste at different ages. **(A)** 3 d; **(B)** 7 d; **(C)** 28 d.

content of AFt tended to be stable. In addition, the RO phase in the system basically did not participate in the hydration reaction, and the hydration entered the stable stage.

$$2H_3AlO_4^{2-} + 3Ca^{2+} + 3CaSO_4 \cdot 2H_2O + 2OH^- + 22H_2O \rightarrow 3CaO \cdot Al_2O_3 \cdot 3CaSO_4 \cdot 32H_2O\,(AFt) \quad (1)$$

The diffraction peak of $Ca(OH)_2$ was low in the early stage of hydration, which was related to its low crystallinity and partial absorption by GBFS hydration (Jiang et al., 2018). With the progress of hydration, the content of $Ca(OH)_2$ increased at 3 d of hydration, the content of $Ca(OH)_2$ basically remained unchanged at 28 d of hydration, and the hydration entered a stable stage. With SS, GBFS and FGDG stimulating each other, the system shows good hydraulic cementing characteristics, and the three synergically promote the hydration reaction to continue.

Compared with Portland cement clinker, SS has fewer contents of CaO and $C_3S$, indicating that it can be regarded as a weak Portland cement clinker. Therefore, it needs to be fully excited. FGDG is a sulfate activator, which can accelerate the crystal precipitation of hydration products and improve the material compactness (Duan et al., 2018). The soundness of SS is improved after mechanical grinding, and GBFS powder can absorb f-CaO and f-MgO of SS to a certain extent. In addition, the activity of GBFS is much higher than that of SS, which can improve the strength of cementing materials, making the advantages of the two materials complementary (Zhang et al., 2019).

### 3.5.2 SEM-EDS analysis

Figure 10 shows the SEM-EDS images of the dried hydration products of PSA paste samples which were cured to different ages and then immediately mixed with the anhydrous ethanol solution to end the hydration. As can be seen from Figure 10, the hydration products of PSA are mainly rod-shaped AFt crystals and amorphous C-S-H gels.

After 3 d of hydration, rod-shaped AFt crystals of about 10 μm and a small number of amorphous C-S-H gels in tiny voids appeared (Figure 10A). However, the crystallization of AFt crystal was incomplete, and the content of C-S-H gels was small, which was

**TABLE 3** The leaching concentrations of heavy metals from some raw materials, the PSA paste block and the BFPBM block after 28d curing age (μg/L).

| Materials | Cu | Pb | Zn | Ni | Cd | Cr | As | Hg |
|---|---|---|---|---|---|---|---|---|
| SS | 6.419 | 0.07 | 25.47 | 0.0175 | 0.3641 | 0.793 | 0.0047 | — |
| GBFS | 0.028 | 0.42 | 0.33 | 0.0009 | 0.0013 | 2.021 | 0.0056 | — |
| FGDG | 0.93 | 1.84 | 24.63 | 0.0049 | 0.2818 | 2.556 | 0.1873 | 0.06258 |
| IOTs | 19.33 | 0.85 | 63.31 | 0.8830 | 0.4231 | 0.879 | 2.5215 | 0.00224 |
| PSA paste block | 1.765 | 0.03 | 12.38 | 0.0438 | 0.1526 | 1.012 | 0.5762 | 0.01360 |
| BFPBM block | 8.246 | 0.18 | 40.62 | 0.0564 | 0.2473 | 1.605 | 0.8525 | 0.00356 |
| Limiting value | 100 | 5 | 100 | 5 | 1 | 5 | 5 | 0.1 |

not enough to obtain a dense surface of the structure. As a result, the strength was not greatly improved.

After 7 d of hydration, the number of C-S-H gels and AFt crystals increased (Figure 10B). This made the structure tend to be reticular and denser, further improving the strength.

After further hydration for 28 d, the EDS spectra of each site showed that the main elements were Ca, Si and Al, which was consistent with those of AFt (Figure 10C). At this curing age, SS, GBFS and FGDG stimulated each other to further promote hydration, and the obtained C-S-H gels and AFt were interwoven. Consequently, we obtained a tight network structure with closer arrangement of particles, further improving the strength of the test blocks. Thus, BFPBM could have good macro strength (Li et al., 2020).

## 3.6 Environmental impact of BFPBM

At present, one of the focuses of iron and steel solid waste application research is its application in the field of building materials, but little attention is attached to its heavy metal leaching problem. SS, GBFS, and FGDG, as the iron and steel waste and the corresponding building materials, contain Cr, Zn, Cu, Ni, Pb, Cd, As and other heavy metals (Zhang et al., 2018; Young et al., 2021; Sarathchandra et al., 2022). They are easy to transfer and transform in the environment, presenting potential environmental risks.

In this study, the leaching toxicity of BFPBM raw materials (SS, GBFS, FGDG, and IOTs), PSA paste blocks and BFPBM blocks were separately tested by the SPLP test. The SSA of SS powder milled for 45 min was 457 $m^2\ kg^{-1}$, that of GBFS was 480 $m^2\ kg^{-1}$, and that of FGDG was 390 $m^2\ kg^{-1}$. The chemical composition of IOTs raw materials is shown in Table 1, and the composition of grain size is shown in Figure 2. PSA mix proportion is SS: GBFS: FGDG=58:32:10. The water-binder ratio for preparing the PSA paste block is 0.5. The cement sand ratio for preparing the BFPBM block is 1:5, PMC is 79%, and the content of WRA is 0.18% of the mass of PSA.

The PSA paste block and the BFPBM block were cured for 28 d, then leaching toxicity was tested. The results of leaching toxicity are shown in Table 3. Although heavy metal leaching was detected in raw materials and samples under acidic environment, the content of heavy metals was still far lower than the standard value of leaching toxicity evaluation stipulated in Chinese National Standard GB/T 5085.3-2007. In addition, as the formation of hydration products C-S-H gels and AFt in PSA and BFPBM contributed to hydration stabilization, the risk of heavy metal leaching was further reduced. Therefore, it can be expected that even if raw materials with heavy metal leaching are added to the BFPBM system, the environmental risk coefficient of its application is still lower than the limit value specified in Chinese National Standard GB/T 5085.3-2007.

# 4 Conclusion

This paper used steel slag (SS), granulated blast furnace slag (GBFS) and flue gas desulfurization gypsum (FGDG) after mechanical activation to prepare building foundation pit backfilling materials (BFPBM) with the coordination of iron ore tailings (IOTs). By studying the composition, performance, hydration mechanism and environmental impact of BFPBM, the following conclusions are drawn.

(1) After mechanical activation, the steel waste (SS, GBFS and FGDG), can replace the cement to prepare the full solid waste PSA. The PSA can be used to prepare the BFPBM with the coordination of IOTs, which provides a new path to study the resource utilization of steel waste.
(2) As the mix proportion of PSA is SS: GBFS: FGDG=58:32:10, PMC is 79%, PSA incorporation ratio is 20%, and the added PC (a water-reducing agent) accounts for 0.18% of PSA total, the slump of BFPBM is 215 mm, and 28 d compressive strength reaches 6.22 MPa. Both meet the requirements of T/CECS 1037-2022 *Technical Standard for filling of Ready-mixed fluidized solidified soil.* The fluidity of PSA paste is 136 mm, and the soundness is qualified and better than that of P·O 42.5 ordinary Portland cement.
(3) In the BFPBM system, SS, GBFS and FGDG can stimulate each other and further promote hydration. PSA hydration products include $C_3S$, $C_2S$, $Ca(OH)_2$, C-S-H gels, AFt, RO phase, $CaCO_3$, and $C_2F$. With the increase of curing time, $C_3S$, $C_2S$, and $CaSO_4$ gradually disappear, and the contents of AFt and C-S-H gels increase continuously.
(4) According to the environmental risk evaluation, BFPBM has low leaching toxicity, lower than the limit stipulated by Chinese National Standard GB5085.3-2007. It proves that it has high strength and good environmental friendliness. Therefore, BFPBM

has a good application prospect in building foundation pit backfilling and mine filling.

## Data availability statement

The original contributions presented in the study are included in the article/Supplementary Material, further inquiries can be directed to the corresponding authors.

## Author contributions

HZ proposes method and writes manuscript; CW and YZho propose and participates in design research and reviews paper; QY, JJ, KZ, YZhe, YZha, and FL participate in design research and reviews paper. All the authors approved the final version of the manuscript.

## Funding

The authors gratefully acknowledge financial support by the National Key Research and Development Program of China (No. 2021YFC1910605), the Natural Science Foundation of Hebei Province (E2020402079), State Key Laboratory of Solid Waste Resource Utilization and Energy Conservation (SWR-2023-007), Science and Technology Research and Development Plan of China Railway Construction Group Co., Ltd. (No. 22-11b, 22-14b), Handan Science and Technology Research and Development Program (21422111260).

## Conflict of interest

Authors YZhe and FL were employed by China Railway Construction Group Co., Ltd. and Construction Development Co., Ltd.

The remaining authors declare that the research was conducted in the absence of any commercial or financial relationships that could be construed as a potential conflict of interest.

## Publisher's note

All claims expressed in this article are solely those of the authors and do not necessarily represent those of their affiliated organizations, or those of the publisher, the editors and the reviewers. Any product that may be evaluated in this article, or claim that may be made by its manufacturer, is not guaranteed or endorsed by the publisher.

## Supplementary material

The Supplementary Material for this article can be found online at: https://www.frontiersin.org/articles/10.3389/feart.2023.1181974/full#supplementary-material

## References

Abdi, M. R., Ghalandarzadeh, A., and Shafiei, C. L. (2021). An investigation into the effects of lime on compressive and shear strength characteristics of fiber-reinforced clays. *J. Rock Mech. Geotech. Eng.* 13 (4), 885–898. doi:10.1016/j.jrmge.2020.11.008

Alanyali, H., Çöl, M., Yilmaz, M., and Karagöz, Ş. (2009). Concrete produced by steel-making slag (basic oxygen furnace) addition in Portland cement. *Int. J. Appl. Ceram. Tec.* 6 (6), 736–748. doi:10.1111/j.1744-7402.2008.02317.x

Aldeeky, H., and Hattamleh, O. A. (2017). Experimental study on the utilization of fine steel slag on stabilizing high plastic subgrade soil. *Adv. Civ. Eng.* 2017, 9230279. doi:10.1155/2017/9230279

Bensted, J., and Barnes, P. (2002). *Structure and performance of cements*. second ed. New York: Spon Press.

Cui, X., Ni, W., and Ren, C. (2017). Hydration mechanism of all solid waste cementitious materials based on steel slag and blast furnace slag. *Chin. J. Mat. Res.* 31 (9), 687–694. doi:10.11901/1005.3093.2016.741

Deng, Y., Zhao, Y., Liu, J., Gu, X., Cha, F., and Zhu, C. (2018). $Na_2SiO_4$-and cement-based activation on steel slag and its application in soft-soil stabilization. *China J. Highw. Transp.* 31 (11), 11–20. (in Chinese).

Dhoble, Y., and Ahmed, S. (2018). Review on the innovative uses of steel slag for waste minimization. *J. Mat. Cycles Waste Manag.* 20, 1373–1382. doi:10.1007/s10163-018-0711-z

Duan, S., Liao, H., Cheng, F., Song, H., and Yang, H. (2018). Investigation into the synergistic effects in hydrated gelling systems containing fly ash, desulfurization gypsum and steel slag. *Constr. Build. Mat.* 187, 1113–1120. doi:10.1016/j.conbuildmat.2018.07.241

Gencel, O., Karadag, O., Oren, O. H., and Bilir, T. (2021). Steel slag and its applications in cement and concrete technology: A review. *Constr. Build. Mat.* 283, 122783. doi:10.1016/j.conbuildmat.2021.122783

Gu, X., Yu, B., Dong, Q., and Deng, Y. (2018). Application of secondary steel slag in subgrade: Performance evaluation and enhancement. *J. Clean. Prod.* 181, 102–108. doi:10.1016/j.jclepro.2018.01.172

Guo, J., Bao, Y., and Wang, M. (2018). Steel slag in China: Treatment, recycling, and management. *Waste Manage* 78, 318–330. doi:10.1016/j.wasman.2018.04.045

Hasita, S., Rachan, R., Suddeepong, A., Horpibulsuk, S., Arulrajah, A., Mohammadinia, A., et al. (2020). Performance improvement of asphalt concretes using steel slag as a replacement material. *J. Mat. Civ. Eng.* 32 (8), 04020227. doi:10.1061/(asce)mt.1943-5533.0003306

Hasita, S., Suddeepong, A., Horpibulsuk, S., Samingthong, W., Arulrajah, A., and Chinkulkijniwat, A. (2020). Properties of asphalt concrete using aggregates composed of limestone and steel slag blends. *J. Mat. Civ. Eng.* 32 (7), 06020007. doi:10.1061/(asce)mt.1943-5533.0003148

Huang, M., Sun, T., and Wang, L. (2020). Application of premixed solidified soil in backfilling of foundation trench. *IOP Conf. Ser. EES.* 510 (5), 052062. doi:10.1088/1755-1315/510/5/052062

Humbert, P. S., and Castro-Gomes, J. (2019). CO2 activated steel slag-based materials: A review. *J. Clean. Prod.* 208, 448–457. doi:10.1016/j.jclepro.2018.10.058

Jiang, L., Li, C., Wang, C., Xu, N., and Chu, H. (2018). Utilization of flue gas desulfurization gypsum as an activation agent for high-volume slag concrete. *J. Clean. Prod.* 205, 589–598. doi:10.1016/j.jclepro.2018.09.145

Jiao, W., Sha, A., Liu, Z., Li, W., Jiang, W., Qin, W., et al. (2020). Study on thermal properties of steel slag asphalt concrete for snow-melting pavement. *J. Clean. Prod.* 277, 123574. doi:10.1016/j.jclepro.2020.123574

Li, J., and Chi, S. (2017). Innovative solidification/stabilization of lead contaminated soil using incineration sewage sludge ash. *Chemosphere* 173, 143–152. doi:10.1016/j.chemosphere.2017.01.065

Li, J., Yu, Q., Wei, J., and Zhang, T. (2011). Structural characteristics and hydration kinetics of modified steel slag. *Cem. Concr. Compos.* 41 (3), 324–329. doi:10.1016/j.cemconres.2010.11.018

Li, N., Farzadnia, N., and Shi, C. (2017). Microstructural changes in alkali-activated slag mortars induced by accelerated carbonation. *Cem. Concr. Res.* 100, 214–226. doi:10.1016/j.cemconres.2017.07.008

Li, X., Li, K., Sun, Q., Liu, L., Yang, J., and Xue, H. (2021). Preparation of cemented oil shale residue–steel slag–ground granulated blast furnace slag backfill and its environmental impact. *Mater* 14 (8), 2052–2073. doi:10.3390/ma14082052

Li, Y., Qiao, C., and Ni, W. (2020). Green concrete with ground granulated blast-furnace slag activated by desulfurization gypsum and electric arc furnace reducing slag. *J. Clean. Prod.* 269, 122212. doi:10.1016/j.jclepro.2020.122212

Liu, J., Yu, B., and Wang, Q. (2020). Application of steel slag in cement treated aggregate base course. *J. Clean. Prod.* 269, 121733. doi:10.1016/j.jclepro.2020.121733

Liu, W., Li, H., Zhu, H., and Xu, P. (2020). The interfacial adhesion performance and mechanism of a modified asphalt–steel slag aggregate. *Mater* 13 (5), 1180–1192. doi:10.3390/ma13051180

Mason, B. (1944). The constitution of some open-heart slag. *J. Iron Steel Res. Int.* 179 (11), 69–80.

Mejdi, M., Wilson, W., Saillio, M., Chaussadent, T., Divet, L., and Tagnit-Hamou, A. (2019). Investigating the pozzolanic reaction of post-consumption glass powder and the role of portlandite in the formation of sodium-rich C-S-H. *Cem. Concr. Res.* 123, 105790. doi:10.1016/j.cemconres.2019.105790

Mo, L., Zhang, F., Deng, M., Jin, F., Al-Tabbaa, A., and Wang, A. (2017). Accelerated carbonation and performance of concrete made with steel slag as binding materials and aggregates. *Cem. Concr. Compos.* 83, 138–145. doi:10.1016/j.cemconcomp.2017.07.018

Ning, J., and Huang, X. (2006). Experiment on structural formation and mechanism of strength increasing of stabilized soil. *J. B. Univ. Aeronaut. Astronaut.* 32 (01), 97–102. doi:10.1016/s1005-8885(07)60042-9

Palankar, N., Shankar, A. U. R., and Mithun, B. M. (2016). Durability studies on eco-friendly concrete mixes incorporating steel slag as coarse aggregates. *J. Clean. Prod.* 129, 437–448. doi:10.1016/j.jclepro.2016.04.033

Peng, Y., and Huang, C. (2010). Carbon steel slag as cementitious material for self-consolidating concrete. *J. Zhejiang Univ-SC. A* 11 (7), 488–494. doi:10.1631/jzus.A0900635

Roslan, N., Ismail, M., Abdul-Majid, Z., Ghoreishiamiri, S., and Muhammad, B. (2016). Performance of steel slag and steel sludge in concrete. *Constr. Build. Mat.* 104, 16–24. doi:10.1016/j.conbuildmat.2015.12.008

Sarathchandra, S. S., Rengel, Z., and Solaiman, Z. M. (2022). Remediation of heavy metal-contaminated iron ore tailings by applying compost and growing perennial ryegrass (Lolium perenne L.). *Chemosphere* 288, 132573. doi:10.1016/j.chemosphere.2021.132573

Shen, J., Xu, Y., and You, G. (2018). Stabilized effect of desulfurized gypsum and steel slag blended clinker free cement on soft clay. *Bull. Am. Ceram. Soc.* 37 (12), 3888–3891. doi:10.16552/j.cnki.issn1001-1625.2018.12.029

Shi, C. J. (2002). Characteristics and cementitious properties of ladle slag fines from steel production. *Cem. Concr. Res.* 32 (3), 459–462. doi:10.1016/S0008-8846(01)00707-4

Shi, C. (2004). Steel slag-its production, processing, characteristics and cementitious properties. *J. Mat. Civ. Eng.* 16 (3), 230–236. doi:10.1061/(asce)0899-1561(2004)16:3(230)

Sun, H., Wang, W., and Ling, S. (2021). Mechanical properties and microstructure of solidified soil with low cement content. *J. Zhejiang Univ-SC. B* 55 (3), 530–538. doi:10.3785/j.issn.1008-973X.2021.03.013

Sun, R., Fang, C., Gao, F., Ge, Z., Zhang, H., Lu, Q., et al. (2021). The participation of basolateral amygdala in the efficacy of acupuncture with deqi treating for functional dyspepsia. *China J. Highw. Transp.* 34 (10), 216–230. doi:10.1007/s11682-019-00249-7

Turner, L. K., and Collins, F. G. (2013). Carbon dioxide equivalent (CO2-e) emissions: A comparison between geopolymer and OPC cement concrete. *Constr. Build. Mat.* 43, 125–130. doi:10.1016/j.conbuildmat.2013.01.023

Wang, A., He, M., Mo, L., Liu, K., Li, Y., Zhou, Y., et al. (2019). Research progress of building materials prepared from the carbonized curing steel slag. *Mat. Rep.* 33 (17), 2939–2948. doi:10.11896/cldb.19040202

Wang, C., Ni, W., Zhang, S., Wang, S., Gai, G., and Wang, W. (2016). Preparation and properties of autoclaved aerated concrete using coal gangue and iron ore tailings. *Constr. Build. Mat.* 104, 109–115. doi:10.1016/j.conbuildmat.2015.12.041

Wang, C., Ren, Z., Huo, Z., Zheng, Y., Tian, X., Zhang, K., et al. (2021). Properties and hydration characteristics of mine cemented paste backfill material containing secondary smelting water-granulated nickel slag. *Alex. Eng. J.* 60 (6), 4961–4971. doi:10.1016/j.aej.2020.12.058

Wang, S., Li, X., Ren, K., and Liu, C. (2020). Experimental research on steel slag stabilized soil and its application in subgrade engineering. *Geotech. Geol. Eng.* 38, 4603–4615. doi:10.1007/s10706-020-01313-6

Wang, S., Wang, C., Wang, Q., Liu, Z., Qian, W., Jin, C., et al. (2018). Study on cementitious properties and hydration characteristics of steel slag. *Pol. J. Environ. Stud.* 27 (1), 357–364. doi:10.15244/pjoes/74133

Wang, Z., and Wang, D. (2022). Performance of industrial residue-cement solidified soils in resisting sulfate erosion. *Chin. J. Geotech. Eng.* 44 (11), 2035–2042. doi:10.11779/CJGE202211009

Wu, M., Zhang, Y., Jia, Y., Sha, W., Liu, G., Yang, Z., et al. (2019). Effects of sodium sulfate on the hydration and properties of lime-based low carbon cementitious materials. *J. Clean. Prod.* 220, 677–687. doi:10.1016/j.jclepro.2019.02.186

Xu, C., Ni, W., Li, K., Zhang, S., Li, Y., and Xu, D. (2019). Hydration mechanism and orthogonal optimisation of mix proportion for steel slag-slag-based clinker-free prefabricated concrete. *Constr. Build. Mat.* 228, 117036. doi:10.1016/j.conbuildmat.2019.117036

Yan, P., Mi, G., and Wang, Q. (2014). A comparison of early hydration properties of cement–steel slag binder and cement–limestone powder binder. *J. Therm. Ann. Calorim.* 115 (1), 193–200. doi:10.1007/s10973-013-3360-4

You, N., Shi, J., and Zhang, Y. (2020). Corrosion behaviour of low-carbon steel reinforcement in alkali-activated slag-steel slag and Portland cement-based mortars under simulated marine environment. *Corros. Sci.* 175, 108874. doi:10.1016/j.corsci.2020.108874

Young, G., Chen, Y., and Yang, M. (2021). Concentrations, distribution, and risk assessment of heavy metals in the iron tailings of Yeshan National Mine Park in Nanjing, China. *Chemosphere* 271, 129546. doi:10.1016/j.chemosphere.2021.129546

Yu, C., Cui, C., Wang, Y., Zhao, J., and Wu, Y. (2021). Strength performance and microstructural evolution of carbonated steel slag stabilized soils in the laboratory scale. *Eng. Geol.* 2021 (3), 106410. doi:10.1016/j.enggeo.2021.106410

Yüksel, I. (2017). A review of steel slag usage in construction industry for sustainable development. *Environ. Dev. Sustain.* 19, 369–384. doi:10.1007/s10668-016-9759-x

Zhang, G., Wu, P., Gao, S., Ye, P., Wang, C., Huo, Z., et al. (2019). Preparation of environmentally friendly low autogenous shrinkage whole-tailings cemented paste backfill material from steel slag. *Acta Microsc.* 28 (5), 961–971.

Zhang, J., Li, S., and Li, Z. (2020). Investigation the synergistic effects in quaternary binder containing red mud, blast furnace slag, steel slag and flue gas desulfurization gypsum based on artificial neural networks. *J. Clean. Prod.* 273, 122972. doi:10.1016/j.jclepro.2020.122972

Zhang, M., Li, K., Ni, W., Zhang, S., Liu, Z., Wang, K., et al. (2022). Preparation of mine backfilling from steel slag-based non-clinker combined with ultra-fine tailing. *Constr. Build. Mat.* 320, 126248. doi:10.1016/j.conbuildmat.2021.126248

Zhang, X., Yang, H., and Cui, Z. (2018). Evaluation and analysis of soil migration and distribution characteristics of heavy metals in iron tailings. *J. Clean. Prod.* 172, 475–480. doi:10.1016/j.jclepro.2017.09.277

Zhao, J., Wang, D., Yan, P., Zhang, D., and Wang, H. (2016). Self-cementitious property of steel slag powder blended with gypsum. *Constr. Build. Mat.* 113 (3), 835–842. doi:10.1016/j.conbuildmat.2016.03.102

Zhao, Y., Wu, P., Qiu, J., Guo, Z., Tian, Y., Sun, X., et al. (2022). Recycling hazardous steel slag after thermal treatment to produce a binder for cemented paste backfill. *Power Technol.* 395, 652–662. doi:10.1016/j.powtec.2021.10.008

Zhu, X., Chen, B., Zhu, L., and Xing, B. (2017). Effects and mechanisms of biochar-microbe interactions in soil improvement and pollution remediation: A review. *Environ. Pollut.* 227, 98–115. doi:10.1016/j.envpol.2017.04.032

Zhuang, S., and Wang, Q. (2021). Inhibition mechanisms of steel slag on the early-age hydration of cement. *Cem. Concr. Res.* 140, 106283. doi:10.1016/j.cemconres.2020.106283

frontiers | Frontiers in Earth Science

TYPE Original Research
PUBLISHED 20 April 2023
DOI 10.3389/feart.2023.1082714



OPEN ACCESS

EDITED BY
Miao Li,
Charles Sturt University, Australia

REVIEWED BY
Shaoda Liu,
Beijing Normal University, China
Jitao Lv,
Chinese Academy of Sciences (CAS), China

*CORRESPONDENCE
Yujing Wang,
wangyujing@meescc.cn

RECEIVED 28 October 2022
ACCEPTED 06 April 2023
PUBLISHED 20 April 2023

CITATION
Han W, Zhao R, Liu W, Wang Y, Zhang S, Zhao K and Nie J (2023), Environmental contamination characteristics of heavy metals from abandoned lead–zinc mine tailings in China.
*Front. Earth Sci.* 11:1082714.
doi: 10.3389/feart.2023.1082714



# Environmental contamination characteristics of heavy metals from abandoned lead–zinc mine tailings in China

Wei Han[1], Ruifeng Zhao[1], Wanrong Liu[1], Yujing Wang[1]*, Shuai Zhang[2], Kang Zhao[1] and Jinglei Nie[1]

[1]Solid Waste and Chemicals Management Center, Ministry of Ecology and Environment, Beijing, China, [2]MOE Key Laboratory of Soft Soils and Geo-environmental Engineering, Zhejiang University, Hangzhou, China

China holds large-scale lead–zinc mineral resources; however, mining activities often cause severe contamination by heavy metals. This study systemically assessed contamination by eight heavy metals (Cu, Zn, Cd, Pb, Cr, Hg, Ni, and As) in mine tailings, soil, and groundwater from 27 contaminated sites across China. Regarding mine tailings, 1% of the mine tailing samples were hazardous waste and 20% were class II non-hazardous waste. Regarding soil, Zn and Pb showed the highest mean concentrations, at 5574.67 mg/kg and 2034.88 mg/kg, respectively. The indexes of geo-accumulation ($I_{geo}$) of eight heavy metals ranged from −3.62 to 7.67, while Zn, Pb, and Cd showed the highest environmental risk levels as the priority pollutants. The contamination levels of these heavy metals in groundwater were generally in the order of Zn>As>Pb>Ni>Cd>Cu>Hg>Cr. In this study, 20% of the soil and 10% of the groundwater samples exceeded the corresponding quality limits. The content of heavy metals in soil, groundwater, and mine tailing were positively correlated, demonstrating the main pollution source and transport paths. The pollution levels of heavy metals in soil and groundwater were listed in the foremost and moderate positions compared with similar sites from other countries, respectively. These results may help determine the pollution levels of lead–zinc mining regions and direct the remediation activities of target sites to support the environmental management of abandoned mining and tailing waste in China.

KEYWORDS

**heavy metals, lead–zinc mine, mine tailing, soil and groundwater, contamination**

## 1 Introduction

Soil and groundwater pollution has become a severe problem worldwide (Li et al., 2014; Yang et al., 2018). Heavy metal pollution has been serious in China with the rapid social and economic development in recent decades (Xiao et al., 2015; Zhu et al., 2021). The main contamination sources mainly include human activities in the industrial, mining, and farming sectors (Liu et al., 2020; Peng et al., 2022). Mining activities are among the most significant sources of heavy metal pollution (MEP of China, 2014), with mine tailings a critical contamination factor of heavy metals (Ganhurrel et al., 2020; Mezned et al., 2022). Heavy metals derived from mined areas may cause adverse effects

on the ecological environment and the health of residents because they enter and accumulate in the soil and are then transported downward to diffuse into groundwater (Lee et al., 2005; Doya et al., 2020; Zhu et al., 2021; Tomiyama and Igarashi, 2022). China is one of the largest global producers and consumers of metals/metalloids such as antimony (Sb), iron (Fe), lead (Pb), manganese (Mn), and zinc (Zn) (Gunson and Jian, 2001). Mining alone has generated about 1,500,000 ha of wasteland in China. Moreover, the wasteland is increasing at a rate of 46,700 ha per year (Zhuang et al., 2009).

China is rich in lead–zinc mine resources (Zhao et al., 2007; Li et al., 2014). The resource reserves of lead and zinc in China are 20.41 million tons and 44.23 million tons (MNR of China, 2022), respectively, ranking third worldwide after the United States and Australia. China produced 7.36 million tons and 6.56 million tons of lead and zinc, respectively, in 2021, increases of 11.2% and 1.7%, which comprise 32.55% and 26.3% of the total global production (MIIT of China, 2022). Therefore, China plays a critical role in the lead–zinc industrial chains worldwide. Lead and zinc mining also threaten the environment by contaminating the surrounding soil and groundwater (Li et al., 2014). During the history of lead–zinc mining, many lead–zinc mine tailing ponds were abandoned in China. Moreover, the environmental risks increase continuously in abandoned mining areas despite the closure of the mining operation and the effects of natural attenuation (Rodríguez et al., 2022). Most early studies evaluated single or limited numbers of mining areas (Zhang et al., 2019; Zhou et al., 2022) and only one study reported on environmental media like soil (Li et al., 2014; Yang et al., 2018; Peng et al., 2022; Shi et al., 2022). Therefore, an overall evaluation of heavy metal pollution in lead–zinc mine areas including soil and groundwater on a national scale is severely lacking and urgently needed for environmental management.

The present study systematically investigated heavy metal pollution in 27 abandoned lead–zinc mine tailing sites in eight provinces in China. The analyzed targets included mine tailings, soil, and groundwater in the mine vicinity. The objectives of this study were to 1) determine the contamination levels of heavy metals in solid waste from abandoned lead–zinc mine tailings and environmental matrices around the sites, 2) determine the prior contaminants with greater environmental risks, and 3) propose policy recommendations for environmental management agencies.

# 2 Materials and methods

## 2.1 Database source

Information on the 27 abandoned zinc–lead mine sites and pollution data of the heavy metals in different environmental matrices including mine tailings, soils, and groundwater surrounding the mine tailing storage sites were collected from the China Knowledge Full-text Literature Database and survey reports provided by the environmental consulting companies and the government. The target samples were collected from southwest, northwest, and middle south regions of China, where rich lead–zinc mine resources are located. Solid waste was present in the mine tailings in the abandoned mining areas. The running and piling times of the mine tailings ranged from 10 to 60 years. The soils were sampled in the vicinity of the mine tailings to a depth of 0–20 cm from the soil surface. The groundwater samples were collected from wells located downstream of the studied mine tailing areas. A typical site field in the present study is shown in Figure 1.

## 2.2 Pollution assessment compared to the limit standards

For solid waste samples, leaching toxicity was applied to identify the environmental risk. The solid waste extraction procedure for leaching toxicity was performed using the sulfuric acid and nitric acid method (HJ/T299-2007). The identification standards (GB 5085.3-2007) for hazardous waste were used to compare the leaching toxicity to identify hazardous wastes. The horizontal vibration method (HJ-557 guideline, pure water as the extracting agent) was used during the extraction for leaching toxicity to identify class I or II non-hazardous industrial wastes.

For soil and groundwater sample treatment and analysis, the sampling strategies and processing methods used are widely accepted by the scientific community. The heavy metal content in the groundwater was compared with the standard for groundwater quality class III (GB/T 14848-2017). The heavy metal contents in the soil samples were compared to the risk screening and risk intervention values for soil contamination for the development of land derived from the soil environmental quality in China (GB 36600-2018).

All statistical analyses were performed using IBM SPSS Statistics version 19.0 and Excel 2013 for Windows. The correlations between the concentrations of different heavy metals in the soil samples were assessed by Pearson correlation coefficients.

## 2.3 Index of geo-accumulation for soil samples

Soil is a critical layer due to its connecting functions between solid waste pollution sources and groundwater. The soil risk was further assessed as follows. The environmental risk of the soil from the abandoned mine tailing was assessed using the geo-accumulation index ($I_{geo}$) calculated using the original equation by Muller (1969):

$$I_{geo} = log_2\left(\frac{C_n}{K \cdot B_n}\right),$$

where $C_n$ is the total concentration of metal n in the soil sample and $B_n$ is the background concentration of this metal in the studied

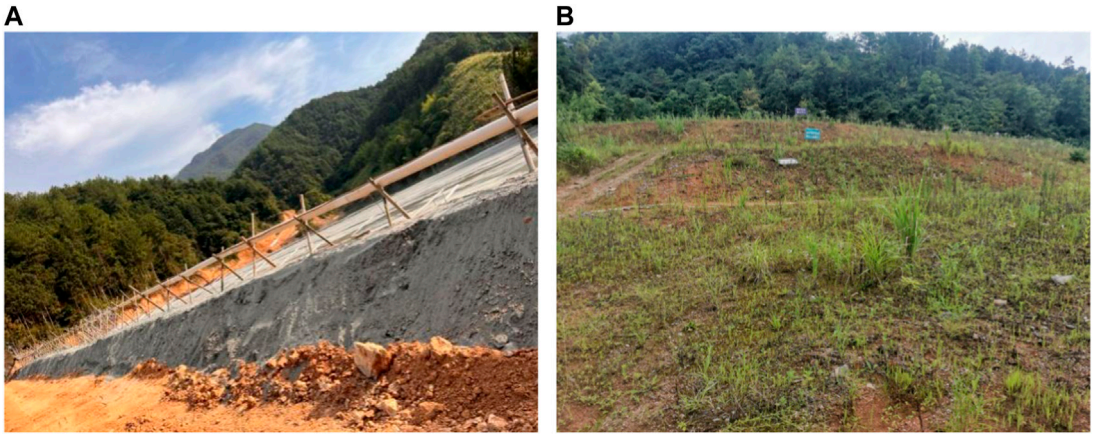


FIGURE 1
Typical lead–zinc mine tailing pile **(A)** and surrounding soil **(B)** in Fujian.

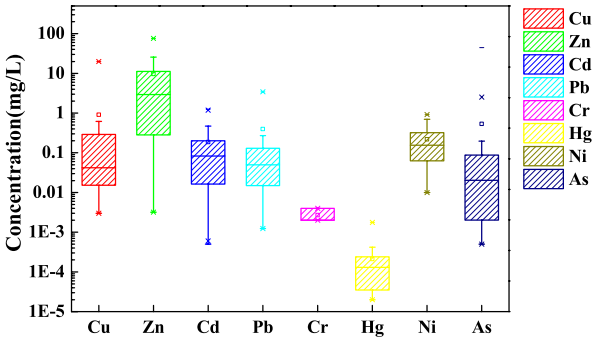


FIGURE 2
Concentrations of heavy metals in the leaches of mine tailings by acid solutions.

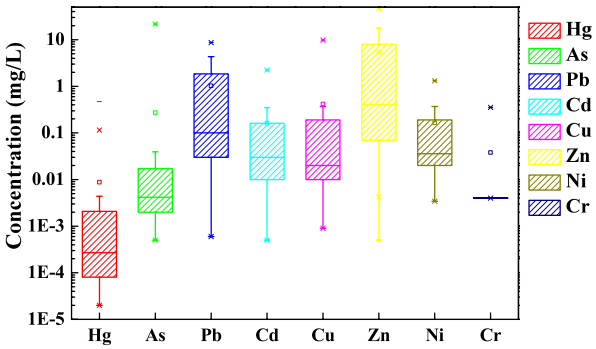


FIGURE 3
Concentrations of heavy metals in the leaches of mine tailings by pure water.

region. The regional background value is determined according to the background sample analysis. The constant K is 1.5 due to potential variations in the baseline data (Li et al., 2014). Based on the calculated values of $I_{geo}$, the soil samples were classified into seven classes in Table 1.

**TABLE 1 Seven classes comprising the geo-accumulation index.**

| Class | Value | Soil quality |
|---|---|---|
| 0 | $I_{geo} \leq 0$ | Practically unpolluted |
| 1 | $0 < I_{geo} \leq 1$ | Unpolluted to moderately polluted |
| 2 | $1 < I_{geo} \leq 2$ | Moderately polluted |
| 3 | $2 < I_{geo} \leq 3$ | Moderately to strongly polluted |
| 4 | $3 < I_{geo} \leq 4$ | Strongly polluted |
| 5 | $4 < I_{geo} \leq 5$ | Strongly to extremely polluted |
| 6 | $5 < I_{geo}$ | Extremely polluted |

# 3 Results and discussion

## 3.1 Identification of hazardous waste

Hazardous material screening was conducted to reveal the properties of the mine tailings as the contamination sources of soils and groundwater in abandoned mining areas. A total of 105 samples were analyzed; the results are shown in Figure 2 and Supplementary Table S1. Zinc showed the highest average concentration (9.68 mg/L) for the acid leaches, compared to <1 mg/L for the other metals. The As and Cd contents in several acid leaches were above the hazardous waste control limits, exceeding the standards of 0.95% and 1.9%, with the highest contents of 44.5 mg/L and 1.25 mg/L, respectively. Therefore, parts of the solid wastes still pose serious threats in some mining sites, although the heavy metals in 98% of the collected samples met the hazardous waste identification standard (GB 5085.3-2007).

**TABLE 2** Pearson correlations of different heavy metals in soils.

| Correlation | As | Cd | Cu | Pb | Hg | Ni | Zn | Cr |
|---|---|---|---|---|---|---|---|---|
| As | 1 | .135[a] | .036 | .138[a] | .357[a] | .054 | .462[a] | .209 |
| Cd | | 1 | .071 | .490[a] | .179 | −.097 | .793[a] | .043 |
| Cu | | | 1 | .016 | .291[b] | .823[a] | .014 | .529[a] |
| Pb | | | | 1 | .129[b] | −.147[a] | .621[a] | .102 |
| Hg | | | | | 1 | .248[b] | .271[a] | .454[a] |
| Ni | | | | | | 1 | −.136[b] | .557[a] |
| Zn | | | | | | | 1 | .120 |
| Cr | | | | | | | | 1 |

[a]Correlation significant at the 0.01 level.
[b]Correlation significant at the 0.05 level.

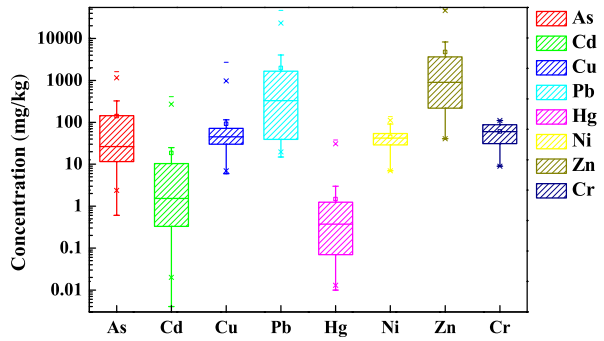


FIGURE 4
Concentration characteristics of heavy metals in soils.

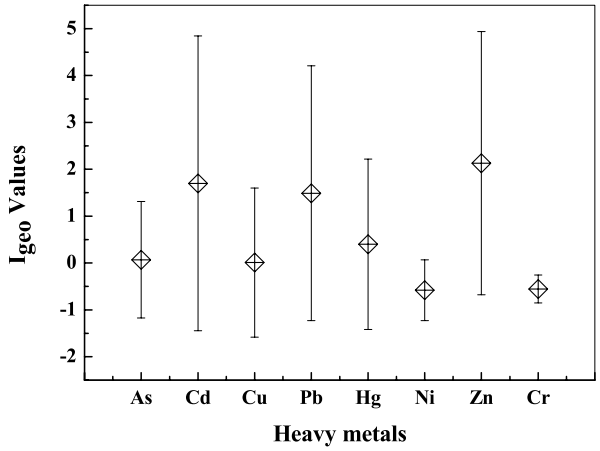


FIGURE 5
Average $I_{geo}$ values of heavy metals from soils.

## 3.2 Identification of non-hazardous waste

The water leaching experiment was conducted to determine the environmental transport ability and risk of heavy metals in the abandoned solid waste in natural environmental effects like raining and leaching. A total of 165 mine tailing samples were collected and analyzed. The results were shown in Figure 3. Zinc showed the highest average concentration (5.37 mg/L) in the water leaches. The percentages of heavy metals exceeding the limits were 28.05%, 18.18%, 15.15%, 13.94%, 6.87%, 2.44%, and 2.24% for Zn, Mn, Cd, Pb, Cu, Ni, and Hg, respectively. Cr and As were less than the limit standard. Therefore, nearly 80% of the collected solid wastes were class I according to the Chinese solid waste management policy. The other samples were classified as type II waste, which poses a more serious environmental risk and requires more attention.

## 3.3 Soil pollution characteristics

The heavy metal contents of the soils are shown in Figure 4. Among the 369 collected soil samples, the As concentrations ranged from below the detection threshold to 1,608 mg/kg (average, 147.38 mg/kg). The Zn concentrations ranged from 40.7 to 49521 mg/kg, (average, 5574.67 mg/kg), showing the highest mean value among all heavy metals. The Cd concentrations ranged from below the detection threshold to 410 mg/kg (average, 21.02 mg/kg). The Pb concentration ranged from 14.8 to 47000 mg/kg (average, 2034.88 mg/kg). The percentages of heavy metal samples exceeding the intervention value limits were as follows: As (25.90%)> Pb (20.44%) > Zn (14.94%) > Cd (2.49%) > Hg (0.67%). Therefore, contaminated sites containing heavy metal concentrations exceeding the standard limits require remediation. However, the other heavy metals including Cr, Ni, Cu, Ti, and Mn, met the soil quality standards. Regarding the screening value standards, 39.78%, 34.43%, 14.94%, 0.67%, and 2.17 of the Pb, As, Zn, Hg, and Ti samples, respectively, exceeded the limits. The environmental risk assessments are needed to determine whether the related sites require remediation for the heavy metals with concentrations below the limit value and above the screening value. According to the total analysis mentioned previously,

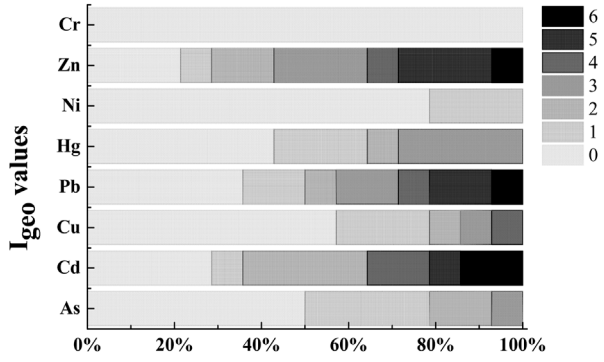


FIGURE 6
Class distributions of the geo-accumulation index for heavy metals.

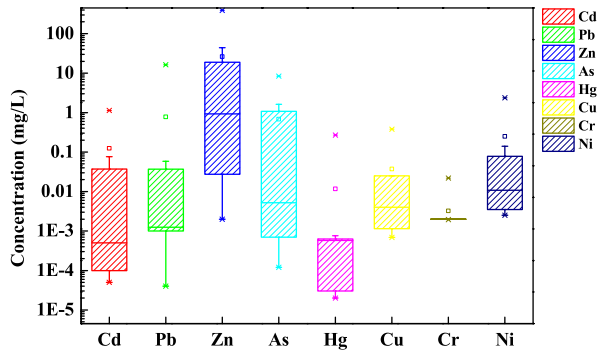


FIGURE 7
Concentrations of heavy metals in groundwater.

compared with the soil quality limits, Pb, Zn, Cd, and As are critical heavy metals in soils in the vicinity of the mine tailing areas that require more attention, while Cr, Ni, and Cu exhibited the lowest risk levels. This finding is similar to those of other reports showing pollution indices of Pb, Zn, and Cd ranging from high to intense contamination, compared to mild and moderate pollution levels for other heavy metal pollution levels for soils from lead/zinc mining sites in Vietnam (Vuong et al., 2022).

The correlations of the contents of the heavy metals in soils are shown in Table 2. As levels were positively correlated with Zn, with a Pearson correlation coefficient of 0.462 ($p$<0.01). Cd was positively correlated with Pb and Zn, with Pearson correlation coefficients of 0.490 and 0.793 ($p$<0.01), respectively. Pb was positively correlated with Zn, with a Pearson correlation coefficient of 0.621. Therefore, Cd is a typical contaminant in lead–zinc mining polluted soils as it is correlated with Pb and Zn levels.

The geo-accumulations index values for the heavy metals are listed in Figure 5. The average $I_{geo}$ index values for heavy metals from different study sites are shown in Supplementary Table S4. The mean indices were >1 for Cd, Zn, and Pb, of which the maximum value was >6, demonstrating the highest contamination level. The average indices of As, Hg, and Cu ranged from 0.01 to 0.4, indicating moderate contamination. The mean $I_{geo}$ values of Cr and Ni were all <0, representing the lowest contamination. The $I_{geo}$ values of Zn, Cd, and Pb in this study were similar to those of samples for other legacy contaminated industrial sites in China (Yang et al., 2018; Peng et al., 2022); however, the average $I_{geo}$ values of the other six heavy metals were much lower than those from other industries by comparison, demonstrating the predominance of Zn, Pb, and Cd as pollutants in lead–zinc mine industries. The $I_{geo}$ values in the present study were higher than those of soils from agricultural regions in China (Yang et al., 2018), especially for Cd and Pb, implying relatively higher environmental risks.

The class distribution of the geo-accumulation index based on the classification system was shown in Figure 6. The $I_{geo}$ values and the percentage distribution of different heavy metals varied significantly. The indices of all samples for Cr were below class 0, meaning practically uncontaminated. For Ni, nearly 80% of the $I_{geo}$ values fell into class 0; the rest are <1. Regarding Hg, >60% of the indices were <1 and the others were <3. Similarly, nearly 80% of the indices were <1 for Cu, although 7% of the soil samples were class 4. Indices <0 were observed for <35.71% of Cd, Pb, and Zn samples, respectively. In contrast, >30% of indices were >4, ranging from "heavily contaminated" to "extremely contaminated." Extremely contaminated classes with indices >6 were observed for approximately 7%–14% of Cd, Pb, and Zn samples. The $I_{geo}$ values for the other heavy metals were all <4. The As pollution level was relatively moderate compared to the $I_{geo}$ values shown in Figure 6. Therefore, the contamination levels of the heavy metals are ranked in the following order: Cd>Zn>Pb>Cu>Hg>Ni>Cr.

## 3.4 Groundwater pollution characteristics

The groundwater quality investigation included 43 groundwater samples collected from 43 wells located in the vicinity of the side and downstream regions of the sites. The detection results were compared with the groundwater quality standard (III) in China (GB/T 148148-2017). The results demonstrated that all eight heavy metals were detected in groundwater samples from the 43 wells as shown in Figure 7. The mean concentrations of the contaminating heavy metals were generally in the order of Zn>As>Pb>Ni>Cd>Cu>Hg>Cr. In this study, 43.24%, 42.5%, 37.5%, and 27.5% of the Zn, Cd, As, and Pb samples, respectively, exceeded the standard limits.

The Zn concentrations ranged from below the detection limit to 388 mg/L (average, 23.35 mg/L), with 27.91% of samples showing concentrations above the standard value and the highest concentration 388 times the standard value. The Pb concentrations ranged from below the detection limit to 16.4 mg/L (average, 0.7 mg/L), with 27.5% of samples exceeding the standard value and the highest concentration 1,640 times the standard value. The Cd concentrations ranged from below the detection limit to 1.14 mg/L (average, 0.11 mg/L), with 42.25% of samples exceeding the standard value is 42.25% and the highest concentration 228 times the standard value. The Ni concentrations ranged from 0.0025 to 2.37 mg/L ( average, 0.25 mg/L), with 42.11% of samples exceeding the standard value and the highest concentration 118 times the limit value.

The heavy metals in the groundwater around the mining and tailing contaminated sites included Cd, Pb, Zn, As, and Ni due to the higher content and percent above the standard rate (>27%).

**TABLE 3 Concentrations of heavy metals in soils in the vicinity of lead–zinc mining areas in other countries and regions (mg/kg).**

| Country | As | | Cd | | Cr | | Cu | | Ni | | Pb | | Zn | | Hg | | Reference |
|---|---|---|---|---|---|---|---|---|---|---|---|---|---|---|---|---|---|
| | Range | Mean | Range | Mean | Range | Mean | Range | Mean | Range | Mean | Range | Mean | Range | Mean | Range | Mean | |
| Vietnam | 3.7–489 | 228 | 0.66–56.2 | 12.6 | / | / | 11.9–697 | 147 | / | / | 273–23300 | 4010 | 231–8,430 | 3540 | / | / | Hien et al. (2012) |
| Tunisia | / | / | 1–186.17 | 20.26 | / | / | / | / | / | / | 1–3457.1 | 549.72 | 2.36–14180 | 2297.4 | / | / | Sebei et al. (2020) |
| Sweden | 700–900 | 800 | 0.5–0.7 | 0.6 | 1.0–2.0 | 1.6 | 18–400 | 64 | 2.7–4.5 | 3.7 | 1.1–4.6 | 3.1 | 8.5–33 | 16 | / | / | Bhattacharya et al. (2006) |
| Poland | / | / | / | / | / | / | / | / | / | / | 69–5260 | / | 42–12100 | / | / | / | Ullrich et al. (1999) |
| Morocco | / | / | / | / | / | / | / | / | / | / | 41–17250 | / | 51–276500 | / | / | / | Iavazzo et al. (2012) |
| Jamaica | / | / | 2–220 | 2.4 | / | / | / | / | / | / | 6–38000 | 170 | 66–39582 | 494 | / | / | Anglin-Brown et al. (1995) |
| Greece | 4.7–369.8 | / | 0.9–174.1 | | / | / | 12.8–1,201 | / | / | / | 31–12567 | / | 47.4–22291 | / | / | / | Nikolaidis et al. (2010) |
| Nigeria | / | / | / | / | / | / | / | / | / | / | 13–16 | 14.25 | 156–246 | 186.75 | / | / | Oje et al. (2010) |
| Spain | 100–1,600 | / | / | / | / | / | 500–1,000 | / | / | / | 3100–62500 | / | 3000–38500 | / | / | / | Gonzalez-Fernandez et al. (2011) |
| China | ND-1608 | 147.38 | ND-410 | 21.02 | 9–1,450 | 89.85 | ND-2698.16 | 95.66 | ND-136 | 46.43 | 14.8–47000 | 2034.88 | 40.7–49521 | 5574.67 | ND-102 | 2.12 | This study |

Note: "/," data not available or not detected; ND, content below the detection limit.





10.3389/feart.2023.1082714

TABLE 4 Heavy metal concentrations in groundwater surrounding the lead–zinc mines regions in other studies.

| Region | As | | Cd | | Cr | | Cu | | Ni | | Pb | | Zn | | Hg | | Reference |
|---|---|---|---|---|---|---|---|---|---|---|---|---|---|---|---|---|---|
| | Range | Mean | Range | Mean | Range | Mean | Range | Mean | Range | Mean | Range | Mean | Range | Mean | Range | Mean | |
| Vietnam | 2–8 | 5.1 | ND-2 | 0.5 | / | / | 2–54 | 29 | / | / | ND-121 | 30 | ND-155 | 71 | / | / | Hien et al. (2012) |
| Nigeria | 0–2.06 | 0.13 | 0–0.51 | 0.24 | 0–10.10 | 0.43 | 0–2.42 | 0.13 | 0–1.26 | 0.09 | 0–4.29 | 2.18 | 0–1.72 | 0.14 | 0–2.3 | 0.50 | Oje et al. (2010) |
| Korean | 7–187 | 0.0667 | 0.005–0.021 | 0.0088 | 21–50 | 0.0264 | / | / | / | / | / | / | 1.758–10.550 | 4.176 | / | / | Lee et al. (2005) |
| China | ND-8.45 | 0.68 | ND-1.14 | 0.11 | ND-0.022 | 0.008 | ND-0.38 | 0.03 | 0.0025–2.37 | 0.25 | ND-16.4 | 0.70 | ND-388 | 23.35 | 0.00002–0.27 | 0.01 | This study |

Note: "/" data not available or not detected; ND, content below the detection limit.

The higher concentration and percent above the standard limit of As were attributed to its higher mobility in soil and water (Zhang et al., 2019), although it showed lower soil contamination compared to the other heavy metals. Similar phenomena were also reported in other studies, where river water in mine tailing areas showed As concentrations exceeding 10 μg/L but low concentrations of Pb and Cd due to the different mobilities of Cd, As, and Pb (Baasansuren et al., 2020). The environmental and health risks to groundwater should be given more emphasis, especially for mining sites located in farmland and residential areas.

## 3.5 Correlations of priority heavy metals in different matrices and running time

The correlation matrix between heavy metal concentrations in mine tailings, soils, groundwater, and piling time is included in the Supporting Materials. As shown in Supplementary Tables S7–S10, the Zn, Pb, As, and Cd contents in solid mine tailings, soil, and groundwater were positively correlated. These results demonstrate the migration pathways from solid waste to groundwater via soil matrices, especially for mine tailing piles lacking leaching protection measures. The Cd and Pb contents in different matrices were positively related to the running time of the mine tailings; thus, more metals were released into the environment with increasing time that the mine tailings remained in piles. Thus, remediation measures should be taken as soon as possible because solid waste could easily release these metals into the environment. Meanwhile, the other heavy metals including Zn and As were weakly related to the running time of the mine tailing pond.

## 3.6 Comparisons of results with other studies

The comparisons of heavy metal concentrations in the soils and groundwater from this study with those found in other countries and regions are listed in Tables 3, 4.

To compare the heavy metal pollution levels of the soils in this paper to those of studies from other countries, the heavy metal content of soils surrounding lead–zinc mine areas om other countries were collected. These regions included Vietnam, Tunisia, Sweden, Poland, Morocco, Jamaica, Greece, Nigeria, and Spain across the European, Asian, African, and North American continents. Table 1 shows that Zn, Pb, and Cd had the highest detection frequencies in other studies among eight heavy metals, with Zn and Pb detected in all studies. As and Cr showed intermediate levels, with detection frequencies of 40%–50%. Ni and Hg were the least commonly identified, with nearly no content data in soils from other studies. Therefore, Zn, Pb, and Cd were the most concentrated related to the detection frequency; moreover, they were detected in all samples. The total Pb and Zn concentrations showed a wide range of values (Pb: 1–62500 mg/kg; Zn: 8.5–276500 mg/kg), with samples from Morocco and Spain showing the highest concentrations (references). The mean soil concentration of Zn in the present study, 5574.67 mg/kg, was higher than the value reported in other regions, although the maximum value was observed in Morocco. These results

illustrate the higher potential environmental risk of Zn in China compared to the soils in the vicinity of lead–zinc mining areas in other regions. The mean Pb values ranked in the middle in the present study compared to other studies. The highest mean value from the soil samples was reported in Vietnam, which was attributed to the long mining operations, which generated considerable amounts of heavy pollution (Ha et al., 2011). The total pollution level of Cd in this study was comparable to that reported in Tunisia and higher than the mean concentrations of other regions. The results of the aforementioned analysis showed that the contamination levels and environmental risks of Zn, Pb, and Cd in this study ranked highest compared to other regions.

Few reports have reported on the association of groundwater contamination surrounding lead–zinc mine areas, implying that groundwater is less concentrated compared to soil. As illustrated in Table 1, only three studies in other countries and regions reported on this subject, including studies in Vietnam, Nigeria, and Korea. The groundwater surrounding the lead–zinc mines from Vietnam contained the highest heavy metal concentrations, with a mean value of 71 mg/L among four selected studies, owing to the higher heavy metal content in soils in the vicinity of lead–zinc mines (Ha et al., 2011; Hien et al., 2012). The mean concentration of the eight heavy metals in groundwater in this study was moderate compared to those of the other three studies. However, the risk of Zn cannot be ignored owing to the maximum value of 388 mg/L in the site measured in the present study.

## 4 Conclusion

This study systemically investigated heavy metal pollution in mine tailings, soils, and groundwater based on a database of 27 abandoned lead–zinc mine tailing sites in China.

1) Zn, Pb, and Cd were the dominant pollutants among the eight heavy metals studied.
2) Hazardous wastes were identified in 1% of the mine tailing samples although most of the waste was non-hazardous. Nearly 20% of the solid mine tailings were class II non-hazardous waste. Meanwhile, 20% of the soil and 10% of the groundwater samples exceeded the corresponding quality limits; thus, remediation measures must be made as soon as possible.
3) The index of $I_{geo}$ of eight heavy metals ranged from −3.62 to 7.67, where Zn, Pb, and Cd exhibit the highest environmental risk level which requires more government attention and control.
4) Heavy metal concentrations in soil, groundwater, and waste mine tailing were positively correlated, demonstrating the main pollution source and transportation paths.
5) The pollution level of the heavy metals in soil and groundwater around the lead–zinc mine tailing areas are ranked foremost and moderate compared to other studies from other countries and regions, respectively.
6) For contaminated sites where the content of heavy metals exceeds the standard limits, remediation and management measures are urgently needed to reduce the environmental levels and assure the health of nearby human populations.

## Data availability statement

The original contributions presented in the study are included in the article/Supplementary Material. Further inquiries can be directed to the corresponding author.

## Author contributions

WH completed the main data analysis and the main writing. RZ and WL participated in data processing and result calculation. YW determined the logical structure of the paper and provided scientific research funding. SZ, KZ, and JN provided valuable suggestions for the paper. All authors contributed to the paper and approved the submitted version.

## Funding

This study was funded by the National Key R&D Program of China (Grant No. 2019YFC1806001).

## Conflict of interest

The authors declare that the research was conducted in the absence of any commercial or financial relationships that could be construed as a potential conflict of interest.

## Publisher's note



## Supplementary material

The Supplementary Material for this article can be found online at: https://www.frontiersin.org/articles/10.3389/feart.2023.1082714/full#supplementary-material

## References

Anglin-Brown, B., Armour-Brown, A., and Lalor, G. C. (1995). Heavy metal pollution in Jamaica 1, Survey of cadmium, lead and zinc concentrations in the Kintyre and Hope Flat districts. *Environ. Geochem. Hlth.* 17, 51–56. doi:10.1007/bf00146708

Baasansuren, G., Fukushi, K., Akehi, A., Takahashi, Y., Zhao, X., and Kawasaki, K. (2020). Comparison of chemical speciation of lead, arsenic, and cadmium in contaminated soils from a historical mining site: implications for different

mobilities of heavy metals. *ACS Earth Space Chem.* 4 (7), 1064–1077. doi:10.1021/acsearthspacechem.0c00087

Bhattacharya, A., Routh, J., Jacks, G., Bhattacharya, P., and Mörth, M. (2006). Environmental assessment of abandoned mine tailings in Adak, Västerbotten district (northern Sweden). *Appl. Geochem.* 21 (10), 1760–1780. doi:10.1016/j.apgeochem.2006.06.011

Doya, R., Nakayama, S. M. M., Nakata, H., Toyomaki, H., Ishizuka, M., Muzandu, K., et al. (2020). Land use in habitats affects metal concentrations in wild lizards around a former lead mining site. *Environ. Sci. Technol.* 54 (22), 14474–14481. doi:10.1021/acs.est.0c00150

Gankhurel, B., Fukushi, K., Akehi, A., Takahashi, Y., Zhao, X., and Kawasaki, K. (2020). Comparison of chemical speciation of lead, arsenic, and cadmium in contaminated soils from a historical mining site, implications for different mobilities of heavy metals. *ACS Earth Space Chem.* 4 (7), 1064–1077. doi:10.1021/acsearthspacechem.0c00087

Gonzalez-Fernandez, O., Queralt, I., Carvalho, M. L., and Garcia, G. (2011). Lead, zinc, arsenic and copper pollution in the Alluvial plain of a mining wadi, the beal case (Cartagena-La Union Mining District, SE Spain). *Water Air Soil Poll.* 220 (1-4), 279–291. doi:10.1007/s11270-011-0753-5

Gunson, A. J., and Jian, Y. (2001). *Artisanal mining in the People's Republic of China*. United Kingdom: International Institute of Environment and Development.

Ha, N. T. H., Sakakibara, M., Sano, S., and Nhuan, M. T. (2011). Uptake of metals and metalloids by plants growing in a lead-zinc mine area, Northern Vietnam. *J. Hazard. Mat.* 184 (2-3), 1384–1391. doi:10.1016/j.jhazmat.2010.12.020

Hien, N. T. T., Yoneda, M., Nakayama, A., Matsui, Y., Quang, N. H., Pho, N. V., et al. (2012). Environmental contamination of arsenic and heavy metals around cho dien lead and zinc mine, Vietnam. *Vietnam. J. Water Environ. Technol.* 10 (3), 253–265. doi:10.2965/jwet.2012.253

Iavazzo, P., Adamo, P., Boni, M., Hillier, S., and Zampella, M. (2012). Mineralogy and chemical forms of lead and zinc in abandoned mine wastes and soils, an example from Morocco. *J. Geochem. Explor.* 113, 56–67. doi:10.1016/j.gexplo.2011.06.001

Lee, J. Y., Choi, J. C., and Lee, K. K. (2005). Variations in heavy metal contamination of stream water and groundwater affected by an abandoned lead-zinc mine in Korea. *Environ. Geochem. Hlth.* 27 (3), 237–257. doi:10.1007/s10653-004-3480-7

Li, Z., Ma, Z., Kuijp, T. J., Yuan, Z., and Huang, L. (2014). A review of soil heavy metal pollution from mines in China, Pollution and health risk assessment. *Sci. Total Environ.* 468, 843–853. doi:10.1016/j.scitotenv.2013.08.090

Liu, K., Li, C., Tang, S., Yu, F., and Li, Y. (2020). Heavy metal concentration, potential ecological risk assessment and enzyme activity in soils affected by a lead-zinc tailing spill in Guangxi, China. *Chemosphere* 251 (126415), 1–12. doi:10.1016/j.chemosphere.2020.126415

MEP of China (Ministry of Environmental Protection of China) (2014). National soil pollution survey bulletin. Available at: http://www.zhb.gov.cn/gkml/hbb/qt/201404/t20140417 [Accessed September 15, 2022].

Mezned, N., Alayet, F., Dkhala, B., and Abdeljaouad, S. (2022). Field hyperspectral data and OLI8 multispectral imagery for heavy metal content prediction and mapping around an abandoned Pb-Zn mining site in northern Tunisia. *Heliyon* 8, e09712–e09724. doi:10.1016/j.heliyon.2022.e09712

MIIT of China (2022) Ministry of industry and information technology of the People's Republic of China. Available at: https://www.miit.gov.cn/search/index.html. [Accessed September 15, 2022].

MNR of China (Ministry of Natural Resources, PRC) (2022). China mineral resources report. Available at: https://www.mnr.gov.cn/sj/sjfw/kc_19263/zgkczybg/202209/t20220921_2759600.html.[Accessed September 15, 2022]

Muller, G. (1969). Index of geoaccumulation in sediments of the Rhine river. *Geo. J.* 2, 108–110.

Nikolaidis, C., Zafiriadis, I., Constantinidis, M. T., and Constantinidis, T. (2010). Heavy metal pollution associated with an abandoned lead–zinc mine in the Kirki region, NE Greece. *Bull. Environ. Contam. Toxicol.* 85, 307–312. doi:10.1007/s00128-010-0079-9

Oje, O. A., Uzoegwu, P. N., Onwurah, I. N. E., and Nwodo, U. U. (2010). Environmental pollution levels of lead and zinc in Ishiagu and Uburu communities of Ebonyi state, Nigeria. *Bull. Environ. Contam. Toxicol.* 85 (3), 313–317. doi:10.1007/s00128-010-0082-1

Peng, J., Zhang, S., Han, Y., Bate, B., Ke, H., and Chen, Y. (2022). Soil heavy metal pollution of industrial legacies in China and health risk assessment. *Sci. Total Environ.* 816, 151632–151643. doi:10.1016/j.scitotenv.2021.151632

Rodríguez, L., González-Corrochano, B., Medina-Díaz, H. L., López-Bellido, F. J., Fernández-Morales, F. J., and Alonso-Azcárate, J. (2022). Does environmental risk really change in abandoned mining areas in the medium term when no control measures are taken? *Chemosphere* 291 (3), 133129. doi:10.1016/j.chemosphere.2021.133129

Sebei, A., Chaabani, A., Abdelmalek-Babbou, C., Helali, M. A., Dhahri, F., and Chaabani, F. (2020). Evaluation of pollution by heavy metals of an abandoned Pb-Zn mine in northern Tunisia using sequential fractionation and geostatistical mapping. *Environ. Sci. Pollut. Res.* 27, 43942–43957. doi:10.1007/s11356-020-10101-x

Shi, J., Du, P., Luo, H., Wu, H., Zhang, Y., Chen, J., et al. (2022). Soil contamination with cadmium and potential risk around various mines in China during 2000-2020. *J. Environ. Manage.* 310, 114509–114523. doi:10.1016/j.jenvman.2022.114509

Tomiyama, S., and Igarashi, T. (2022). The potential threat of mine drainage to groundwater resources. *Curr. Opin. Environ. Sci. Hlth.* 27, 100347–100358. doi:10.1016/j.coesh.2022.100347

Ullrich, S. M., Ramseya, M. H., and Helios-Rybicka, E. (1999). Total and exchangeable concentrations of heavy metals in soils near Bytom, an area of Pb/Zn mining and smelting in Upper Silesia, Poland. *Appl. Geochem.* 14, 187–196. doi:10.1016/s0883-2927(98)00042-0

Vuong, X. T., Vu, L. D., Duong, A. T. T., Duong, H. T., Hoang, T. H. T., Luu, M. N. T., et al. (2022). Speciation and environmental risk assessment of heavy metals in soil from a lead/zinc mining site in Vietnam. *Int. J. Environ. Sci. Technol.* 27, 1–16. doi:10.1007/s13762-022-04339-w

Xiao, Q., Zong, Y., and Lu, S. (2015). Assessment of heavy metal pollution and human health risk in urban soils of steel industrial city (Anshan), Liaoning, Northeast China. *Ecotoxicol. Environ. Saf.* 120, 377–385. doi:10.1016/j.ecoenv.2015.06.019

Yang, Q., Li, Z., Lu, X., Duan, Q., Huang, L., and Bi, J. (2018). A review of soil heavy metal pollution from industrial and agricultural regions in China, Pollution and risk assessment. *Sci. Total Environ.* 642, 690–700. doi:10.1016/j.scitotenv.2018.06.068

Zhang, M., Wang, J., Liu, X., Yan, X., Hu, X., Zhong, J., et al. (2019). Geographical distribution and risk assessment of heavy metals, a case study of mine tailings pond. *Chem. Ecol.* 36 (5), 1–15. doi:10.1080/02757540.2019.1676420

Zhao, F. (2007). The present situation of the concentration of Lead-zinc ore. *Non-Fer. Min. Metall.* 23 (6), 20–25.

Zhou, L., Zhao, X., Meng, Y., Fei, Y., Teng, M., Song, F., et al. (2022). Identification priority source of soil heavy metals pollution based on source-specific ecological and human health risk analysis in a typical smelting and mining region of South China. *Ecotoxicol. Environ. Saf.* 242, 113864. doi:10.1016/j.ecoenv.2022.113864

Zhu, W., Yang, X., He, J., Wang, X., and Zhang, Z. (2021). Investigation and systematic risk assessment in a typical contaminated site of hazardous waste treatment and disposal. *Front. Public Health* 9, 764788. doi:10.3389/fpubh.2021.764788

Zhuang, P., Micbride, M. B., Xia, H. P., Li, N. Y., and Li, Z. A. (2009). Health risk from heavy metals via consumption of food crops in the vicinity of Dabaoshan mine, South China. *Sci. Total Environ.* 407, 1551–1561. doi:10.1016/j.scitotenv.2008.10.061

frontiers | Frontiers in Earth Science

TYPE Original Research
PUBLISHED 21 April 2023
DOI 10.3389/feart.2023.1158715



OPEN ACCESS

EDITED BY
Xing Wang,
Guangzhou University, China

REVIEWED BY
Yi Shan,
Guangzhou University, China
Shuai Cao,
University of Science and Technology Beijing, China
Yue Qin,
Wuhan University of Technology, China

*CORRESPONDENCE
Guodong Mei,
meiguodong@bgrimm.com
Lijie Guo,
guolijie@bgrimm.com

RECEIVED 04 February 2023
ACCEPTED 10 April 2023
PUBLISHED 21 April 2023

CITATION
Wang S, Mei G, Wang W, Wang Y, Cui Y, Guo L and Chu Y (2023), Experimental study of triaxial shear features of concentrated full tailings considering the effect of curing age.
*Front. Earth Sci.* 11:1158715.
doi: 10.3389/feart.2023.1158715



# Experimental study of triaxial shear features of concentrated full tailings considering the effect of curing age

Sha Wang[1,2], Guodong Mei[1,2]*, Weixiang Wang[1,2], Yali Wang[1,2], Yiyuan Cui[1,2], Lijie Guo[1,2]* and Yifan Chu[1,2]

[1]BGRIMM Technology Group, Beijing, China, [2]National Centre for International Research on Green Metal Mining, Beijing, China

The strength evolution law of concentrated full tailings is closely related to the storage construction method, especially the growth law of shear strength with curing age. This study aims to investigate the influence of curing materials on the shear strength of full tailings and reveal the change law of the shear strength of concentrated full tailings with the curing age. Therefore, we carried out a comparative triaxial shear test between pure full tailings and concentrated full tailings with different curing ages. The test results show that concentrated full tailings had a 70.7% higher cohesion and a 10% larger internal friction angle (IFA) than that of pure full tailings at the age of 0 days. Moreover, the concentrated full tailings cured for 3 days had a 170.2% higher cohesion and a 12.1% larger IFA than that cured for 0 days. In addition, the concentrated full tailings cured for 7 days had a 149.4% higher cohesion and a 12.1% larger IFA than that cured for 0 days. The stress-strain curve exhibits that the shear strength of full tailings is significantly influenced by the curing material and curing age. The stress-strain curve gradually moved from strain hardening to strain softening as the curing age increased, and the failure curve had two steps. This indicates that the specimen still has a certain shear capacity despite having a shear zone. The entire specimen instantly fails when the strain exceeds that capacity. The results of this study can be used as scientific bases for the design and construction of the surface storage structures of concentrated full tailings.

KEYWORDS

**concentrated full tailings, triaxial shear test, curing age, shear strength, stress-strain curve**

## 1 Introduction

Mine tailings stored in the tailings storage facilities (TSFs) are normally failure-prone due to liquefaction, erosion, overtopping, piping, and excess pore water pressure. Investigating of the mechanical behavior of tailings is essentially important for engineering design and safety evaluation of the TSF. For the storage and disposal of metal ore tailings, researchers are seeking more reasonable ways to mitigate the negative impacts of wet and dry discharges. The harmless ground storage of concentrated full tailings presents an effective way to improve the TSF. The first step of harmless ground storage is to overcome the problem with the high concentration of tailings. The current approach of concentrated storage increases the concentration of tailings to 60%–70% in which a deep

**TABLE 1** Mix ratio for the triaxial shear test on concentrated full tailings.

| SN | Tailings slurry concentration (%) | Aggregate-cement ratio | Tailings | Curing material (kg/kg) | | | | | Water | Unit weight (kN/m$^3$) | Max/Min void ratio (%) |
|---|---|---|---|---|---|---|---|---|---|---|---|
| | | | | Slag powder | Quicklime | Cement | Latex | Fiber | | | |
| | 74 | 20 | 180.8 | 4.97 | 2.26 | 0.72 | 0.36 | 0.72 | 66.7 | 18.6 | 45/40 |

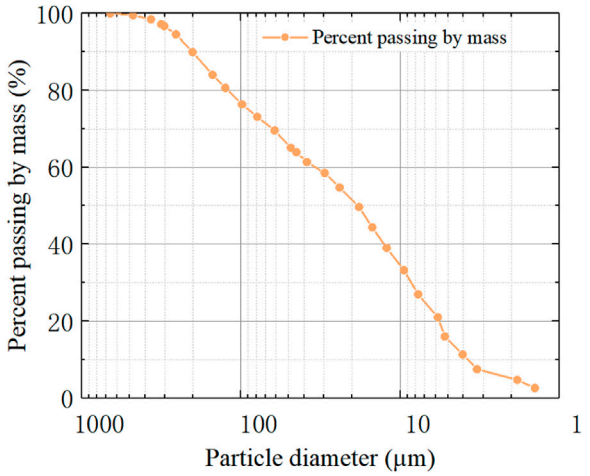


FIGURE 1
Particle size distribution curve of full tailings.

cone thickener is used, which directly discharges the water and steams the tailings dry. The ensuing problems include the poor permeability of the discharge and the difficulty of consolidation (Yao et al., 2012; Yan et al., 2019). The concentration problem restricts the curing and storage of tailings (Indraratna, 1994) attempted to alter the mechanics of fine tailings by mixing coarse and fine tailings and improved the utilization of fine tailings.

Concentrated full tailings are a type of enhanced tailings whose mechanical properties are altered by adding curing agents to highly concentrated tailings. The preparation of concentrated full tailings is under the field of comprehensive tailings utilization. (Yin et al., 2020), (Xu et al., 2019), (Paiva et al., 2019) . explored material modification by adding waste rock, fiber, rod mill tailings, and cement to the tailings and identified the strength change pattern of tailings modified material with different mix ratios and the main factors affecting the strength. (Li et al., 2023), (Đurđevac Ignjatović et al., 2022), (Jin et al., 2022), (Hou et al., 2018), (Cui et al., 2020), (Kiventerä et al., 2019), (Wang et al., 2008; Wang et al., 2009) examined the influence law of admixtures (e.g., slag powder, quicklime, industrial gypsum, and bentonite) on tailings strength and recommended the optimal addition ratio. Temperature has a considerable effect on the strength growth of cured tailings because it influences the hydration of cement. (Wang et al., 2021). and (Li, 2019). investigated the influence law of temperature on cemented tailings strength, revealing that low temperature has an impact on the early strength of cemented tailings backfill.

In engineering practice, cyclic loading and long-term operation lead to creep deformation. (Zou et al., 2020). and (Hou et al., 2019). investigated the strength development law of cemented tailings in the presence of cyclic loading and freeze-thaw cycles to clarify the strength development law and

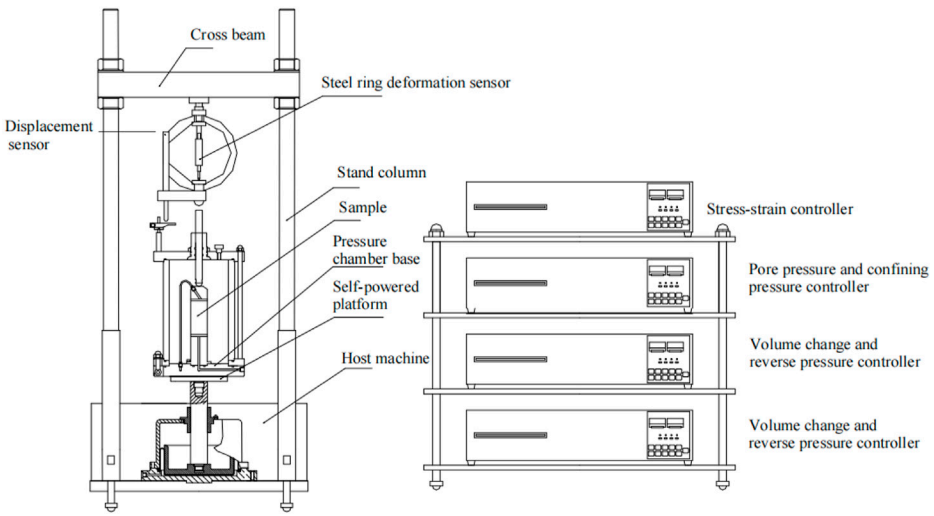


FIGURE 2
SLB-1A stress-strain controlled triaxial shear instrument.

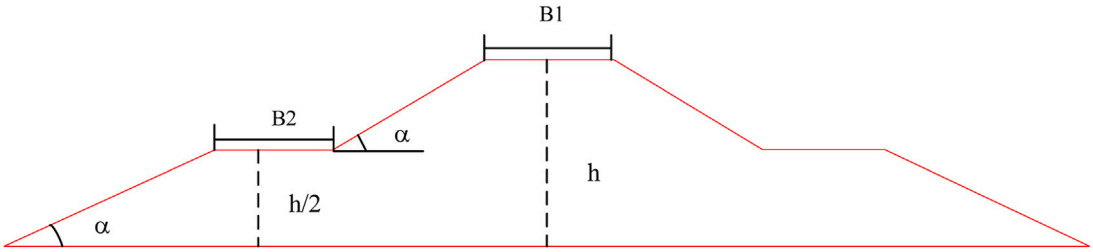


FIGURE 3
The primary section of the concentrated full tailings structure.


FIGURE 4
Curing situation of triaxial shear test specimens **(A)** 0 days **(B)** 3 days **(C)** 7 d.


FIGURE 5
Specimen mounting of triaxial shear test. **(A)** Specimen loaded into rubber membrane and **(B)** specimen loaded into pressure chamber cover and filled with water.

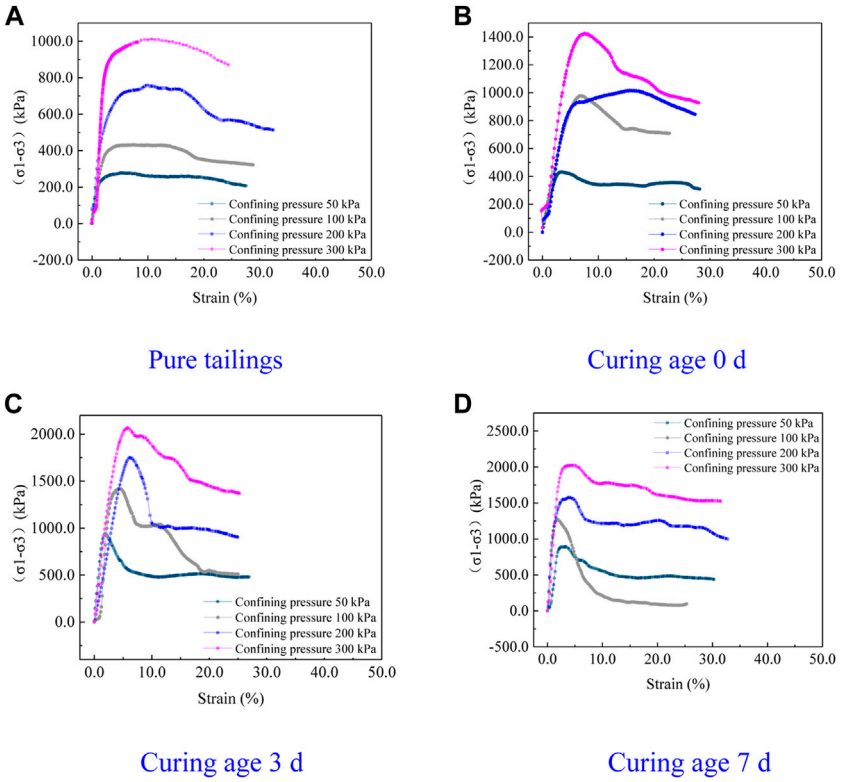


FIGURE 6
Stress-axial strain of different curing age specimen.

deformation features of cemented tailings under the two actions. (Ke, 2016), (Li, 2018), and (Zhao et al., 2016). tested the creep features and long-term strength of cemented tailings, determined the long-term strength of cemented tailings, and suggested the corresponding damage model. Since age is an important impactor on strength, (Yilmaz et al., 2015), (Jiang et al., 2022), (Yilmaz et al., 2015), and (Dong, 2017). studied the effect of the curing age on the strength of cemented tailings and reported on the evolution law and mechanism of the mechanical and chemical properties of cemented tailings with age.

Structural studies are necessary for structural design and safety assessment. The tailings used in our experiment are fine-grained tailings produced from gold beneficiation, so their mechanical properties differ from those of coarse tailings. (Agapito and Bareither, 2018), (Qin et al., 2021), and (Islam, 2021). investigated the mechanical properties of fine tailings or backfill slurry and drew conclusions on the shear, seepage, and consolidation properties of fine tailings. (Suazo et al., 2016). investigated the effects of confining stress, initial static shear stress, and void ratio on the liquefaction resistance of fine-grained tailings through triaxial tests and revealed the importance of density on liquefaction susceptibility of compressible tailings and proposed a combined correction factor to account for overburden stress and density on cyclic resistance. (Roshani et al., 2017). investigated the hydro-mechanical behavior and physical properties of mature fine tailings (MFT) under atmospheric drying through a column study and found that the hydraulic-mechanical properties of the deposited tailings are closely coupled because of several mechanisms, such as evaporation, drainage, self-consolidation, suction, and crack development. Since controlling and reducing the fluid fine tailings build-up through practical methods has been an ongoing challenge, (Beier et al., 2013) explored the geotechnical aspects of meeting regulatory strength performance criteria by employing flocculation-based dewatering of fluid fine tailings. Here, artificial mine tailings/clay mixtures were used to prepare concentrated slurries, from which beds with different compositions, thicknesses, and ages were obtained through sedimentation. (Dimitrova and Yanful, 2012). added clay to mine tailings and found that the effective friction angle varied between 35.2° and 40.4° depending on the percentage of clay in the mixtures and the type of the clay additive. Shearing under partially drained conditions yielded a total friction angle of the mixtures that was always lower than the effective friction angle and varied between 15.1° and 23.3°. Since a clear understanding on the triaxial mechanical properties of cemented pasted backfill (CPB) is important to the CPB design and the stability analysis of the backfilled CPB structure, (Xiu et al., 2021; Xiu et al., 2022). carried out triaxial compression tests of the CPB samples using the geotechnical consulting and testing system (GCTS) with different curing times, drainage conditions, and curing temperatures. The results show that the shear mechanical

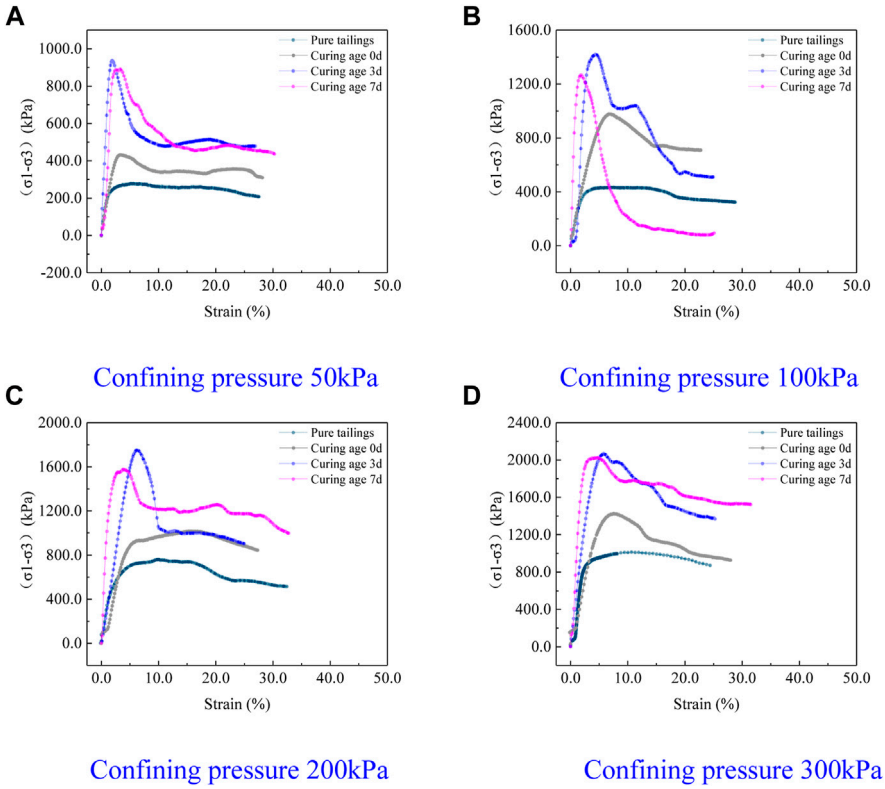


FIGURE 7
Stress-axial strain of different confining pressure under same curing age.

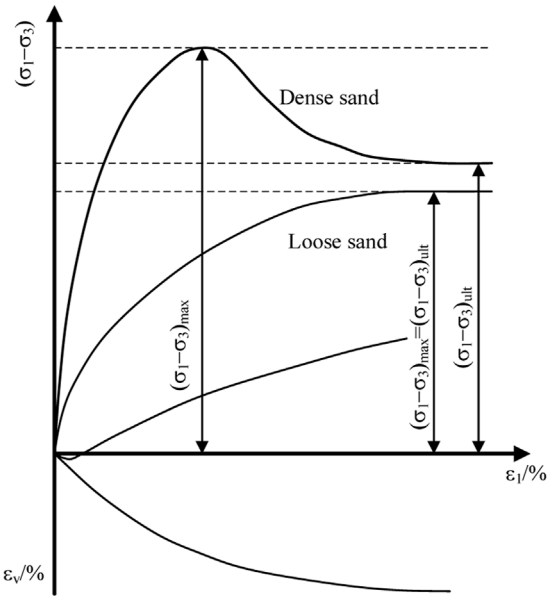


FIGURE 8
Triaxial test results for loose and concentrated tailings.

parameters of CPB can significantly affect the vertical stress distribution inside the CPB structure, and the strength of CPB is gradually enhanced with increasing curing time.

In this study, the hydration mechanism of cementitious materials, swelling materials, and polymers is used to develop a low-cost, modified, and enhanced curing agent by exciting the alkaline activity. The proposed curing agent employs the economical and harmless concentration and storage of full tailings from metal mines. Since the surface curing environment greatly differs from the underground, a triaxial shear test under low stress is designed to identify the relationship between the shear strength and the curing age in the surface environment. So the main innovations of this study is firstly developing a new proportion of concentrated full tailings, which is supposed to resolve the disadvantage of upstream TFS, secondly carrying out a triaxial shear strength test focusing the influence of curing age to the strength of this new material, which will reveal the increasing mechanism of strength of the concentrated full tailings and provide a scientific reference for engineering practice. Through the test, the authors explored the change law of shear strength with different curing ages. This study can be used as a basis for the structural design of surface storage facilities for concentrated tailings.

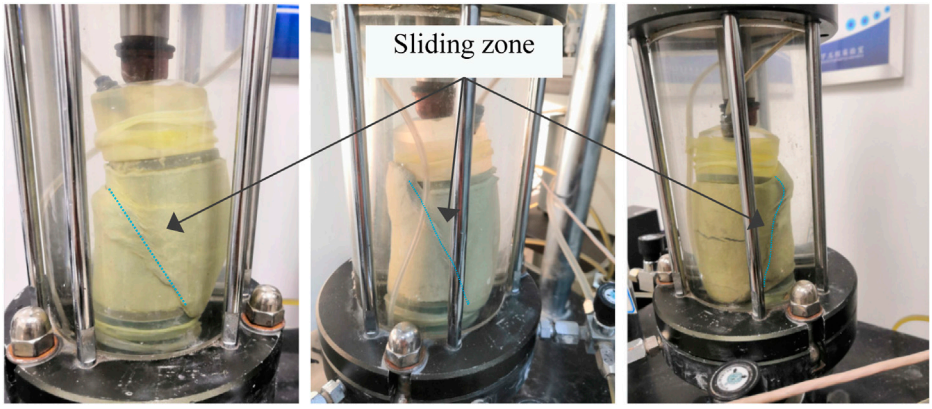


FIGURE 9
Strain softening accompanied by shear zone formation.

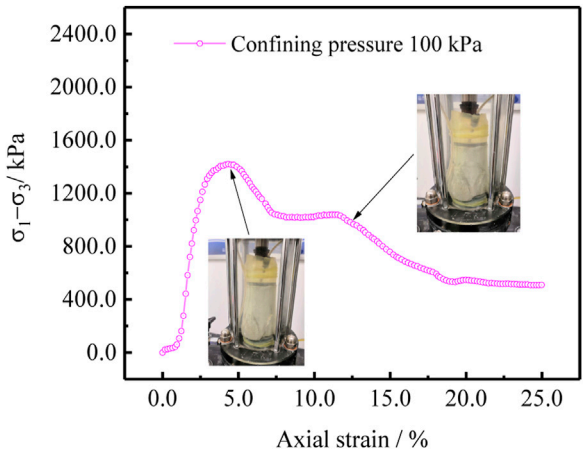


FIGURE 10
Double strain softening processes.

## 2 Mix ratio

Table 1 lists the mix ratio for the triaxial shear test on concentrated full tailings. Figure 1 presents the gradation of the tailings used. First, tailings were added to the 74% tailings slurry, making the slurry thicker. Next, curing materials were added, including slag powder, quicklime, cement, latex, and fiber. Each cubic meter of the mix includes 4.97 kg of slag powder, 2.26 kg of quicklime, 0.72 kg of cement, 0.36 kg of latex, and 0.72 kg of fiber.

## 3 Test methods and procedure

The triaxial shear test on concentrated full tailings was performed using an SLB-1A stress-strain controlled triaxial shear instrument manufactured by Nanjing Soil Instrument Factory Co., Ltd., as shown in Figure 2. SLB-1A type stress-strain control triaxial shear permeability tester can carry out equal stress and equal strain control for triaxial test, can carry out UU, CU, CD test, equal consolidation, equal consolidation, back pressure saturation, K0 test, stress path test and permeability test. Each part of the instrument is controlled by single chip microcomputer and can work independently, it can exchange data with the computer, thus realizing centralized data acquisition and processing. The instrument belongs to multifunctional flexible control triaxial test instrument. The main technical parameters are as follows.

1 Axial force: 0–20 kN measurement accuracy ±1% (10%-95%FS)
2 Control mode: a. Equal strain control: 0.002–4 mm/min ±10%;
b. Equal stress control: 0 kN–20 kN, control precision ±1%;
3 Sample size: Φ 61.8×125, Φ 39.1 × 80 mm;
4 Confining pressure: 0–1.99MPa, control precision ±0.5%FS
5 Back pressure: 0–0.99 MPa, control precision ±0.5%FS
6 Volume change: 0–480 mL, digital display.

After mixing the full tailings slurry with a curing agent, the mixture was placed in a curing vessel with a diameter of 39.1 mm. Before testing, the excess height was removed with a geokhod knife to obtain a standard specimen with a diameter of 39.1 mm and a height of 80 mm. There were cases in which the diameter of the specimen was less than 39.1 mm because of dry shrinkage deformation. Thus, the actual diameter of the specimen was measured before the test, and the actual measured value was entered in the test system.

The test steps are as follows.

### 3.1 Specimen preparation

First, approximately 5 kg of full tailings is weighed, and the mass of fiber, cement, slag powder, water, and latex are weighed according to the designed mix ratio, as listed in Table 1. The above materials are evenly mixed, and specimens are prepared by the compaction method. Each specimen is divided into 5 to 8 layers with equal soil mass for compaction. After compacting a layer to the required height, that layer is polished and the next layer of the mix is added. This procedure is repeated until the last layer is compacted. Then, level the ends of the specimen in the compaction cylinder, and the

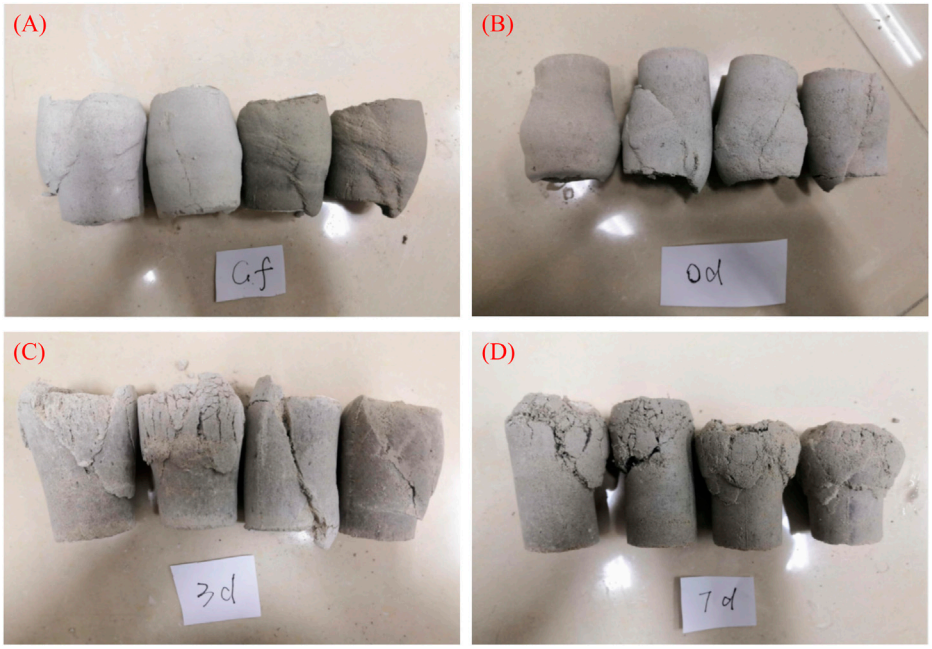


FIGURE 11
Damage patterns of specimens at different curing ages. **(A)** Pure tailings, **(B)** 0 days specimen, **(C)** 3 days specimen, and **(D)** 7 days specimen.

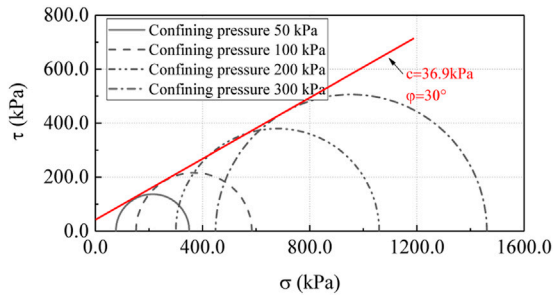


FIGURE 12
Shear strength of pure tailings.

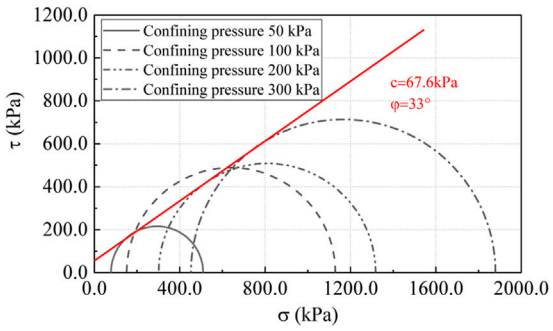


FIGURE 13
Shear strength of 0 days curing age specimen.

specimen is taken out to weigh its mass. Standard curing (the room temperature 20°±2°, and relative humidity above 95% RH) is performed on the compacted samples to the age of 0 days, 3 days, and 7 days. Among them, the 0 days specimen is directly subjected to the triaxial shear test.

## 3.2 Specimen mounting

The pressure chamber base is filled with water, an impermeable plate is placed on the base, and the specimen, impermeable plate, and specimen cap are put in turn. Subsequently, the rubber membrane is applied inside the membrane tube, the tube is turned out at both ends, air is sucked through the suction hole, the membrane adheres to the inner wall of the membrane tube. The membrane that is applied outside the specimen is deflated, the two ends of the rubber membrane are turned up, and the membrane tube is taken out. Afterward, the rubber membrane is tightly tied to the pressure chamber base and specimen cap, respectively, with a rubber band. The pressure chamber cover is installed in the following steps. First, the piston is lifted to prevent colliding into the specimen, the pressure chamber cover is placed, the piston is aligned with the center of the specimen cap, and the screws are evenly tightened. Moreover, the vent is opened to fill the pressure chamber with water. The inflow rate is reduced when the pressure chamber is almost full of water. The vent is closed when water flows over the hole. The volumetric change sensor/volumetric change tube valve and pore

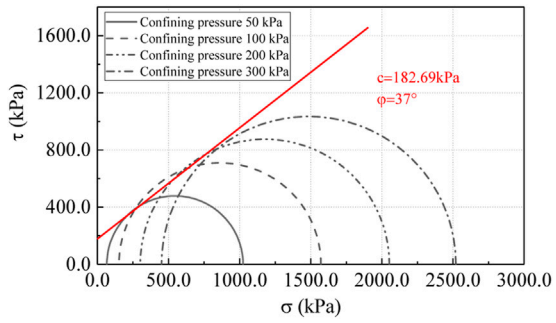


FIGURE 14
Shear strength of 3 days curing age specimen.

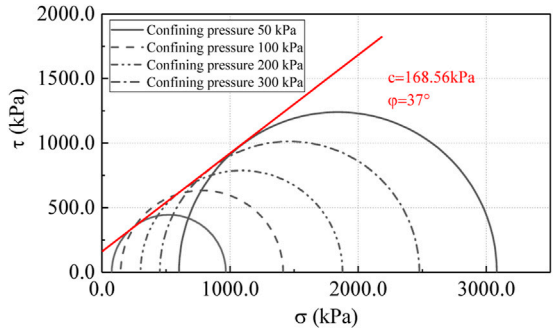


FIGURE 15
Shear strength of 7 days curing age specimen.

**TABLE 2 Triaxial shear test results of concentrated full tailings.**

| SN | Type | Curing age (d) | Cohesion (kPa) | IFA (°) |
|---|---|---|---|---|
| 1 | Pure tailings | — | 36.9 | 30 |
| 2 | Cured tailings | 0 | 67.6 | 33 |
| 3 | | 3 | 182.7 | 37 |
| 4 | | 7 | 168.6 | 37 |

pressure valve are closed, the surrounding pressure valves are opened, and the required confining pressure is applied. Subsequently, the lift table is raised. The piston is in contact with the specimen cap when axial force gauge has micro-readings. Finally, the readings of the axial load sensor or force gauge and axial displacement sensor or displacement gauge are set to zero.

The required confining pressure is determined by the stress state of the researched structure. In this study, the basic section of the concentrated full tailings accumulation body can be seen in Figure 3, the height of the body h=1.8 m, the unit weight of the concentrated full tailings is about 18.6 kN/m$^3$, the maximum principal stress of this structure is not exceeding 1.8m×18.6 kN/m$^3$=33.48kPa, so confining pressures (50, 100, 200, and 300 kPa) are adopted to simulate the stress state of the structure.

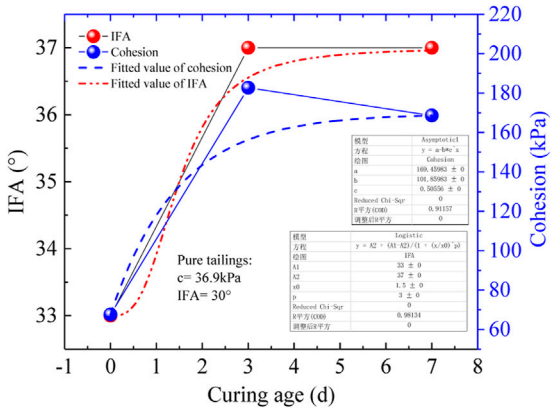


FIGURE 16
Triaxial shear test results with the growing of curing age.

## 3.3 Shear test

The shear speed is set to 1.0%/min. The test machine is started to initiate the shearing process. In the beginning, measure and record the axial force and axial displacement readings once, every time the specimen produces an axial strain of 0.3%–0.4%. After the axial strain reaches 3%, extend the reading interval by measuring and recording the readings once, every time the specimen produces an axial strain of 0.7%–0.8%. The measuring/recording frequency is measured, as the readings get close to the peak values. At the end of the test, the motor is turned off, the lift table is lowered, the vent is opened to drain the water inside the pressure chamber, the pressure chamber is uncovered, the remaining water around the specimen is dried, the rubber membrane outside the chamber is removed, and the deformed shape is described.

Figure 4 presents the curing situation of the concentrated full tailings specimens. Figure 5 shows the specimen mounting of the triaxial shear test.

# 4 Results and discussions

## 4.1 Stress-strain results

The relationship curves between the main stress difference (σ1−σ3) and axial deformation were plotted according to the data collected during the test, with the peak of (σ1−σ3) as the failure point. The stress-strain curves of pure tailings, 0 days concentrated full tailings, 3 days concentrated full tailings, and 7 days concentrated full tailings are displayed in Figure 6. Based on the test results, the stress-strain relationship of the concentrated full tailings exhibited a certain trend of strain softening compared with that of the pure tailings. For specimens of the same curing age, the strain softening increased with the confining pressure. The peak stress increased with the growing confining pressure. After the stress reached the peak, the stress difference (σ1−σ3) greatly decreased.

The stress-axial strain curve of different curing time under the same circumferential pressure are displayed in Figure 7. It can be seen that for the pure tailings, the type of stress-strain under

different confining pressure is mainly strain hardening, when cementitious materials added, the stress-strain curves change into strain-softening type, even in a low confining pressure. With the increase of confining pressure, the strain-softening tendency of concentrated full tailings of different ages decreases on the whole.

Figure 8 shows the comparison of the triaxial test results of loose and concentrated tailings. By comparing the results of pure tailings with those of full tailings with different curing ages, it shows that the stress-strain curve of the pure tailings, which has no curing agent, was strain hardened. The strain hardening was accompanied by volume contraction (shear expansion) and a reduction in pore ratio. The stress-strain curve of the 0 days concentrated full tailings fell between strain hardened and strain softened, while that of the 3 days and 7 days concentrated full tailings have significant strain-softening features, which is accompanied by shear expansion and an increase in the pore ratio. Strain softening comes along with strain localization and the formation of the shear slip zone, as shown in Figure 9. The shear zone has a large local pore ratio, which suppresses the shear strength of the concentrated full tailings (Libos and Cui, 2020; Yu et al., 2022). The stress-strain curve of some specimens had two strain-softening processes, as shown in Figure 10. After the first strain softening, the deformation greatly increased. This is followed by the second strain softening, where the stress-strain curve stepped down again. Then, the deformation worsened until specimen failure occurred.

## 4.2 Shear failure patterns of specimens

Figure 11 shows the shear failure images of the pure tailings, as well as the 0 days, 3 days, and 7 days concentrated full tailings. The shear failure of the pure tailings was approximately soft plastic deformation without an apparent shear zone. The test on this specimen was terminated when the strain reached the limit. For the concentrated full tailings cured at different ages, the failure was accompanied by the formation of the shear zone. The shear strength greatly decreased, and the specimen failed when the zone penetrated the specimen. The shear zone of the failed 3 days specimen was more apparent than that of the failed 0 days specimen. For the 7 days concentrated full tailings, the failure pattern can be summarized as follows: local weak zones were deformed under compression. Then, the zones were further crushed, resulting in a larger deformation area. The test was terminated when the strain reached the limit. Dual strain softening processes occurred. At the end of the test, no through-shear surface was formed, and part of the specimen remained intact.

## 4.3 Shear strength c and φ

Since the stress-strain curve of concentrated full tailings under low confining pressure is a strain softening type, the peak point of each curve is taken as the failure point. Therefore, the peak value of (σ1−σ3) is taken as the diameter of the Mohr stress circle, and the value of (σ1+σ3)/2 is taken as the centre of the circle to draw the stress circles under different confining pressures. The common tangent of the stress circles is taken as the tanφ value, and the intercept between the common tangent and the σ-axis is taken as the c value. That is, the damage envelope is approximated into a straight line, which can be expressed as follows:

$$\tau_f = c + \sigma \tan \varphi$$

Figures 12–15 show the shear strengths of pure tailings and concentrated full tailings at different ages. It can be seen from the figures that the strength envelope of mohr-stress circle under different confining pressures is basically liner, indicating that under low confining pressures, the shear strength of different curing-age concentrated full tailings presents a linear increase trend with the increase of vertical stress.

Based on the test results, the concentrated full tailings, which were added cementitious material, have an overall greater shear strength than that of the pure tailings. The test results are summarized in Table 2 and Figure 16, it can be derived that, with the extension of the curing age, the cohesion increased first and then decreased. In addition, the internal friction angle (IFA) grew first and then stabilized. Concentrated full tailings exhibited a 70.7% higher cohesion and a 10% larger IFA than that of pure full tailings after being cured for 0 days. In comparison to those cured for 0 days, the concentrated full tailings cured for 3 days and 7 days exhibited 170.2% and 149.4% higher cohesion, respectively, and a 12.1% large IFA in both cases. This means, as the curing age lengthens, the degree of hydration grows, and the cohesion increases. When the age reaches a certain value, the shrinkage deformation creates micro-cracks inside the specimen (Yu et al., 2022). This is the reason for the reduction of cohesion.

The quantitative comparison results are calculated by the following equation:

$$\vartheta_{\text{growth rate}} = \frac{I_{\text{After}} - I_{\text{Before}}}{I_{\text{Before}}} \times 100\%$$

Where, $I_{\text{After}}$ refers to the comparing index of cohesion and IFA; $I_{\text{Before}}$ refers to the compared index of cohesion and IFA.

# 5 Conclusion

This study carried out a triaxial shear test on pure tailings and concentrated full tailings cured at different ages to investigate how the curing agent affects the shear strength of tailings and how the curing age influences the shear strength. The main conclusions are as follows.

(1) Concentrated full tailings exhibited a 70.7% higher cohesion and a 10% large IFA than that of pure full tailings after being cured for 0 days. In comparison to those cured for 0 days, the concentrated full tailings cured for 3 days and 7 days exhibited 170.2% and 149.4% higher cohesion, respectively, and a 12.1% large IFA in both cases.
(2) The shear failure pattern of the concentrated full tailings, which were added as curing agents, differs from that of pure tailings. The former tends to be brittle failure with a distinct shear zone, while the latter is a plastic failure without such a zone.
(3) With the extension of the curing age, the hydration tends to be sufficient, the brittle failure becomes more apparent, and the shear zone becomes clearer and tends to penetrate the specimen. However, the shear zone of the 7 days specimen is

not apparent because the local strength is reduced by irregular internal microcracks due to the dry shrinkage deformation of the specimen. So the intermittent time between construction layers is suggested to be no longer than 3days, when intermittent time is longer than 7days, the shear strength will be reduced, which will not benefit for the overall stability of the concentrated full tailings structure, and other measurements need to be adopted to increase the shear strength of construction layers, such as the hydraulic roughing measurement.

The concentrated full tailings, which were added curing agents, have a much higher shear strength than that of the pure tailings. Even if no curing is implemented, the cohesion of concentrated full tailings is nearly twice that of the pure tailings. This suggests that the curing agents effectively work and stabilize the specimen structure. The test results show that the shear strength is positively correlated with the curing age in the early stage. After 3 days, the shear strength declines, which is related to the dry shrinkage deformation of cement and other factors. In actual construction, the specimens between construction layers are cured no longer than 3 days. In this manner, the concentrated full tailings can experience the strength growth due to hydration, while preventing the dry shrinkage deformation produced by the long drying time from weakening the structural strength.

## Data availability statement

The original contributions presented in the study are included in the article/Supplementary Material, further inquiries can be directed to the corresponding authors.

## Author contributions

Conceptualization, GM and WW; methodology, SW; validation, LG; formal analysis, SW; investigation, SW; resources, SW and YW; data curation, SW and YfC; writing—original draft preparation, SW; writing—review and editing, LG; visualization, SW; supervision, LG; project administration, GM; funding acquisition, GM and LG. All authors have read and agreed to the published version of the manuscript.

## Funding

This research was funded by National Key Research and Development Plan of China (grant number 2018YFC0604605) and National Natural Science Foundation project of China (grant number 52274122); The APC was funded by Exploration Fund of BGRIMM Technology Group (grant number 02-2271).

## Conflict of interest

SW, GM, WW, YW, YyC, LG, and YfC were employed by the company BGRIMM Technology Group.

## Publisher's note

All claims expressed in this article are solely those of the authors and do not necessarily represent those of their affiliated organizations, or those of the publisher, the editors and the reviewers. Any product that may be evaluated in this article, or claim that may be made by its manufacturer, is not guaranteed or endorsed by the publisher.

## References

Agapito, L. A., and Bareither, C. A. (2018). Application of a one-dimensional large-strain consolidation model to a full-scale tailings storage facility. *Miner. Eng.* 119, 38–48. doi:10.1016/j.mineng.2018.01.013

Beier, N., Wilson, W., Dunmola, A., and Sego, D. (2013). Impact of flocculation-based dewatering on the shear strength of oil sands fine tailings. *Can. Geotechnical J.* 50, 1001–1007. doi:10.1139/cgj-2012-0262

Cui, Y., Mei, G., Chang, B., and Wang, Y. (2020). Mechanical properties of modified solidification tailings. *Nonferrous Met. Sect.* 072 (003), 93–98.

Dimitrova, R. S., and Yanful, E. K. (2012). Factors affecting the shear strength of mine tailings/clay mixtures with varying clay content and clay mineralogy. *Eng. Geol.* 125, 11–25. doi:10.1016/j.enggeo.2011.10.013

Dong, Q. (2017). *Study of evolution and mechanism of the strength to sulfur content lead-zinc tailings cemented paste backfill. doctor's thesis.* Fuxin City: Liaoning Technical University. (in Chinese).

Đurđevac Ignjatović, L., Krstić, V., Radonjanin, V., Jovanović, V., Malešev, M., Ignjatović, D., et al. (2022). Application of cement paste in mining works, environmental protection, and the sustainable development goals in the mining industry. *Sustainability* 14, 7902–7913. doi:10.3390/su14137902

Hou, C., Zhu, W., Yan, B., Guan, K., and Du, J. (2018). Influence of binder content on temperature and internal strain evolution of early age cemented tailings backfill. *Constr. Build. Mater.* 189, 585–593. doi:10.1016/j.conbuildmat.2018.09.032

Hou, Y., Cao, S., Ding, P., Zhang, X., and Han, D. (2019). Effect of freeze-thaw cycle on the intensity of consolidated full tailings. *Metal. Mine* 1, 34–39. (in Chinese).

Indraratna, B. (1994). Geotechnical characterization of blended coal tailings for construction and rehabilitation work. *Q. J. Eng. Geol. Hydrogeology* 27, 353–361. doi:10.1144/GSL.QJEGH.1994.027.P4.06

Islam, S. (2021). *A study on the mechanical behaviour of three different fine-grained mine tailings.* Riyadh City: journal of King Saud University-Engineering Sciences. doi:10.1016/j.jksues.2021.04.001

Jiang, H., Ren, L., Gu, X., Zheng, J., and Cui, L. (2022). Synergistic effect of activator nature and curing temperature on time-dependent rheological behavior of cemented paste backfill containing alkali-activated slag. *Environ. Sci. Pollut. Res.* 30, 12857–12871. doi:10.1007/s11356-022-23053-1

Jin, J., Qin, Z., Lü, X., Liu, T., Zhang, G., Shi, J., et al. (2022). Rheology control of self-consolidating cement-tailings grout for the feasible use in coal gangue-filled backfill. *Constr. Build. Mater.* 316, 125836. doi:10.1016/j.conbuildmat.2021.125836

Ke, X. (2016). *Study on structure and properties of the consolidation mass of cemented tailings backfill. Doctor's thesis.* Wuhan City: Wuhan University. (in Chinese).

Kiventerä, J., Piekkari, K., Isteri, V., Ohenoja, K., Tanskanen, P., and Illikainen, M. (2019). Solidification/stabilization of gold mine tailings using calcium sulfoaluminate-belite cement. *J. Clean. Prod.* 239, 118008. doi:10.1016/j.jclepro.2019.118008

Li, J., Ren, W., Zhang, A., Li, S., Tan, J., and Liu, H. (2023). Mechanical properties and microstructure analysis of cement mortar mixed with iron ore tailings. *Buildings* 13, 1–20. doi:10.3390/buildings13010149

Li, J. (2018). *The experimental research of creep characteristic and long-term strength for cemented full tailings backfill. master's thesis.* Nanchang City: Jiangxi University of Science and Technology. (in Chinese).

Li, K. (2019). "Study on mechanical and acoustic emission characteristics of uniaxial compression of cemented tailings backfill subjected to temperature,". Master's Thesis (China: Wuhan University of Science and Technology).

Libos, I. L. S., and Cui, L. (2020). Effects of curing time, cement content, and saturation state on mode-I fracture toughness of cemented paste backfill. *Eng. Fract. Mech.* 235, 107174. doi:10.1016/j.engfracmech.2020.107174

Paiva, H., Yliniemi, J., Illikainen, M., Rocha, F., and Ferreira, V. (2019). Mine tailings geopolymers as a waste management solution for a more sustainable habitat. *Sustainability* 11, 995–1015. doi:10.3390/su11040995

Qin, J., Zheng, J., and Li, L. (2021). An analytical solution to estimate the settlement of tailings or backfill slurry by considering the sedimentation and consolidation. *Int. J. Min. Sci. Technol.* 31, 463–471. doi:10.1016/j.ijmst.2021.02.004

Roshani, A., Fall, M., and Kennedy, K. (2017). A column study of the hydro-mechanical behavior of mature fine tailings under atmospheric drying. *Int. J. Min. Sci. Technol.* 27, 203–209. doi:10.1016/j.ijmst.2017.01.023

Suazo, G., Fourie, A., Doherty, J., and Hasan, A. (2016). Effects of confining stress, density and initial static shear stress on the cyclic shear response of fine-grained unclassified tailings. *Géotechnique* 66, 401–412. doi:10.1680/jgeot.15.P.032

Wang, B., Gan, S., Dong, P., Wang, R., Li, Q., and Gao, L. (2021). Experimental study on consolidation characteristics of tailings cemented backfill in alpine regions. *Chin. J. Nonferrous Metals* 32, 2446–2457. (in Chinese).

Wang, S., Zhang, C., and Zhu, W. (2008), Influence of solidified tailing concentration on initial fluidity and strength. *Metal. Mine* 2, 136–145. (in Chinese).

Wang, S., Zhang, C., and Zhu, W. (2009), Influence of solidifying additive on the initial fluidity and strength of solidified tailings. *Metal. Mine* 2, 30–33.

Xiu, Z., Wang, S., Ji, Y., Wang, F., and Ren, F. (2022). Experimental study on the triaxial mechanical behaviors of the cemented paste backfill: Effect of curing time, drainage conditions and curing temperature. *J. Environ. Manag.* 301, 113828. doi:10.1016/j.jenvman.2021.113828

Xiu, Z., Wang, S., Ji, Y., Wang, F., and Wang, P. (2021). An analytical model for the triaxial compressive Stress-strain relationships of Cemented Pasted Backfill (CPB) with different curing time. *Constr. Build. Mater.* 313, 125554. doi:10.1016/j.conbuildmat.2021.125554

Xu, W., Li, Q., and Tian, M. (2019). Strength and deformation properties of polypropylene fiber-reinforced cemented tailings backfill. *Chin. J. Eng.* 41, 1618–1626. (in Chinese). doi:10.13374/j.issn2095-9389.2018.12.14.002

Yan, B., Han, L., Xiao, H., Zhang, J., Huang, J., Hu, W., et al. (2019). Rapid dewatering and consolidation of concentrated colloidal suspensions: Mature fine tailings via self-healing composite hydrogel. *acs Appl. Mater. interfaces* 11 (24), 21610–21618. doi:10.1021/acsami.9b05692

Yao, Y., Van Tol, A. F., and Van Paassen, L. A. (2012). "The effect of flocculant on the geotechnical properties of mature fine tailings: An experimental study," in IOSTC 2012: Proceedings of the 3rd International Oil Sands Tallings Conference, Edmonton, Canada (Edmonton: university of Alberta).

Yilmaz, E., Belem, T., Bussière, B., Mbonimpa, M., and Benzaazoua, M. (2015). Curing time effect on consolidation behaviour of cemented paste backfill containing different cement types and contents. *Constr. Build. Mater.* 75, 99–111. doi:10.1016/j.conbuildmat.2014.11.008

Yin, S., Liu, J., Shao, Y., Zhang, H., Armelle, B., and Kou, Y. (2020). Influence rule of early compressive strength and solidification mechanism of full tailings paste with coarse aggregate. *J. Central South Univ. Sci. Technol.* 51, 11–17. (in Chinese).

Yu, X., Song, W., Tan, Y., Kemeny, J., and Wang, J. (2022), Energy dissipation and 3d fracturing of Backfill-encased-rock under triaxial compression. *Constr. Build. Mater.* 341, 127877. doi:10.1016/j.conbuildmat.2022.127877

Zhao, S., Su, D., Zhang, Y., and Wu, W. (2016). Study on creep test of cemented tailings backfill and statistical damage model. *Metal. Mine* 5, 26–30. (in Chinese).

Zou, Y., Yang, T., and Zhang, X. (2020). Experimental study and analysis on variation characteristics of mechanical parameters of tailings filled material under cyclic loading and unloading. *Value Eng.* 39, 276–280. (in Chinese).

frontiers | Frontiers in Earth Science

TYPE Original Research
PUBLISHED 03 May 2023
DOI 10.3389/feart.2023.1141345



OPEN ACCESS

EDITED BY
Marcelo Cohen,
Federal University of Pará, Brazil

REVIEWED BY
Bing Bai,
Beijing Jiaotong University, China
Wei Ge,
Zhengzhou University, China

*CORRESPONDENCE
Sha Wang,
wangsha@bgrimm.com
Lijie Guo,
guolijie@bgrimm.com

†These authors have contributed equally to this work and share first authorship

RECEIVED 10 January 2023
ACCEPTED 10 April 2023
PUBLISHED 03 May 2023

CITATION
Mei G, Wang S and Guo L (2023), Optimized algorithm of auxiliary drainage scheme in tailings reservoir rainfall prediction: illustrated with a case study. *Front. Earth Sci.* 11:1141345. doi: 10.3389/feart.2023.1141345



# Optimized algorithm of auxiliary drainage scheme in tailings reservoir rainfall prediction: illustrated with a case study

Guodong Mei[1,2†], Sha Wang[1,2*†] and Lijie Guo[1,2*]

[1]BGRIMM Technology Group, Beijing, China, [2]National Centre for International Research on Green Metal Mining, Beijing, China

Under forecasting rainfall condition, rainfall flows into the tailings pond instantaneously, causing water level rising rapidly, thus threatening the safety of the tailings pond. Therefore, it is of great importance to give auxiliary flood discharge measures in emergency situation. This study investigated the optimized calculation algorithm of two combined schemes of lowering the coverplate of tailing ponds and installing additional drainage pumps to determine the recommended scheme of auxiliary drainage measures for tailing ponds under forecast rainfall and proposed the corresponding prediction and calculation method based on the basic data of the water level-reservoir capacity curve of tailing ponds, forecast rainfall parameters, and flood discharge system parameters. The results showed that compared with the precise algorithm, the optimized algorithm does not need to call the main procedure of flood regulation calculation and is of high calculation efficiency and accuracy, calculation time can be controlled within 0.05s. Through the optimized algorithm, the recommended auxiliary drainage scheme for forecast rainfall can be obtained immediately, which can effectively guide tailing pond flood control and drainage activities during the flood season.

KEYWORDS

**predicted forecast rainfall, tailings ponds, auxiliary drainage, precise algorithm, optimized algorithm**

## 1 Introduction

The tailings pond, a special structure attached to the mine, is mainly used to stockpile tailings and waste slag from ore beneficiation. Upstream tailings ponds are designed with a flood drainage structure to discharge the clarified reservoir water that enters the pond with the tailings, as well as to discharge the incoming floods to ensure that the tailings pond can withstand floods under the design standard. Due to the dynamic changes in the accumulation height and reservoir water level of upstream tailings ponds, the design of the intake structure uses a sloping flume or a drainage shaft with coverplates (Forbes et al., 1991). As the tailings' elevation rises, the number of coverplates is gradually increased, realizing dynamic regulation (Saliba et al., 2011). The design of the coverplates is similar to the role of gates in hydraulic buildings. From the load bearing point of view, the coverplate of the flood discharge facility of the tailings pond can withstand sediment or water pressure. Therefore, when the coverplate is covered by the tailings, it should not be opened again; however, the coverplate within the clarified water range can be opened again to increase the discharge capacity of the flood discharge system under a higher hydraulic head. As the flood discharge capacity of the tailings pond is generally very limited, a overtopping dam failure is very likely to occur when the tailings pond encounters flooding, especially when the prior emptying

time is short or the flood discharging capacity is insufficient (Grimalt et al., 1999; Rico et al., 2008; Cambridge and Shaw, 2019). Meanwhile, the rise of water level increases the risk of liquefaction of the dam surface (Cambridge, 2014; Zanbak, 2019), which in turn reduces the anti-sliding stability of the dam. Therefore, it is important to develop a tailings pond coverplate lowering and auxiliary drainage scheme to increase the temporary drainage capacity to prevent dam failure and overtopping due to extreme rainfall during the flood season.

Owing to global warming, extreme weather is increasing every year. At present, the prediction of extreme weather mainly relies on meteorological rainfall forecasts. Because of the timing-constraint nature of weather forecasts and the generally limited discharge capacity of flood discharge systems, the incoming flood from the rainfall confluence will pose a greater threat to the safe operation of the tailings pond if the reservoir level cannot be lowered below the safe elevation within a short time after the extreme rainfall warning is issued (Cheng et al., 2021; Wu et al., 2022). The current government laws, regulations, technical specifications, and departmental guidelines (Ministry of Emergency Management of the People's Republic of China, 2020; Order of the State Administration of Work Safety, 2011; Ministry of Housing and Urban-Rural Development, 2013) offer no specific guidance for the tailings pond discharge scheme in an emergency, and emergency rescue is often organized by experts after an accident (Coldewey, 2009). It is an ex-post control of risk that is aimed at reducing accident losses.

It has become a consensus that extreme rainfall can significantly increase the risk of tailings pond failure. A series of theoretical studies have been conducted by researchers focusing on tailings pond risk prediction under extreme rainfall conditions, and some changing processes and pre-assessment methods of dam failure risk (Bai et al., 2021a) under rainfall confluence have been obtained. Joyce et al. (2018) demonstrated that the method of coupling flood risk and infrastructure resilience is achievable through the careful formulation of flood risk associated with a resilience metric, which is a function of the predicted hazards, vulnerability, and adaptive capacity. Komljenovic et al. (2020) proposed a holistic resilience-based approach for analyzing the safety of the tailings dam's closure stage, including the risk of overflow over the dam crest. As uncontrolled leakage from mine tailing pond can pose a serious environmental threat (Huang et al., 2016), Sammarco et al. (2003) studied the forecast of emergency situations owing to excessive water inflows into tailings ponds, pointing that in case of tunnel overflow and/or obstruction, water could flow from the tunnel into ponds thus causing over-topping risk, some measurements were suggested to reduce water inflow into the ponds, without preventing, but rather promoting, water outflow. Yang et al. (2020) proposed a hybrid network- Long-Short- Term Memory (LSTM) and Convolutional Neural Network (CNN), namely, CNN-LSTM network for predicting the tailings pond risk. Khalil et al. (2015) also carried out short-term water level forecasting research under conditions of mine-tailings recharge using wavelet ensemble neural network models, which ensures model robustness along with improved reliability by reducing variance. In recent years, with the development of monitoring technology, quantitative mathematical methods for predicting the extreme condition of tailings ponds, such as the risk of dam failure, together with the results of monitoring (internet of things monitoring or remote sensing monitoring) have become a research hotspot. Jing and Gao (2022) studied the deep learning bidirectional recurrent long and short memory network and proposed an infiltration line prediction model with univariate input and an infiltration line prediction model with multivariate input. Chang et al. (2013) and Liao et al. (2021) studied monitoring data of tailings dam and obtained the Lyapunov exponent as well as the calculation method for the correlation dimension D2 of the dynamical characteristics of tailings pond system. Che et al. (2018) proposed a remote sensing method based on support vector machine (SVM) to evaluate the safety risk of tailings pond under rainfall condition. Chen et al. (2019) used the method of data classification and regression analysis to establish a method of analyzing and predicting risk of tailings pond during operation. Jianfei et al. (2020) proposed a prediction model based on PAC and LSTM neural network. Besides, some experiment about tailings (Benzaazoua et al., 2004) or draining system designing method (Bánik et al., 2002) to grasp the influence factor of safety for tailings pond. The above research results have to some extent grasped the prediction method of tailings pond dam failure risk and were applied to early warning research. However, because of the transient and sudden nature of dam failure landslides (Cardinali et al., 2006), prior prevention of accidents and calculation of scenarios are still important measures to ensure the operation of tailings ponds.

In this study, based on the flood regulation algorithm calculation procedure, the auxiliary flood discharge calculation method of flood discharge system under predicted forecast rainfall is examined for the specific characteristics of tailing pond flood discharge facilities, which provides a scientific basis for the safe flood control of tailing ponds in short time.

# 2 Methods

## 2.1 Precise algorithm

The precise algorithm is a method to increase the number of cycles by continuously increasing the number of coverplates that should be lowered or the number of pumps that should be added, updating the discharge flow curve, calling the main program of the flood regulation algorithm for trial calculation, and calculating whether the highest water level determined by the algorithm exceeds the warning after each trial. Finally, the number of coverplates that should be lowered or the number of pumps that should be added is obtained.

The flowchart of the precise algorithm is shown in Figure 1.

From the flowchart shown in Figures 1, 2, it can be seen that the method requires constant calls to the main program of flood regulation algorithm. Although the calculation accuracy is high, the calculation efficiency is very low, which affects the stability of the program operation.

## 2.2 Optimized algorithms

In order to solve the problems of the above-mentioned precise algorithm, this study developed an optimized

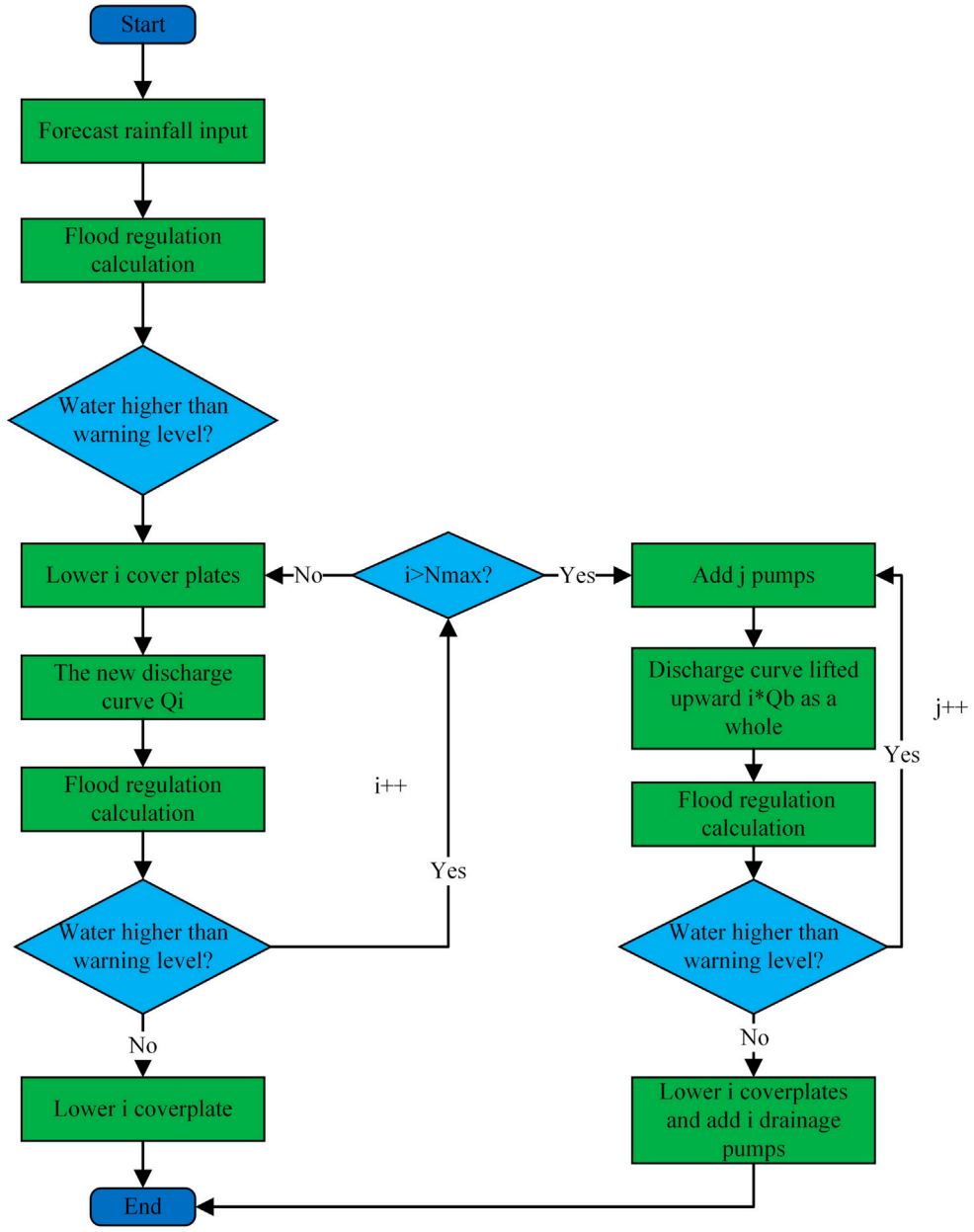


FIGURE 1
Flowchart of the precise algorithm.

algorithm for increasing the discharge capacity of the flood discharge system in the tailings pond prediction and forecasting system, which realizes the automatic calculation of the emergency assistance scheme through the judgement of maximum water level $z_{max}$ and $z_{yj}$ (warning water level), translation of the discharge flow curve of the flood discharge system, and parameters such as the water level-volume curve of the tailings pond. The flowchart of this algorithm is shown in Figures 3, 4.

According to the flowchart of the optimization algorithm for increasing the discharge capacity of the flood discharge system in the tailings pond prediction and forecasting system described above, the optimized algorithm includes the following steps and judgment processes.

### 2.2.1 Determination of whether to activate the auxiliary drainage scheme

Derive the maximum water level $z_{max}$ obtained in the previous flood regulation calculation, and determine if $z_{max}$ exceeded the warning level $z_{yj}$. If the warning level $z_{yj}$ is exceeded, the auxiliary discharge scheme is required. Otherwise, the auxiliary discharge scheme is not required.

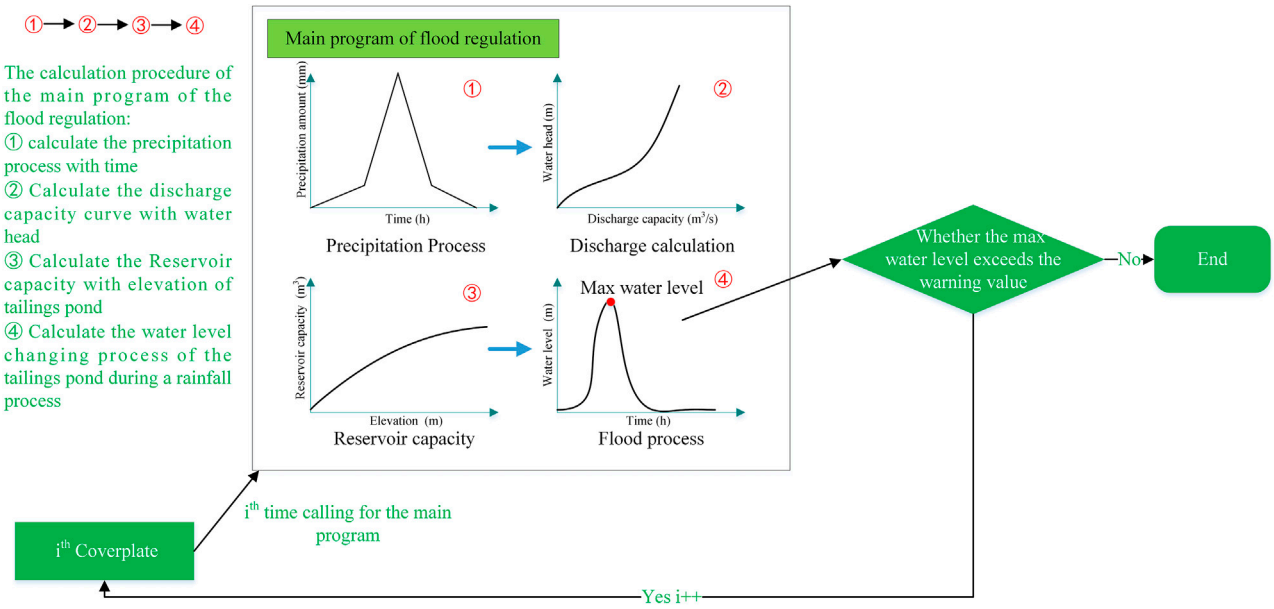


FIGURE 2
Simplified flowchart of the precise algorithm.

The auxiliary discharge scheme includes two types of lowering coverplates and adding a drainage pump, which are divided into two cases according to the actual situation: ① only lowering the coverplate elevation; ② lowering the coverplate elevation+ add drainage pump. Therefore, this algorithm prioritizes lowering the coverplate elevation, and when the drainage capacity is still insufficient after lowering the coverplate elevation, the combination of lowering the coverplate elevation+ drainage pump is used for auxiliary drainage.

### 2.2.2 Calculating the amount of water need to be discharged

The precise amount of water to be discharged is defined as $\Delta V$ (Figure 5), which is the difference between the volume corresponding to the current water level and the volume corresponding to the target water level $z_2$, it cannot be calculated because the target water level $z_2$ is unknown. However, it can be calculated approximately using Eq. 1, i.e., the difference between the capacity corresponding to the warning level and the capacity corresponding to the maximum water level.

$$\Delta \boldsymbol{V} = V_{\boldsymbol{hl}} - \boldsymbol{V}_{\boldsymbol{wl}} \tag{1}$$

Where $V_{hl}$ is the reservoir capacity corresponding to the highest water level of the flood regulation calculation, $m^3$, $V_{wl}$ is the reservoir capacity corresponding to the warning water level $z_{yj}$, $m^3$.

### 2.2.3 Calculating the required discharge capacity of the flood discharge system

According to the amount of water need to be discharged and the forecasting time, the minimum required discharge capacity of the flood discharge system can be calculated, the calculation method is detailed in Eq. 2.

$$\bar{\boldsymbol{Q}}_{\boldsymbol{min}} = \frac{\Delta V}{\boldsymbol{T}_{\boldsymbol{max}}} \tag{2}$$

Where $T_{max}$ is the time interval of the weather forecast.

### 2.2.4 Calculating the auxiliary discharge scheme

Compare the magnitude of $\bar{Q}_{min}$ and the theoretical maximum discharge capacity of the drainage system $Q_{max}$. If $\bar{Q}_{min} > Q_{max}$, then a direct determination is required to lower the coverplate to the lowest elevation and activate the pump discharge option. If $\bar{Q}_{min} < Q_{max}$, then a second determination is required to judge that if the lowering of the coverplate method alone may satisfy the need for discharging.

If $\bar{Q}_{min} > Q_{max}$, then the maximum discharge capacity of the discharge system does not meet the target discharge capacity requirement; therefore, all liftable coverplates need to be removed, and pump discharge measures need to be added. The number of coverplates that should be lowered and the amount of pump added are calculated using steps 1) to 3).

1) Calculate the minimum elevation to which the coverplate can be lowered using the following equation:

$$\boldsymbol{z}_1 = \max\{\boldsymbol{z}_{\boldsymbol{dl}}, \boldsymbol{z}_{\boldsymbol{fb}}\} \tag{3}$$

where $z_{dl}$ is the dead storage water level of the tailings pond and $z_{fb}$ is the elevation of the flume bottom (or bottom of the well) of the flood discharge system.

The above equation uses the water level at the bottom of the flume and the dead water level, to determine the lowest position to which the coverplate can be lowered. If the dead water level is higher than the flume bottom level (Figure 6), the coverplate can

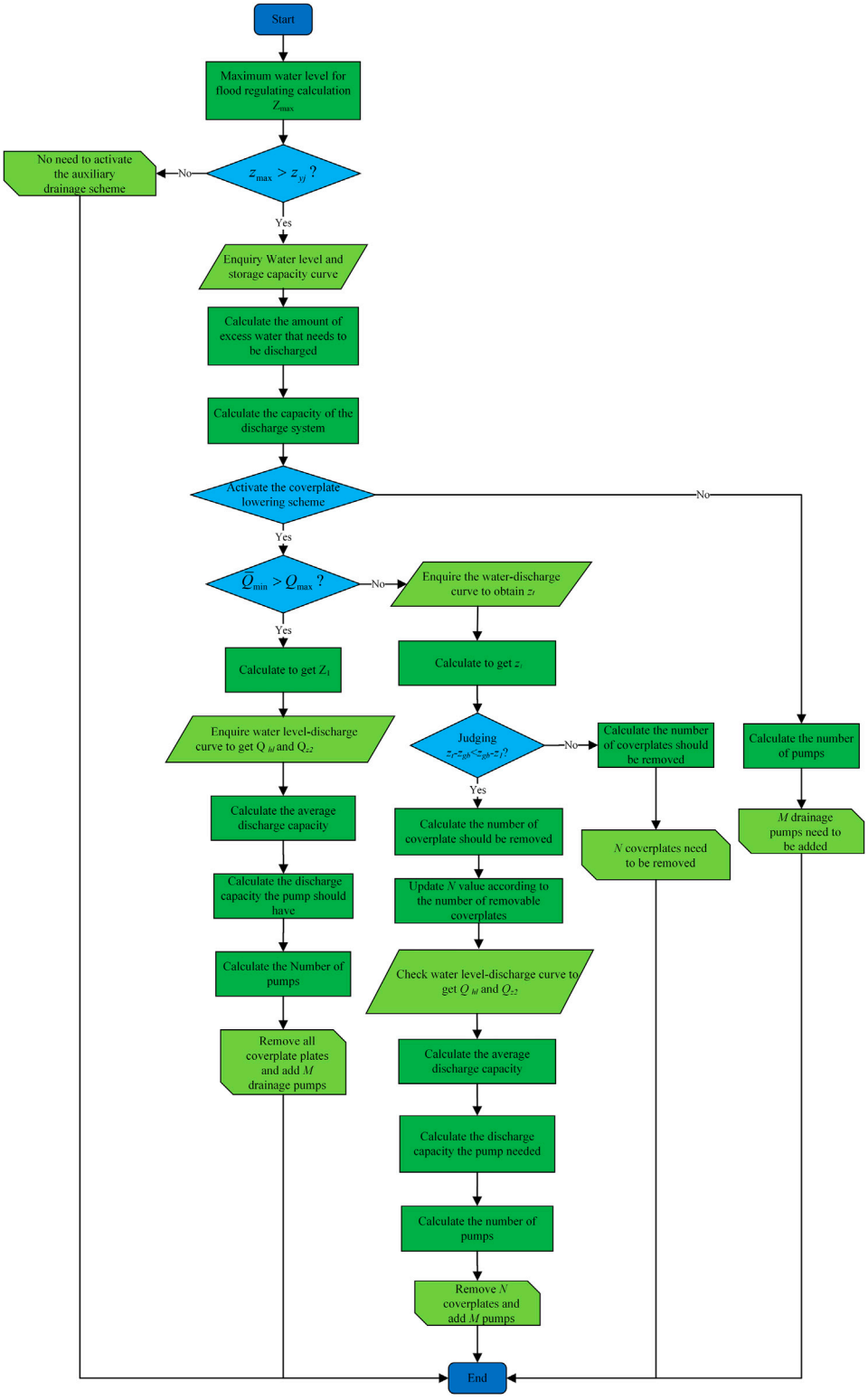


FIGURE 3
Flow chart of the optimized algorithm.

only be lowered to the dead water level elevation. If the dead water level is lower than the flume bottom level (Figure 7), the coverplate can be lowered to the flume bottom position. Dead water levels below the bottom of the flume are less common and occur mainly when there is a tandem discharge system, or during the initial stages of tailings storage operation.

The amount of coverplate need to be removed is calculated using the following equation:

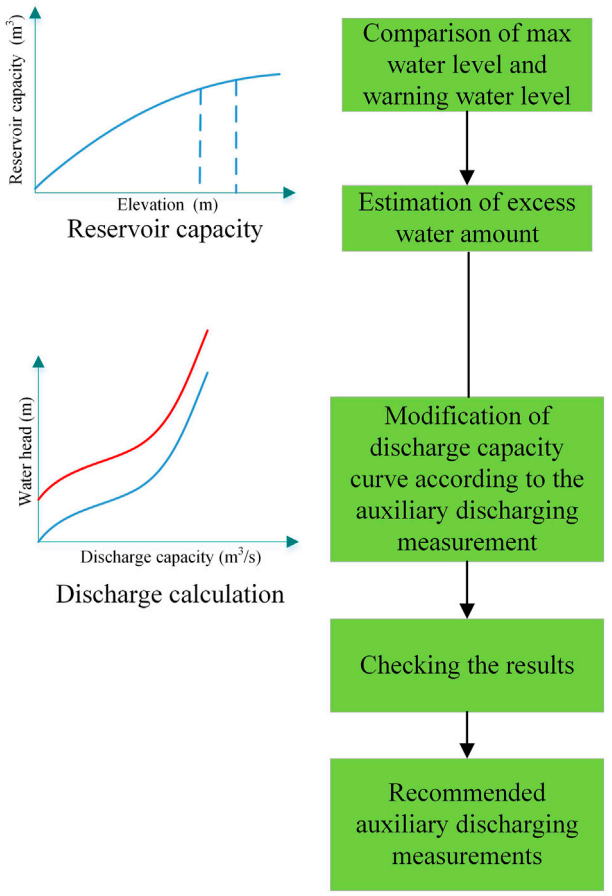


FIGURE 4
Simplified flowchart of the optimized algorithm.

$$N = \frac{z_{gb} - z_1}{L_{gb} \cdot \sin\beta} \tag{4}$$

Where $L_{gb}$ is the length of the single coverplate and β is the angle between the inclined groove and the horizontal direction.

2) Calculate the average discharge volume the coverplate lowering scheme by an optimization algorithm, which includes the steps ① and ②.

① Shift the water level-discharge flow curve downward along the $y$ axis ($z_{gb} - z_1$) to obtain the new water level-discharge flow curve, as shown in Figure 8. Query the new water level-discharge flow curve to obtain the discharge flows $Q_{yj}$ and $Q_{z_2}$ corresponding to the warning water level $z_{yj}$ and water level $z_2$ under this scenario.

The method of acquiring the whole discharge curve is, calculating the results of free flow, semi-pressure flow and pressure flow at different water levels, and taking their minimum values as the final discharge curve after comparing the three at each water level, as shown in Figure 9.

② The average flow capacity of the flood discharge system under this scheme is obtained using the following equation:

$$\bar{Q} = \frac{Q_{yj} + Q_{z_2}}{2} \tag{5}$$

3) Calculate the minimum number of mechanical pump that should be added based on the difference between the discharge capacity $\bar{Q}_{min}$ that the discharge system should have and the current average discharge capacity $\bar{Q}$, and the specific parameters of the pumps using a simplified calculation of the number of pumps.

The calculate of the minimum amount of mechanical drainage that should be added including steps ① to ②.

① Calculate the required mechanical drainage flood capacity using the following equation:

$$Q_{pump} = \bar{Q}_{min} - \bar{Q} \tag{6}$$

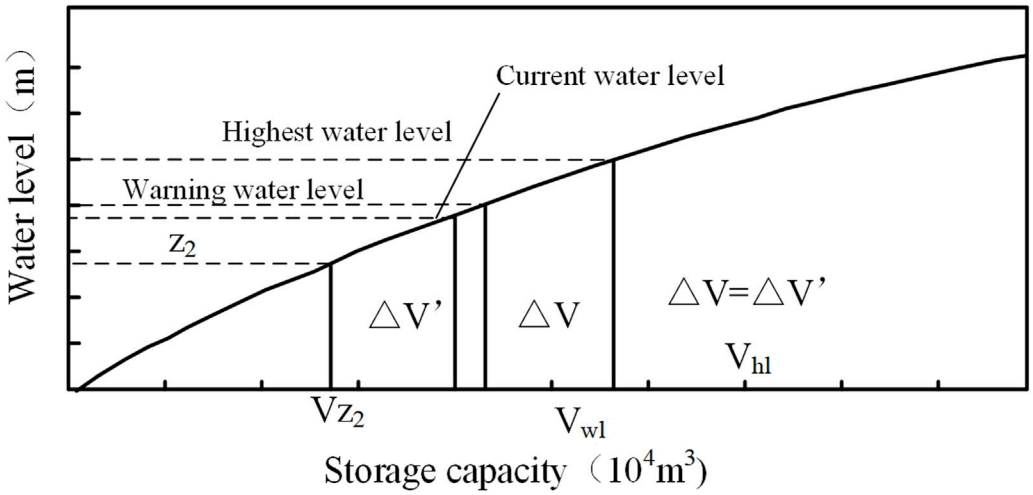


FIGURE 5
Water level-reservoir storage capacity curve and required discharge volume diagram.

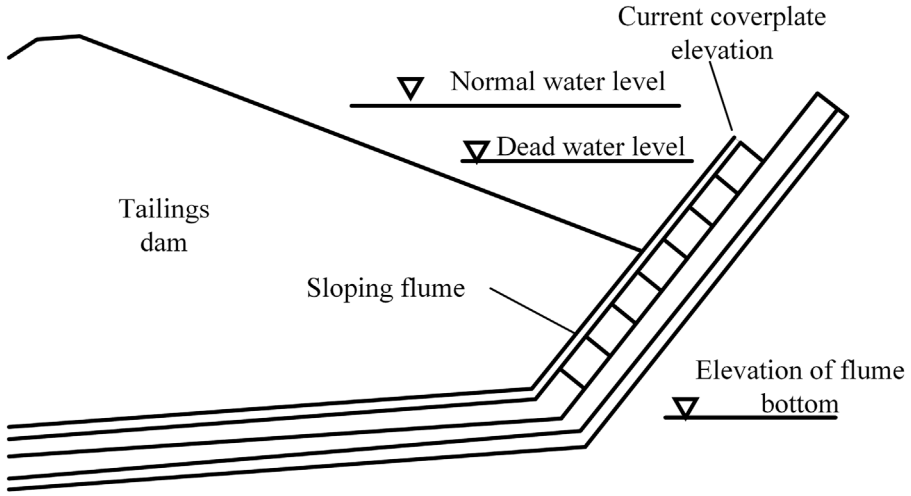


FIGURE 6
Schematic of flume bottom elevation and dead water level (dead water level above flume bottom elevation).

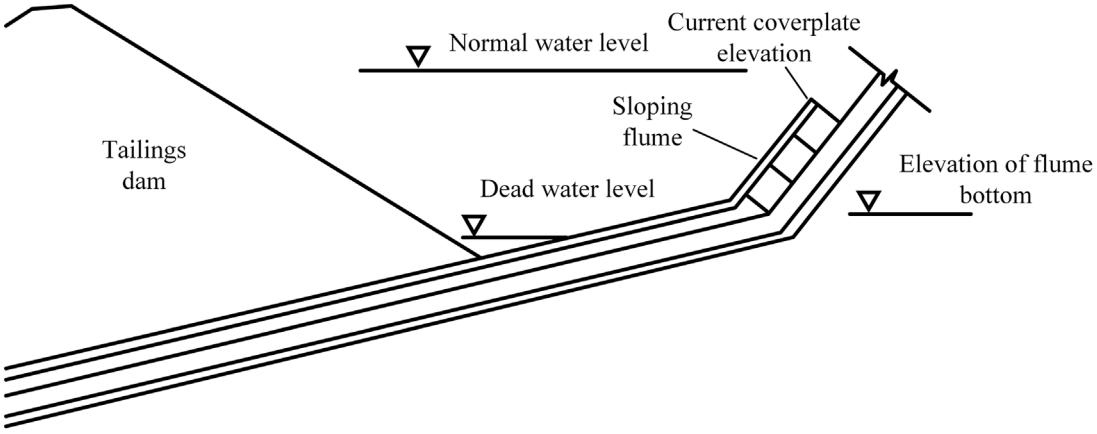


FIGURE 7
Schematic of flume bottom elevation and dead water level (dead water level is below the flume bottom elevation).

② Calculate the number of pumps required, which is $M$, using the following equation:

$$\boldsymbol{M} = \left[\boldsymbol{Q_{pump}}/\boldsymbol{Q_{rf}}\right] \tag{7}$$

where $Q_{rf}$ is the rated flow rate of the selected pump, Brackets in Eq. 7 means rounding up to an integer.

If $\bar{Q}_{min} < Q_{max}$, it indicates that the coverplate lowering option is expected to meet the target discharge volume, but further judgment is needed on specific measures to increase drainage capacity.

When $\bar{Q}_{min} < Q_{max}$, the water head required to reach $\bar{Q}_{min}$ is $H_{x1}$ ($H_{x1} = z_t - z_{gb}$), the current water head is defined as $H_{x2}$ ($H_{x2} = z_{max} - z_{gb}$), and the elevation corresponding to $\bar{Q}_{min}$ is obtained by interpolation, which is the elevation corresponding to the target head $z_t$. It is important to predetermine and calculate the minimum amount that the coverplate should be lowered using the following equation:

If $z_t - z_{gb} \geq z_{gb} - z_1$, this indicates the theoretical target elevation of coverplate need to be lowered is higher than $z_1$ and the discharging requirements can be met without initiating a mechanical discharge scheme. Then, the minimum amount that the coverplate should be lowered can be calculated by the following equation:

$$\mathbf{N} = \frac{\boldsymbol{H_{x1}} - \boldsymbol{H_{x2}}}{\boldsymbol{L_{gb}} \cdot \boldsymbol{sin\,\beta}} \tag{8}$$

If $z_t - z_{gb} < z_{gb} - z_1$, this indicates that the coverplate can not be lowered to the desired position and the mechanical drainage scheme still needs to be activated. Thus, the amount by which the coverplate should be lowered is calculated using the following equation:

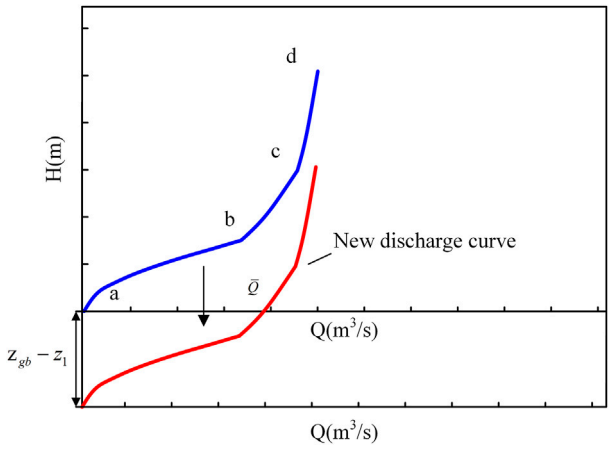


FIGURE 8
New water level-discharge capacity curve.

$$\mathbf{N} = \frac{z_{gb} - z_1}{L_{gb} \cdot \sin\beta} \tag{9}$$

where, $L_{gb}$ is the length of the single coverplate and β is the angle between the inclined flume and the horizontal direction.

After the number of lowered coverplates is determined, the same procedure as in steps (2) to (3) is used to calculate the minimum number of mechanical drainage facilities that should be added.

When mechanical drainage measures are selected to increase the discharge capacity without lowering the coverplate, the amount of mechanical drainage is calculated using the following formula:

$$\mathbf{M} = \left[\frac{\bar{Q}_{min}}{Q_{rf}}\right] \tag{10}$$

Brackets in Eq. 10 means rounding up to an integer.

The parameters required for the above calculation process are listed as follows.

$z_{max}$, The highest water level calculated in the previous flood regulation calculation, m.
$z_{yj}$, Early warning water level, m.
$\Delta V$, The amount of water to be drained during the forecast time, $m^3$.
$V_{hl}$, Capacity of the reservoir corresponding to the highest water level of the flood regulation calculation, $m^3$.
$V_{el}$, Reservoir capacity corresponding to the early warning level, $m^3$.
$\bar{Q}_{min}$, Minimum discharge capacity that the flood discharge system should have, $m^3/s$.
$Q_{max}$, Maximum discharge capacity of the flood discharge system, $m^3/s$.
$Q_{hl}$, Discharge flow corresponding to the highest water level, $m^3/s$.
$Q_{el}$, Discharge capacity corresponding to the early warning water level, $m^3/s$.
$\bar{Q}$, Average flow capacity of the flood discharge system, $m^3/s$.
$Q_{pump}$, Flood discharge capacity of water pumps, $m^3/s$.
$Q_{z_1}$, Discharge capacity corresponding to water level $z_1$, $m^3/s$.
$Q_{rf}$, Rated flow rate of the selected drainage pump, $m^3/s$.
$T_{max}$, Time interval of the weather forecast, s.
$M$, Number of auxiliary relief facility pumps required, units.
$z_t$, Elevation corresponding to the target water head, m.
$z_{gb}$, Current elevation of the coverplate, m.
$z_1$, The lowest elevation to which the coverplate can be lowered, m.
$z_{dl}$, Dead water level elevation, m.
$z_{tb}$, Elevation of the trough bottom of the flood discharge ramp, m.
$H_{x1}$, the water head required to reach $\bar{Q}_{min}$, m.
$H_{x2}$, The current water head, m.
$N$, Number of coverplate plates to be lowered.
$L_{gb}$, Length of the single coverplate, m.
$\beta$, Angle of the inclined flume to the horizontal, °.

## 3 Physical model

A tailings reservoir (Figure 10) is a second-class reservoir with a sloping flume-culvert pipe type flood discharge system, the single vertical height of the coverplate is 0.2009 m, and the dead water

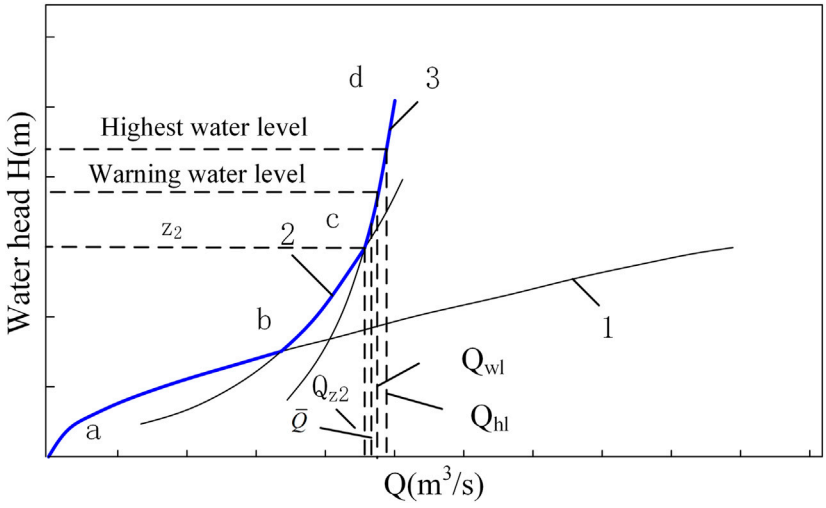


FIGURE 9
Water level-discharge capacity curve; 1 - Free flow; 2 - Semi-pressure flow; 3 - Pressure flow.

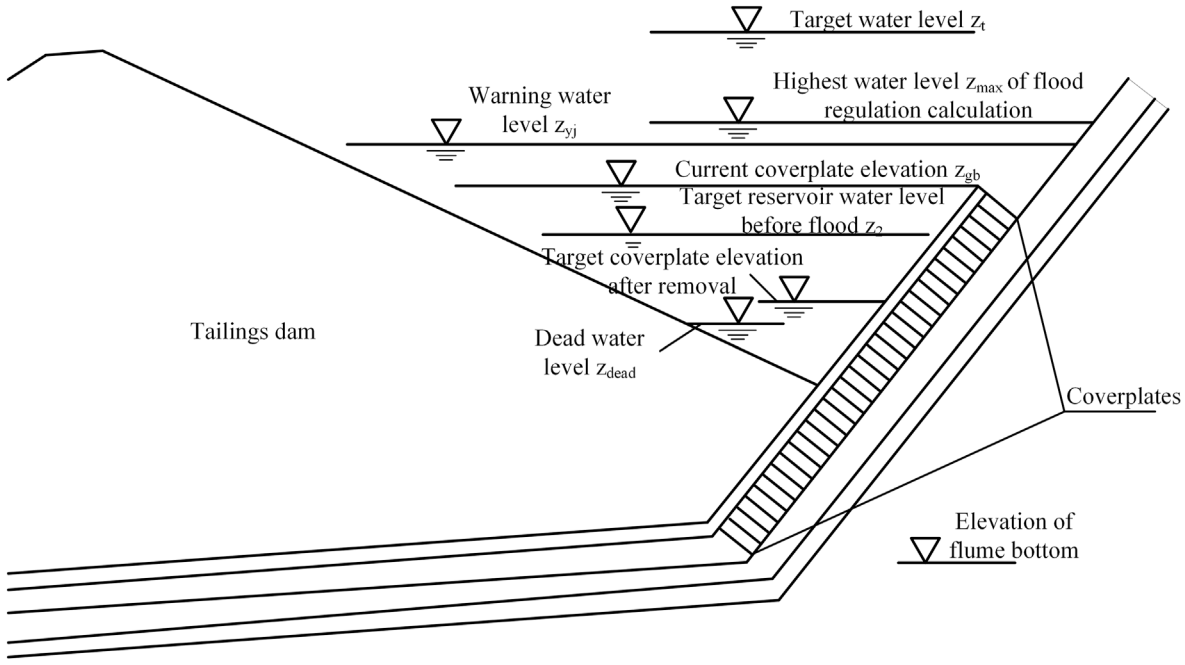


FIGURE 10
Schematic of a tailings pond.

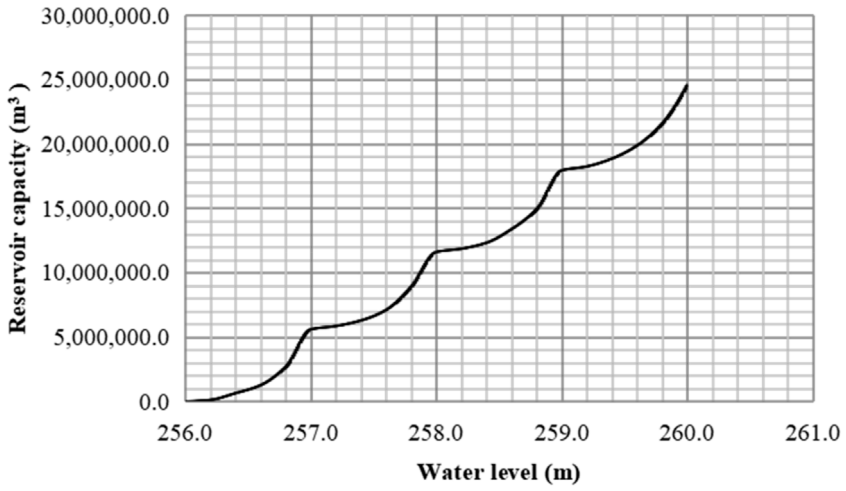


FIGURE 11
Water level-volume curve of a tailings pond.

elevation is 253.5 m. The tailings reservoir water level-capacity curve is shown in Figure 11, and the water level-discharge capacity curve is shown in Figure 12. The blue warning water level is 257.0 m. A 200-min weather forecast indicates that a heavy rainfall will occur. The incoming flood and flood regulation calculations are performed according to the forecasted rainfall process. The calculation results show that this forecasted rainfall can raise the water level to 257.5 m, exceeding the blue warning water level.

## 4 Results and discussion

In order to cope with the forecasted rainfall, an emergency relief plan is needed to increase the discharge capacity so that the reservoir water level does not exceed the warning water level. The flood regulation calculation results show that the rainfall inflow causes the highest water level of tailings pond to rise to $z_{max}$ = 257.5 m, which is higher than the blue warning water level $z_{yj}$ = 257 m. Therefore, it is

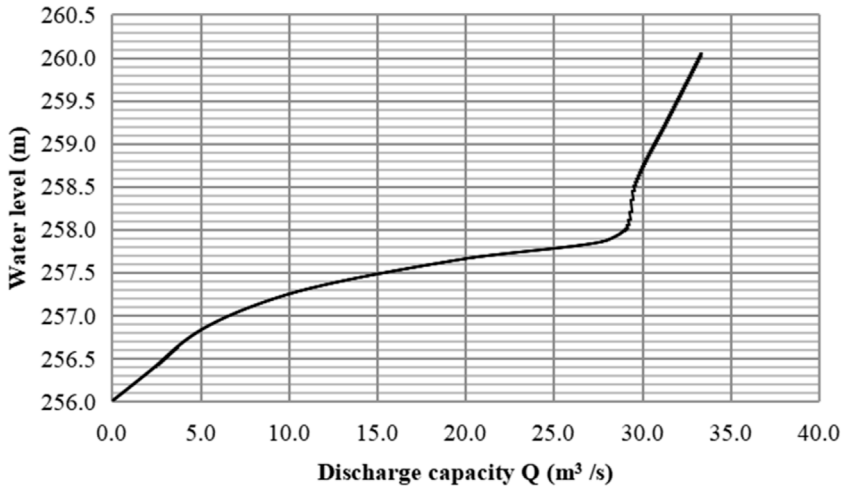


FIGURE 12
Water level-discharge capacity curve of a tailings pond.

necessary to start the auxiliary discharge scheme. According to $z_{max}$, $z_{yj}$, and Figure 9, the water volume to be discharged $\Delta V$ is derived by subtracting the volume of the reservoir corresponding to the highest water level from the volume corresponding to the warning level to obtain: $\Delta V = 380000m^3$. To discharge the excess water, the minimum discharge capacity of the flood discharge system should be no less than: $\bar{Q}_{min} = \frac{380000}{200 \times 60} = 31.667m^3/s$ . Compare the magnitude of $\bar{Q}_{min}$ and $Q_{max}$. According to Figure 12, $Q_{max}$ (33.37 $m^3$/s) > $\bar{Q}_{min}$ (31.67 $m^3$/s). The water elevation corresponding to $\bar{Q}_{min}$, i.e., $z_t = 259.362m$. Then, the following judgments are carried out: ① calculate the lowest elevation coverplate can be lowered: $z_1 = \max\{z_{dl}, z_{tb}\} = z_{dl} = 253.5$ m;② determine the relationship between $z_t$ and $z_1$: $z_t - z_{gb} \geq z_{gb} - z_1$. This implies that the target elevation of the lowered coverplate is higher than $z_1$, which indicates that the flood discharge needs can be satisfied by only using the lowered coverplate measures. Then, the number of lowered coverplates required is calculated as follows:

$$N = \frac{H_{x1} - Z_{x2}}{L_{gb} \cdot \sin\beta} = \frac{(259.362 - 256) - (257.5 - 256)}{0.2009} = 9.3$$

Based on the above calculations, 10 coverplates (rounded up) need to be lowered before the flood to ensure the water level in the tailings pond does not exceed the warning when suffered forecast rainfall.

The calculated result using the precise algorithm shown in Figure 1 is also 10 coverplate plates. It can be seen that the calculation result of the optimized algorithm is the same as that of the precise algorithm.

Computation time of the precise algorithm and the optimized algorithm is listed in Table 1. For physical model in Figure 10, the computation time by precise algorithm is 5.3 s, 10 times of the main program is called during trial computing, whereas, the computation time by the optimized algorithm is only 0.05 s, without calling the main program of flood regulation.

The calculation time of the precise algorithm is related to the calculation time of one single flood regulation, whose efficiency is relied on factors such as iterative method, water level step size, the non-linearization degree of water-reservoir capacity curve and so on. The more complex the input parameter is, the lower the calculation efficiency is. However, the optimized algorithm does not need to call the main program of the flood regulation, so it has a competitive computation efficiency.

The upstream tailings pond adopts hydraulic discharging method, so in the tailings discharging process, reservoir bottom is gradually covered by tailings with the processing of hydraulic deposition (Bai et al., 2021b), and a triangle zone (from the cross section) formed by the original topography and the sedimentary beach at the reservoir tail is the water storage zone. Therefore, the variation amplitude of the water level in tailings pond is actually limited. As stipulated in Tailings Pond Safety Regulation (National regulation of People's Republic of China), the minimum safety free height (height between water level and breach crest) of different class tailings pond are listed in Table 2, taking the first-class tailings pond as an example, the minimum safety free height is only 1.5 m, which indicates that the variation range of water level in tailings pond will not be too large, otherwise, overtopping accident will occur. Therefore, the method of estimating the water amount to be discharged, and the discharging capacity under the scheme of auxiliary discharging measurement by the linear simplified formula in a small water variation range has a relatively high calculation accuracy.

The simplified algorithm proposed in the study is not applicable to the initial discharge stage in the starter dam, because the starter dam is mostly one-time constructed, so the free height for safety is enough and the allowable variation of water is large, what's more, the non-linearity of water level storage capacity curve in the initial stage is obvious, therefore, the linear simplified estimation method proposed in this study will cause a certain amount of calculation errors when applied to the initial construction stage of tailings pond.

**TABLE 1 Computation time of the precise algorithm and the optimized algorithm.**

| Computing method | Computation time (s) | The times the main program is called |
|---|---|---|
| precise algorithm | 5.3 | 10 |
| optimized algorithm | 0.05 | 0 |

**TABLE 2 The minimum free height of upstream tailings pond (m).**

| Class of tailings dam | 1 | 2 | 3 | 4 | 5 |
|---|---|---|---|---|---|
| Maximum free height | 1.5 | 1.0 | 0.7 | 0.5 | 0.4 |

## 5 Conclusion

This study designed and examined the algorithm for an emergency increase in flood discharge capacity under extreme rainfall condition. Based on the calculation algorithm of tailings pond flood diversion and prediction method, the coverplate lowering scheme and auxiliary discharge scheme under the forecast condition were established based on rainfall forecast time, water level-volume curve, water level-discharge curve, coverplate size of flood discharge system and other parameters.

A method for predicting whether to activate the auxiliary discharge measures was established, and the estimation of whether to activate the auxiliary discharge measures was performed by comparing the size of the maximum water level calculated by the flood regulation calculation and the warning water level. Then, a simplified calculation method for the amount of water to be released under forecast and prediction conditions was derived, and the amount of water to be released was obtained based on the maximum and warning levels and the water level-volume curve. In addition, an estimation method for the target discharge capacity was developed. The target discharge capacity of the drainage system was estimated based on the time interval of rainfall forecasts and $\Delta V$.

An optimization algorithm for estimating the average discharge capacity of the flood discharging system under the coverplate lowering scheme was proposed. The optimization algorithm comprised two processes: 1) obtaining a new water level-discharge flow curve by translating the discharge flow curve; and 2) using the average of the discharge flows corresponding to the warning level and the $z_2$ level at the new water level-discharge flow curve as the average discharge capacity of the current flood discharge system under the predicted forecast scenario. The comparison results of the optimized algorithm and the precise algorithm showed that the former method has high calculation accuracy and does not need to call the main program of the flood regulation algorithm, thus significantly improving the calculation efficiency of the auxiliary drainage module.

The proposed simplified algorithm greatly reduces the calculation complexity of auxiliary discharging scheme under rainfall prediction, and improves the robustness and efficiency of calculation program. When the discharge capacity in insufficient, the contingency engineering measurements will be calculated and be recommended immediately, thus reducing the risk of overtopping accident to the largest extent, and ensuring the safety of downstream area.

## Data availability statement

The original contributions presented in the study are included in the article/supplementary material, further inquiries can be directed to the corresponding authors.

## Author contributions

Conceptualization, GM; methodology, SW; software, SW; validation, LG; formal analysis, SW; investigation, SW; resources, SW; data curation, SW; writing—original draft preparation, SW; writing—review and editing, LG; visualization, SW; supervision, LG; project administration, GM; funding acquisition, GM and LG. All authors have read and agreed to the published version of the manuscript.

## Funding

This research was funded by National Natural Science Foundation project of China, grant number 52274122; The APC was funded by Youth Science and Innovation Fund of BGRIMM Technology Group, grant number 02-2271 and 04-2213. The funder was not involved in the study design, collection, analysis, interpretation of data, the writing of this article or the decision to submit it for publication.

## Conflict of interest

Authors GM, SW, and LG were employed by BGRIMM Technology Group.

## Publisher's note

# References

Bai, B., Jiang, S., Liu, L., Li, X., and Wu, H. (2021). The transport of silica powders and lead ions under unsteady flow and variable injection concentrations. *Powder Technol.* 387, 22–30. doi:10.1016/j.powtec.2021.04.014

Bai, B., Zhou, R., Cai, G., Hu, W., and Yang, G. (2021). Coupled thermo-hydro-mechanical mechanism in view of the soil particle rearrangement of granular thermodynamics. *Comput. Geotechnics* 137 (8), 104272. doi:10.1016/j.compgeo.2021.104272

Bánik, J., Csicsák, J., and Berta, Z. (2002). "Experience on application of continuous drain trench during the remediation of tailings ponds in Hungary," in *Uranium in the aquatic environment* (Berlin, Heidelberg: Springer), 899–906.

Benzaazoua, M., Bussière, B., Dagenais, A. M., and Archambault, M. (2004). Kinetic tests comparison and interpretation for prediction of the Joutel tailings acid generation potential. *Environ. Geol.* 46, 1086–1101. doi:10.1007/s00254-004-1113-1

Cambridge, M. (2014). "Liquefaction failure in a Derbyshire fluorspar tailings dam. Maintaining the Safety of our Dams and Reservoirs," in *Proceedings of the 18th biennial conference of the British dam society at queen's university, belfast, from 3–6 september 2014* (ICE Publishing), 414–425.

Cambridge, M., and Shaw, D. (2019). Preliminary reflections on the failure of the Brumadinho tailings dam in January 2019. *Dams Reservoirs* 29, 113–123. doi:10.1680/jdare.19.00004

Cardinali, M., Galli, M., Guzzetti, F., Ardizzone, F., Reichenbach, P., and Bartoccini, P. (2006). Rainfall induced landslides in december 2004 in south-western umbria, central Italy: Types, extent, damage and risk assessment. *Nat. Hazards Earth Syst. Sci.* 6, 237–260. doi:10.5194/nhess-6-237-2006

Chang, L. S., Yang, T. Y., and Deng, H. J. (2013). Disaster prediction and preventive measures of constructing a waste dump on an abandoned tailing pond. *Appl. Mech. Mater.* 405, 2427–2430. Trans Tech Publications Ltd. doi:10.4028/www.scientific.net/AMM.405-408.2427

Che, D., Liang, A., Li, X., and Ma, B. (2018). Remote sensing assessment of safety risk of iron tailings pond based on runoff coefficient. *Sensors* 18, 4373. doi:10.3390/s18124373

Chen, Y., Li, Q., and Liang, Y. (2019). "Research and application of data classification in risk prediction for tailings reservoirs," in *Proceedings of the 3rd international conference on computer science and application engineering*, 1–5. doi:10.1145/3331453.3362058

Cheng, D., Cui, Y., Li, Z., and Iqbal, J. (2021). Watch out for the tailings pond, a sharp edge hanging over our heads: Lessons learned and perceptions from the Brumadinho tailings dam failure disaster. *Remote Sens.* 13, 1775. doi:10.3390/rs13091775

Coldewey, W. G. (2009). "Emergency planning for tailing dams," in *Optimisation of disaster forecasting and prevention measures in the context of human and social dynamics*, 52, 115.

Forbes, P. J., Cale, S. A., and Clelland, L. F. (1991). "Spillway systems for tailings dams," in *The embankment dam: Proceedings of the sixth conference of the British Dam Society held in Nottingham on 12–15 September 1990* (Thomas Telford Publishing), 85–91. doi:10.1680/ted.16477.0013

Grimalt, J. O., Ferrer, M., and Macpherson, E. (1999). The mine tailing accident in Aznalcollar. *Sci. Total Environ.* 242, 3–11. doi:10.1016/S0048-9697(99)00372-1

Huang, X., Deng, H., Zheng, C., and Cao, G. (2016). Hydrogeochemical signatures and evolution of groundwater impacted by the Bayan Obo tailing pond in northwest China. *Sci. Total Environ.* 543, 357–372. doi:10.1016/j.scitotenv.2015.10.150

Jianfei, D. A. I., Peng, Y., and Liyi, Z. H. U. (2020). A PCA-LSTM neural network-integrated method for phreatic line prediction. *China Saf. Sci. J.* 30, 94. doi:10.16265/j.cnki.issn1003-3033.2020.03.015

Jing, Z., and Gao, X. (2022). Monitoring and early warning of a metal mine tailings pond based on a deep learning bidirectional recurrent long and short memory network. *PloS one* 17 (10), e0273073. doi:10.1371/journal.pone.0273073

Joyce, J., Chang, N. B., Harji, R., and Ruppert, T. (2018). Coupling infrastructure resilience and flood risk assessment via copulas analyses for a coastal green-grey-blue drainage system under extreme weather events. *Environ. Model. Softw.* 100, 82–103. doi:10.1016/j.envsoft.2017.11.008

Khalil, B., Broda, S., Adamowski, J., Ozga-Zielinski, B., and Donohoe, A. (2015). Short-term forecasting of groundwater levels under conditions of mine-tailings recharge using wavelet ensemble neural network models. *Hydrogeology J.* 23, 121–141. doi:10.1007/s10040-014-1204-3

Komljenovic, D., Stojanovic, L., Malbasic, V., and Lukic, A. (2020). A resilience-based approach in managing the closure and abandonment of large mine tailing ponds. *Int. J. Min. Sci. Technol.* 30, 737–746. doi:10.1016/j.ijmst.2020.05.007

Liao, G., Li, Q., and Sun, X. (2021). "The chaos of the prediction for tailings pond dam break disasters," in *2021 7th international conference on hydraulic and civil engineering & smart water conservancy and intelligent disaster reduction forum (ICHCE & SWIDR).* (IEEE), 929–937. doi:10.1109/ICHCESWIDR54323.2021.9656433

Ministry of Emergency Management of the People's Republic of China (2020). *State administration for market regulation, People's Republic of China*. Beijing: Safety regulation for tailings pond.

Ministry of Housing and Urban-Rural Development (2013). "PRC; general administration of quality supervision, inspection and quarantine, PRC," in *Code for design of tailings facilities(GB-50863 2013)* (Beijing.

Order of the State Administration of Work Safety (2011). *Regulations on safety supervision and administration of tailings pond.* Beijing.

Rico, M., Benito, G., Salgueiro, A. R., Díez-Herrero, A., and Pereira, H. (2008). Reported tailings dam failures: A review of the European incidents in the worldwide context. *J. Hazard. Mater.* 152, 846–852. doi:10.1016/j.jhazmat.2007.07.050

Saliba, A. P. M., Mafra, J. M. Q., and Luís, F. (2011). "On the effect of climate change on water balances of tailings reservoirs," in *Pan-Am CGsGeotechnical Conference.October 2-6, 2011* (Toronto, Ontario, Canada: ASCE). Available at: http://geoserver.ing.puc.cl/info/conferences/PanAm2011/panam2011/pdfs/GEO11Paper273.pdf.

Sammarco, O., Ovi, M., and Costabile, M. (2003). "Forecast of emergency situations owing to excessive water inflows into tailings ponds," in *Proc. 8th IMWA congress* (Johannesburg: Mine Water and the Environment), 109–127. Available at: http://mwen.info/docs/imwa_2003/imwa_2003_109-127.pdf.

Wu, P., Liang, B., Jin, J., Zhou, K., Guo, B., and Yang, Z. (2022). Solution and stability analysis of sliding surface of tailings pond under rainstorm. *Sustainability* 14, 3081. doi:10.3390/su14053081

Yang, J., Qu, J., Mi, Q., and Li, Q. (2020). A CNN-LSTM model for tailings dam risk prediction. *IEEE Access* 8, 206491–206502. doi:10.1109/ACCESS.2020.3037935

Zanbak, C. (2019). Compiled information and opinions on Córrego do Feijão Mine "Dam I" failure in Brazil. Available at: https://www.researchgate.net/publication/331089028. 2(18732.92806). doi:10.13140/RG

frontiers | Frontiers in Earth Science

TYPE Original Research
PUBLISHED 09 May 2023
DOI 10.3389/feart.2023.1181984



OPEN ACCESS

EDITED BY
Lijie Guo,
Beijing Mining and Metallurgy Technology Group Co., Ltd., China

REVIEWED BY
Lin Chi,
University of Shanghai for Science and Technology, China
Shuhua Liu,
Wuhan University, China

*CORRESPONDENCE
Yongxiang Zhou,
zhouyx@bjut.edu.cn

RECEIVED 08 March 2023
ACCEPTED 06 April 2023
PUBLISHED 09 May 2023

CITATION
Wang C, Jing J, Qi Y, Zhou Y, Zhang K, Zheng Y, Zhai Y and Liu F (2023), Basic characteristics and environmental impact of iron ore tailings.
*Front. Earth Sci.* 11:1181984.
doi: 10.3389/feart.2023.1181984



# Basic characteristics and environmental impact of iron ore tailings

Changlong Wang[1], Jianlin Jing[1], Yang Qi[1], Yongxiang Zhou[2]*, Kaifan Zhang[1], Yongchao Zheng[3], Yuxin Zhai[4] and Feng Liu[5]

[1]Collaborative Innovation Center for Intelligent Regulation and Integrated Management of Water Resources Jointly Built by Provinces and Ministries, School of Civil Engineering, Hebei University of Engineering, Handan, China, [2]Faculty of Architecture, Civil and Transportation Engineering, Beijing University of Technology, Beijing, China, [3]State Key Laboratory of Solid Waste Reuse for Building Materials, Beijing Building Materials Academy of Science Research, Beijing, China, [4]Technical Center, China Railway Construction Group Co., Ltd., Beijing, China, [5]Construction Development Co., Ltd., China Railway Construction Group, Baoding, China

**Introduction:** In our study, various test methods were adopted to explore the mineralogical characteristics, grindability, particle morphology, particle size distribution, and environmental leaching toxicity of iron ore tailings (IOTs).

**Methods:** The methods include petrographic analysis, X-ray diffraction (XRD), scanning electronic microscopy (SEM), synchronous thermal analyzer (DSC-TGA), electron probe X-ray microanalyser (EPMA), and synthetic precipitation leaching Procedure (SPLP).

**Results:** The results show that the used IOTs contained 14.54% iron which was mainly stored in magnetite and pyrite. The content of iron silicate accounted for 11.82% of the total iron content. Most of it existed in silicate minerals, including grunerite and hornblende. A small amount of iron was contained in biotite, chlorite and augite. Besides, the grindability of IOTs was much better than that of granulated blast furnace slag (GBFS). After grinding for 140 min, the mass fraction of IOTs particles with the particle size less than 5 um was 44.19%. These particles could be used to fill in the voids in the cement-powder-packed structure. IOTs also contained a large number of submicron and nanoscale particles.

**Discussion:** With great strength and environmental friendliness, the composite cementitious material (CCM) prepared from IOTs can be well applied to the building material field and environmental remediation.

KEYWORDS

**iron ore tailings (IOTs), mineralogical characteristics, grindability, Particle size distribution, particle morphology, composite cementitious material (CCM)**

## 1 Introduction

Peak carbon dioxide emissions and carbon neutrality are the main development goals of all countries in the world (Nielsen et al., 2019; Yan et al., 2020). Cement manufacture, as one of the traditional industries with heavy energy consumption and emission, generates 5%–8% of the global $CO_2$ emissions per year (Turner and Collins, 2013; Mo et al., 2017). To save resources and reduce the emission of $CO_2$, various industrious solid wastes have been adopted to replace cement as the supplementary cementitious material, including granulated

**TABLE 1 Particle size distribution of IOTs.**

| Sieve size/mm | +1.0 | 0.45–1.0 | 0.30–0.45 | 0.15–0.30 | 0.074–0.15 | 0.043–0.074 | −0.043 |
|---|---|---|---|---|---|---|---|
| Meter sieve/% | 5.61 | 22.21 | 13.10 | 28.69 | 20.60 | 5.62 | 4.17 |
| Cumulative sieve/% | 5.61 | 27.82 | 40.92 | 69.61 | 90.21 | 95.83 | 100 |

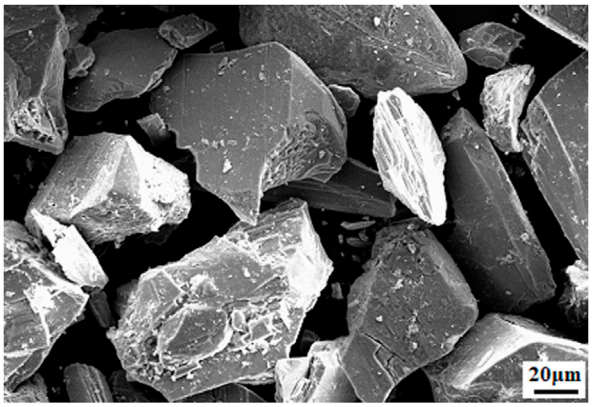


FIGURE 1
SEM image of IOTs.

blast furnace slag (GBFS) (Zhao et al., 2015), fly ash (FA) (Gunasekara et al., 2020), and silica fume (Campos Teixeira et al., 2020). Some researchers have founded that (Soliman and Nehdi, 2013; Ghafari et al., 2016; Meng and Khayat, 2018), adding appropriate amount of cementitious material can not only reduce the consumption of cement, but also improve the workability, mechanical properties, volume stability and durability of the concrete. With the wide application of the supplementary cementitious material (SCM) in the concrete industry, a large number of industrial by-products are rapidly consumed. To ensure the sustainable development of this industry, it is necessary to find SCM which are more accessible and more economical.

Iron ore tailings (IOTs) are the industrious solid waste discharged by concentrating mills after processing iron ores and selecting "valuable components" (Yao et al., 2020). In China, 600 million tons of IOTs are discharged every year and the IOTs deposition has reached 5 billion tons. However, the utilization efficiency across China is generally low, only 7% (Chen et al., 2021). In this case, large-scale harmless utilization of IOTs has attracted much attention. Currently, IOTs are mainly used for IOTs recleaning (Wang et al., 2018; Yuan et al., 2020; Yuan et al., 2020; Zhai et al., 2020) and mine filling (Onitiri and Akinlabi, 2017; Qiu et al., 2017; Coura et al., 2021), or used as the building material (Menders et al., 2019; Li et al., 2020; Zhang et al., 2022) and soil conditioner (Santana et al., 2020; Castro e Silva et al., 2021; Cui et al., 2021). IOTs are rich in $SiO_2$ and $Al_2O_3$ whose chemical composition is similar to that of cement (Han et al., 2017) and the physical properties are similar to those of natural sands (Huang et al., 2013). If IOTs can be adopted to prepare composite cementitious material (CCM), it will increase the utilization of IOTs, reduce its deposition, and lower the production cost, thus ensuring the sustainable development of the concrete industry. IOTs can be used as the mineral admixture or alkali-activated cementitious material, and some can also replace ordinary Portland cement (OPC) (Zhao et al., 2014). Li et al. (2010) prepared CCM containing 30% clinker, 34% GBFS, 30% IOTs and 6% gypsum, whose mechanical properties are equivalent to OPC. Cheng et al. (2016) found that IOTs after mechanical activation had pozzolanic activity and could be used as SCM for concrete. Ling et al. (2021) used IOTs as the CCM to prepare environment friendly ultra-high performance concrete (UHPC), which facilitated the development of long-term compressive strength and the improvement of pore structure, thus ensuring the durability of UHPC. Cheng et al. (2020) prepared concrete with strong permeability resistance and good freeze-thaw resistance by replacing part of OPC with IOTs after mechanical grinding. The technology of preparing high-strength structural materials with IOTs has been studied in recent years. It aims to produce high value-added products from very fine-grained tailings. Zheng et al. (2010) reported that IOTs can be used to prepare high-strength structural materials with IOTs content of 70% and compressive strength of more than 100 MPa. For the high-strength structural material prepared with IOTs, superfine grinding technology was further required to process some ground IOTs, so as to generate some submicron and nanoscale IOTs particles. This process gives full play to the IOTs' filling effect, bonding effect, and nanometer effect during the preparation of building materials. However, there are not many research results at home and abroad. In this case, fully utilizing the refinement effect of ground IOTs is of great importance to systematically study the physical and chemical characteristics and grindability of IOTs. Lawrence et al. (2003) found that inert quartz powder could facilitate the early hydration of OPC, because it could promote the process of heterogenous nucleation, and the finer the quartz powder, the more it attributed to heterogenous nucleation. Therefore, it is concluded that the incorporation of small amounts of low-activity ultrafine admixtures into UHPC has the potential to be an important means of improving concrete properties. Besides, for non-lime aerated concrete and foam cement products, it is also necessary to ultra-finely grind some siliceous raw materials to improve the pore structure of the products. Therefore, systematically exploring the physical and chemical characteristics, grindability and basic characteristics of very fine-grained IOTs after grinding is the basis for the overall utilization of such IOTs in the field of building materials.

To solve the above problems, X-ray diffraction (XRD), scanning electronic microscopy (SEM), synchronous thermal analyzer (DSC-TGA), and electron probe X-ray microanalyser (EPMA) were adopted to explore the mineralogical characteristics of IOTs, including the size composition, chemical composition, chemical phase composition, mineralogical phase composition, and microstructure. On this basis, SEM and particle size analysis were used to study the particle morphology and particle size distribution

**TABLE 2 Chemical phase composition of IOTs (mass fraction, %).**

| Classification | Magnetite | Pyrrhotite | Carbonate iron | Sulfide iron | Hematite and limonite | Silicate iron | Total |
|---|---|---|---|---|---|---|---|
| Iron content | 1.08 | 0.36 | 0.49 | 0.39 | 0.40 | 11.82 | 14.54 |
| Iron distribution rate | 7.43 | 2.48 | 3.37 | 2.68 | 2.75 | 81.29 | 100 |

**TABLE 3 Radioactive test results of IOTs (mass fraction, %).**

| Sample | Specific activity of radionuclides ($Bq \cdot kg^{-1}$) | | | Internal exposure index | External exposure index | Test results |
|---|---|---|---|---|---|---|
| IOTs | $^{226}Ra$ | $^{232}Th$ | $^{40}K$ | 0.0 | 0.1 | Qualified |
| | 5.1 | 6.3 | 113.2 | | | |

Note: Internal exposure index =CRa/370 + CTh/260 + CK/4,200, external exposure index = CRa/200; uncertainty of measurement results (1σ) ≤20%.

**TABLE 4 PDF card number and peak value corresponding to IOTs XRD pattern in Figure 3.**

| Mineral phase | PDF card number | 2Theta |
|---|---|---|
| Quartz | 46–1,045 | 20.7°, 26.6°, 40.2°, 59.8°, 68.3° |
| Plagioclase | 09–0456 | 27.9°, 29.8°, 33.9°, 50.1°, 53.2° |
| Chlorite | 29–0854 | 5.8°, 12.4°, 18.6°, 25.1°, 36.5°, 44.9°, 47.4°, 54.8° |
| Hornblende | 23–1,046 | 28.5°, 29.1°, 38.4°, 45.7° |
| Calcite | 72–1937 | 22.8°, 35.7°, 39.4°, 77.6°, 81.4°, 83.8° |
| Grunerite | 17–1,622 | 9.7°, 32.3°, 55.3°, 66.6°, 67.7°, 75.6°, 79.8° |
| Biotite | 80–1,106 | 19.5°, 21.9°, 27.2°, 34.6°, 42.3°, 61.4° |
| Augite | 23–1,046 | 30.3°, 41.7°, 56.2°, 64.6°, 73.4° |
| Magnetite | 88–0315 | 21.2°, 31.7°, 32.9°, 48.3° |
| Pyrite | 29–0724 | 27.9°, 29.7°, 33.8°, 50.1°, 53.1° |

characteristics of IOTs. Besides, specific surface area (SSA) was chosen as the evaluation index to compare the grindability of IOTs and GBFS. Finally, we adopted synthetic precipitation leaching procedure (SPLP) to test the leaching behavior of heavy metals in solidified body, so as to provide technical support for the utilization of IOTs.

# 2 Test materials and methods

## 2.1 Test materials

The IOTs used for our study was provided by Haoyang Mine Co., Ltd., in Ling Qiu county in Shanxi Province. The GBFS was offered by Qian'an Steel Co., Ltd., with the particle size of 0.30–2.5 mm and the grain size rate reaching 92.0%. For the 42.5 OPC, the initial setting time is 118 min and the final setting time 190 min, which meets the requirements of Chinese National Standard GB 175-2007 *Common Portland Cement*. Phosphogypsum (PG) is a kind of gray powder whose particle size is between 5 μm and 150 μm, density is 2.56 $g \cdot cm^{-3}$, and the SSA is 640 $m^2 \cdot kg^{-1}$. The main mineral components are $CaSO_4 \cdot 2H_2O$ and $CaSO_4 \cdot 1/2H_2O$.

## 2.2 Test methods

### 2.2.1 Sampling method of raw materials

IOTs were taken from the middle of the IOTs pond by cutting the vertical section of the pit walls. The cutting depth was 1.2 m and the total weight of the samples was 640 kg. After mixed thoroughly, the samples were divided into 8 parts by the method of coning and quartering, and then sent back to the laboratory. Before the test, each pile of 80 kg IOTs was further divided into piles of 5 kg by the method of coning and quartering as the test samples.

### 2.2.2 Test of grinding characteristics

Firstly, IOTs and GBFS were dried in oven (CS101-3E) at 105°C for 24 h to make moisture content less than 1 wt%, and then ground with the SMΦ500 mm × 500 mm 5 kg small ball grinder ($W \cdot L^{-1}$) at the speed of 48 r $min^{-1}$. The grinding media consisted of several steel balls and a steel forging. The loading mass of the grinding media should be 100 kg. The steel balls added up to 40 kg, in which the Φ70 mm balls took up 19.7%, the Φ60 mm balls 33.1%, the Φ50 mm balls 29.6%, and Φ40 mm balls 17.6%. The Φ25 mm × 30 mm steel forging weighed 40 kg. The grinding periods were chosen at 20 min, 40 min, 60 min, 80 min, 100 min, 120 min and 140 min in order to obtain different SSA.

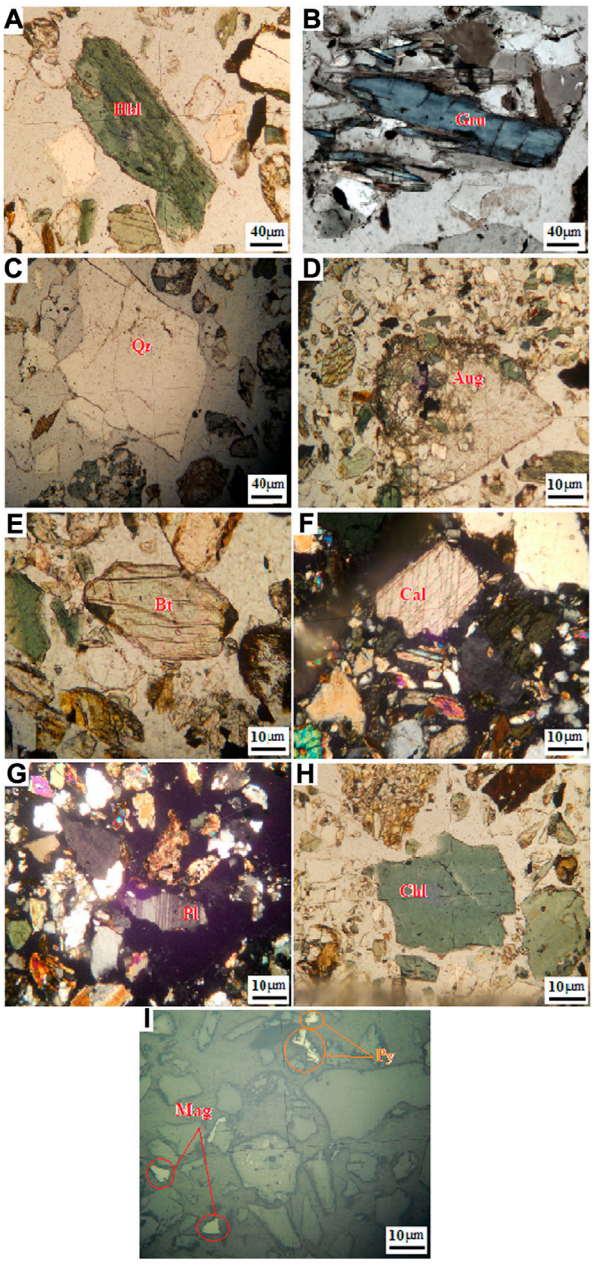


FIGURE 2
The microstructure of IOTs. **(A)** Hbl-hornblende (single polarizing light); **(B)** Gru-grunerite (orthogonal slice light); **(C)** Qz-quartz (single polarizing light); **(D)** Aug-augite (single polarizing light); **(E)** Bt-biotite (single polarizing light); **(F)** Cal-calcite (orthogonal slice light); **(G)** Pl-plagioclase (orthogonal slice light); **(H)** Chl-chlorite (single polarizing light); **(I)** Mag-magnetite (reflected light) and Py-pyrite (reflected light).

## 2.3 Property characterizations

According to Chinese National Standard GB/T 19,077-2016 *Particle size analysis - Laser diffraction methods*, the particle size distribution of ground IOTs were analyzed through MASTER SIZER 2000 (a laser particle size analyzer with the analysis range of 0.02 μm–2,000.00 μm) with ethanol as the dispersant. The SSA of IOTs was measured by SSA-3200 (a dynamic specific surface area analyzer). The XRD pattern was obtained by a D/Max-RC diffractometer (Japan) with Cu-K$\alpha$ radiation, voltage of 40 kV, current of 150 mA and 2 $\theta$ scanning ranging between 10° and 90°. And the wavelength was 1.5406 nm. SEM observation was performed to analyse the mineral phase and the hydration products of the paste samples using a Zeiss SUPRA™55 scanning electron microscope coupled with a Be4-U92 energy spectrum. Leica DM4 P polarizing microscope was adopted for the petrographic analysis of IOTs. Netzsch STA 409 was used to heat the solidified powder from 25°C to 1,000°C at the heating rate of 10°C·min$^{-1}$ under $N_2$, so as to explore the thermal decomposition rule of IOTs. IOTs were scanned with the JXA-8100 Electron probe microanalyzer (EPMA) to analyze the surface elements and their contents. SPLP was conducted to test the leaching behavior of heavy metals in solidified body, thus confirming the environmental safety. During SPLP, the leach liquor was prepared by adding 60%/40% (mass fraction) of sulfuric acid/nitric acid and diluting appropriately with deionized water, in order to adjust the pH to 4.20 ± 0.05 (Li and Chi, 2017) The leach liquor and solidified powder (0.075 mm) were mixed according to the ratio of 20:1, and shaken for 18 h in a gyrate shaker. Then, the screened mixture (0.45 μm) was put into Prodigy 7 Inductively coupled plasma emission spectrometer (ICP-OES) to analyze the concentration of Cr, Ni, Cu, Cd, Pb, Zn, As, and Hg (Zhu et al., 2017).

# 3 Results and discussion

## 3.1 Mineralogical properties of IOTs

### 3.1.1 Physicochemical properties of IOTs

The square hole screens with the screen size of 1.0 mm, 0.45 mm, 0.30 mm, 0.074 mm and 0.043 mm were used for the screen analysis of IOTs. The analysis results are displayed in Table 1. It can be seen that IOTs have large particle size, mainly between 0.074 mm and 1.0 mm. The grain size rate reaches 84.60%. Figure 1 shows that most of the IOTs are the particles with the size of tens of microns to hundreds of microns, and they are irregular or angular particles. As for the chemical composition of IOTs, inorganic components are the main content. The $Fe_2O_3$+FeO content is 19.59% and total Fe (TFe) content reaches 14.54%, which exceeds the minimum grade of some iron ores mined in China. In the tailings, the content of $SiO_2$ is 54.41%, $Al_2O_3$ 7.99%, CaO+MgO 12.41%, and $Na_2O$+$K_2O$ 1.81%. For the harmful elements, S content is as high as 0.104% while P content is relatively low (0.052%). The contents of other harmful elements are small, too. Among the components of IOTs, the ratio of basic oxides to acid oxides is (CaO+MgO)/($SiO_2$+$Al_2O_3$) = 0.199 < 0.5, indicating that IOTs are acid tailings. To determine the occurrence state of iron in the samples, iron chemical phase analysis was conducted. The results are shown in Table 2. We can see that the iron in IOTs is mainly in the form of silicate iron and the distribution rate of iron is 81.29%. Then come the magnetite and carbonate with the iron distribution rate of 7.43% and 3.37%, respectively. In this case, the IOTs used for our study are the tailings with high silicate iron. The radioactivity index of the IOTs meets the requirement of Chinese National Standard GB/T 6566-2010 *Limits of radionuclides in building materials* (See Table 3).

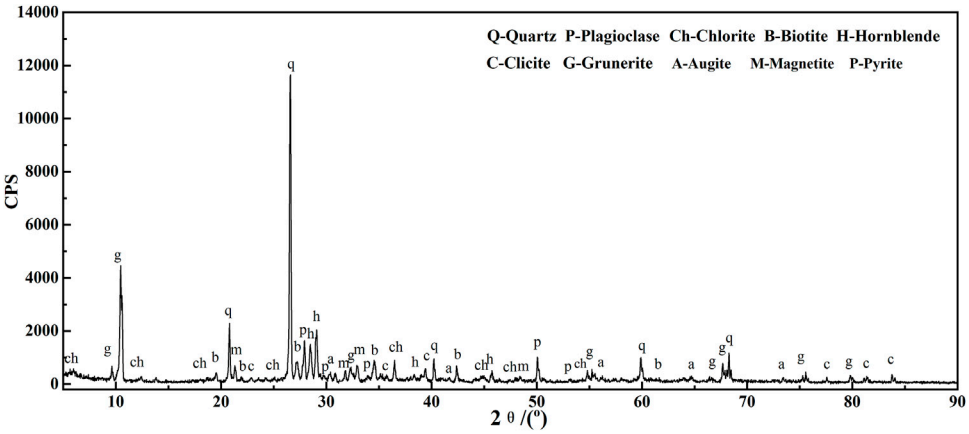


FIGURE 3
XRD pattern of IOTs.

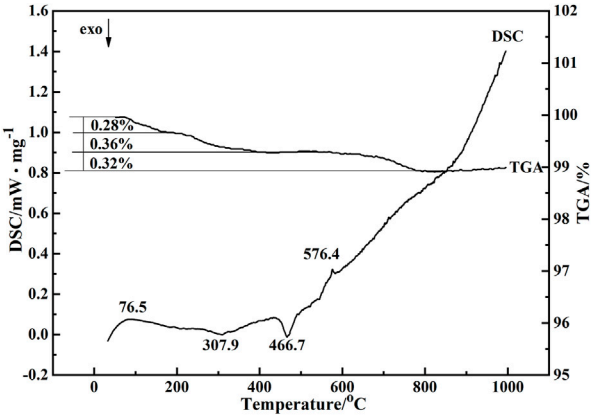


FIGURE 4
DSC-TGA curve of IOTs.

## 3.1.2 Structure and composition of IOTs

### 3.1.2.1 Petrographic analysis

To determine the material composition, structure, mineral composition, particle size, embedded features, and symbiotic relationship of IOTs, a polarizing microscope was used to observe the optical property differences of different minerals, thus identifying the minerals. The observed results are shown in Figure 2. From Figure 2, we can see that the metallic minerals identified in IOTs include pyrite and magnetite. There are 8 kinds of gangue minerals (high content: quartz, hornblende, grunerite, and plagioclase; low content: biotite, chlorite, calcite, and augite). Here are the characteristics:

Hornblende. With strong pleochroism and absorbency, it is one of the main rock-forming minerals in igneous rocks and metamorphic rocks. The color is dark green (Figure 2A).

Grunerite. It is a dark greenish-brown and columnar mineral with complete cleavage. It can turn into limonite and mainly exists in transmutative iron-bearing rock series (Figure 2B).

Quartz. It is one of the main rock-forming minerals. With the granular structure, it belongs to the stable mineral and is resistant to weathering (Figure 2C).

Augite. It is black green. See the two sets of pyroxene-type cleavage joints which are nearly orthorhombic in Figure 2D.

Biotite. It is in the form of pseudohexagonal plate and fully cleavaged. It is brown with a slightly greenish tinge. There are opaque darkening edges around its phenocryst (Figure 2E).

Calcite. It has rhombic cleavage and paralleled twin striations. As the main mineral in calcareous rocks, it is widely distributed in sedimentary and metamorphic rocks (Figure 2F).

Plagioclase. With polysynthetic twin and complete cleavage, it is a tabular or columnar crystal (Figure 2G).

Chlorite. It has a layered structure with different shades of green. The color is getting darker with the increasing iron content (Figure 2H).

Magnetite and pyrite. With the cataclastic structure, they exist in the form of microgranular particles with the size of 3–4 μm (Figure 2I). They are filled with gangue minerals and are extremely refractory. Pyrite is pale yellow and it is a ubiquitous mineral that can occur in a variety of deposits. Magnetite is a brownish-gray mineral with no pleochroism.

### 3.1.2.2 XRD analysis

To determine the phase composition of IOTs, XRD was adopted to analyze the samples. The results are shown in Figure 3.

According to the XRD results in Figure 3, the main mineral components of IOTs are quartz, plagioclase, chlorite, biotite, hornblende, grunerite, augite, calcite, magnetite, and pyrite. The corresponding PDF card number and peak value are listed in Table 4. Based on the material balance principle (Huang et al., 2019; Ren et al., 2021; Yu et al., 2021), we used the linear programming program LINPRO (Faghihi et al., 2019; Bam et al., 2020) to calculate the content of each mineral phase: quartz (40%), hornblende (21%), grunerite (21%), plagioclase (9%), and others (9%). In hornblende ($Al_{3.2}Ca_{3.4}Fe_{4.02}K_{0.6}Mg_6NaSi_{12.8}O_{44}(OH)_4$), the iron content is 12.73%, while the iron content is 39.03% in grunerite ($Fe_7Si_8O_{22}(OH)_2$). Thus,

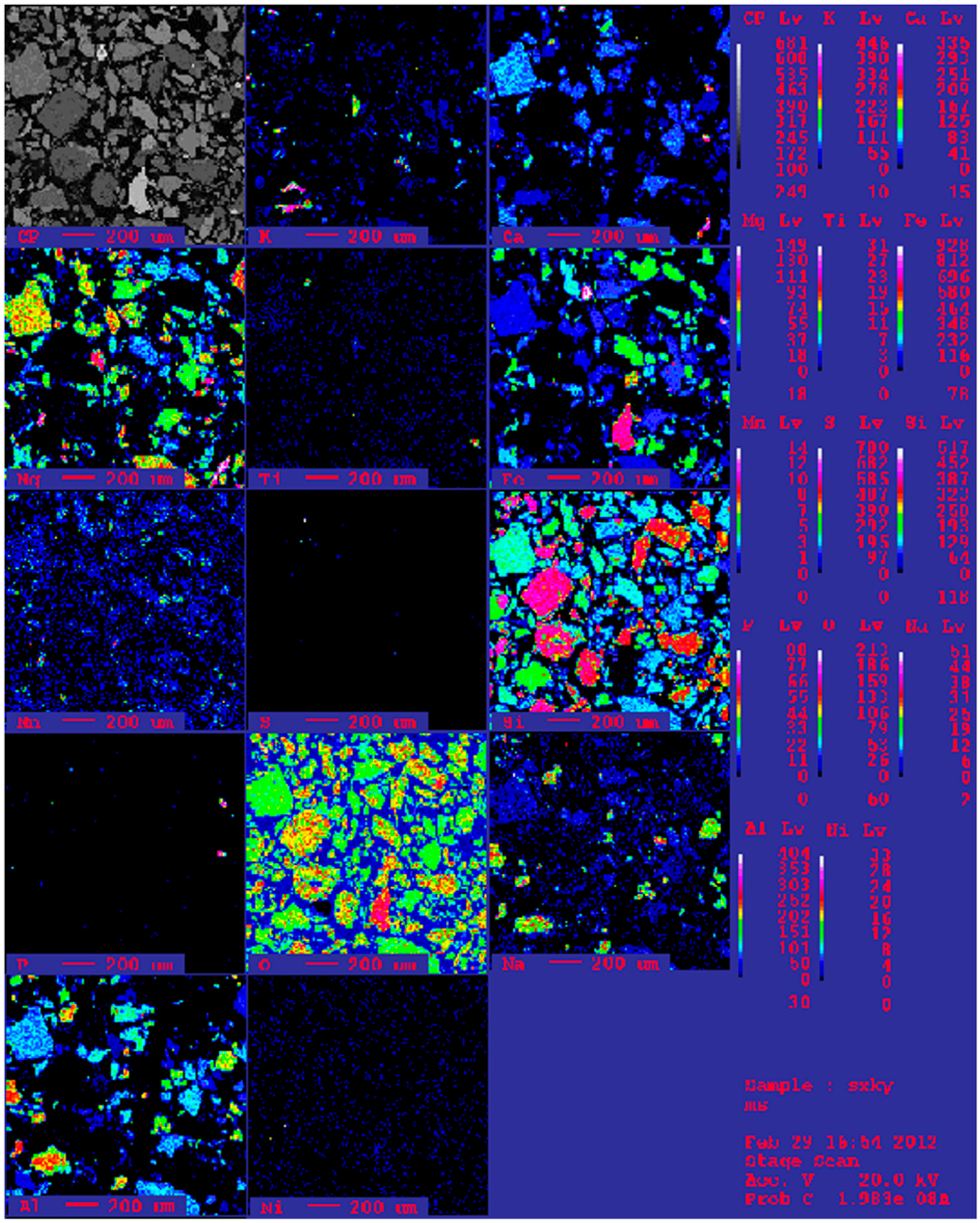


FIGURE 5
EPMA images of IOTs.

the total iron content of amphibole accounts for 10.87% of the IOTs. According to the chemical phase analysize results in Table 2, the content of silicate iron in IOTs is 11.82%, which indicates that most of the iron of IOTs exists in silicate mineral amphibole. Only a small amount of iron is contained in biotite, chlorite, and augite.

### 3.1.2.3 DSC-TGA analysis

Figure 4 is the DSC-TGA curve of IOTs. It can be seen that with the increase of temperature, the TGA curve shows a decline trend. It means that continuous weight loss occurs during the heating process of IOTs, with a wide temperature range from 52°C (initial weight loss temperature) to 780°C (final weight loss temperature) and above. In the TGA curve, there are three obvious weight loss phases during the heating of IOTs.

In the first phase, the temperature range is 52°C–175°C and the weight loss rate is 0.28%. This phase mainly corresponds to the removal of the physically absorbed water in IOTs. Since the IOTs used for the analysis have been dried at 100°C, a large amount of water in IOTs has been removed. The endothermic peak of 76.5°C in this temperature range represents the removal of the remaining

**TABLE 5 Quantitative analysis results of chemical elements detected by EPMA.**

| Chemical element | Mass ratio (%) | Atomic ratio (%) |
|---|---|---|
| Si | 16.622 | 37.075 |
| Ca | 4.523 | 7.851 |
| K | 0.243 | 0.365 |
| Na | 0.921 | 2.558 |
| Ni | 0 | 0 |
| S | 0.239 | 0.341 |
| Mg | 4.256 | 16.36 |
| Ti | 0.099 | 0.121 |
| Fe | 8.937 | 16.112 |
| Al | 5.559 | 9.52 |
| Mn | 0.206 | 0.22 |
| P | 0.031 | 0.054 |
| O | 3.11 | 9.423 |
| Total | 44.746 | 100 |

physically adsorbed water. In the second phase, the temperature range is 175°C–400°C and the weight loss rate is 0.36%. A wide and flat exothermic peak appears at 307.9°C, mainly referring to the exothermic process of magnetite and pyrite at around 350°C. During this process, part of magnetite is oxidized to hematite and pyrite is oxidized to magnetite. In the third phase, the temperature range is 400°C–780°C and the weight loss rate is 0.32%. A sharp exothermic peak appears at 466.7°C while an endothermic peak occurs at 576.4°C. The exothermic peak mainly corresponds to the exothermic process where part of magnetite in IOTs is oxidized to hematite at the temperature between 400°C and 500°C. The endothermic peak refers to the endothermic process at the curie point temperature of magnetite (around 560°C) and the endothermic process where α-quartz in IOTs is transformed into β-quartz. The DSC-TGA analysis of the dried IOTs is basically similar to the iron phase analysis of IOTs.

#### 3.1.2.4 EPMA analysis

Figure 5 shows the EPMA analysis results, including the distribution of K, Ca, Na, Mg, Ti, Fe, Al, Mn, S, Ni, P, and O. The element names are shown below each image. The scanning result of each element is represented with a colored tape, and the color density increases from bottom to top. In Figure 5, CP means the secondary electronic image.

Figure 5 shows that there is no Ni in the scanned area. The content of K is low, and most of it exists around the particles in the lower left corner of the scanned area. In the scanned area, the Ca content is also low while the Na content is relatively high which is scattered in IOTs particles. The reason is that there are plagioclase-type minerals in IOTs (Figure 2G). Mg is concentrated near the middle of the scanned area. The content of Ti is not high. Fe is concentrated in two brighter regions in the CP secondary image, where the O content of larger particles is higher, indicating that they may be magnetite particles (Figure 2I). Al is distributed dispersively. However, the Al content is relatively higher in the particles containing Al and K. Mn and Ni are present in trace amounts in the scanned area, and the content of Mn is slightly higher than that of Ni. The Si content is high, and the color intensity is higher in the scanning area (red and pink). Considering the distribution of O, we can find that the scanned area has a high content of quartz (Figure 2C). The two harmful elements, P and S, are distributed sporadically in the scanned area and their contents are low. The quantitative analysis results of the elements in Table 5 also confirm the EPMA analysis results, which are similar to the analysis results in Table 6.

## 3.2 Grinding characteristics of IOTs

### 3.2.1 Grindability

The grinding energy consumption of GBFS is a well-known parameter in the field of building material. The energy consumption required for the one-time treatment of GBFS powder with the SSA of 400 $m^2\ kg^{-1}$ or more is about 80 kW $h{\cdot}t^{-1}$ for a large industrial ball mill. However, that for the advanced vertical mill is 50–60 kW $h{\cdot}t^{-1}$. Therefore, in our test, the grindability of GBFS was used as a reference to study the grindability of IOTs. The IOTs and GBFS were ground in different batches by the SMΦ500 mm × 500 mm experimental ball mill, and we compared the difference in the SSA of their powder after grinding for the same time. Figure 6 shows the SSA of IOTs and GBFS at different grinding time.

It can be seen that the grindability of IOTs is much better than that of GBFS. Specifically, after grinding for 70 min, the SSA of GBFS is 400 $m^2\ kg^{-1}$ while that of IOTs is 756 $m^2\ kg^{-1}$. After grinding for 120 min, the SSA of GBFS is 515 $m^2\ kg^{-1}$ while that of IOTs powder is 1,041 $m^2\ kg^{-1}$. Besides, the SSA increase rate of IOTs is greater than that of GBFS. In other words, with the extension of grinding time, the SSA increment of IOTs is greater than that of GBFS. This is represented by the increasing slope of the curve of IOTs powder in Figure 6. It further confirms that IOTs have better grindability compared to GBFS.

Figure 7 shows the SEM images of IOTs and GBFS after grinding for 120 min. It can be directly seen that the fineness of IOTs at the same grinding time (Figure 7A) is much smaller than that of GBFS (Figure 7B). The SSA of IOTs after grinding for 120 min and 140 min are 1,041 $m^2\ kg^{-1}$ and 1,059 $m^2\ kg^{-1}$, respectively. Then, the SSA of IOTs remains relatively stable with the increase of grinding time. So it is of little significance to extend the grinding

**TABLE 6 Chemical composition of IOTs (mass fraction, %).**

| Composition | $SiO_2$ | $Al_2O_3$ | $Fe_2O_3$ | FeO | MgO | CaO | $Na_2O$ | $K_2O$ | $SO_3$ | $P_2O_5$ | LOI |
|---|---|---|---|---|---|---|---|---|---|---|---|
| Content | 54.41 | 7.99 | 8.94 | 10.65 | 5.85 | 6.56 | 1.18 | 0.63 | 0.26 | 0.12 | 3.41 |

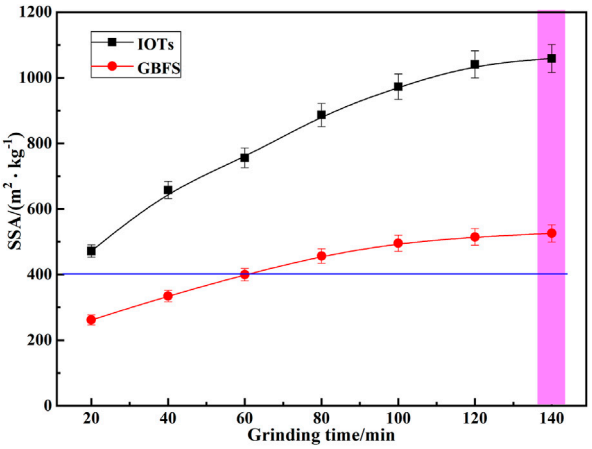


FIGURE 6
SSA of IOTs and GBFS at different grinding time.

time to improve the fineness of the powder after grinding for 140 min.

### 3.2.2 Particle size distribution of IOTs

A laser particle size analyzer (LPSA) was used to analyze the particle size distribution of IOTs at different grinding time. The results are shown in Table 7; Figure 8. It can be seen that with the extension of grinding time, the particle size distribution range of IOTs narrows and gradually concentrates towards the small particle size value. When the grinding time increases from 20 min to 140 min, $D_{50}$ (median diameter) of IOTs powder decreased from 12.51 μm to 3.31 μm, and $D_{90}$ decreased from 40.61 μm to 17.16 μm $D_{90}$ represents the particle size when the cumulative particle size distribution percentage reaches 90%. At the early stage of grinding, the particle size distribution of IOTs powder changed greatly. After grinding for 120 min, $D_{50}$ and $D_{90}$ only changed slightly with the increase of time, corresponding to the change of SSA.

In the concrete industry, mineral admixtures are an important component to improve the performance of concrete. Especially, they have better physical and chemical filling effects on cement-based materials (Jindal, 2019; Sharma et al., 2022). The physical filling effect of mineral admixtures can effectively improve the compactness and fluidity of the fresh cement slurry, and reduce the porosity of the hardened slurry, thus improving its mechanical properties (Jiang et al., 2020; Ji et al., 2021). To give the full play of the physical filling effect, the mineral admixtures must have a suitable particle size and reasonable particle size distribution. Therefore, the core problem is to use the close packing principle of particles to obtain a dense filling structure of cement-based materials (Sun and Zhang, 2021; Wang et al., 2021). Chen et al. (2004) found that there are a large number of voids less than 5 μm in the cement powder packed structure, and adding into the powder with the particle size less than 5 μm could fill the voids among the cement particles, thus obtaining a closely packed structure. Figure 8 shows that, the particles with the size of less than 5 μm account for around 46.37% in the IOTs ground for 100 min, while those account for 51.75% in the IOTs ground for 140 min. With a great number of particles whose size is less than 5 μm, ground IOTs can be used to fill the voids in the cement powder packed structure, so as to make the structure more closed. The closely packed structure can reduce the water-cement ratio of the initial slurry, and significantly improve the mechanical properties and durability of the final cement-based materials (Lange et al., 1997; Peng et al., 2009). The reactive powder concrete with high strength and durability is also produced based on this principle (Richard and Cheyrezy, 1995). It can be expected that adding such inert particles can reduce water to a certain extent. The research team's previous research on using IOTs as mineral admixtures has shown that due to IOTs (Zhao et al., 2016; Wu et al., 2018). Most of the powder particles themselves exist in the form of polygonal irregular shapes. Compared to GBFS, the "interlocking function" between particles is stronger when they exist inside the mortar specimen. Under the standard curing conditions of high water binder ratio (0.48) and low water binder ratio (0.34) for 180 days, the main role of IOTs in the mortar blocks is the physical filling effect, regardless of the initial or late hydration period. No secondary hydration reaction of IOTs as mineral admixtures has been found. However, for the cementitious material products accepting high temperature steam or autoclave curing and mixed with ground IOTs, a large amount of crystalline silica in the IOTs can participate in the hydration reaction at a high temperature. In

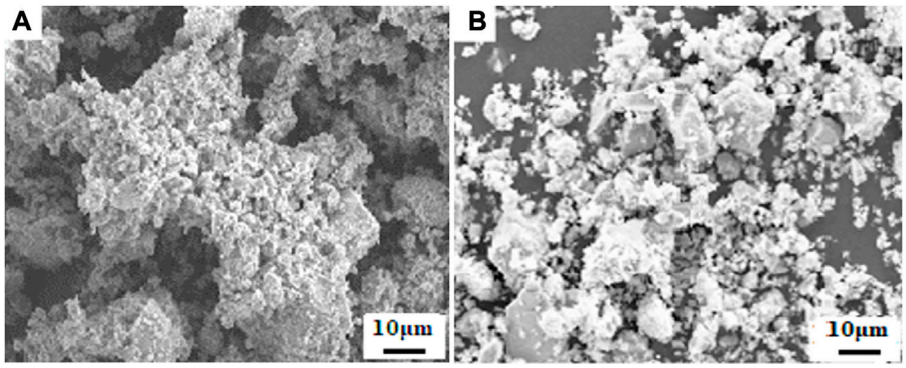


FIGURE 7
SEM images of IOTs and GBFS after grinding for 120 min **(A)** IOTs; **(B)** GBFS.

**TABLE 7 Characteristic particle size of IOTs at different grinding time.**

| Grinding time/min | $D_{50}$/μm | $D_{90}$/μm |
|---|---|---|
| 20 | 12.51 | 40.61 |
| 60 | 8.94 | 27.27 |
| 80 | 7.66 | 23.85 |
| 100 | 4.41 | 20.92 |
| 120 | 3.53 | 17.68 |
| 140 | 3.31 | 17.16 |

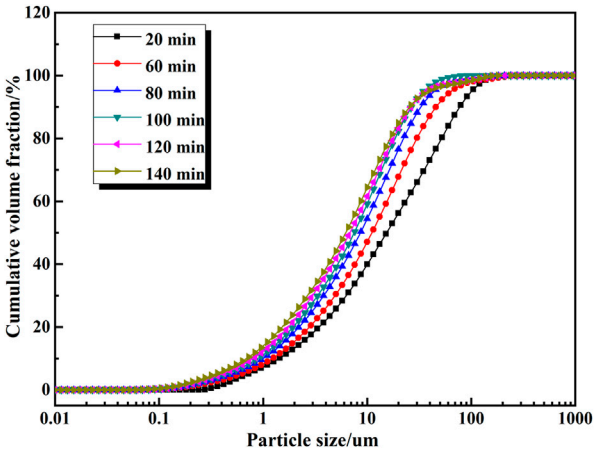


FIGURE 8
Cumulative distribution curves of IOTs at different grinding time.

this situation, the ground IOTs can not only realize physical filling, but also further exert its chemical filling effect. Meanwhile, Figure 6 shows that to obtain the GBFS with the SSA of 400–500 $m^2\ kg^{-1}$ which is more widely used in the field of building material, the GBFS needs to be ground by an experimental ball mill for 90–120 min. However, at least 100 min is required to obtain the IOTs, 40% of whose particles have a size of less than 5 μm. It can be preliminarily predicted that when a large industrial mill is used, the energy consumption for grinding IOTs is close to that for grinding commonly used GBFS. This indicates that, in terms of technology requirement and energy consumption, it is feasible to apply the ground IOTs with a large number of ultrafine particles to the field of concrete.

Figure 9 shows microstructure and particle size distribution of IOTs at different grinding time. In Figure 9A, most of the coarse particles in IOTs ground for 20 min have irregular shapes. The size of some IOTs particles rapidly decreases to less than 5 μm after grinding, while some large particles are about 15 μm in size and they are mainly flaky and irregular polygonal blocks with sharp edges and corners. Figure 9B shows that after grinding for 60 min, the large particles in the IOTs are still clearly visible with the size reduced to about 10 μm. The edges and corners of the particles tend to be smooth, and the irregularity decreases. From Figure 9C, we can find that most of the IOTs particles after grinding for 100 min have the size of below 10 μm. The powder particles are significantly refined, and a certain number of submicron particles less than 1 μm appear. Besides, they have arc-shaped edges, indicating the good sphericity. This shows that with the extension of grinding time, the sphericity of IOTs particles and the smoothness of the edges are both increased. In Figure 9D, flocculent weak agglomeration appears for the particles ground after 140 min. It can be clearly seen that nanoscale particles exist in the IOTs after ultrafine grinding. Their morphology tends to be spherical and the edges are smooth. With large surface energy, these nanoscale particles can agglomerate each other, or can be adsorbed on the surface of coarser particles. Therefore, ultrafine grinding of IOTs can not only generate a large number of submicron particles, but also obtain nanoscale particles with good sphericity. Figure 9E shows the particle size interval distribution curve of IOTs at different grinding time. As can be seen from the Figure 9E, as the grinding time progresses, the average particle size of IOTs also presents a regular decline with the change of grinding time. The range of particle sizes of IOTs with peak particle sizes gradually shifts towards fine particle sizes, while the peak particle sizes gradually decrease, gradually concentrating in the direction of small particle sizes, and the proportion of fine particle size components in the particle group gradually increases. After 20 min of grinding, the particle size decreases rapidly. With the extension of grinding time, the particle size of IOTs decreases gently. When grinding for 100–140 min, the particle size decreases slowly, indicating that there is a weak agglomeration phenomenon during mechanical grinding of IOTs. At this point, the weak bond is broken, making it more difficult for the stronger high-energy bond to break, increasing the fracture energy, and therefore reducing the grinding efficiency. This can also effectively illustrate the change rule in Figures 9A–D. The spherical shape of FA is one of the reasons why it plays an important role in the concrete industry. Adding spherical FA to concrete can effectively improve the fluidity of slurry, thereby improving the workability and mechanical properties of concrete. Therefore, when the IOTs after ultrafine grinding are applied as an inert filling component to concrete, the good particle sphericity will contribute to exerting the filling effect. In addition, with the rapid increase of lattice distortion and surface energy of some submicron and nano IOTs particles generated by grinding, the ground IOTs have certain volcanic ash reactivity. When they are applied as mineral admixtures to cement-concrete systems, these submicron and nanoparticles can undergo volcanic ash reaction, which will further improve the strength and durability of concrete (Cheng et al., 2020; Gunasekara et al., 2020; Ji et al., 2021).

## 3.3 Environmental impact of IOTs

At present, the application in the field of concrete is one of the focuses on IOTs research, while the leaching of heavy metals is still less concerned. As the iron and steel waste, IOTs contain heavy metals including Cr, Zn, Cu, Ni, Pb, Cd, Hg, and As (Zhang et al., 2018; Young et al., 2021; Sarathchandra et al., 2022), which are easy to migrate and transform in the environment. This poses a potential threat to the environment. In our test, SPLP was conducted to separately test the leaching toxicity of each raw material for preparing the CCM and that of the CCM hardened OPC paste. The raw materials included IOTs, OPC, and PG. The IOTs with the grinding time of 40 min and the SSA of 658 $m^2\ kg^{-1}$ were assumed as

10.3389/feart.2023.1181984

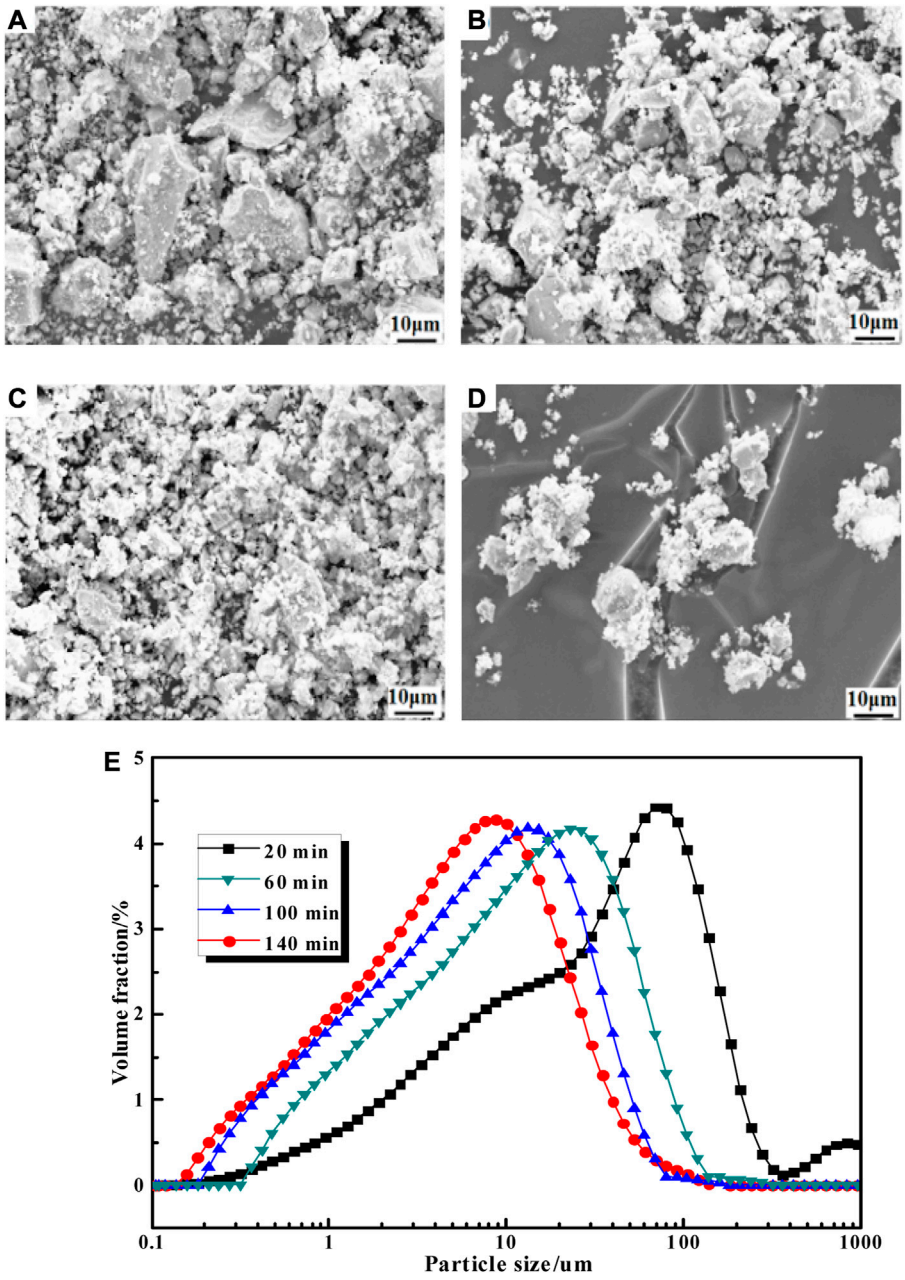


FIGURE 9
Microstructure and particle size distribution of IOTs at different grinding time. **(A)** 20 min; **(B)** 60 min; **(C)** 100 min; **(D)**140 min and **(E)** Interval distribution curves.

**TABLE 8 The leaching concentrations of heavy metals from some raw materials and mortar blocks of CCM after 28-day curing age (μg/L).**

| Materials | Cu | Pb | Zn | Ni | Cd | Cr | As | Hg |
|---|---|---|---|---|---|---|---|---|
| IOTs-1 | 18.42 | 0.77 | 54.47 | 0.6275 | 0.3641 | 0.793 | 2.1047 | — |
| IOTs-2 | 20.23 | 0.92 | 72.14 | 1.1384 | 0.4818 | 0.964 | 2.9382 | — |
| OPC | 5.637 | 1.36 | 30.39 | 0.4538 | 0.5421 | 0.948 | 1.8525 | 0.04356 |
| PG | 26.161 | 0.16 | 37.71 | 0.0110 | 0.0908 | 1.176 | 0.6716 | 0.00224 |
| CCM-1 | 12.368 | 0.52 | 33.93 | 0.5702 | 0.3518 | 0.684 | 1.3845 | 0.02711 |
| CCM-2 | 16.581 | 0.84 | 46.82 | 0.9428 | 0.4903 | 0.825 | 1.6604 | 0.03326 |
| Limiting value | 100 | 5 | 100 | 5 | 1 | 5 | 5 | 0.1 |

IOTs-1. Those with the grinding time of 80 min and the SSA of 887 $m^2 kg^{-1}$ were assumed as IOTs-2. The mix proportion of CCM was OPC: IOTs: PG=27:12:1. The CCM prepared with IOTs-1 was denoted as CCM-1, while that prepared with IOTs-2 was represented by CCM-2. The two kinds of CCM are the samples with better performance and more application value. The results are shown in Table 8. Although the leaching of heavy metals is detected from the raw materials in an acidic environment, the leaching concentrations are still far lower than the standard evaluation value stipulated in Chinese National Standard GB 5085.3-2007. In addition, the hydration and solidification of CCM can further reduce the risk of heavy metal leaching. Therefore, it is expected that even if IOTs are incorporated in the CCM system, the environmental risk coefficient of its application is still very low, compared to the limit value specified in Chinese National Standard GB 5085.3-2007.

## 4 Conclusion

This study systematically explores the physical and chemical properties, grindability, and basic characteristics of extremely fine particle iron ore tailings (IOTs), providing the basis for the comprehensive utilization of such IOTs in the field of building materials. The following conclusions are obtained:

1) The IOTs used for our study contain 14.54% iron and 54.41% $SiO_2$. The main ferrous metal minerals are magnetite and pyrite. The content of silicate iron accounts for 11.82% of the total iron, most of which are found in silicate minerals, including grunerite and hornblende. A small amount of iron exists in minerals such as biotite, chlorite, and augite.
2) IOTs have good grindability which is much better than that of GBFS. After grinding for 120 min, the SSA of GBFS is 515 $m^2 \cdot kg^{-1}$ while that of IOTs powder reaches 1,041 $m^2 \cdot kg^{-1}$. From that time on, the SSA of IOTs basically remains stable even if the grinding time is extended.
3) The ultrafine grinding of IOTs can generate a lot of particles with the size of less than 5 μm which can fill in the voids in the cement powder packed structure. After grinding for 140 min, these particles account for 44.19% in the IOTs. The ultrafine grinding of IOTs can also generate submicron and nanoparticles with good sphericity. Therefore, IOTs after ultrafine grinding are expected to be applied to the cement-concrete industry, which is of great significance to improve the material property.
4) According to the environmental risk assessment, the CCM containing IOTs has low leaching toxicity. Its environmental risk coefficient is lower than the limit stipulated in Chinese National Standard GB5085.3-2007. Therefore, the CCM containing IOTs have good application prospects in the field of building materials and environmental remediation.

## Data availability statement

The original contributions presented in the study are included in the article/supplementary material, further inquiries can be directed to the corresponding author.

## Author contributions

JJ proposes method and writes manuscript; CW and YXZ propose and participates in design research and reviews paper; YQ, KZ, YCZ, YuZ, and FL participate in design research and reviews paper. All the authors approved the final version of the manuscript.

## Funding

The authors gratefully acknowledge financial support by the National Key Research and Development Program of China (No. 2021YFC1910605), the Natural Science Foundation of Hebei Province (E2020402079), State Key Laboratory of Solid Waste Resource Utilization and Energy Conservation (SWR-2023-007), Science and Technology Research and Development Plan of China Railway Construction Group Co., Ltd., (No. 22-11b, 22-14b), Handan Science and Technology Research and Development Program (21422111260). The funder was not involved in the study design, collection, analysis, interpretation of data, the writing of this article or the decision to submit it for publication.

## Conflict of interest

Authors ZYu and LF were employed by China Railway Construction Group Co. Ltd, China.

The remaining authors declare that the research was conducted in the absence of any commercial or financial relationships that could be construed as a potential conflict of interest.

## Publisher's note



## References

Bam, L. C., Miller, J. A., and Backer, M. (2020). A Mineral X-ray linear attenuation coefficient tool (MXLAC) to assess mineralogical differentiation for X-ray computed tomography scanning. *Minerals* 10 (5), 441–455. doi:10.3390/min10050441

Campos Teixeira, A. H., Soares Junior, P. R. R., Silva, T. H., Barreto, R. R., and Silva Bezerra, A. C. da. (2020). Low-carbon concrete based on binary biomass ash-silica fume binder to produce eco-friendly paving blocks. *Materials* 13 (7), 1534–1565. doi:10.3390/ma13071534

Castro e Silva, H. L. C., Silva, A. M. L., Barros, R. M., Dos Santos, I. F. S., and de Freitas, J. V. R. (2021). Addition of iron ore tailings to increase the efficiency of anaerobic digestion of pig manure: A technical and economic analysis. *Biomass. Bioenerg.* 148, 1–18. doi:10.1016/j.biombioe.2021.106013

Chen, G., Ji, G., Lei, A., and Tian, J. (2004). Study on synergistic effects of multi-component cementitious material. *J. Chin. Creamic. Soc.* 32 (3), 351–357. doi:10.3321/j.issn:0454-5648.2004.03.027

Chen, T., Jian, S., Xie, X., Zhang, Y., Li, J., Li, B., et al. (2021). Research progress on comprehensive utilization of vanadium-titanium magnetite tailings. *Conserv. Util. Minerl. Res.* 41 (2), 174–178. doi:10.13779/j.cnki.issn1001-0076.2021.02.023

Cheng, Y., Huang, F., Li, W., Liu, R., Li, G., and Wei, J. (2016). Test research on the effects of mechanochemically activated iron tailings on the compressive strength of concrete. *Constr. Build. Mat.* 118, 164–170. doi:10.1016/j.conbuildmat.2016.05.020

Cheng, Y., Huang, F., Qi, S., Li, W., Liu, R., and Li, G. (2020). Durability of concrete incorporated with siliceous iron tailings. *Constr. Build. Mat.* 242, 118147–147. doi:10.1016/j.conbuildmat.2020.118147

Coura, I. R., Carmignano, O. R. D. R., Heitmann, A. P., Lameiras, F. S., Lago, R. M., and Patricio, P. S. (2021). Use of iron mine tailing as fillers to polyethylene. *Sci. Rep-UK* 11 (1), 7091–7099. doi:10.1038/s41598-021-86456-z

Cui, X., Geng, Y., Li, T., Zhao, R., Li, X., and Cui, Z. (2021). Field application and effect evaluation of different iron tailings soil utilization technologies. *Resour. Conserv. Recy.* 173, 1–12. doi:10.1016/j.resconrec.2021.105746

Faghihi, S., Keykhosravi, A., and Shahbazi, K. (2019). Modeling of kinetic adsorption of natural surfactants on sandstone minerals: Spotlight on accurate prediction and data evaluation. *Colloid. Interfac. Sci.* 33, 100208. doi:10.1016/j.colcom.2019.100208

Ghafari, E., Ghahari, S. A., Costa, H., Julio, E., Portugal, A., and Duraes, L. (2016). Effect of supplementary cementitious materials on autogenous shrinkage of ultra-high performance concrete. *Constr. Build. Mat.* 127, 43–48. doi:10.1016/j.conbuildmat.2016.09.123

Gunasekara, C., Zhou, Z., Law, D. W., Sofi, M., Sejeeva, S., and Mendis, P. (2020). Microstructure and strength development of quaternary blend high-volume fly ash concrete. *J. Mat. Sci.* 55 (15), 6441–6456. doi:10.1007/s10853-020-04473-1

Han, F., Li, L., Song, S., and Liu, J. (2017). Early-age hydration characteristics of composite binder containing iron tailing powder. *Powder. Technol.* 315, 322–331. doi:10.1016/j.powtec.2017.04.022

Huang, X., Fan, X., Chen, X., Gan, M., Ji, Z., and Zheng, R. (2019). A novel blending principle and optimization model for low-carbon and low-cost sintering in ironmaking process. *Powder. Technol.* 355, 629–636. doi:10.1016/j.powtec.2019.07.085

Huang, X., Ranade, R., Ni, W., and Li, V. C. (2013). Development of green engineered cementitious composites using iron ore tailings as aggregates. *Constr. Build. Mat.* 44, 757–764. doi:10.1016/j.conbuildmat.2013.03.088

Ji, G., Peng, X., Wang, S., Hu, C., Ran, P., Sun, K., et al. (2021). Influence of magnesium slag as a mineral admixture on the performance of concrete. *Constr. Build. Mat.* 295, 123619. doi:10.1016/j.conbuildmat.2021.123619

Jiang, H., Fall, M., Yilmaz, E., Li, Y., and Yang, L. (2020). Effect of mineral admixtures on flow properties of fresh cemented paste backfill: Assessment of time dependency and thixotropy. *Powder. Technol.* 327, 258–266. doi:10.1016/j.powtec.2020.06.009

Jindal, B. B. (2019). Investigations on the properties of geopolymer mortar and concrete with mineral admixtures: A review. *Constr. Build. Mat.* 227, 116644. doi:10.1016/j.conbuildmat.2019.08.025

Lange, F., Mörtel, H., and Rudert, V. (1997). Dense packing of cement pastes and resulting consequences on mortar properties. *Cem. Concr. Res.* 27 (10), 1481–1488. doi:10.1016/S0008-8846(97)00189-0

Lawrence, P., Cyr, M., and Ringot, E. (2003). Mineral admixtures in mortars: Effect of inert materials on short-term hydration. *Cem. Concr. Res.* 33 (12), 1939–1947. doi:10.1016/S0008-8846(03)00183-2

Li, C., Sun, H., Bai, J., and Li, L. (2010). Innovative methodology for comprehensive utilization of iron ore tailings. *J. Hazard. Mat.* 174 (1-3), 71–77. doi:10.1016/j.jhazmat.2009.09.018

Li, J., and Chi, S. (2017). Innovative solidification/stabilization of lead contaminated soil using incineration sewage sludge ash. *Chemosphere* 173, 143–152. doi:10.1016/j.chemosphere.2017.01.065

Li, X., Wang, P., Qin, J., Liu, Y., Qu, Y., Liu, J., et al. (2020). Mechanical properties of sintered ceramsite from iron ore tailings affected by two-region structure. *Constr. Build. Mat.* 240, 117919. doi:10.1016/j.conbuildmat.2019.117919

Ling, G., Shui, Z., Gao, X., Sun, T., Yu, R., and Li, S. (2021). Utilizing iron ore tailing as cementitious material for eco-friendly design of ultra-high performance concrete (UHPC). *Materials* 14 (8), 1829–1843. doi:10.3390/ma14081829

Menders, B. C., Pedroti, L. G., Fontes, M. P. F., Ribeiro, J. C. L., Vieira, C. M. F., Pacheco, A. A., et al. (2019). Technical and environmental assessment of the incorporation of iron ore tailings in construction clay bricks. *Constr. Build. Mat.* 227, 1–13. doi:10.1016/j.conbuildmat.2019.08.050

Meng, W., and Khayat, K. H. (2018). Effect of graphite nanoplatelets and carbon nanofibers on rheology, hydration, shrinkage, mechanical properties, and microstructure of UHPC. *Cem. Concr. Res.* 105, 64–71. doi:10.1016/j.cemconres.2018.01.001

Mo, L. W., Zhang, F., Deng, M., Jin, F., Al-Tabbaa, A., and Wang, A. (2017). Accelerated carbonation and performance of concrete made with steel slag as binding materials and aggregates. *Cem. Concr. Comp.* 83, 138–145. doi:10.1016/j.cemconcomp.2017.07.018

Nielsen, P., Boone, M. A., Horckmans, L., Snellings, R., and Quaghebeur, M. (2019). Accelerated carbonation of steel slag monoliths at low $CO_2$ pressure–microstructure and strength development. *J. $CO_2$. Util.* 36, 124–134. doi:10.1016/j.jcou.2019.10.022

Onitiri, M. A., and Akinlabi, E. T. (2017). Effects of particle size and particle loading on the tensile properties of iron-ore-tailing-filled epoxy and polypropylene composites. *Mech. Compos. Mat.* 52 (6), 817–828. doi:10.1007/s11029-017-9633-4

Peng, Y., Hu, S., and Ding, Q. (2009). Dense packing properties of mineral admixtures in cementitious material. *Particuology* 7 (5), 399–402. doi:10.1016/j.partic.2009.06.003

Qiu, J., Yang, L., Sun, X., Xing, J., and Li, S. (2017). Strength characteristics and failure mechanism of cemented super-fine unclassified tailings backfill. *Minerals* 58 (7), 58–13. doi:10.3390/min7040058

Ren, S., Aldahri, T., Liu, W., and Liang, B. (2021). $CO_2$ mineral sequestration by using blast furnace slag: From batch to continuous experiments. *Energy* 214, 118975. doi:10.1016/j.energy.2020.118975

Richard, P., and Cheyrezy, M. (1995). Composition of reactive powder concretes. *Cem. Concr. Res.* 25 (7), 1501–1511. doi:10.1016/0008-8846(95)00144-2

Santana, P. H. L., Burak, D. L., Thiengo, C. C., Pecanha, A. L., Neves, M. A., and Mendonca, E. de. S. (2020). Jack beans and vetiver grass growth on iron ore tailing sediments from the doce river dam disaster in Brazil: Plant growth regulator effects under different edaphic conditions. *J. Soil. Sediment.* 20 (2), 4103–4110. doi:10.1007/s11368-020-02774-1

Sarathchandra, S. S., Rengel, Z., and Solaiman, Z. M. (2022). Remediation of heavy metal-contaminated iron ore tailings by applying compost and growing perennial ryegrass (Lolium perenne L.). *Chemosphere* 288, 132573. doi:10.1016/j.chemosphere.2021.132573

Sharma, R., Jang, J. G., and Bansal, P. P. (2022). A comprehensive review on effects of mineral admixtures and fibers on engineering properties of ultra-high-performance concrete. *J. Bulid. Eng.* 45, 103314. doi:10.1016/j.jobe.2021.103314

Soliman, A. M., and Nehdi, M. L. (2013). Effect of partially hydrated cementitious materials and superabsorbent polymer on early-age shrinkage of UHPC. *Constr. Build. Mat.* 41, 270–275. doi:10.1016/j.conbuildmat.2012.12.008

Sun, J., and Zhang, P. (2021). Effects of different composite mineral admixtures on the early hydration and long-term properties of cement-based materials: A comparative study. *Constr. Build. Mat.* 294, 123547. doi:10.1016/j.conbuildmat.2021.123547

Turner, L. K., and Collins, F. G. (2013). Carbon dioxide equivalent ($CO_2$-e) emissions: A comparison between geopolymer and OPC cement concrete. *Constr. Build. Mat.* 43, 125–130. doi:10.1016/j.conbuildmat.2013.01.023

Wang, D., Ma, Y., Kang, M., Ju, Y., and Zeng, C. (2021). Durability of reactive powder concrete containing mineral admixtures in seawater erosion environment. *Constr. Build. Mat.* 306, 124863. doi:10.1016/j.conbuildmat.2021.124863

Wang, W., Ye, P., Zhou, L., Wang, C., Huo, Z., Zhang, K., et al. (2018). Effects of reductant type on coal-based direct reduction of iron ore tailings. *Ann. Chim-sci. Mat.* 42 (3), 453–466. doi:10.3166/acsm.42.453-466

Wu, P. C., Wang, C. L., Zhang, Y. P., Chen, L., Qian, W., Liu, Z. Y., et al. (2018). Properties of cementitious composites containing active/inter mineral admixtures. *Pol. J. Environ. Stud.* 27 (3), 1323–1330. doi:10.15244/pjoes/76503

Yan, W., Meng, Z., Zou, M., Miao, H., Ma, F., Yu, R., et al. (2020). Neutralization reaction in synthesis of carbon materials for supercapacitors. *Chem. Eng. J.* 381, 122547. doi:10.1016/j.cej.2019.122547

Yao, G., Wang, Q., Su, Y., Wang, J., Qiu, J., and Lyu, X. J. (2020). Mechanical activation as an innovative approach for the preparation of pozzolan from iron ore tailings. *Min. Eng.* 145, 106068. doi:10.1016/j.mineng.2019.106068

Young, G., Chen, Y., and Yang, M. (2021). Concentrations, distribution, and risk assessment of heavy metals in the iron tailings of Yeshan National Mine Park in Nanjing, China. *Chemosphere* 271, 129546. doi:10.1016/j.chemosphere.2021.129546

Yu, J., Qin, Y., Gao, P., Han, Y., and Li, Y. (2021). An innovative approach for determining the grinding media system of ball mill based on grinding kinetics and linear superposition principle. *Powder. Technol.* 378, 172–181. doi:10.1016/j.powtec.2020.09.076

Yuan, S., Zhang, Q., Yin, H., and Li, Y. (2020). Efficient iron recovery from iron tailings using advanced suspension reduction technology: A study of reaction kinetics, phase transformation, and structure evolution. *J. Hazard. Mat.* 404, 124067. doi:10.1016/j.jhazmat.2020.124067

Yuan, S., Zhou, W., Han, Y., and Li, Y. (2020). Efficient enrichment of iron concentrate from iron tailings via suspension magnetization roasting and magnetic separation. *J. Mat. Cycles. Waste.* 22 (1), 1152–1162. doi:10.1007/s10163-020-01009-2

Zhai, J., Wang, H., Pan, C., Hu, Y., and Sun, W. (2020). Recycling of iron and titanium resources from early tailings: From fundamental work to industrial application. *Chemosphere* 242, 1–8. doi:10.1016/j.chemosphere.2019.125178

Zhang, X., Yang, H., and Cui, Z. (2018). Evaluation and analysis of soil migration and distribution characteristics of heavy metals in iron tailings. *J. Clean. Prod.* 172, 475–480. doi:10.1016/j.jclepro.2017.09.277

Zhang, Y., Wang, L., Duan, Y., Liu, B., and Liang, J. (2022). Preparation and performance of Ce-doped far-infrared radiation ceramics by single iron ore tailings. *Ceram. Int.* 48 (8), 11709–11717. doi:10.1016/j.ceramint.2022.01.029

Zhao, H., Sun, W., Wu, X., and Gao, B. (2015). The properties of the self-compacting concrete with fly ash and ground granulated blast furnace slag mineral admixtures. *J. Clean. Pr.* 95, 66–74. doi:10.1016/j.jclepro.2015.02.050

Zhao, S., Fan, J., and Sun, W. (2014). Utilization of iron ore tailings as fine aggregate in ultra-high performance concrete. *Constr. Build. Mat.* 50, 540–548. doi:10.1016/j.conbuildmat.2013.10.019

Zhao, X. M., Wang, C. L., Zheng, Y. C., Liu, S. C., and Yang, J. (2016). Properties of complex binder containing fly ash or iron ore tailings powder. *J. Chin. Coal Soc.* 41 (S1), 229–234. doi:10.13225/j.cnki.jccs.2015.1037

Zheng, Y., Ni, W., Xu, L., Li, D., and Yang, H. (2010). Mechanochemical activation of iron ore tailings and preparation of high-strength construction materials. *J. Univ. Sci. Technol. B* 32 (4), 504–508. doi:10.13374/j.issn1001-053x.2010.04.016

Zhu, X., Chen, B., Zhu, L., and Xing, B. (2017). Effects and mechanisms of biochar-microbe interactions in soil improvement and pollution remediation: A review. *Environ. Pollut.* 227, 98–115. doi:10.1016/j.envpol.2017.04.032

frontiers | Frontiers in Earth Science

TYPE Original Research
PUBLISHED 15 June 2023
DOI 10.3389/feart.2023.1214184



OPEN ACCESS

EDITED BY
Lijie Guo,
Beijing Mining and Metallurgy Technology Group Co., Ltd., China

REVIEWED BY
Lin Chi,
University of Shanghai for Science and Technology, China
Xiaodan Li,
Chongqing Technology and Business University, China

*CORRESPONDENCE
Changlong Wang,
baistuwong@139.com

RECEIVED 29 April 2023
ACCEPTED 05 June 2023
PUBLISHED 15 June 2023

CITATION
Bao P, Jing J, Qi Y, Ma J, Ping H, Wang C, Liu Z, Zheng Y, Zhai Y and Liu F (2023), Firing mechanism and benefit evaluation of high-strength fired water permeable brick containing vanadium-titanium iron ore tailings.
*Front. Earth Sci.* 11:1214184.
doi: 10.3389/feart.2023.1214184



# Firing mechanism and benefit evaluation of high-strength fired water permeable brick containing vanadium-titanium iron ore tailings

Pingju Bao[1], Jianlin Jing[2], Yang Qi[2], Jintao Ma[2], Haoyan Ping[2], Changlong Wang[2]*, Zhibing Liu[2], Yongchao Zheng[3], Yuxin Zhai[4] and Feng Liu[5]

[1]School of Management Engineering and Business, Hebei University of Engineering, Handan, China, [2]Collaborative Innovation Center for Intelligent Regulation and Integrated Management of Water Resources Jointly Built by Provinces and Ministries, School of Civil Engineering, Hebei University of Engineering, Handan, China, [3]Beijing Building Materials Academy of Science Research, State Key Laboratory of Solid Waste Reuse for Building Materials, Beijing, China, [4]China Railway Construction Group Co., Ltd., Beijing, China, [5]Construction Development Co., Ltd., China Railway Construction Group Co., Ltd., Beijing, China

**Introduction:** The vanadium-titanium iron ore tailings (VTIOTs) has a significant amount of discharge, and serious pollution, which makes it difficult to use directly as a resources resource.

**Methods:** High-strength fired water permeable brick (HSFWPB) was prepared using VTIOTs as the main raw material. The orthogonal test, X-ray diffraction analysis (XRD), scanning electron microscope (SEM), energy dispersive spectrometry (EDS), and synthetic precipitation leaching procedure (SPLP) were obtained to study the basic properties and firing mechanism of HSFWPB containing VTIOTs, and an economic benefit evaluation was conducted on the project investment of HSFWPB containing VTIOTs.

**Results:** The results show that when the content of VTIOTs in HSFWPB is 78%, the firing temperature (FT) is 1080°C and the holding time is 120 min, the compressive strength and permeability coefficient of the fired product reach 70.4 MPa and 0.055 $cm \cdot s^{-1}$, respectively, which meet the requirements of Cc60 grade products in *Water permeable brick* (JC/T 945–2005). The products of HSFWPB containing VTIOTs after firing are diopside ($CaMgSi_2O_6$) and augite (Ca (Mg, Fe, Al) (Si, $Al)_2O_6$), with the increase of FT and the extension of HT, the low melting point elements of P, Na, K dissolve out, and the content of Fe and Al in the firing products increases, most of $Ca^{2+}$ in diopside is replaced by $Fe^{3+}$, so that augite becomes the main crystal phase. With the increase of FT, the pores in the fired products are changed from: closed pores with different sizes→ connected pores with irregular diameters→ irregular collapse pores→ small and uniform circular pores, which provides a guarantee for the permeability of HSFWPB containing VTIOTs.

**Discussion:** The full investment payback period of the project of HSFWPB containing VTIOTs is 1.77 years. When the production reaches 48.585% of the design output, it reaches a breakeven point, and the project has strong risk resistance ability. The research has improved the utilization rate of VTIOTs and provided a new approach for the large-scale application of VTIOTs.

KEYWORDS

vanadium-titanium iron ore tailings (VTIOTs), high-strength fired water permeable brick (HSFWPB), basic property, firing mechanism, benefit evaluation, augite

# 1 Introduction

With the increasing exploitation of mineral resources, tailings production has also increased (Jiang et al., 2019; Sun H. Y. et al., 2021). At present, building tailings ponds to store tailings is a common tailings treatment method (Rey et al., 2020; Chen D. Q. et al., 2021). However, tailings ponds occupy a large amount of arable land and forest land, which can easily lead to geological disasters such as landslides and mudslides (Zhao et al., 2020; Li et al., 2021; Li et al., 2022; Peng et al., 2020; Tang et al., 2021). In addition, the harmful substances formed by heavy metal ions in tailings can also pollute the water and soil resources near the tailings pond, affecting normal production and the lives of surrounding residents (Jiang et al., 2018; Wang et al., 2018; Luo L. Q. et al., 2019; Tang et al., 2019). Tailings storage isan optimal solution. Vanadium-titanium iron ore tailings (VTIOTs) are industrial solid waste produced by vanadium-titanium magnetite ore after beneficiation containing element such as Fe, Ti, and V that yet to be recovered, scattered and rare elements such as Co, Ga, and Sc, and possessing high comprehensive utilization value. Presently, the storage of tailings ponds has not realized its potential value, which is also a waste of secondary resources (Li et al., 2020; Zhu et al., 2021; Gan et al., 2022; Huang et al., 2023). Therefore, it is of great significance to promote the comprehensive utilization of VTIOTs for improving resource efficiency, improving environmental quality and promoting the comprehensive transformation of economy and society (Chen et al., 2015; Yu et al., 2019; Zhang et al., 2019; Chen et al., 2021; Sun et al., 2021; Li et al., 2022). In recent years, VTIOTs have been applied to extract valuable metals (Zhang et al., 2019) and prepare building materials, such as foamed ceramics (Xi et al., 2018; Li et al., 2020; Zhu et al., 2021; Li L. et al., 2022), composite cementitious materials (Liu and Zhao, 2020; Wang et al., 2023a), sound insulation panels (Wang C. L. et al., 2022), concrete (Wang and Qin, 2019; Wang C. L. et al., 2021), cement clinker (Yang and Sun, 2020), autoclaved aerated concrete (Shi and Song, 2020), and so on.

Due to the widespread use of cement and asphalt in urban areas, pavement hardening has reduced the exchange of heat and water vapor between the air and ground, leading to an increasing number of environmental problems in cities. The advanced thought and design applied to sponge city construction can conducive to promoting the transformation and development of urban stormwater management mode and guaranteeing the security of water ecosystem (Xu et al., 2018; Nguyen et al., 2019; Guan et al., 2021). Permeable materials are a crucial factor of sponge city construction that can help alleviate the problem of urban rainwater drainage and utilization at the source (Yu et al., 2021; Song, 2022; Qi et al., 2023). Water permeable bricks (WPB), as a type of permeable material with high porosity, breathability, and moisture retention that other road paving materials lack (Wang C. L. et al., 2019; Li J. H. et al., 2021; Wang H. F. et al., 2022; Lv et al., 2022). WPB can infiltrate rainwater into the ground, and there is no obvious runoff in case of rainstorm, achieving the effect of drying when the rain stops. This has played a positive role in the replenishment of soil water and groundwater resources, effectively alleviating the negative impact of hardened roads on urban groundwater resources. The compressive strength (CS) and permeability coefficient (PC) of WPB are generally 30–55 MPa and $1.5\times10^{-2}$~$4\times10^{-2}$ cm·s$^{-1}$, respectively (Liu et al., 2019; Liu et al., 2020; Cai et al., 2021; Yang et al., 2021). WPB not only meets the mechanical performance requirements of general road surfaces, but its own water permeability, breathability, and water retention also bring many benefits to the urban environment: it can alleviate the heat island effect and urban waterlogging (Asaeda and Ca, 2000; He et al., 2019; Luo et al., 2022; Seifeddine et al., 2022), replenish groundwater (Sansalone et al., 2008; Han et al., 2023), absorb sound and reduce noise (Fang et al., 2022), and achieve comprehensive utilization of waste (Wang Y. G. et al., 2019; Yan et al., 2020). Industrial solid waste contains many inorganic components such as $Al_2O_3$ and $SiO_2$ which are high-quality raw materials for preparing WPB products. High-strength fired water permeable brick (HSFWPB) can be prepared by high-temperature firing using solid waste such as coal gangue, waste ceramics, and granulated blast furnace slag (GBFS) as aggregates, clay, shale, or other waste as binders, and appropriate pore forming or foaming agents. Kim et al. (2019) improved the traditional preparation process of WPB, greatly increasing the porosity of WPB, but did not further study the CS, so the practical value of the prepared WPB is relatively low; Xu et al., 2019 selected tailings sand as aggregate and sludge as binder to prepare WPB, but the properties of WPB are not ideal. The main problem is that the binder used in the prepared WPB has poor properties; Luo X. et al., 2019 used tailings and sludge as raw materials, and added shale as an additional binder, but the CS of the fired water permeable bricks (FWPB) samples was low. Wang Z. Y. et al., 2019 prepared WPB with foundation glass as binder and tailing ore as aggregate, but the CS of the WPB did not reach 30 MPa. The above research uses industrial solid waste to prepare WPB, but the performance indicators of the prepared products are low and cannot be applied in industry. In order to further improve the performance of WPB, based on previous research by the research group (Wang S. X. et al., 2021; Ye, 2021), the effects of aggregate content (AC), firing temperature (FT), and holding time (HT) on the basic properties of HSFWPB were studied using VTIOTs as the main raw material and using "three factors and four levels" orthogonal experiments. On this basis, X-ray diffraction (XRD), scanning electron microscope (SEM), and energy dispersive spectrometry (EDS) were used to analyze the effects of HT and FT on the phase composition and mineral transformation of HSFWPB. The firing mechanism of HSFWPB was studied, and the economic benefits of the project investment in HSFWPB containing VTIOTs were evaluated. Prior to this study, various scholars had investigated the effects of process conditions on SWPB. However, there were notable differences in the raw materials used in their studies compared to ours, and the previous trend patterns may not be fully applicable. As a result, our research provides a necessary and comprehensive understanding of the effects of process conditions on SWPB

**TABLE 1 Chemical composition of raw materials (wt. %).**

| Materials | $SiO_2$ | $Al_2O_3$ | $Fe_2O_3$ | CaO | $K_2O$ | MgO | $Na_2O$ | $P_2O_5$ | $TiO_2$ | Other | LOI |
|---|---|---|---|---|---|---|---|---|---|---|---|
| VTIOTs | 41.13 | 7.83 | 11.05 | 20.38 | 0.42 | 12.52 | 0.54 | 0.26 | 0.87 | 1.90 | 3.10 |
| LM | 51.41 | 14.32 | 5.29 | 5.18 | 2.12 | 2.36 | 0.58 | 1.84 | 0.12 | 2.35 | 14.43 |
| GTs | 62.21 | 15.14 | 4.22 | 3.57 | 2.83 | 2.15 | 3.64 | 0.12 | 0.32 | 1.35 | 4.45 |
| Shale | 56.21 | 22.15 | 5.32 | 2.73 | 3.20 | 2.11 | 1.07 | 0.43 | 0.84 | 1.64 | 4.30 |

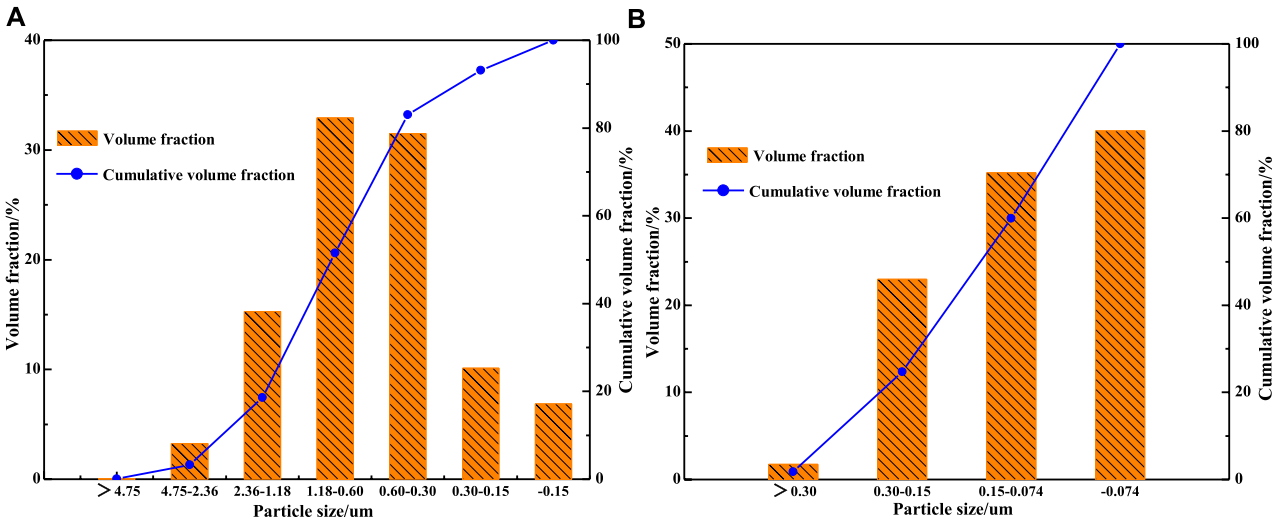


FIGURE 1
Particle size distribution of raw materials. **(A)** VTIOTs, **(B)** GTs.

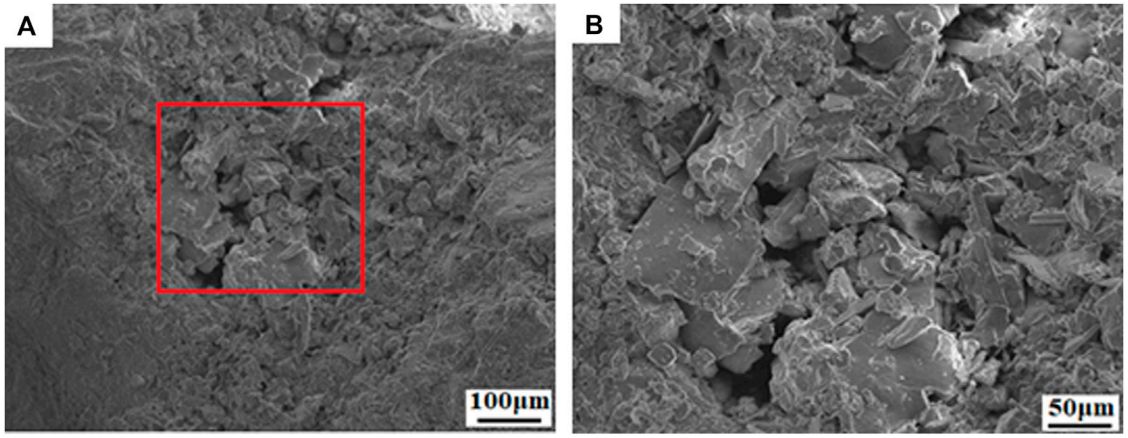


FIGURE 2
SEM images of VTIOTs. **(A)** 500 times; **(B)** 1,000 times.

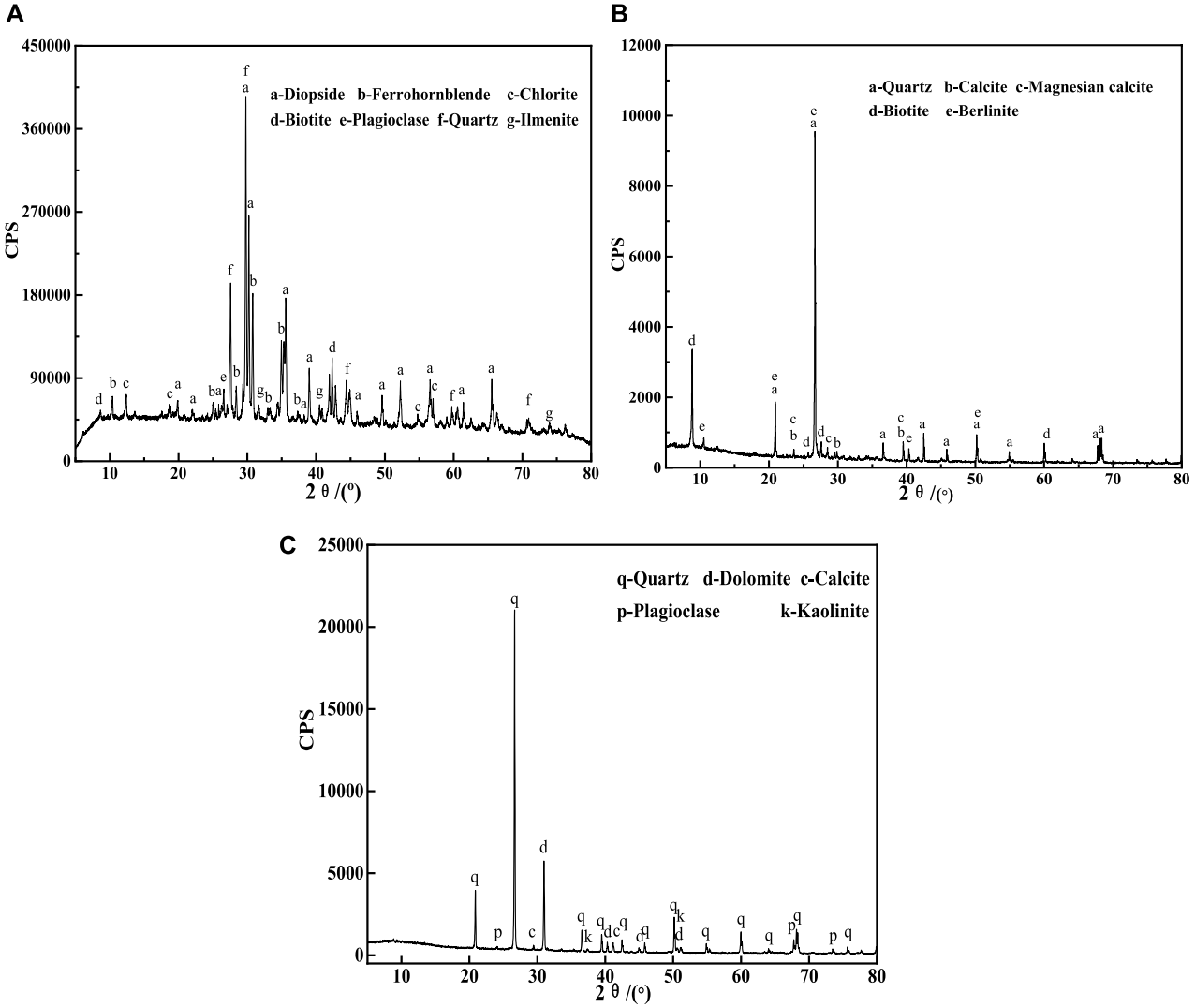


FIGURE 3
XRD patterns of raw materials. **(A)** VTIOTs, **(B)** LM, **(C)** GTs.

using VTIOTs and GTs, which have not been widely studied in the past.

# 2 Experimental materials and methods

## 2.1 Experimental materials

The industrial solid waste raw materials used in the preparation of HSFWPB in the study include VTIOTs, lake mud (LM), gold tailings (GTs), and shale. The chemical composition is shown in Table 1.

(1) VTIOTs. The stacking density of VITOs is 1.84 g $cm^{-3}$, with a particle size range of 0.30–1.18 mm accounting for 64.81%, and particles with a particle size greater than 1.18 mm (see Figure 1A) are beneficial for the formation of pores and expansion of pore size in WPB. From Figure 2, the surface of VITOs particles is rough and the texture is dense. The rough outer surface can provide mechanical interlocking force for the accumulation of particles, and when used as a WPB aggregate, it can form a skeleton structure and form certain pores between the particles, which is conducive to the permeability of the WPB. In addition, the diameters present in the particles range from 50 to 100 μm. The pores can absorb the molten liquid phase generated at high temperatures, which not only promotes the bonding between particles, but also improves the compactness of the structure, providing an important guarantee for the CS of WPB. The main mineral composition of VITOs is silicate minerals, including diopside, biotite, chlorite, quartz, and so on (see Figure 3A). Its chemical composition is mainly CaO, MgO, $SiO_2$ (see Table 1). Combined with the surface properties of the particles, it can be concluded that VTITOs are conducive to the formation of a MgO-CaO-$SiO_2$ system and can be used as an ideal firing material.

(2) LM. The LM particles used are fine, with a small number of impurities such as water plants, and the surface is gray with a water content of about 70%. After precipitation and dehydration, the LM is placed in a cool place in the interior for air drying. It is then dried in a drying oven (105°C), and then crushed to −2 mm by rolling. The mixed sample is then placed in a drying oven and dried for 24 h at 105°C. The dried sample obtained is ground to −0.074 mm by an agate grinder for later use. From Table 1, the raw materials of LM are mainly inorganic components, with $Al_2O_3$ content of 14.32%, $SiO_2$ content of 51.41%, and organic matter content of approximately 14.43%, indicating that the pyrolysis LM has good gas-production performance. The constituent minerals of LM are: berlinite, biotite, magnesium calcite, calcite, and quartz (see Figure 3B).

(3) GTs. The appearance of GTs was gray, mainly powdery particles with particle size less than 0.30 mm, and the yield below 0.15 mm was 75.24% (see Figure 1B). The main chemical component of GTs is $SiO_2$, its content is as high as 62.21%, belonging to a high-silicon mineral material. The main mineral composition of GTs is quartz, dolomite, calcite, a small amount of kaolinite and plagioclase (see Figure 3C).

(4) Shale. Shale has a beige appearance and is predominantly powdery with a size of −0.074 mm. The chemical composition of GTs is as follows: $SiO_2$ accounts for 56.21%, $Al_2O_3$ accounts for 22.15%, and $Fe_2O_3$ accounts for 5.32% (see Table 1).

## 2.2 Experimental method

### 2.2.1 Preparation of HSFWPB

Firstly, weigh the VITOs aggregate according to the required ratio in the experiment and place it in a cement mortar mixer for 30 s, while adding 5% water; Afterwards, pour the powder with different proportions into the mixer and mix with the aggregate again for 1 min to obtain the mixture used in the experiment; Finally, place the mixture in a sealed bag and age for 12 h. Then, each weighing 500 g aged mixture and place it in the φ75×50 mm mold, press and shape at a corresponding pressure of 25 MPa; Dry the pressed body in a 105°C air dryer for 12 h; Place the dried body into a muffle furnace and burn it into shape under the relevant firing system required by the experiment. The firing system of the pressed body is as follows: First, rising temperature from the room temperature to 60°C, which the heating rate is 0.5°C $min^{-1}$. Then, the rising temperature from 60°C to 300°C with the heating rate for 2°C $min^{-1}$. Then increasing the temperature from 300 to 800°C at a rate of 3°C $min^{-1}$, insulation for 60 min; Finally, rising temperature from 800°C to the required temperature for the experiment (1,050, 1,060, 1,070, 1,080°C), with a heating rate of 1°C $min^{-1}$, holding for a certain time (60, 90, 120, 150 min), and finally decrease from the highest firing temperature to room temperature with the furnace.

### 2.2.2 Property characterization

The porosity of HSFWPB was determined by the boiling method in the *Test method for apparent porosity and bulk density of porous ceramic* (GB/T 1966-1996); The flexural strength (FS), splitting tensile strength (STS) and PC of HSFWPB were determined according to the method specified in Appendix A, B and C of *Permeable paving bricks and permeable paving flags* (GB/T 25993-2010); The determination of CS of HSFWPB was carried out according to the method in Appendix A of *Water permeable brick* (JC/T 945-2005). SPLP was conducted to test the leaching behavior of heavy metals in HSFWPB containing VTIOTs, thus confirming the environmental safety. The phase composition of HSFWPB was analyzed using a German Bruker D8 Advance X-ray diffractometer under operating conditions of voltage 40 kV, current 30 mA, Cu target, 2 $\theta$ range 10°–90°, step size 0.02°, scanning rate 8° $min^{-1}$; Through the Zeiss SUPRA™55 scanning electron microscope coupled with a Be4-U92 energy spectrum, SEM observation was performed to analyze the microstructure of HSFWPB samples.

# 3 Results and discussion

## 3.1 Basic properties of HSFWPB containing VTIOTs

### 3.1.1 Orthogonal design of HSFWPB

The research aims to improve the comprehensive utilization rate of VTIOTs and minimize energy consumption, to prepare HSFWPB that meet the requirements of *Permeable paving bricks and permeable paving flags* (GB/T 25993-2010) and *Water permeable bricks* (JC/T 945-2005). Therefore, based on previous research (Wang C. L. et al., 2021; Ye, 2021), the undisturbed VTIOTs were sieved into three particle size ranges: 1.18–4.75 mm (coarse particle size), 0.60–1.18 mm (medium particle size), and 0.15–0.60 mm (fine particle size). The measured stacking densities were 1.56 g·$cm^{-3}$, 1.58 g·$cm^{-3}$, and 1.76 g·$cm^{-3}$, respectively. Due to the main particle size range of VTIOTs from 0.60 to 1.18 mm ensure high utilization of VTIOTs, the medium particle size was selected as the main particle size, and other particle sizes were studied. The ratio of GTs, LM and shale in the binder was 2: 2: 1. Optimize the mix proportion and property of HSFWPB using orthogonal experiments. Three main factors of AC (represented by A), FT (represented by B) and HT (represented by C), were selected in orthogonal experiments, with four level values taken for each factor. The levels of AC are selected 77%, 78%, 79%, and 80%, and FT are 1,050, 1,060, 1,070, and 1,080°C, HT are 60, 90, 120, and 150 min.

### 3.1.2 Results and analysis of orthogonal experiment for HSFWPB

The test results of PC, and CS for HSFWPB containing VTIOTs in the orthogonal experiment are shown in Table 2. WPB fired from VTIOTs has the potential for high strength and high permeability. When the AC is between 77% and 80%, the PC variation range of HSFWPB are 0.058–0.118 cm $s^{-1}$, the CS is reduced from 67.5 MPa to 36.3 MPa, and its PC and CS meet the requirements of Cc35 grade products in the *Water permeable brick* (JC/T 945-2005). At the same time, its PC meets the requirement of Grade A product in *Permeable paying bricks and permeable paying flags* (GB/T 25993-2010), its PC value is greater than or equal to 0.02 cm·$s^{-1}$. PC and CS are two opposing performance indicators. When the AC increases, the internal porosity of HSFWPB increases, which enhances the water permeability. The overall density of HSFWPB decreases, leading to a decrease in CS. Therefore, the most excellent combination of CS for HSFWPB containing VTIOTs is $A_1B_4C_4$, the combination that only considers the best PC is $A_4B_1C_4$.

The range analysis method for orthogonal experimental is to solve the existing problems by using the average range of each pair of

**TABLE 2** Orthogonal test scheme and results for HSFWPB containing VTIOTs.

| Number | Factor | | | Test scheme | PC/(cm·s$^{-1}$) | CS/MPa |
|---|---|---|---|---|---|---|
| | A (AC/%) | B (FT/°C) | C (HT/min) | | | |
| 1 | 1(77%) | 1(1,050°C) | 1(60 min) | $A_1B_1C_1$ | 0.108 | 40.2 |
| 2 | 1(77%) | 2(1,060°C) | 2(90 min) | $A_1B_2C_2$ | 0.093 | 49.6 |
| 3 | 1(77%) | 3(1,070°C) | 3(120 min) | $A_1B_3C_3$ | 0.080 | 60.7 |
| 4 | 1(77%) | 4(1,080°C) | 4(150 min) | $A_1B_4C_4$ | 0.058 | 67.5 |
| 5 | 2(78%) | 1(1,050°C) | 2(90 min) | $A_2B_1C_2$ | 0.114 | 38.1 |
| 6 | 2(78%) | 2(1,060°C) | 1(60 min) | $A_2B_2C_1$ | 0.099 | 42.2 |
| 7 | 2(78%) | 3(1,070°C) | 4(150 min) | $A_2B_3C_4$ | 0.076 | 58.3 |
| 8 | 2(78%) | 4(1,080°C) | 3(120 min) | $A_2B_4C_3$ | 0.061 | 65.7 |
| 9 | 3(79%) | 1(1,050°C) | 3(120 min) | $A_3B_1C_3$ | 0.116 | 37.6 |
| 10 | 3(79%) | 2(1,060°C) | 4(150 min) | $A_3B_2C_4$ | 0.087 | 44.2 |
| 11 | 3(79%) | 3(1,070°C) | 1(60 min) | $A_3B_3C_1$ | 0.089 | 45.4 |
| 12 | 3(79%) | 4(1,080°C) | 2(90 min) | $A_3B_4C_2$ | 0.078 | 58.5 |
| 13 | 4(80%) | 1(1,050°C) | 4(150 min) | $A_4B_1C_4$ | 0.118 | 36.3 |
| 14 | 4(80%) | 2(1,060°C) | 3(120 min) | $A_4B_2C_3$ | 0.113 | 38.7 |
| 15 | 4(80%) | 3(1,070°C) | 2(90 min) | $A_4B_3C_2$ | 0.086 | 42.5 |
| 16 | 4(80%) | 4(1,080°C) | 1(60 min) | $A_4B_4C_1$ | 0.083 | 44.6 |

**TABLE 3** Range analysis of PC and CS for HSFWPB containing VTIOTs.

| Property index | Factor | A (AC/%) | B (FT/°C) | C (HT/min) |
|---|---|---|---|---|
| PC/(cm·s$^{-1}$) | $\bar{k}_1$ | 0.08475 | 0.114 | 0.09475 |
| | $\bar{k}_2$ | 0.0875 | 0.098 | 0.09275 |
| | $\bar{k}_3$ | 0.0925 | 0.08275 | 0.0925 |
| | $\bar{k}_4$ | 0.1 | 0.07 | 0.08475 |
| | $R_1$ | 0.01525 | 0.044 | 0.01 |
| CS/MPa | $\bar{k}_1$ | 54 | 37.75 | 42.75 |
| | $\bar{k}_2$ | 50.75 | 43.25 | 46.75 |
| | $\bar{k}_3$ | 46 | 51.25 | 50 |
| | $\bar{k}_4$ | 40 | 58.5 | 51.25 |
| | $R_2$ | 14 | 20.75 | 8.5 |

influencing factors. An increase in the range indicates that this element has a more significant impact on the experimental results, while a decrease in the range indicates that the impact is not significant. Table 3 shows the range analysis results of the orthogonal test. $R_1$ and $R_2$ represent the average range of PC and CS for HSFWPB containing VTIOTs, respectively in Table 3. The main and secondary factors affecting the PC of HSFWPB are as follows: FT > AC> HT. The PC of HSFWPB containing VTIOTs increases with the increase of AC content, and gradually decreases as FT and HT increase; The CS decreases with the increase of AC content, and further increases with the increase of FT and HT. Therefore, the $A_4B_1C_1$ is considered as the optimal experimental plan for HSFWPB containing VTIOTs that only consider PC. The $A_1B_4C_4$ is considered the optimal experimental for HSFWPB, that only considers CS. Due to the conflict between the two property indicators, further analysis of variance is required to achieve the optimal experimental plan with ideal balance (see Table 4).

It can be seen from the variance analysis of HSFWPB's PC in Table 4 that the test statistics of AC, FT and HT are 0.26, 0.21, and 0.12, respectively. Therefore, the main and secondary affecting factors on the PC of HSFWPB are as follows: AC > FT > HT. Since the test statistics of all factors are less than the critical value, the influence of factors on the PC is not significant. The influence level factors among the insignificant factors can be selected from the perspective of cost reduction. According to the variance analysis of HSFWPB's CS, the test statistics of AC, FT and HT are 35.05, 78.21, and 13.65, respectively. Therefore, the main and secondary factors affecting the CS of HSFWPB are as follows: FT> AC> HT. Since the test statistics of each factor are greater than the critical value, each factor has a significant impact on CS. The level of significant factors should be the best level. In summary, the best combination of various factors is $A_1B_4C_4$, which means that the AC is 77%, the HT is 1,080°C, and the HT is 150 min. The prepared HSFWPB containing VTIOTs has a PC and CS of 0.058 cm·s$^{-1}$ and 67.5 MPa, respectively. However, the combination scheme of $A_2B_4C_2$ on property indicators in Table 2 are not significantly different from $A_1B_4C_4$, its PC and CS in $A_2B_4C_2$ reach 0.061 cm·s$^{-1}$ and 65.7 MPa, respectively. In the combination scheme of $A_2B_4C_2$, the AC, HT, and HT of HSFWPB containing VTIOTs are 78%, 1,080°C, and 120 min, respectively. From

**TABLE 4 Variance analysis table of PC and CS for HSFWPB containing VTIOTs.**

| Property index | Variance source | Sum of squares of deviations | Freedom | Mean square | Test statistic | Critical value | Significance |
|---|---|---|---|---|---|---|---|
| PC | AC | 0.00054 | 3 | 0.000180 | 0.26 | $F_{0.05}(3,6)=4.76$ | non significant |
| | FT | 0.00044 | 3 | 0.000147 | 0.21 | $F_{0.25}(3,6)=1.78$ | non significant |
| | HT | 0.00024 | 3 | 0.000080 | 0.12 | | non significant |
| | Error | 0.00412 | 6 | 0.000687 | | | |
| | Sum | 0.00534 | 15 | — | | | |
| CS | AC | 444.6875 | 3 | 148.229 | 35.05 | $F_{0.05}(3,6)=4.76$ | significant |
| | FT | 992.1875 | 3 | 330.729 | 78.21 | $F_{0.25}(3,6)=1.78$ | significant |
| | HT | 173.1875 | 3 | 57.729 | 13.65 | | significant |
| | Error | 25.375 | 6 | 4.229 | | | |
| | Sum | 1,635.4375 | 15 | — | | | |

**TABLE 5 Different mix proportion of binder and property indicators for HSFWPB containing VTIOTs.**

| Number | | | A | B | C | D | E | F | G |
|---|---|---|---|---|---|---|---|---|---|
| Binder composition/% | GT | | 1 | 1 | 1 | 1 | 2 | 2 | 2 |
| | LM | | 1 | 2 | 1 | 2 | 1 | 2 | 1 |
| | Shale | | 1 | 1 | 2 | 2 | 1 | 1 | 2 |
| Properties indicators | Porosity/% | | 23.29 | 24.94 | 23.15 | 23.21 | 22.61 | 24.55 | 22.45 |
| | PC/(cm·s$^{-1}$) | | 0.069 | 0.078 | 0.063 | 0.058 | 0.055 | 0.061 | 0.066 |
| | CS/MPa | | 68.2 | 60.6 | 69.4 | 66.5 | 70.4 | 65.7 | 69.0 |
| | FS/MPa | | 12.9 | 11.7 | 13.2 | 12.6 | 13.5 | 12.5 | 13.0 |
| | STS/MPa | | 4.9 | 4.5 | 5.2 | 4.6 | 5.4 | 4.7 | 5.1 |
| | WQ/mm | | 31 | 35 | 29 | 32 | 26 | 33 | 30 |
| | FR | CSFC/MPa | 62.7 | 55.2 | 64.0 | 61.1 | 65.1 | 60.3 | 63.5 |
| | | CSLR/% | 8.06 | 8.91 | 7.78 | 8.12 | 7.53 | 8.22 | 7.97 |

Note: WR (Water retention); WQ (wear quality); FR (freezing resistance); CSFC (compressive strength after 25 freeze-thaw cycles); CSLR (loss rate of compressive strength after 25 freeze-thaw cycles).

the perspective of comprehensive utilization rate and energy consumption reduction of VTIOTs, the PC and CS of the $A_2B_4C_2$ meet the requirements of Cc60 grade products in *Water permeable brick* (JC/T 945-2005), and its PC meets the requirements of A-grade products in GB/T 25993-2010.

## 3.2 Properties of HSFWPB containing VTIOTs under optimal conditions

### 3.2.1 Effect of binder mix ratio on the properties of HSFWPB containing VTIOTs

Binders are important materials used to bond aggregates and form a certain mechanical strength. It binds particles to each other, enhance the bonding degree of WPB and plays a crucial role in improving the strength of WPB, ensuring product yield, and reducing FT. The appropriate mix proportion of the binder can transfer and fully encapsulate the aggregate in a molten state, and provide important guarantees for various properties. The orthogonal experimental study on aggregate content in Section 3.1.2 shows that the various property indicators of HSFWPB containing VTIOTs are relatively ideal in the content of 78%. Therefore, this section selects an aggregate content of 78%, a binder content of 22%, a FT of 1,080°C, and a HT of 120 min to explore the influence of the binder mix proportion on the physical property indicators of WPB. The binders with different mix proportions and corresponding property indicators are shown in Table 5.

Table 5 shows the property indicators of HSFWPB with different binder mix proportions. From the PC and porosity, it can be seen

that the two property indicators correspond to each other and present a certain regularity, that is, when the porosity decreases, the PC also decreases accordingly, is that, the porosity decreases with the decrease of PC. According to the research in Section 3.1, it can be preliminarily understood that when the permeability of the adobe increases, its related mechanical property indicators decrease, such as CS, FS, and STS. Compared to this, the permeability and mechanical properties didn't show corresponding regularity in different binder mix proportions. The reason for this is that there is a significant difference in the properties of different binders in high-temperature melting conditions. The number of pores is directly determined by the amount of liquid phase formed. The more liquid phase there is, the less pores there are, leading to a decrease in PC and porosity. However, the amount of liquid phase formed does not necessarily indicate that the binder has sufficient adhesion, so it presents different macroscopic intensities. Among all groups, E group showed the best property, with a porosity of 22.61%, a PC of 0.055 $cm \cdot s^{-1}$, CS, FS, and STS are respectively 70.4, 13.5, and 5.4 MPa and with a wear quality (WQ) of 26 mm. The maximum strength loss rate after 25 freeze-thaw experiments is 7.53% which is far less than the 20% required in the *Water permeable brick* (JC/T 945–2005) and *Permeable paving bricks and permeable paving flags* (GB/T 25993-2010). C, D, and G groups can be seen that when the shale content is high, the porosity is higher compared to other groups, and the liquid phase generated at FT of 1,080°C is less, which is not conducive to the mechanical properties of HSFWPB containing VTIOTs. Therefore, from this perspective, the shale content should not be too high. In addition, from B, D, and F groups, it can be seen that the property indicators of HSFWPB containing VTIOTs are relatively low, because the FT of LM is relatively high, and it cannot achieve the best bonding property at 1,080°C.

### 3.2.2 Environmental impact of HSFWPB containing VTIOTs

At present, one of the focuses of industrial solid waste application research is its application in the field of building materials, but little attention is attached to its heavy metal leaching problem. VTIOTs, GTs, LM and shale, as the industrial solid waste and the corresponding building materials, contain Cr, Zn, Cu, Ni, Pb, Cd, As and other heavy metals (Zhang et al., 2018; Young et al., 2021; Sarathchandra et al., 2022). They are easy to transfer and transform in the environment, presenting potential environmental risks. During SPLP, the leach liquor was prepared by adding 60%/40% (mass fraction) of sulfuric acid/nitric acid and diluting appropriately with deionized water, in order to adjust the pH to 4.20 ± 0.05 (Wang et al., 2023b; Zhang et al., 2023). The leach liquor and solidified powder (<0.075 mm) were mixed according to the ratio of 20:1, and shaken for 18 h in a gyrate shaker. Then, the screened mixture (0.45 μm) was put into Prodigy 7 Inductively coupled plasma emission spectrometer (ICP-OES) to analyze the concentration of Cr, Ni, Cu, Cd, Pb, Zn, As, and Hg (Wang et al., 2023c).

In this study, the leaching toxicity of HSFWPB raw materials (VTIOTs, GTs, LM, and shale), and HSFWPB samples were separately tested by the SPLP test. HSFWPB was prepared from 78% VTIOTs and 22% binder (GTs: LM: shale=2: 1: 1) at a FT of 1,080°C and a HT of 120 min. A block of HSFWPB sample was prepared into a powder after drying. The test results are shown in Table 6.

From Table 6, it can be seen that compared to the relevant national standards of heavy metal leaching concentration, the heavy metal leaching concentration in HSFWPB products and the raw materials used for their preparation can meet the standard values of Class II water quality required in the *Technical specification for collaborative disposal of solid waste in cement kilns* (GB 30760-2014) and *Environmental quality standards for surface water* (GB3838-2002). At the same time, it also meets the standard value requirements for Class III water quality in the *Standard for groundwater quality* (GB/T14848-2017) and the standard value requirements in the *Identification standards for hazardous wastes- Identification for extraction toxicity* (GB 5085.3-2007). Therefore, HSFWPB containing VTIOTs can be used as building materials, and their heavy metal leaching concentration meets environmental safety requirements.

## 3.3 Composition and structure of HSFWPB containing VTIOTs

### 3.3.1 Phase composition of HSFWPB containing VTIOTs

Figure 4 shows the phase composition of HSFWPB containing VTIOTs under different conditions. Figure 4A shows the XRD patterns of HSFWPB containing VTIOTs at the FT of 1,080°C and the HT of 60, 90, 120, and 150 min. Figure 4B shows the XRD pattern of HSFWPB when the HT is 120 min and the FT is 1,050, 1,060, 1,070, and 1,080°C. A block of HSFWPB sample is prepared into a powder after drying and its mineral composition is tested by XRD.

As can be seen from Figure 4A, the main mineral phases in HSFWPB containing VTIOTs are diopside and augite (Ca(Mg Fe,Al)(Si,Al)$O_6$). The "steamed bun peak" isobserved in the 2$\theta$ range of 25°–35°, indicating the presence of a certain amount of glass phase in the HSFWPB, which increases with the extension of HT. The diffraction peaks at 2$\theta$ values of 27.54°, 29.86°, 30.36°, and 35.72° are augite. With the extension of HT, augite increases, while diopside decreases gradually. The reason for this trend is that with the extension of HT, more molten liquid phase is produced in the system, and the molten $Fe^{3+}$ and $Al^{3+}$ produced in the system gradually displace $Ca^{2+}$ in diopside to form augite. The liquid phase in the system bonded with the remaining solid particles and crystals, making the structure dense. Therefore, the CS of the HSFWPB containing VTIOTs continuously increases with the extension of HT, while the PC gradually decreases.

Figure 4B shows that the HSFWPB system is mainly composed of MgO-CaO-$SiO_2$ ternary system. As the FT rises, the MgO, CaO and $SiO_2$ in the system react to produce diopside, which in turn combines with $Fe^{3+}$ and $Al^{3+}$ in the liquid phase of the system to transform into augite. The reaction is shown in Eqs 1, 2.

$$MgO + CaO + 2SiO_2 \xrightarrow{1000 \sim 1130℃} Ca_2MgSiO_6\,(\text{diopside}) \quad (1)$$

$$Ca_2MgSiO_6 + Fe^{3+} + Al^{3+} \xrightarrow{1000 \sim 1130℃} Ca\,(Mg, Fe, Al)\,(Si, Al)_2O_6\,(\text{augite}) \quad (2)$$

**TABLE 6** The leaching concentrations of heavy metals from some raw materials and HSFWPB containing VTIOTs (μg/L).

| Materials | Cu | Pb | Zn | Ni | Cd | Cr | As | Hg |
|---|---|---|---|---|---|---|---|---|
| VTIOTs | 19.33 | 0.85 | 63.31 | 0.8830 | 0.4231 | 0.879 | 2.5215 | 0.00224 |
| GTs | 20.23 | 0.92 | 72.14 | 1.1384 | 0.4818 | 0.964 | 2.9382 | — |
| LM | 5.637 | 1.36 | 30.39 | 0.4538 | 0.5421 | 0.948 | 1.8525 | 0.04356 |
| Shale | 26.161 | 0.16 | 37.71 | 0.0110 | 0.0908 | 1.176 | 0.6716 | 0.00224 |
| HSFWPB | 28.353 | 1.52 | 46.93 | 0.6915 | 0.4518 | 0.783 | 2.3845 | 0.03618 |
| Limiting value | 100 | 5 | 100 | 5 | 1 | 5 | 5 | 0.1 |

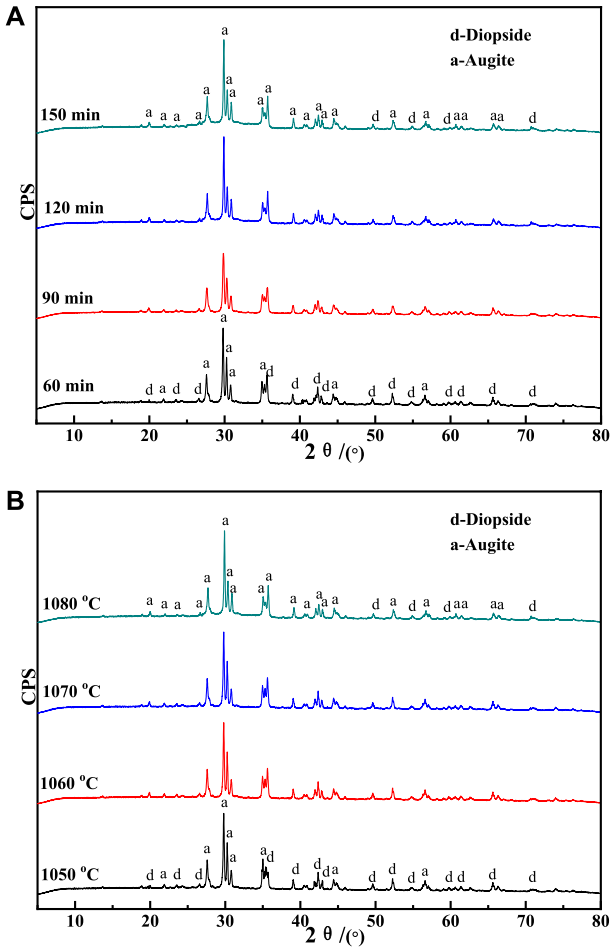


FIGURE 4
XRD patterns of HSFWPB containing VTIOTs. **(A)** Different HT; **(B)** Different FT.

When the FT reaches 1,060°C, a certain amount of molten glass phase is generated in the system, which promotes the migration of crystals under the action of capillary force, and the particles are arranged towards a higher packing density. Currently, the HSFWPB has better mechanical properties on a macro level. When the FT is 1,070°C, the diopside in the system is further combined and transformed with liquid phase ions, which makes the solid particles in the system precipitate again, thus making the material migrate again, and the density of the structure constantly strengthened.

When the FT is 1,080°C, the continuous pores inside the HSFWPB begin to turn into isolated pores. If the FT is further increased, the permeability of the HSFWPB will decrease rapidly. When the FT reaches 1,060–1,080°C, the mineral phase composition inside the HSFWPB with VTIOTs is augite, which indicates that a large amount of liquid phase has been produced in the system at this time, and the porosity has sharply decreased. Although the structure is dense, the production of a large amount of liquid phase makes the particle skeleton peristaltic. The internal structure of the HSFWPB begins to deform and the strength and porosity decrease gradually.

## 3.3.2 Microstructure of HSFWPB containing VTIOTs

### 3.3.2.1 SEM analysis

Figure 5 shows SEM images of HSFWPB containing VTIOTs at different levels of HT and FT. HSFWPB samples are prepared from 78% VTIOTs and 22% binder (GTs: LM: shale=2: 1: 1). The HT is 120 min and the FT is 1,050, 1,060, 1,070, and 1,080°C, the porosity of four HSFWPB samples obtained are 24.82%, 24.14%, 23.63%, and 22.61%, respectively. When the FT is 1,050°C, a large number of unconnected and irregularly shaped pores (yellow area in Figure 5A) are generated in the HSFWPB. The surface of the fired product is layered with a tendency to form short columns, indicating that at this time, the crystal of the HSFWPB begins to transform and diopside and a small amount of augite are gradually formed. In Figure 5B, where the HSFWPB is FT 1060°C and the HT is 120 min, the fired products of the HSFWPB gradually become denser, and the short columnar crystals on the surface gradually grow into elongated rod-like clusters. With the changes in the morphology of the fired products, the connected holes with irregular pore sizes are formed in the firing system, which improves the permeability of the HSFWPB.

When the FT reaches 1,070°C (Figure 5C), the round "water droplet" like glass phase appears as a chain bond, forming a skeleton. Meanwhile, irregular collapse holes appear in the visual field, which should be the collapse formed after liquid phase condensation formed by high-temperature melting. In Figure 5D (FT 1080°C, HT 120 min), the internal structure of the HSFWPB begins to deform, leading the formation of many micrometer-level round "water drop" glass-like grains, with some grains agglomerate together to form aggregates. The pore size of the system also reduces, becoming more homogeneous, with a pore size of about 3–5 μm. The whole system is denser, which guarantees the CS and water permeability of HSFWPB. As observed from the comparison shown in Figure 5, the change in FT results in a

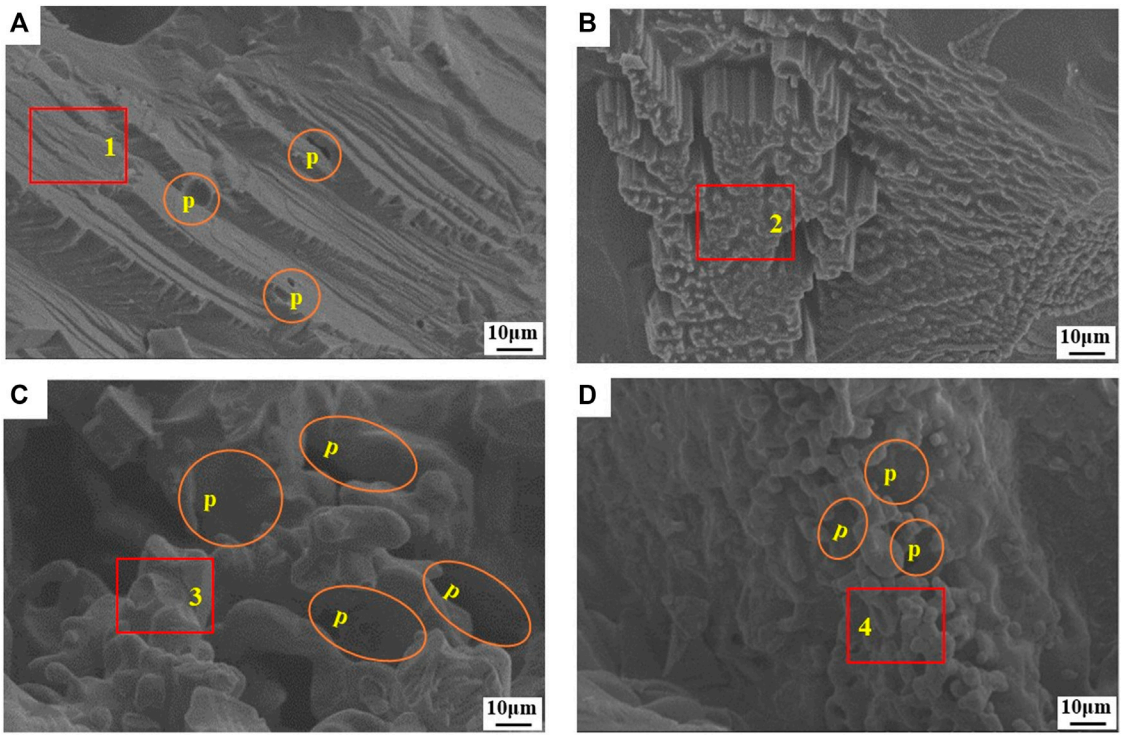


FIGURE 5
SEM images of HSFWPB containing VTIOTs at different FT. **(A)** 1,050°C; **(B)** 1,060°C; **(C)** 1,060°C; **(D)** 1,080°C.

transition of the pores in the fired products, from closed pores of different sizes to connected pores with irregular diameters, to irregular collapse pores, and lastly, to small uniform circular pores, meanwhile, the porosity in fired products also changes from high to low with the increase of FT. This change in trend provides a guarantee for the permeability of HSFWPB.

#### 3.3.2.2 EDS analysis

Figure 6 shows the EDS spectrums of HSFWPB containing VTIOTs. Figure 6A~ Figure 6D correspond to marked region 1–4 in Figure 5.

As shown in Figure 6A, when the HT is 120 min and the FT is 1,050°C, HSFWPB containing VTIOTs products are mainly composed of Ca, Si, Mg and a small amount of Fe and Al elements. The proportion of its main elements is close to that of $CaMgSi_2O_6$. Combined with Figure 4, it is analyzed that the mineral is diopside. Diopside is a one-dimensional chain structure, and its single-chain structure is an infinitely long chain with $[Si_2O_6]^{4-}$ as the structural unit. Compared with Figure 6A, the marked region in Figure 6B showed no change in the types of elements, but the contents of Fe and Al increased, and the proportion of major elements was close to $Ca(Mg, Fe, Al)(Si, Al)_2O_6$. Combined with Figure 4, the mineral was analyzed as augite. The elongated rod-like objects seen in the SEM image of Figure 5B are clusters of augite.

In Figure 6C, low-melting point elements such as P, Na, and K, indicating the presence of a certain amount of liquid phase. A large number of molten glass phases gradually grow in the liquid phase and transform into augite, combined with a part of Fe and Al elements. This finding is consistent with the SEM analysis shown in Figure 5C. In Figure 6D, where the FT is 1,080°C, the content of Fe and Al elements increases, resulting in an increase in the formation of augite. Fe element increases significantly, while the Ca element decreased, indicating that most $Ca^{2+}$ in diopside is replaced by $Fe^{3+}$ at this stage, and diopside changes to augite, making augite the main crystalline phase. Ti element in Figure 6D is the "nucleating agent" of high-temperature fired products (Wang Z. Y. et al., 2019; Zhang et al., 2021; Liu et al., 2023). The presence of Ti element can effectively promote the nucleation of the fired product system, which is conducive to the preparation of high-strength fired products, which also verifies the formation of micron-sized grains in Figure 5D.

## 3.4 Economic benefit evaluation on HSFWPB containing VTIOTs

### 3.4.1 Cost analysis

It is planned to build a factory covering an area of 40,000 $m^2$ with an annual production scale of 400,000 tons of HSFWPB. The optimal ratio $A_2B_4C_2$ of HSFWPB was selected to calculate the raw material cost and freight cost, energy consumption cost, management and wage and welfare cost, plant and facility construction cost (see Table 7).

### 3.4.2 Economic benefit analysis

Economic benefit analysis includes sales revenue and revenue estimates. According to the sale price of HSFWPB on the market, 30–50 CNY·$m^{-2}$, equivalent to 240 CNY·$t^{-1}$, the lowest price of HSFWPB is 240 CNY· $t^{-1}$, and the annual sales income will be

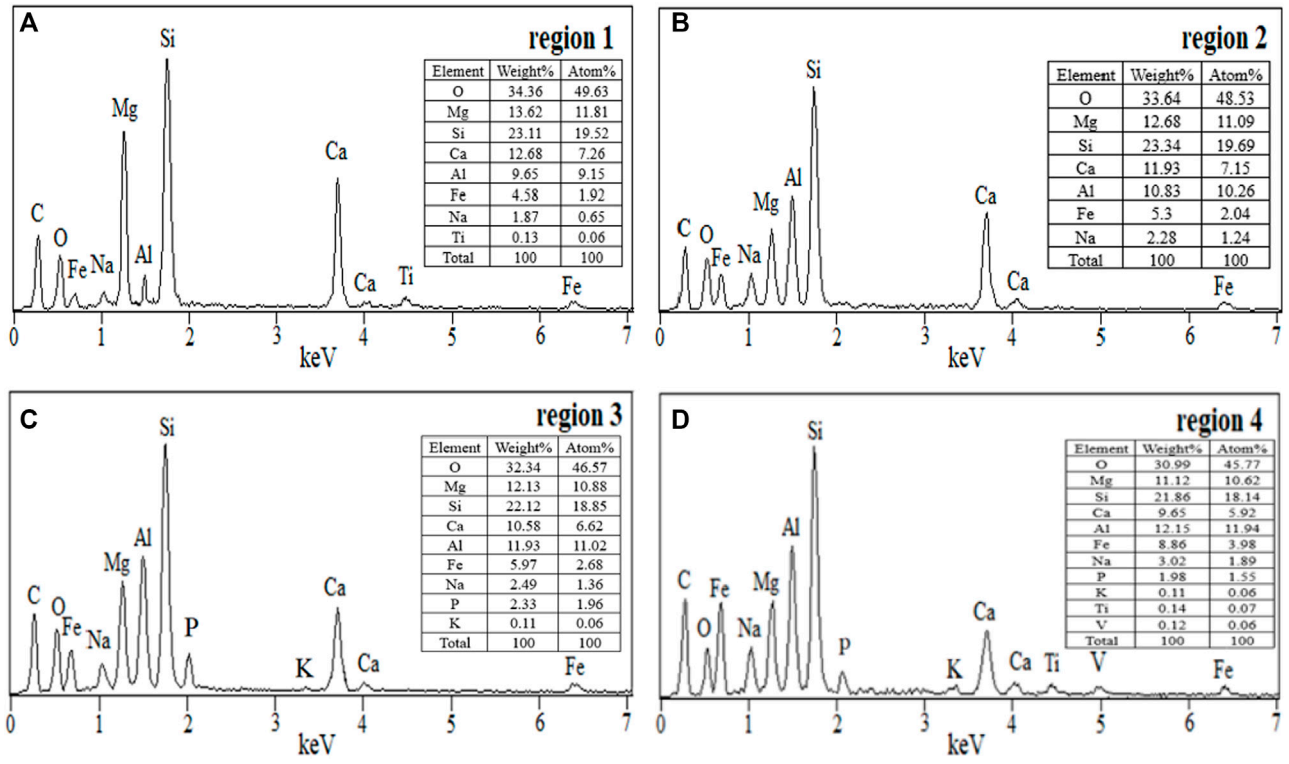


FIGURE 6
EDS spectrums of marked region 1–4 in the Figure 5. **(A)** region 1; **(B)** region 2; **(C)** region 3; **(D)** region 4.

**TABLE 7 Cost estimation for the production project of HSFWPB containing VTIOTs (10,000 CNY).**

| Number | Item | | Cost estimation |
|---|---|---|---|
| 1 | Raw material cost and freight cost | raw material cost | 756.2 |
| 2 | | freight cost | 2000 |
| 3 | Energy consumption cost | electricity consumption | 488 |
| 4 | | natural gas | 1,440 |
| 5 | Management, salary and welfare costs | employee salaries and welfares | 100 |
| 6 | | Production workshop management fee | 84 |
| 7 | Construction cost of factory building and facility | construction cost of the factory building | 800 |
| 8 | | equipment cost | 1,200 |
| 9 | | depreciation expenses for factory buildings | 26.7 |
| 10 | | depreciation expenses for equipment | 120 |
| Total | | | 7,014.9 |

9,600 CNY. According to the relevant policies of our country, enterprises comprehensively use solid waste can be exempt from paying environmental protection tax. When the utilization rate of solid waste reaches more than 30%, value-added tax and the income tax of previous 5 years can be reduced, and the proceeds of the projects are shown in Table 8.

Return on investment=(annual average total profit/total project investment)×100%=(4585.1÷7014.9) × 100%=65.3%.

Profits and taxes on investments=(annual total profit and tax/total project investment)×100%=(5492.9÷7014.9) × 100%=78.3%.

In conclusion, the investment in the production project of HSFWPB containing VTIOTs shows good economic benefits, with a higher return on investment profit and taxes on investments compared to the average industry profit rate (14%) and average profit and tax rate (22%). The economic parameters are summarized in Table 9 to obtain the project investment cash flow statement.

**TABLE 8 Project income statement of HSFWPB containing VTIOTs (10,000 CNY).**

| Number | Item | Capital construction period | Production period | | | | |
|---|---|---|---|---|---|---|---|
| | | | Tax reduction period | | | | Non tax reduction period |
| | Year | 1 | 2 | 3 | 4 | 5–6 | 7–11 |
| 1 | Sale income | | 9,600 | 9,600 | 9,600 | 9,600 | 9,600 |
| 2 | Total cost | 2000 | 5,014.9 | 5,014.9 | 5,014.9 | 5,014.9 | 5,014.9 |
| 3 | Profit | 0 | 4,585.1 | 4,585.1 | 4,585.1 | 4,585.1 | 4,585.1 |
| 4 | Income tax | 0 | 0 | 0 | 0 | 0 | 1,513.1 |
| 5 | after-tax profits | 0 | 4,585.1 | 4,585.1 | 4,585.1 | 4,585.1 | 3,072 |

Note: after-tax profits= sale income-total cost-income tax (The income tax rate is calculated at 33% of gross profit).

**TABLE 9 Project investment cash flow statement of HSFWPB (10,000 CNY).**

| Year | 1 | 2 | 3 | 4 | 5 | 6 | 7 | 8 | 9 | 10 | 11 |
|---|---|---|---|---|---|---|---|---|---|---|---|
| Raw material cost | | 2,756.2 | 2,756.2 | 2,756.2 | 2,756.2 | 2,756.2 | 2,756.2 | 2,756.2 | 2,756.2 | 2,756.2 | 2,756.2 |
| Energy cost | | 1928 | 1928 | 1928 | 1928 | 1928 | 1928 | 1928 | 1928 | 1928 | 1928 |
| Salary | | 100 | 100 | 100 | 100 | 100 | 100 | 100 | 100 | 100 | 100 |
| Depreciation expense | | 146.7 | 146.7 | 146.7 | 146.7 | 146.7 | 146.7 | 146.7 | 146.7 | 146.7 | 146.7 |
| Management expenses | | 84 | 84 | 84 | 84 | 84 | 84 | 84 | 84 | 84 | 84 |
| Fixed assets | 2000 | | | | | | | | | | |
| Sale income | | 9,600 | 9,600 | 9,600 | 9,600 | 9,600 | 9,600 | 9,600 | 9,600 | 9,600 | 9,600 |
| Cash outflow | 2000 | 5,014.9 | 5,014.9 | 5,014.9 | 5,014.9 | 5,014.9 | 5,014.9 | 5,014.9 | 5,014.9 | 5,014.9 | 5,014.9 |
| Cash inflow | 0 | 9,600 | 9,600 | 9,600 | 9,600 | 9,600 | 9,600 | 9,600 | 9,600 | 9,600 | 9,600 |
| Profit | 0 | 2,585.1 | 4,585.1 | 4,585.1 | 4,585.1 | 4,585.1 | 4,585.1 | 4,585.1 | 4,585.1 | 4,585.1 | 4,585.1 |
| Income tax | 0 | 0 | 0 | 0 | 0 | 0 | 1,513.1 | 1,513.1 | 1,513.1 | 1,513.1 | 1,513.1 |
| Net profit | 0 | 2,585.1 | 2,585.1 | 2,585.1 | 2,585.1 | 2,585.1 | 3,072 | 3,072 | 3,072 | 3,072 | 3,072 |
| Net Cashflow | −2000 | 2,585.1 | 2,585.1 | 2,585.1 | 2,585.1 | 2,585.1 | 3,072 | 3,072 | 3,072 | 3,072 | 3,072 |
| Accumulated cashflow | −2000 | 585.1 | 3,170.2 | 5,755.3 | 8,340.4 | 10925.5 | 13997.5 | 17069.5 | 20141.5 | 23213.5 | 26285.5 |

The full investment payback period is: 1 + 2,000 ÷ 2,585.1=1.77 (year), All investments in the production project of HSFWPB containing VTIOTs can be quickly recovered in 1.77, indicating that the unit investment has reached the average level of the industry and the investment risk is relatively small.

In normal production years when the project reaches the design capacity and the production load reaches 100%, the total cost is 50.149 million CNY, of which the total annual fixed cost is 29.029 million CNY, the annual variable cost is 21.12 million yuan and the annual sales tax is 15.131 million CNY.

Utilization rate of production capacity = annual fixed cost/(annual sales revenue - annual variable cost - annual sales tax) × 100%=2,902.9÷(9,600–2,112–1,513.1) × 100% = 48.58%

Break-even production = designed production capacity × production capacity utilization rate = 400,000% × 48.58% = 194,320 tons.

The calculation results show that when the production capacity of the project is 194,432 tons, that is, when it reaches 48.585% of the designed output, the project will not lose money, so it has substantial risk resistance ability. The raw materials used in the HSFWPB containing VTIOTs products prepared in this project are all industrial solid wastes. Compared with the FWPB products studied by He et al. (2023) and Kong et al. (2022) the FT of the HSFWPB containing VTIOTs product is only 1,080°C, while the FT of FWPB products from He et al. (2023) and Kong et al. (2022) are 1,180 °C and 1,090°C, respectively, and their property indicators are much lower than those of the products in this project. Therefore, the

energy consumption of HSFWPB containing VTIOTs products is lower than that of FWPB products studied by He et al. (2023) and Kong et al. (2022). So the investment in HSFWPB containing VTIOTs products is feasible.

## 4 Conclusion

(1) HSFWPB was prepared using VTIOTs as the main raw material. When the content of VTIOTs is 78%, the multi-source solid waste binder accounts for 22% (GTs: LM: shale=2:1:1), forming pressure is 25 MPa, FT is 1,080°C and HT is 120 min, CS and PC of HSFWPB can reach 70.4 MPa and 0.055 $cm \cdot s^{-1}$, respectively, which meet the requirements of Cc60 grade products in *Water permeable brick* (JC/T 945–2005). Meanwhile, the PC reaches the requirements of grade A products in *Permeable paving bricks and permeable paving flags* (GB/T 25993–2010).

(2) The products of HSFWPB containing VTIOTs after firing are diopside ($CaMgSi_2O_6$) and augite ($Ca(Mg,Fe,Al)(Si,Al)_2O_6$). With the increase of FT and the extension of HT, the low melting point elements such as P, Na, K dissolve out, and the content of Fe and Al in the firing products increases. Most of $Ca^{2+}$ in diopside is replaced by $Fe^{3+}$, so that augite becomes the main crystal phase. With the increase of FT, the changes in the pores of the fired products provide a guarantee for water permeability of HSFWPB containing VTIOTs. The pore structure changes from closed pores with different sizes→ connected pores with irregular diameters→ irregular collapse pores→ small and uniform circular pores.

(3) The full investment payback period of the project of HSFWPB containing VTIOTs is 1.77 years. At 48.585% of the design output production, the project reaches the break-even point, reflecting strong risk resistance ability.

(4) The combination of the comprehensive utilization of VTIOTs with HSFWPB, the use of appropriate technology and additives to produce high-value-added products can not only improve the utilization rate of VTIOTs, reducing land occupation and environmental pollution, but also improve profits and create considerable economic benefits. The research improves the utilization rate of VTIOTs and provides a new approach to the large-scale application of VTIOTs.

## Data availability statement

The original contributions presented in the study are included in the article/Supplementary Material, further inquiries can be directed to the corresponding author.

## Author contributions

PB proposes method and writes manuscript; CW proposes and participates in design research and reviews the paper; JJ, YQ, JM, HP, ZL, YoZ, YuZ, and FL participate in design research and reviews paper. All authors contributed to the article and approved the submitted version.

## Funding

The authors gratefully acknowledge financial support by the National Key Research and Development Program of China (2021YFC1910605), the Natural Science Foundation of Hebei Province (E2020402079), State Key Laboratory of Solid Waste Resource Utilization and Energy Conservation (SWR-2023-007), Science and Technology Research and Development Plan of China Railway Construction Group Co., Ltd. (No. 22-11b, 22-14b), Handan Science and Technology Research and Development Program (21422111260). The funder was not involved in the study design, collection, analysis, interpretation of data, the writing of this article or the decision to submit it for publication.

## Conflict of interest

Authors YZ and FL were employed by the China Railway Construction Group Co., Ltd.

The remaining authors declare that the research was conducted in the absence of any commercial or financial relationships that could be construed as a potential conflict of interest.

## Publisher's note



## Supplementary material

The Supplementary Material for this article can be found online at: https://www.frontiersin.org/articles/10.3389/feart.2023.1214184/full#supplementary-material

## References

Asaeda, T., and Ca, V. T. (2000). Characteristics of permeable pavement during hot summer weather and impact on the thermal environment. *Build. Environ.* 35 (4), 363–375. doi:10.1016/s0360-1323(99)00020-7

Cai, J. W., Lv, N. W., Jia, X. Y., Zhang, R. F., Xu, G. L., Cai, L. X., et al. (2021). Properties of permeable ceramic brick prepared with felsite tailing. *J. Build. Eng.* 44, 103426. doi:10.1016/j.jobe.2021.103426

Chen, D. Q., Cui, Y. F., Li, Z. H., and Iqbal, J. (2021). Watch out for the tailings pond, a sharp edge hanging over our heads: Lessons learned and perceptions from the Brumadinho tailings dam failure disaster. *Remote Sens-basel.* 13 (9), 1775–1796. doi:10.3390/rs13091775

Chen, S. Y., Fu, X. J., Chu, M. S., Liu, Z. G., and Tang, J. (2015). Life cycle assessment of the comprehensive utilisation of vanadium titano-magnetite. *J. Clean. Prod.* 101, 122–128. doi:10.1016/jjclepro.2015.03.076

Chen, T., Jian, S., Xie, X., Zhang, Y., Li, J., Li, B. Q., et al. (2021). Research progress on comprehensive utilization of vanadium-titanium magnetite tailings. *Conserv. Util. Min. Res.* 41 (2), 174–178. doi:10.13779/i.cnki.issn1001-0076.2021.02.023

Fang, M. J., Wang, X., Liu, J. J., Xu, Z. Y., and Chen, Y. M. (2022). Design, application and performance improvement of eco-permeable pavement materials (Eco-PPMs): A review. *Constr. Build. Mater* 360, 129558. doi:10.1016/j.conbuildmat.2022.129558

Gan, C. D., Cui, S. F., Wu, Z. Z., and Yang, J. Y. (2022). Multiple heavy metal distribution and microbial community characteristics of vanadium-titanium magnetite tailing profiles under different management modes. *J. Hazare Mater* 429, 128032. doi:10.1016/j.jhazmat.2021.128032

Guan, X., Wang, J. Y., and Xiao, F. P. (2021). Sponge city strategy and application of pavement materials in sponge city. *J. Clean. Prod.* 303, 127022. doi:10.1016/J.JCLEPRO.2021.127022

Han, J., Wang, C. Q., Demg, S. H., and Lichtfouse, E. (2023). China's sponge cities alleviate urban flooding and water shortage: A review. *Environ. Chem. Lett.* 21, 1–18. doi:10.1007/s10311-022-01559-x

He, B. J., Zhu, J., Zhao, D. X., Gou, Z. H., Qi, J. D., and Wang, J. S. (2019). Co-benefits approach: Opportunities for implementing sponge city and urban heat island mitigation. *Land Use Policy* 86, 147–157. doi:10.1016/j.landusepol.2019.05.003

He, X. M., Duan, X. C., Guo, W., and Cui, W. L. (2023). Experimental study on preparation of sintered permeable brick with high coal gangue content. *Ceramic* 3, 17–20. doi:10.19397/j.cnki.ceramics.2023.03.058

Huang, Y., Zhou, D., Wang, L., Jiao, G. H., Gou, H., Li, Z. J., et al. (2023). Role of tailing colloid from vanadium-titanium magnetite in the adsorption and cotransport with vanadium. *Envir sci Pollut R* 30, 34069–34084. doi:10.1007/S11356-022-24621-1

Jiang, F., Ren, B. Z., Hursthouse, A. S., and Zhou, Y. Y. (2018). Trace metal pollution in topsoil surrounding the xiangtan man-ganese mine area (south-Central China): Source identification, spatial distribution and assessment of potential eco-logical risks. *Int. J. Env. Res. Pub He* 15 (11), 2412–2427. doi:10.3390/ijerph15112412

Jiang, P., Lv, S. W., Wang, Y., Li, N., and Wang, W. (2019). Investigation on direct shear and energy dissipation characteristics of iron tailings powder reinforced by polypropylene fiber. *Appl. Sci-basel.* 9 (23), 5098–5113. doi:10.3390/app9235098

Kim, Y., Lee, Y., Kim, M., and Park, H. (2019). Preparation of high porosity bricks by utilizing red mud and mine tailing. *J. Clean. Prod.* 207, 490–497. doi:10.1016/jjclepro.2018.10.044

Kong, X. F., Shan, Y. X., Zhou, Z. L., Fan, C. G., and Zhang, Y. (2022). Analysis of influencing factors on properties of permeable brick sintered with iron tailings based on orthogonal test. *J. Anhui Univ. Technol. Nat. Sci.* 39 (2), 145–152. doi:10.3969/j.issn.1671-7872.2022.02.004

Li, L., Jiang, T., Zhou, M., and Chen, C. (2020). Overall utilization of vanadium–titanium magnetite tailings to prepare lightweight foam ceramics. *Process Saf. Environ.* 139, 305–314. doi:10.1016/jpsep.2020.04.034

Li, J. H., Li, X. L., Liang, S., Zhang, Y. S., Ye, Q., Zhang, L., et al. (2021). Preparation of water-permeable bricks derived from fly ash by autoclaving. *Constr. Build. Mater* 271, 121556. doi:10.1016/J.CONBUILDMAT.2020.121556

Li, L., Sun, J. W., Jiang, J. J., and Wang, J. (2021). The effect of environmental regulation competition on haze pollution: Evidence from China's province-level data. *Environ. Geochem Hlth* 44, 3057–3080. doi:10.1007/s10653-021-00854-w

Li, L., Jiang, T., Chen, B. J., Wen, J., and Yang, G. D. (2022). Integrated utilization of vanadium-titanium magnetite tailings for synthesis of lightweight foamed ceramics: Effect of chemical composition on the properties and phase evolution. *J. Sustain Metall.* 8, 646–657. doi:10.1007/S40831-022-00517-9

Li, X. S., Li, Q. H., Hu, Y. J., Chen, Q., Peng, J., Xie, Y., et al. (2022). Study on three-dimensional dynamic stability of open-pit high slope under blasting vibration. *Lithosphere-us* 2021, 6426550. doi:10.2113/2022/6426550

Liu, H. J., and Zhao, L. L. (2020). Experimental study on activation of vanadium-titanium magnetite tailings and its use as cement admixture. *Iron Stl Vanadium Titan.* 41 (4), 97–102. doi:10.7513/i.issn.1004-7638.2020.04.018

Liu, Y., Tang, W., and Singh, R. P. (2019). Study on Compressive strength and water permeability of steel slag-fly ash mixed permeable brick. *Appl. Sci-basel.* 9 (8), 1542–1552. doi:10.3390/app9081542

Liu, L., Cheng, X., Miao, X. W., Shi, Y. L., Zhang, M. X., Guo, M., et al. (2020). Preparation and characterization of majority solid waste based eco-unburned permeable bricks. *Constr. Build. Mater* 259, 120400. doi:10.1016/j.conbuildmat.2020.120400

Liu, X. M., Li, B., and Wu, Y. F. (2023). The pretreatment of non-ferrous metallurgical waste slag and its research progress in the preparation of glass-ceramics. *J. Clean. Prod.* 404, 136930. doi:10.1016/j.jclepro.2023.136930

Luo, L. Q., Li, K. Y., Fu, W., Liu, C., and Yang, S. Y. (2019). Preparation, characteristics and mechanisms of the composite sintered bricks produced from shale, sewage sludge, coal gangue powder and iron ore tailings. *Constr. Build. Mater* 232, 117250–250. doi:10.1016/j.conbuildmat.2019.117250

Luo, X., Ren, B. Z., Hursthouse, A. S., Jiang, F., and Deng, R. J. (2019). Potentially toxic elements (PTEs) in crops, soil, and water near Xiangtan manganese mine, China: Potential risk to health in the foodchain. *Environ. Geochem Hlth* 42, 1965–1976. doi:10.1007/s10653-019-00454-9

Luo, P. P., Liu, L. M., Wang, S. T., Ren, B. M., He, B., and Nover, D. (2022). Influence assessment of new Inner Tube Porous Brick with absorbent concrete on urban floods control. *Case Stud. Constr. Mater* 17, e01236. doi:10.1016/J.CSCM.2022.E01236

Lv, R. B., Liang, S., Li, X. L., Hou, H. J., Ke, Y., Li, X. W., et al. (2022). Production of water-permeable ceramic bricks derived from fly ash via a simple pellet method: Mechanism of mechanical strength and permeability. *Constr. Build. Mater* 351, 128989. doi:10.1016/j.conbuildmat.2022.128989

Nguyen, T. T., Ngo, H. H., Guo, W. S., Wang, X. C., Ren, N. Q., Li, G. B., et al. (2019). Implementation of a specific urban water management-Sponge city. *Sci. Total Environ.* 652, 147–162. doi:10.1016/j.scitotenv.2018.10.168

Peng, J. S., Guan, Y. H., Lin, X. J., Xu, X. J., Xiao, L., Wang, H. H., et al. (2020). Comparative understanding of metal hyperaccumulation in plants: A mini-review. *Environ. Geochem Hlth* 43, 1599–1607. doi:10.1007/s10653-020-00533-2

Qi, B. W., Gao, S. W., and Xu, P. L. (2023). The application of rubber aggregate-combined permeable concrete mixture in sponge city construction. *Coating* 13 (1), 87–100. doi:10.3390/COATINGS13010087

Qin, Z., Yao, Y. J., Zhao, J. W., Fu, H. L., Zhang, S., and Qiu, L. Y. (2022). Investigation of migration rule of rainwater for sponge city roads under different rainfall intensities. *Environ. Geochem Hlth* 44, 3395–3407. doi:10.1007/S10653-021-01104-9

Rey, N. J., Demers, I., Bussière, B., Mbonimpa, M., and Gagnon, M. (2020). A geochemical evaluation of a monolayer cover with an elevated water table for the reclamation of the Doyon-Westwood tailings ponds, Canada. *Environ. Earth Sci.* 79, 58–69. doi:10.1007/s12665-019-8797-8

Sansalone, J. J., Kuang, X., and Ranieri, V. (2008). Permeable pavement as a hydraulic and filtration interface for urban drainage. *Irrig. Drain. Eng.* 134 (5), 666–674. doi:10.1061/(asce)0733-9437(2008)134:5(666)

Sarathchandra, S. S., Rengel, Z., and Solaiman, Z. M. (2022). Remediation of heavy metal-contaminated iron ore tailings by applying compost and growing perennial ryegrass (Lolium perenne L). *Chemosphere* 288, 132573. doi:10.1016/j.chemosphere.2021.132573

Seifeddine, K., Amziane, S., and Toussaint, E. (2022). Experimental investigation of physical characteristics to improve the cooling effect of permeable pavements. *Constr. Build. Mater* 345, 128342. doi:10.1016/J.conbuildmat.2022.128342

Shi, L., and Song, X. (2020). Influence of vanadium-titanium magnetite tailings on autoclaved aerated concrete blocks. *Iron Stl Vanadium Titan.* 41 (3), 84–89. doi:10.7513/i.issn.1004-7638.2020.03.014

Song, C. (2022). Application of nature-based measures in China's sponge city initiative: Current trends and perspectives. *Nature-Based Solu.* 2, 100010. doi:10.1016/j.nbsj.2022.100010

Sun, H. Y., Wei, X. F., Sun, X. M., Jia, F. C., Li, D. J., and Li, J. (2021). Bioaccumulation and translocation characteristics of heavy metals in a soil-maize system in reclaimed land and surrounding areas of typical vanadium-titanium magnetite tailings. *Environ. Sci.* 42 (3), 1166–1176. doi:10.13227/j.hjkx.202007200

Sun, Y., Gu, X. W., and Xu, X. C. (2021). Ecological restoration and mechanical reinforcement effect of slope of tailings reservoir. *Environ. Earth Sci.* 80, 80–12. doi:10.1007/s12665-020-09325-4

Tang, Z. E., Deng, R. J., Zhang, J., Ren, B. Z., and Hursthouse, A. (2019). Regional distribution characteristics and ecological risk assessment of heavy metal pollution of different land use in an antimony mining area—xikuangshan, China. *Hum. Ecol. Risk Assess.* 26, 1779–1794. doi:10.1080/10807039.2019.1608423

Tang, Y., Lin, H., Wang, Y. X., and Zhao, Y. (2021). Rock slope stability analysis considering the effect of locked section. *B Eng. Geol. Environ.* 80, 7241–7251. doi:10.1007/s10064-021-02366-4

Wang, X. G., and Qin, L. Y. (2019). Experimental study on preparation of high-strength concrete with vanadium-titanium magnetite tailings. *Iron Stl Vanadium Titan.* 40 (3), 77–82. doi:10.7513/i.issn.1004-7638.2019.03.014

Wang, K., Yang, P., Karen, H. E., Lv, W. S., and Bu, L. (2018). Status and development for the prevention and management of tailings dam failure accidents. *Chin. J. Eng.* 240 (5), 526–539. doi:10.13374/j.issn2095-9389.2018.05.002

Wang, C. L., Ren, Z. Z., Zheng, Y. C., Ye, P. F., Zhang, K. F., and Cui, X. W. (2019). Effects of heat treatment system on mechanical strength and crystallinity of CaO-MgO-$Al_2O_3$-$SiO_2$ glass-ceramics containing coal gangue and iron ore tailings. *J. New Mat.* 22 (2), 70–78. doi:10.14447/jnmes.v22i2.a02

Wang, Y. G., Gao, S., Liu, X. M., Tang, B. W., Mukiza, E., and Zhang, N. (2019). Preparation of non-sintered permeable bricks using electrolytic manganese residue: Environmental and NH3-N recovery benefits. *J. Hazard Mater* 378, 120768. doi:10.1016/j.jhazmat.2019.120768

Wang, Z. Y., Guo, J. L., and Li, C. (2019). Study on the preparation and performance of iron tailing-based glass permeable bricks. *Mine Prot. Util.* 34 (4), 66–70. doi:10.13779/j.cnki.issn1001-0076.2019.04.011

Wang, C. L., Li, Y., Cai, H., and Xiao, J. Z. (2021). *New type of concrete based industrial solid waste*. Beijing: Science Press.

Wang, S. X., Zhang, K. F., Zang, S. H., Ye, P. F., Wang, Y. B., Zhai, Y. X., et al. (2021). Preparation and properties study of high-strength sintered permeable brick with multiple solid waste. *Metal. Mine* 9, 206–215. doi:10.19614/j.cnki.jsks.202109029

Wang, C. L., Wang, Z. J., Yang, F. H., and Zheng, Y. C. (2022). *Preparation of new green building materials from tailings and steel slag*. Beijing: Science Press.

Wang, H. F., Liu, Y., and Mei, Z. (2022). Basic physical characteristics of the water-permeable brick with composite structure. *J. Wuhan. Univ. Techonl* 37, 645–655. doi:10.1007/S11595-022-2579-Y

Wang, C. L., Jing, J. L., Qi, Y., Zhou, Y. X., Zhang, K. F., Zheng, Y. C., et al. (2023a). Basic characteristics and environmental impact of iron ore tailings. *Front. Earth Sci.* 11, 1181984. doi:10.3389/feart.2023.1181984

Wang, C. L., Ma, J. T., Yang, F. H., Zhang, G. Q., Chen, J. L., Jing, J. L., et al. (2023b). Preparation and properties of composite cementitious materials containing vanadium-titanium iron ore tailings. *Iron Stl Vanadium Titan.* 44 (1), 98–105. doi:10.7513/j.issn.1004-7638.2023.01.017

Wang, C. L., Qi, Y., Jing, J. L., Ma, J. T., Zhou, Y. X., Ping, H. Y., et al. (2023c). Properties and microstructure of total tailings cemented paste backfill material containing mining and metallurgical solid waste. *Front. Earth Sci.* 11, 1181952. doi:10.3389/feart.2023.1181952

Xi, C. P., Zheng, F., Xu, J. H., Yang, W. G., Peng, Y. Q., Li, Y., et al. (2018). Preparation of glass-ceramic foams using extracted titanium tailing and glass waste as raw materials. *Constr. Build. Mater* 190, 896–909. doi:10.1016/j.conbuildmat.2018.09.170

Xu, Y. S., Shen, S. L., Lai, Y., and Zhou, A. N. (2018). Design of sponge city: Lessons learnt from an ancient drainage system in Ganzhou, China. *J. Hydrol.* 563, 900–908. doi:10.1016/jjhydrol.2018.06.075

Xu, S., Cao, B. Y., Liu, X., Wu, J., Wang, J., and Du, M. L. (2019). Study on preparation of permeable brick by activated sludge doping tailings and its performance. *Non-metallic Min.* 42 (5), 28–30.

Yan, Z. Q., Qing, Z. Q., Guo, M., Yi, G. L., Shi, Y. L., Cheng, F. Q., et al. (2020). Pilot and industrial scale tests of high-performance permeable bricks producing from ceramic waste. *J. Clean. Prod.* 254, 120167. doi:10.1016/j.jclepro.2020.120167

Yang, F., and Sun, X. M. (2020). Preparation of ordinary Portland clinker with vanadium-titanium magnetite tailings. *Iron Stl Vanadium Titan.* 41 (2), 75–81. doi:10.7513/i.issn.1004-7638.2020.02.015

Yang, M., Ju, C. G., Xue, K. R., Peng, Y. Z., Han, H., Wan, Q. Q., et al. (2021). Environmental-friendly non-sintered permeable bricks: Preparation from wrap-shell lightweight aggregates of dredged sediments and its performance. *Constr. Build. Mater* 273, 121751. doi:10.1016/j.conbuildmat.2020.121751

Ye, P. F. (2021). *Preparation and mechanism of high-strength permeable brick from vanadium-titanium iron ore tailings*. Handan: University of Engineering.

Young, G., Chen, Y., and Yang, M. (2021). Concentrations, distribution, and risk assessment of heavy metals in the iron tailings of Yeshan National Mine Park in Nanjing, China. *Chemosphere* 271, 129546. doi:10.1016/j.chemosphere.2021.129546

Yu, X. M., Kang, X., Li, Y. M., Cui, Y. L., Tu, W. G., Shen, T., et al. (2019). Rhizobia population was favoured during *in situ* phytoremediation of vanadium-titanium magnetite mine tailings dam using Pongamia pinnata. *Environ. Pollut.* 255, 113167. doi:10.1016/j.envpol.2019.113167

Yu, T. J., Liu, D. G., Zhang, H. T., and Wang, H. D. (2021). Influence of pore water phase change on service performance for permeable pavement in sponge city. *Water Sci. Technol.* 84 (12), 3769–3779. doi:10.2166/WST.2021.459

Zhang, X., Yang, H., and Cui, Z. (2018). Evaluation and analysis of soil migration and distribution characteristics of heavy metals in iron tailings. *J. Clean. Prod.* 172, 475–480. doi:10.1016/j.jclepro.2017.09.277

Zhang, Y., Zhang, T. A., Dreisinger, D., Lv, C. X., Lv, G. Z., and Zhang, W. G. (2019). Recovery of vanadium from calcification roasted-acid leaching tailing by enhanced acid leaching. *J. Haz Mat.* 369, 632–641. doi:10.1016/j.jhazmat.2019.02.081

Zhang, J. J., Liu, B., and Zhang, S. G. (2021). A review of glass ceramic foams prepared from solid wastes: Processing, heavy-metal solidification and volatilization, applications. *Sci. Total Environ.* 781, 146727. doi:10.1016/j.scitotenv.2021.146727

Zhang, H. Z., Qi, Y., Jing, J. L., Wang, C. L., Zhou, Y. X., Zhang, K. F., et al. (2023). Properties and environmental impact of building foundation pit backfilling materials containing iron and steel solid waste. *Front. Earth Sci.* 11, 1181974. doi:10.3389/feart.2023.1181974

Zhao, X., Fourie, A., and Qi, C. C. (2020). Mechanics and safety issues in tailing-based backfill: A review. *Int. J. Min. Met. Mater* 27 (9), 1165–1178. doi:10.1007/s12613-020-2004-5

Zhu, X. Y., Sun, N., Huang, Y., Zhu, Y. G., and Wang, W. Q. (2021). Preparation of full tailings-based foam ceramics and auxiliary foaming effect of vanadium-titanium magnetite tailings. *J. Non-Cryst Solids.* 571, 121063. doi:10.1016/j.jnoncrysol.2021.121063

frontiers | Frontiers in Earth Science

TYPE Original Research
PUBLISHED 23 June 2023
DOI 10.3389/feart.2023.1212017



OPEN ACCESS

EDITED BY
Lijie Guo,
Beijing Mining and Metallurgy Technology Group Co. Ltd., China

REVIEWED BY
Xinglan Cui,
General Research Institute for Nonferrous Metals, China
Zhihong Zhang,
Beijing University of Technology, China

*CORRESPONDENCE
Zhongqun Guo,
guozhongqun_jxust@163.com

RECEIVED 25 April 2023
ACCEPTED 12 June 2023
PUBLISHED 23 June 2023

CITATION
Guo Z, Liu L, Zhou K, Wang X and Zhong W (2023), Research on the saturated/unsaturated seepage laws of ionic rare earth ore under different leaching conditions.
*Front. Earth Sci.* 11:1212017.
doi: 10.3389/feart.2023.1212017



# Research on the saturated/unsaturated seepage laws of ionic rare earth ore under different leaching conditions

Zhongqun Guo[1,2]*, Lingfeng Liu[1], Kefan Zhou[1], Xiaojun Wang[2] and Wen Zhong[2]

[1]School of Civil Engineering and Surveying and Mapping Engineering, Jiangxi University of Science and Technology, Ganzhou, China, [2]Jiangxi Key Laboratory of Mining Engineering, Jiangxi University of Science and Technology, Ganzhou, China

The seepage law of the ionic rare earth leaching process plays an important role in the efficient development and utilization. The saturation permeation test of ionic rare earth under different leaching conditions was carried out using the variable head method, and the influence of type, concentration, and leaching path on the saturation permeability coefficient was revealed. The relationship between the water content and the matric suction of ionic rare earths under different leaching conditions was measured with the Geo-Experts pressure plate apparatus, and the soil-water characteristic curves under different leaching conditions were obtained. Based on the soil-water characteristic curve model, the unsaturated permeability coefficient function of ionic rare earths under different conditions was studied. The results show that the saturated-unsaturated permeability coefficients of ionic rare earths are pure water, 3% $(NH_4)_2SO_4$, and 3% $MgSO_4$, in descending order, when the type of leaching solution is different. For different concentrations of the leaching solution, when the concentration of $(NH_4)_2SO_4$ increases from 2% to 5%, the saturated permeability coefficient first increases and then decreases. The matrix suction is an important factor affecting the unsaturated permeability coefficient when the ore body is unsaturated, and the unsaturated permeability coefficient decreases with the increase of the leaching solution concentration under the same matric suction. The seepage law is related to the leaching path, and the permeability coefficient increases when leaching at high concentrations followed by low concentrations, in reverse order, the permeability coefficient decreases. The research results can provide theoretical guidance for the design of injection parameters, and improve the theory of in-situ leaching.

KEYWORDS

**ionic rare earths, in-situ leaching, soil-water characteristic curve, saturated permeability coefficient, unsaturated permeability**

## 1 Introduction

Ionic rare earths are an important strategic mineral resource and play an important role in the national defense industry and high-precision technology products (Ilankoon et al., 2018; Nie et al., 2020; Liu et al., 2021). In these ores, rare earth elements, which are adsorbed on the clay minerals through hydrated cations or hydroxyl-hydrated cations, are difficult to enrich by conventional selection techniques. After years of research by scientific and technological workers, ionic rare earths have successively experienced the mining methods of pool leaching, heap

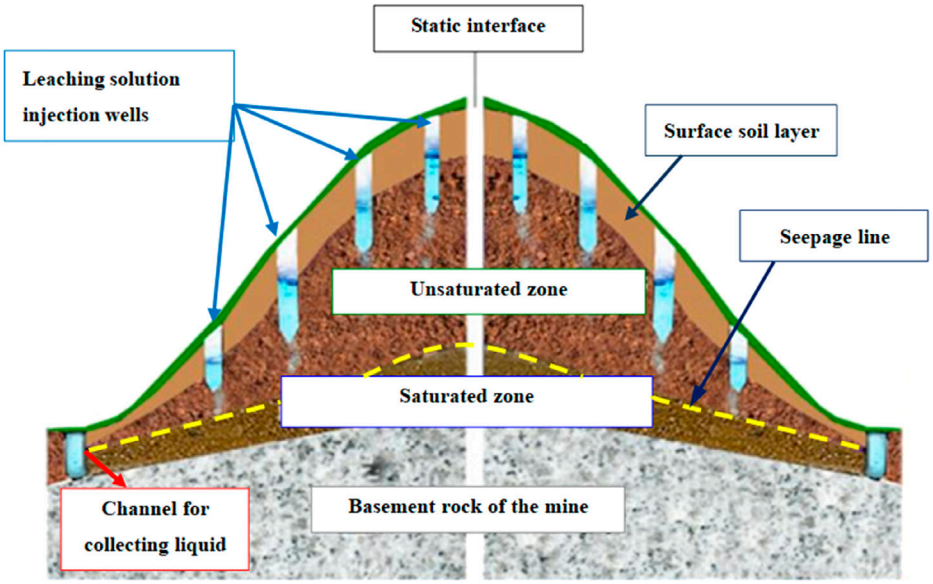


FIGURE 1
Diagram of ionic rare earth *in situ* leaching.

leaching, and *in-situ* leaching (Zhang et al., 2016; Chi et al., 2019; Zhou et al., 2019). *In-situ* leaching has the advantages of being a simple process with low cost and low disruption, and is currently widely recommended (Deng et al., 2016; He et al., 2017). The schematic diagram of *in situ* leaching is shown in Figure 1. The permeability of the ore body has an important impact on the *in situ* leaching velocity and leaching rate, which are directly related to the efficient recovery and utilization of rare earth resources. The seepage of *in situ* leaching is a dynamic process that includes two stages: unsaturated and saturated seepage. It is of great significance to study the saturated-unsaturated permeation characteristics of ionic rare earths under different leaching conditions to improve leaching efficiency.

During the *in situ* leaching process, parameters such as water content, matric suction, and permeability coefficient all changed (Wu et al., 2005; Long et al., 2019). Many scholars have conducted relevant studies on the saturation permeation characteristics of ionic rare earths. (Yin et al., 2015; Yin et al., 2018) studied the relationship between particle size and capillary rise rate, pore ratio, and permeability of ionic rare earth ore. (Jin et al., 2015; Guo et al., 2017) investigated the influence of particle size of ionic rare earth ore on the one-dimensional vertical seepage law. (Guo et al., 2020) wrote about the effects of particle size and grain composition on the two-dimensional infiltration characteristics of ionic rare earths. (Wang et al., 2017) studied the seepage mechanism of ionic rare earths at the microscopic and mesoscopic scales. Currently, the research on the seepage characteristics of ionic rare earth ore mainly focuses on saturated permeation, and the research on unsaturated permeability characteristics is inadequate. Since the unsaturated permeability coefficient is difficult to be directly measured by experiments, the soil-water characteristic curve model and the saturated permeability coefficient are typically used to derive the unsaturated permeability coefficient function and reveal the unsaturated permeability law of rock and soil (Ma et al., 2016).

In this study, rare earth ore samples from Jiangxi Province were selected to carry out saturation seepage experiments and soil-water characteristic experiments; the saturated permeability coefficient and soil-water characteristic curve of the ore body under different leaching conditions were obtained and revealed the saturated/unsaturated seepage law of ionic rare earths under different types, concentrations, and leaching paths, which provided a theoretical basis for the prediction of the *in situ* leaching rate and the regulation of the leaching solution injection.

## 2 Test materials and methods

### 2.1 Test materials

The ore samples were selected from a rare earth mine in Longnan, Jiangxi Province. The basic physical parameters of the samples are listed in Table 1. The particle size distribution curve of rare earth ore is shown in Figure 2.

The samples were remolded in accordance with the dry density and water content of the undisturbed soil. The quantitative X-ray diffraction (XRD) analysis of the ore samples was carried out, and the results are shown in Figure 3.

### 2.2 Test devices and methods

The saturation permeability coefficient was measured using the TST-55 variable head permeameter (Gao et al., 2008). The device is shown in Figure 4. The samples were saturated with a vacuum saturator for 24 h, and then the saturation penetration experiment was carried out to measure the saturation

**TABLE 1** Basic physical parameters of rare earth ores.

| Density $\rho$/ (g·cm$^{-3}$) | Water content $\theta$/% | Specific gravity $G_s$/ (g·cm$^{-3}$) | Void ratio $e$ | Liquid limit $w_L$/% | Plastic limit $w_P$/% | Plastic index $I_p$ |
|---|---|---|---|---|---|---|
| 1.43 | 16.46 | 2.68 | 0.86 | 41.17 | 30.83 | 10.34 |

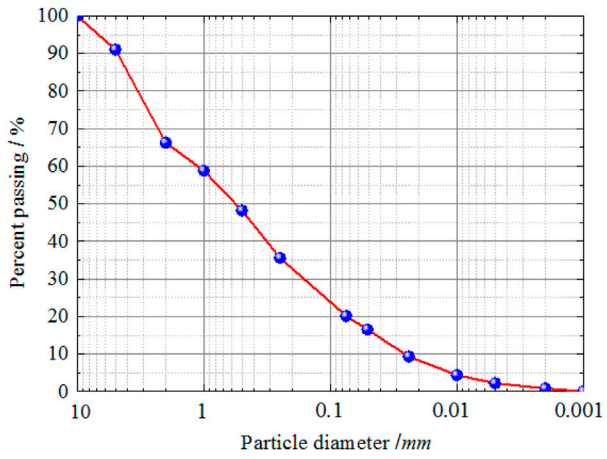


FIGURE 2
Particle size distribution curve of rare earth ore sample.

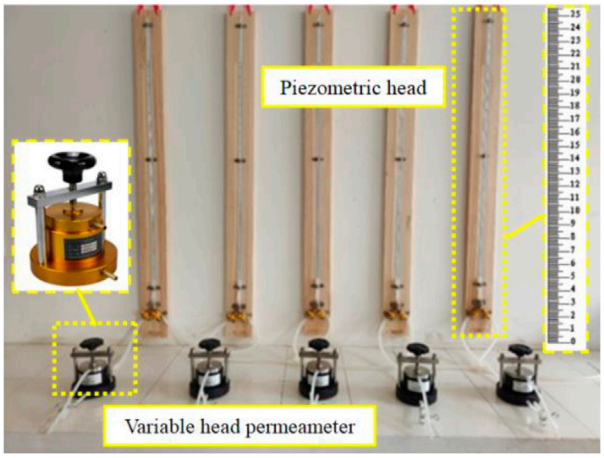


FIGURE 4
The saturation penetration apparatus.

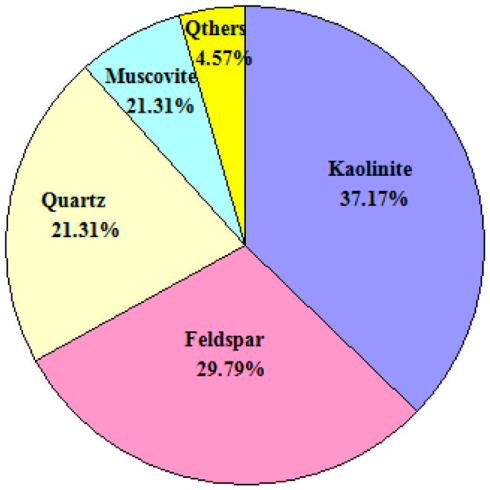


FIGURE 3
XRD mineral composition analysis of rare earth ore samples.

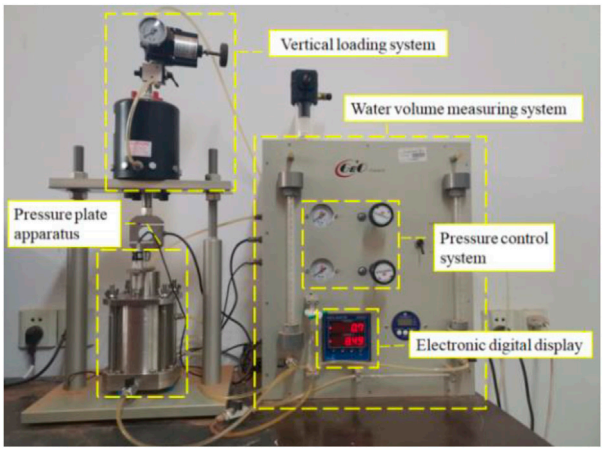


FIGURE 5
The Geo-Experts pressure plate test apparatus.

permeability coefficient of ionic rare earth under different types, concentrations, and leaching paths.

The Geo-Experts pressure plate apparatus was used for the soil-water characteristic experiment, and the device is shown in Figure 5. First, ionic rare earth samples were prepared and saturated with leaching solution under the same conditions, and then the soil-water characteristic experiments were carried out to measure the corresponding soil-water content under different matrices of suction. For a single matrix suction, when the 24 h change was less than 0.1 mm, the equilibrium state was considered to have been reached under that specific matric suction (Pham et al., 2005; Fredlund et al., 2006).

## 2.3 Data calculation

The following logarithmic formula was used to calculate the saturated permeability coefficient of ionic rare earths:

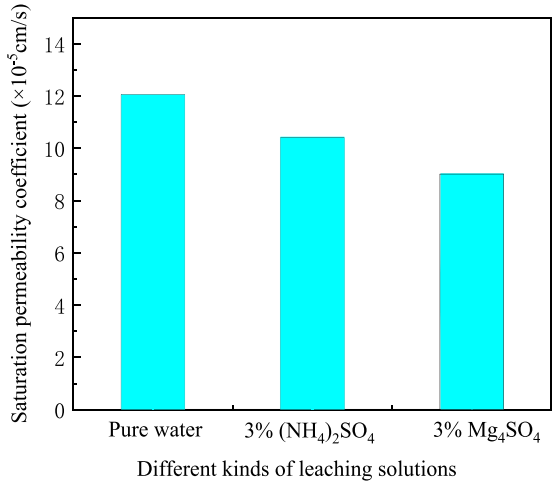


FIGURE 6
Saturated permeability coefficients for different leaching solutions.

$$k_T = 2.3\frac{aL}{A\Delta t}\ln\frac{h_1}{h_2} \quad (1)$$

where $k_T$ is the saturation permeability coefficient; $a$ is the cross-sectional area of the variable head pipe; A is the cross-sectional area of the cutting ring; the value of 2.3 is the conversion factor of ln; L is the height of the cutting ring; $\Delta t$ is the start and end interval of the measured water head; $h_1$ and $h_2$ are the start and end water heads.

For the soil-water characteristic curve of ionic rare earths, the mass water content under different matric suction was measured experimentally and converted into volume water content, and the matric suction and volume water content at all levels were plotted in a semi-logarithmic coordinate system to obtain the corresponding soil-water characteristic curve. The corresponding volume water content of the different matrices suction is:

$$\theta = \frac{w\rho_d}{\rho_w} \quad (2)$$

where $\theta$ is the volume water content, $w$ is the mass water content, $\rho_d$ is the dry density of soil, and $\rho_w$ is the density of water.

The soil-water characteristic curve is the basis for research on the permeability characteristics of unsaturated soil, and many scholars have proposed the relevant soil-water characteristic curve model (Van Genuchten et al., 1980; Rajkai et al., 1996; Chiu et al., 2012). Research shows that the Fredlund and Xing model has high adaptability to the soil-water characteristic curve of ionic rare earths (Guo et al., 2021); therefore, their three-parameter model was used for analysis. The expression of Fredlund and Xing's three-parameter model (Fredlund et al., 1994) is as follows:

$$\frac{\theta}{\theta_s} = \frac{1}{\left\{\ln\left[e + \left(\frac{\psi}{a}\right)^n\right]\right\}^m} \quad (3)$$

where $\theta$ is the volume water content, $\theta_s$ is the saturated water content, and $\psi$ is the matrix suction. $a$, $n$, and $m$ are the three optimization parameters of the model. The parameter $a$ is related to the air-entry value, $n$ is a parameter related to the drying rate and it controls the slope of the SWCC, $m$ is a parameter related to the residual water and it is correlated with the overall symmetry of the curve. This model assumes that there is a small $\theta_r$. For simplification of the models, it is hypothesized that $\theta_r$=0.

# 3 Saturation seepage law for ionic rare earths under different leaching conditions

## 3.1 Saturation permeability under different leaching solutions

The saturated permeability coefficients of ionic rare earth under the different types of leaching solutions are shown in Figure 6. When the leaching solution was pure water, 3% $(NH_4)_2SO_4$, and 3% $MgSO_4$, the corresponding saturation permeability coefficients were 12.05 × $10^{-5}$ cm/s, 10.4 × $10^{-5}$ cm/s, and 9.01 × $10^{-5}$ cm/s, respectively. It can be seen that the saturation permeability coefficient decreased sequentially. The analysis suggests that in the seepage process, pure water did not undergo a chemical exchange reaction with rare earth ions, the migration and agglomeration of soil particles resulted in an increase of the effective seepage channel in the soil, and then the saturated permeability coefficient of pure water was greater.

When the leaching solution was 3% $MgSO_4$ and 3% $(NH_4)_2SO_4$, both underwent chemical exchange reactions with rare earth ions adsorbed on clay minerals. The exchange reactions between $NH^{4+}$, $Mg^{2+}$ and rare earth ions cause the agglomeration, disintegration, and migration of soil particles, resulting in the blockage of seepage channels; therefore, the permeability characteristic was reduced. Consequently, the saturated permeability coefficients of 3% $(NH_4)_2SO_4$ and 3% $MgSO_4$ were significantly smaller than those of pure water. The chemical exchange reaction formula is as follows:

$$\left[Al_2Si_2O_5(OH)_4\right]_m \cdot 2nRE^{3+}(s) + 3nMg^{2+}(aq) \rightleftharpoons \left[Al_2Si_2O_5(OH)_4\right]_m \cdot \left[Mg^{2+}\right]_{3n}(s) + 2nRE^{3+}(aq)$$

$$\left[Al_2Si_2O_5(OH)_4\right]_m \cdot 2nRE^{3+}(s) + 3nNH_4^+(aq) \rightleftharpoons \left[Al_2Si_2O_5(OH)_4\right]_m \cdot \left[NH_4^+\right]_{3n}(s) + nRE^{3+}(aq)$$

The results show that the cations adsorbed on the clay can exchange with the divalent cation in the solution during the permeation experiment, thereby resisting the dispersion of soil particles and preventing the formation of micro-fissures. Similar results were obtained with $Mg^{2+}$ in this experiment. For the leaching solution of 3% $MgSO_4$, $Mg^{2+}$ not only reacted with the divalent cations adsorbed by clay minerals but also exchanged reactions with the monovalent cation therein, adsorbed on the surface of ionic rare earth particles, so that the thickness of the combined water layer increased, at the same time leading to the reduction of the porous channel between the particles, further reducing the permeability characteristic of ionic rare earth. Consequently, the permeability coefficient of 3% $MgSO_4$ appeared to be slightly lower than that of 3% $(NH_4)_2SO_4$.

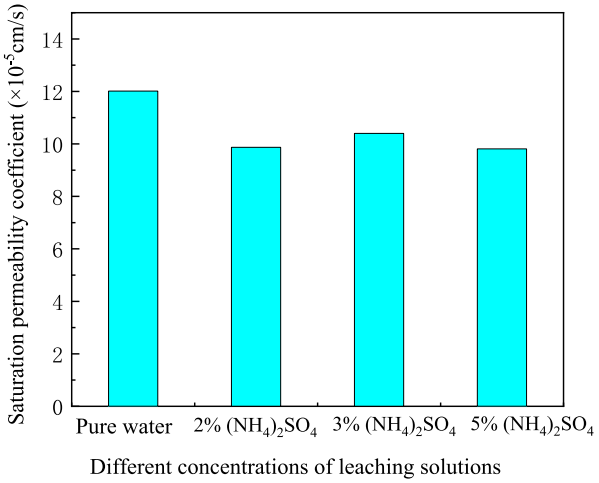


FIGURE 7
Saturated permeability coefficient under different concentrations of leaching solution.

## 3.2 Saturation permeability at different leaching solution concentrations

The saturated permeability coefficients of ionic rare earth under different concentrations of leaching solution are shown in Figure 7, and the saturated permeability coefficients of ionic rare earth corresponding to pure water, 2% $(NH_4)_2SO_4$, 3% $(NH_4)_2SO_4$, and 5% $(NH_4)_2SO_4$ are 12.05× $10^{-5}$ cm/s, 9.87 × $10^{-5}$ cm/s, 10.4 × $10^{-5}$ cm/s, and 9.81 × $10^{-5}$ cm/s, respectively. It can be seen that the saturation permeability coefficient is the largest under the leaching of pure water, and when the concentration of the leaching solution increased from 2% to 5%, the saturation permeability coefficient increased and then decreased, with the saturation permeability coefficient under the leaching of 3% $(NH_4)_2SO_4$ being greater than in the other two conditions.

It is believed that the concentrations of leaching solution have a certain influence on the structure of the electrical double layer of the soil. The double layer on the surface of the soil particles includes an adsorption layer and a diffusion layer, and during the seepage process, the diffusion layer moved with the cations. The thickness of the electrical double layer is closely related to the ion concentration, and with the increase in concentration of the leaching solution, the diffusion layer will decrease, so the seepage channel will expand, and the permeability coefficient will increase.

In the seepage process, $NH^{4+}$ and the rare earth ions on the surface of the clay mineral underwent chemical exchange reactions, and the more $NH^{4+}$ of leaching solution, the smaller saturation permeability coefficient appears. At the same time, the electrical double layer on the surface of the soil particles was affected, but the effect of the ion exchange reaction was less than the weakening effect of the thickness of the double electrical layer.

With the increase of concentration, the ion exchange reaction became more violent , and the weakening effect of the electric double layer began to be lower than that of the ion exchange reaction, thereby inhibiting the seepage effect, making the permeation characteristics smaller. Considering the combined influence of the double electrical layer and the ion exchange reaction degree, the saturation permeability coefficient of the ore body under the leaching of 5% $(NH_4)_2SO_4$ was found to be smaller than that of 3% $(NH_4)_2SO_4$.

## 3.3 Saturation permeability under different leaching paths

The leaching solution was set as $(NH_4)_2SO_4$, and two groups of experiments were set up for control: "first high concentration followed by low concentration" and "first low concentration followed by high concentration," respectively. "First high concentration followed by low concentration" means that ionic rare earths used a high concentration leaching solution for saturated leaching for 24 h before the seepage experiment, and then used a low concentration leaching solution for seepage. Three working conditions were set: 3%→3%, 3%→1%, 3%→0%. In contrast, a low concentration leaching solution was used for saturation solution for 24 h, and then a high concentration leaching solution was used to seep, with three working conditions being set: 0%→3%, 1%→3%, 3%→3%. The relationship between the saturated permeability coefficient of the ore body under different leaching paths is shown in Figure 8.

It can be seen from Figure 8A that the saturated permeability coefficient of ionic rare earths under the leaching of 3%→3%, 3%→1%, 3%→0% was 10.40 × $10^{-5}$ cm/s, 10.67 × $10^{-5}$ cm/s, and 8.42 × $10^{-5}$ cm/s, respectively. The saturation permeability coefficient of the ore body showed little difference. The saturated permeability coefficient under the leaching of 3%→1% increased slightly, and the leaching of 3%→0% was the smallest.

Our analysis shows that during the "first high concentration followed by low concentration" phase, as the free water diffused from a high concentration to a low concentration, the soil particles produced a repulsive force from the inside to the outside, causing the soil particles to break, blocking the seepage channel, and reducing permeability. At the same time, the ion exchange reaction was weakened, the effect on soil particles was reduced, and the permeability of ionic rare earths improved. Under 3%→0% working conditions, the permeability was reduced by the larger concentration difference. At this time, the effect of the ion exchange reaction was less than that of the seepage; therefore, its saturation permeability coefficient was minimal. Under 3% →1% working conditions, the difference in concentration was smaller than that of 3%→0% working conditions, the repulsive force was also smaller, and the degree of permeability was relatively small.

It can be seen from Figure 8B that the saturated permeability coefficient of ionic rare earth under the leaching of 3%→3%, 1%→3%, 0%→3% was 10.40 × $10^{-5}$ cm/s, 7.91 × $10^{-5}$ cm/s, and 8.87 × $10^{-5}$ cm/s, respectively. The first path had the largest saturation permeability coefficient, and the 1% →3% path had the smallest.

The analysis shows that during the "first low concentration followed by high concentration" phase, the concentration difference also produced a repulsive force from the outside to the inside of the soil particles, promoting the agglomeration of soil particles,

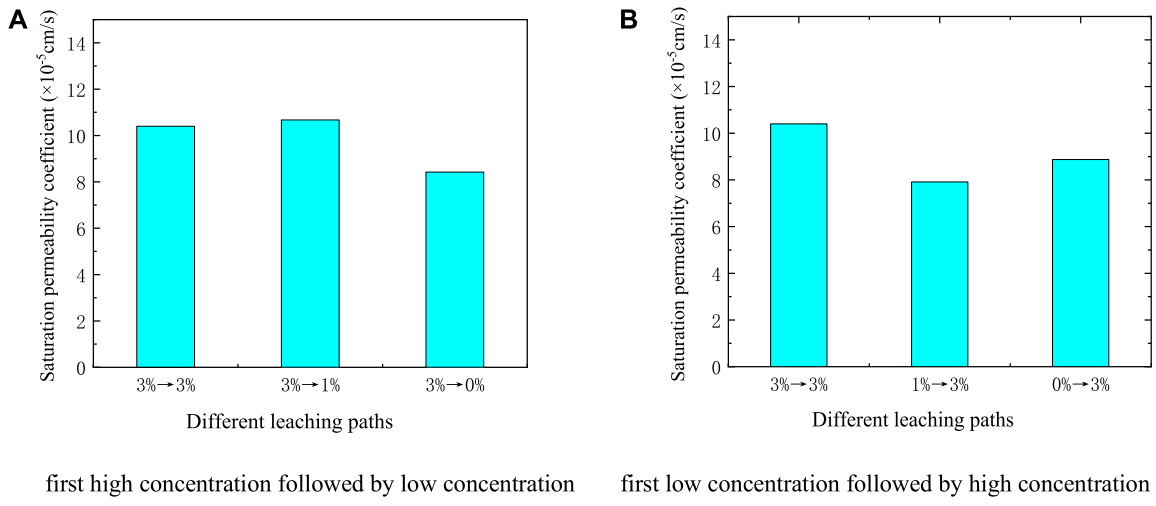


FIGURE 8
The saturated permeability coefficient of different leaching paths **(A)** First high concentration followed by low concentration **(B)** First low concentration followed by high concentration.

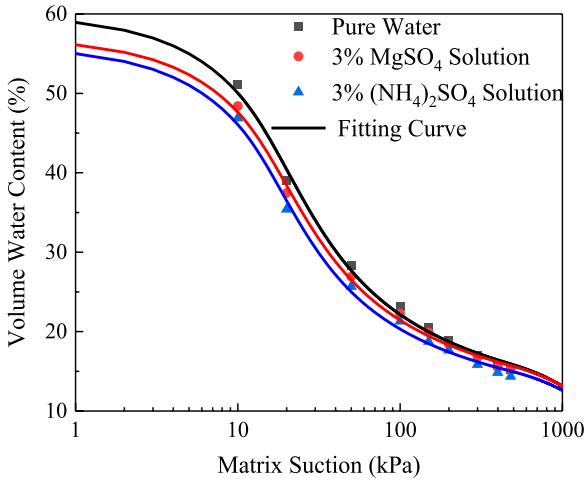


FIGURE 9
Soil-water characteristic curves under different types of leaching solutions.

expanding the seepage channel, and increasing the permeability. When high concentration seepage was used, the ion exchange reaction of rare earths worsened, resulting in the fragmentation and migration of soil particles, and the permeability decreased. Under 1%→3% working conditions, because the effect of the ion exchange reaction was greater than that of the seepage, caused the smallest permeability coefficient by joint action. Under 0%→3% working conditions, the concentration difference caused by the seepage was larger than that under 1%→3% working conditions, and the permeability improved. Therefore, the saturation permeability coefficient under 0%→3% working conditions was larger than that of the former.

# 4 Soil-water characteristic curves of ionic rare earths under different leaching conditions

## 4.1 Soil-water characteristic curves under different types of leaching solutions

In order to study the effect of different types of leaching solutions on the soil-water characteristics of ionic rare earths, drying tests were carried out using 3% $(NH_4)_2SO_4$, 3%$MgSO_4$, and pure water, and the water content data were recorded under different matrixes of suction. In this study, the influence of the "hysteresis effect" was not considered, and the drying curve was used to represent the typical soil-water characteristic curve of the ore body. Based on the Fredlund and Xing model, a fitting analysis was carried out, and the obtained soil-water characteristic curves are shown in Figure 9.

The test results show that under pure water conditions, the saturated volume of water content was the largest. Under 3% $(NH_4)_2SO_4$ conditions, the saturated volume water content was the smallest. Under the same matric suction, the water-holding performance of ionic rare earth appeared to be significantly different; pure water had the best water-holding performance, and 3% $(NH_4)_2SO_4$ had the poorest.

Our analysis suggests that pure water did not react with rare earth ions; therefore, the pores of ionic rare earths under pure water conditions basically did not change, resulting in a large, saturated volume of water content. Concentrations of 3% $(NH_4)_2SO_4$ and 3% $MgSO_4$ exchanged with the ionic rare earth, which changed the structure of the soil, resulting in poorer water-holding performance. The capacity of bound water in 3% $(NH_4)_2SO_4$ was stronger than that of 3% $MgSO_4$, but under the same matric suction range, the water content of ionic rare earth under the condition of 3% $(NH_4)_2SO_4$ was lower than that of 3% $MgSO_4$.

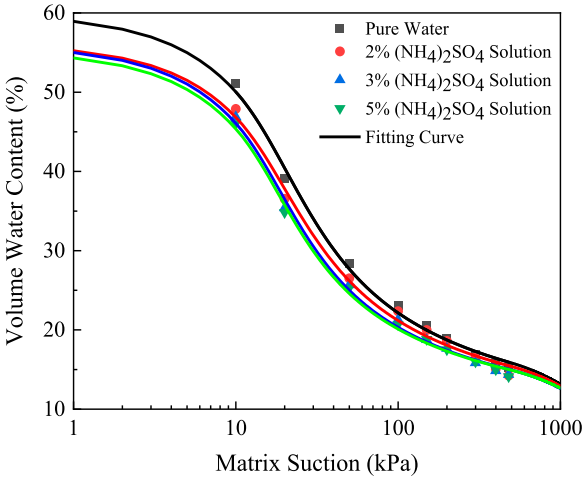


FIGURE 10
Soil-water characteristic curves at different concentrations of leaching solution.

## 4.2 Soil-water characteristic curves at different concentrations of leaching solution

The soil-water characteristic curves at different concentrations of leaching solutions are shown in Figure 10. It can be seen that the SWCC under pure water conditions was significantly higher than that of other concentrations. Under the same matric suction, the water content of the low concentration leaching solution was slightly higher than that of the high concentration leaching solution. As the concentration of the leaching solution decreased, the volume water content of the ionic rare earth increased, and the water holding capacity also increased.

The analysis suggests that pure water had the greatest water-holding capacity, and that it did not undergo chemical exchange reactions with rare earth ions, which had little effect on the size of ionic rare earth particles. Under other concentrations of leaching conditions, ion exchange reactions occurred, resulting in changes in the internal structure of the soil and changes in water holding capacity. As the concentration of the leaching solution increased, the chemical reaction that occurred during the leaching process became more intense, and the pore structure changed greatly, resulting in the deterioration of the water-holding performance of the ore body at high concentrations.

## 4.3 Soil-water characteristic curves under different leaching paths

The SWCCs of ionic rare earth under different leaching paths are shown in Figure 11. It can be seen that for 0% →3% working conditions, the water-holding characteristic of an ionic rare earth ore body was the best. Under the same matric suction, its water content was greater than that of other working conditions. For 3%→0% working conditions, ionic rare earth samples had the worst water-holding characteristics. When the matric suction was small, the water content was minimal compared to other working conditions. It can be seen that their water-holding performance was poor, but their residual water content was large. For different path conditions composed of 3% $(NH_4)_2SO_4$ and 1% $(NH_4)_2SO_4$, there was little difference between the two.

The analysis indicates that under "0%→3%" working conditions, because the free water diffused from the high concentration solution to the low concentration solution, this concentration difference produced diffusion force, promoted the formation of agglomerates of fine particles in ionic rare earth samples, and expanded the pores, resulting in a large, saturated volume water content. Under "3%→0%" working conditions, the

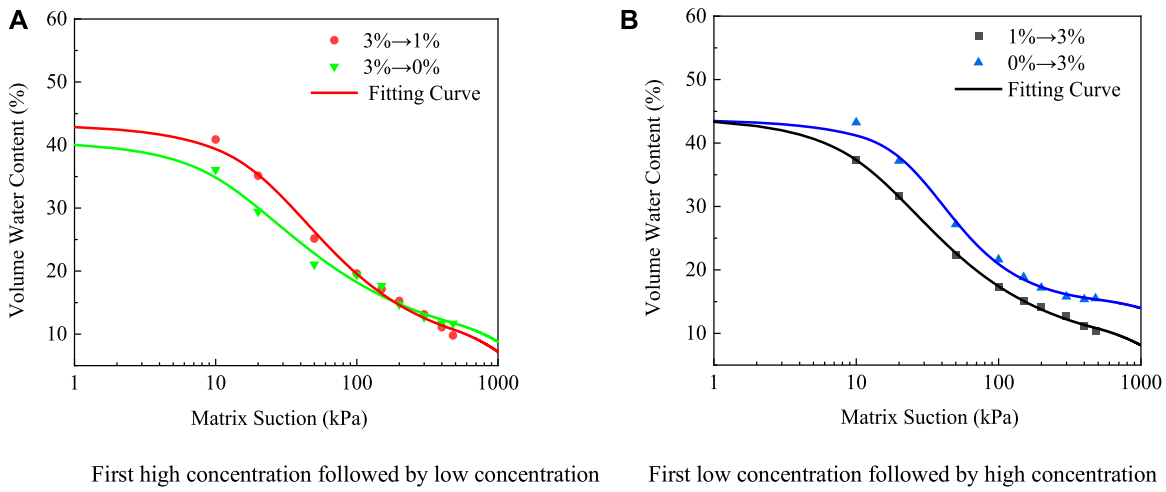


FIGURE 11
Soil-water characteristic curves under different leaching paths **(A)** First high concentration followed by low concentration **(B)** First low concentration followed by high concentration.

10.3389/feart.2023.1212017

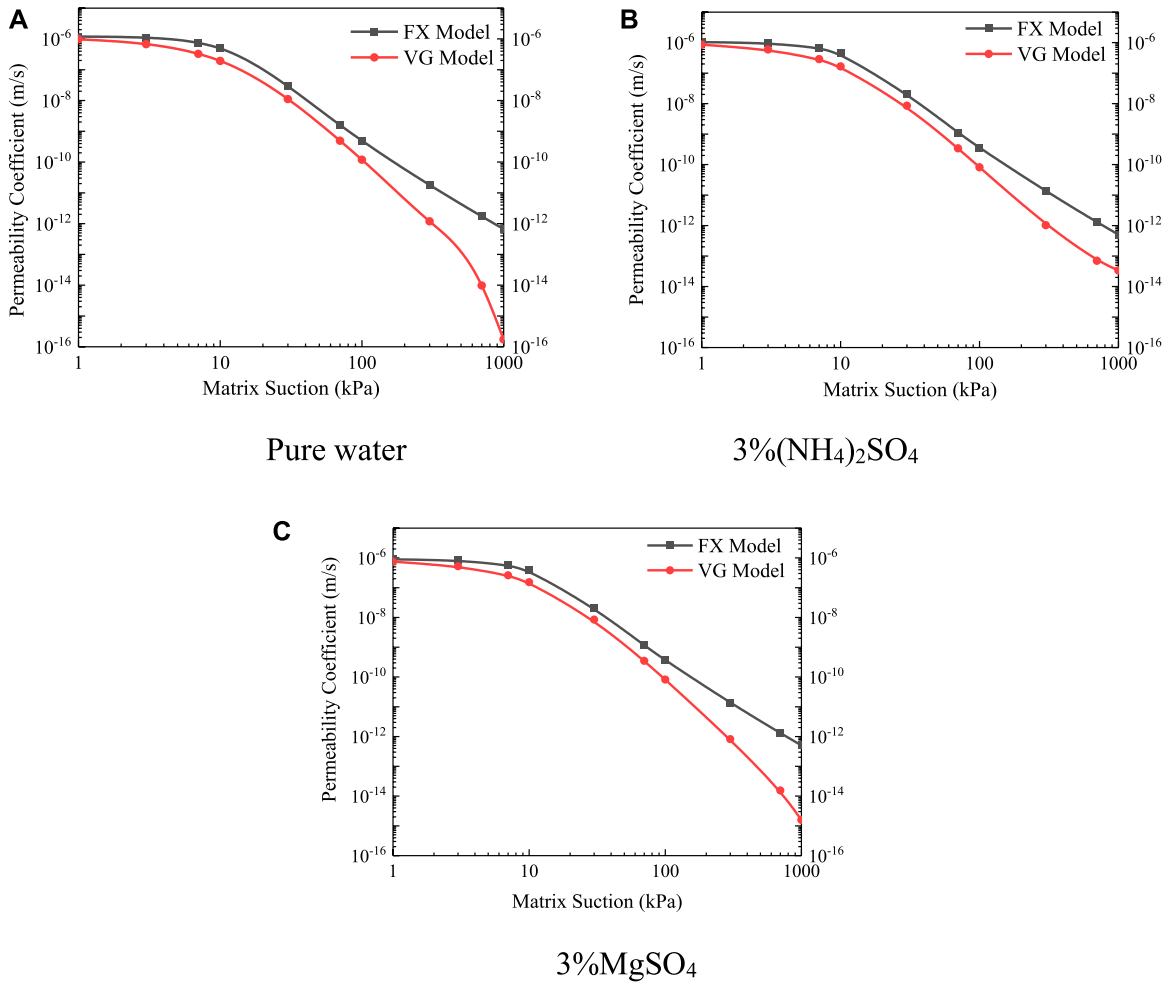


FIGURE 12
Unsaturated permeability curves under different types of leaching solutions **(A)** Pure water **(B)** 3% $(NH_4)_2SO_4$ **(C)** 3% MgSO4.

high concentration of leaching solution disintegrated and transported the ore body particles, resulting in the blockage of pores in the soil and the narrowing of the voids, therefore minimizing the saturated volume water content. For 3%→1% and 1%→3% working conditions, because of the small concentration difference, the diffusion force brought by the concentration difference was smaller than the effect of the ion exchange reaction, its internal structure changed marginally, and so did the water-holding performance of the ore body under these two working conditions.

# 5 Unsaturated seepage law of ionic rare earths under different leaching conditions

## 5.1 Unsaturated permeability coefficient function

Unsaturated permeation parameters are difficult to obtain directly from experiments and were calculated indirectly (Zhai et al., 2019). In this study, the Van Genuchten-Mualem model and the Fredlund unsaturated permeability coefficient function were used to calculate the unsaturated permeability function of ionic rare earths, and the unsaturated permeability coefficient was characterized by the saturated permeability coefficient and matric suction.

The Van Genuchten-Mualem model used the Van Genuchten soil-water characteristic curve model and the Mualem permeability equation to obtain the unsaturated permeability coefficient $k_u$ under different matrixes of suction, and is expressed as follows:

$$k_u = k_s \frac{\left\{1 - (a\psi)^{n-1}\left[1 + (a\psi)^n\right]^{-m}\right\}^2}{\left[1 + (a\psi)^n\right]^{m/2}} \quad (4)$$

where $k_s$ is the permeability coefficient in the saturated state; $\psi$ is the matrix suction; $a$, $m$, and $n$ are all fitting parameters, where $m$=1−1/$n$.

The Fredlund unsaturated permeability function model was obtained by combining the Fredlund and Xing model formula with the Child and Collis-George statistical pore size distribution model, and its expression is as follows:

10.3389/feart.2023.1212017

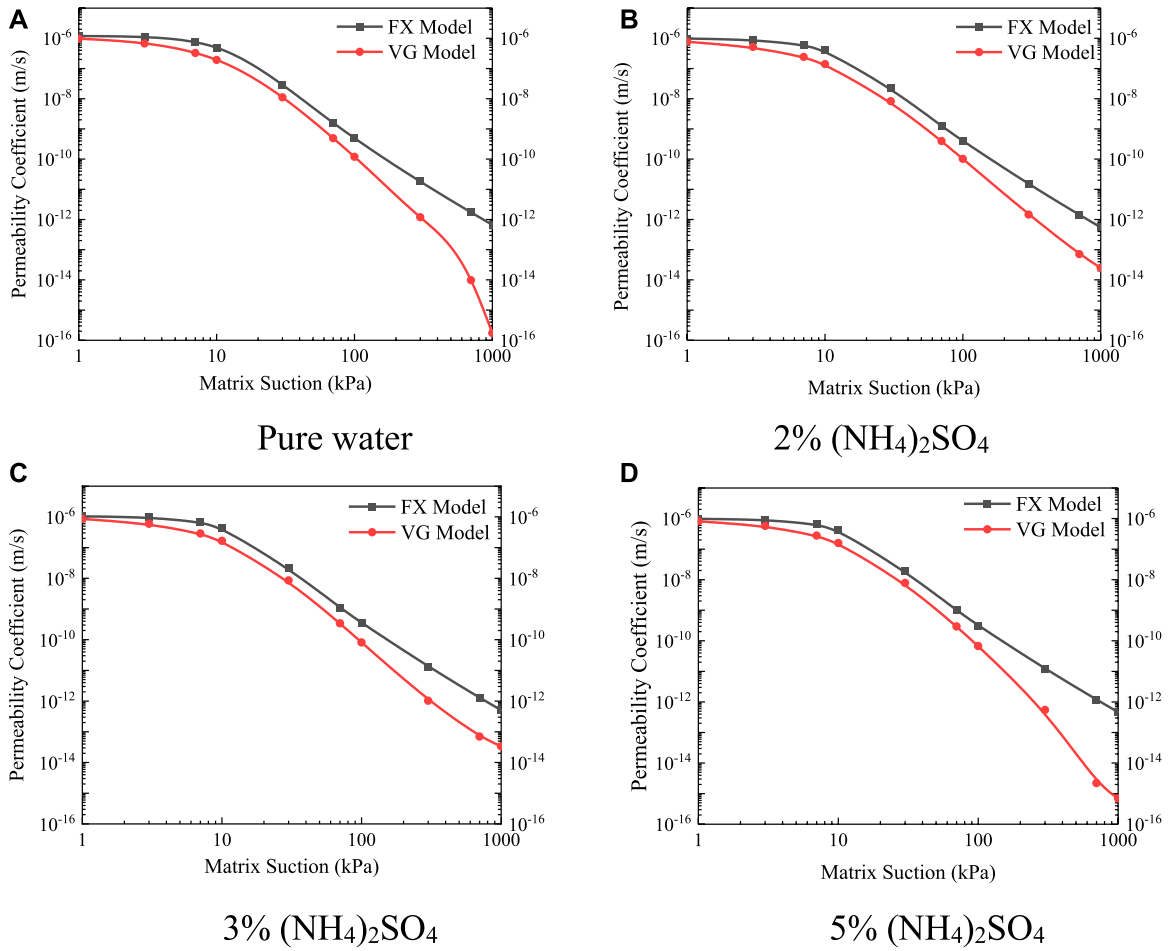


FIGURE 13
Unsaturated permeability curves at different leaching solution concentrations **(A)** Pure water **(B)** 2% (NH4)2SO4 **(C)** 3% (NH4)2SO4 **(D)** 5% (NH4)2SO4.

$$k_u = k_s \frac{\int_{\ln(\psi)}^{b} (\theta(e^y) - \theta(\psi)/e^y)\theta'(e^y)dy}{\int_{\ln(\psi_{aev})}^{b} (\theta(e^y) - \theta_s/e^y)\theta'(e^y)dy} \quad (5)$$

where $k_s$ is the permeability coefficient in the saturated state, $\psi$ is the matrix suction, $y$ is the imaginary variable of the integral $\ln(\psi)$, $b$ generally takes $\ln(10^6)$; $\psi_{aev}$ is the air-entry pressure value, and $\theta'$ is the derivative of $\psi$.

## 5.2 Unsaturated permeation characteristics under different types of leaching solutions

This study describes the unsaturated permeability characteristics based on the unsaturated permeability coefficient function. The function curves of the unsaturated permeability coefficient under different types of leaching solutions are shown in Figure 12.

The influence of different types of leaching solutions on the unsaturated permeability function of ionic rare earth ores was analyzed, and there was a high correlation between the unsaturated permeability function and the saturated permeability coefficient. In the saturated state, the saturated permeability coefficient of pure water was the largest, followed by 3% $(NH_4)_2SO_4$, and the smallest was 3% $MgSO_4$. In the unsaturated state, the same relationship existed for the unsaturated permeability coefficient of different types of leaching solutions.

In the unsaturated state, the corresponding unsaturated permeability coefficient was the largest in the case of pure water. The types of water in soil are roughly divided into capillary water, membrane water, and gaseous water. By correcting the capillary water model and the valve model of unsaturated soil, it can be seen that the infiltration of capillary water in unsaturated soil was proportional to the effective area of the seepage pore size (31). Combined with the results of saturated permeability characteristics and water-holding properties, it is believed that the main reason is that pure water did not undergo an ion exchange reaction with ionic rare earth ores during the saturated-unsaturated seepage process, and its corresponding effective pore size was the largest and the permeability characteristics are the best. Under the same matric suction, the unsaturated permeability coefficient functions of 3% $(NH_4)_2SO_4$ and 3% $MgSO_4$ were smaller than those of pure water because the exchange reaction between cations and rare earth ions,

10.3389/feart.2023.1212017

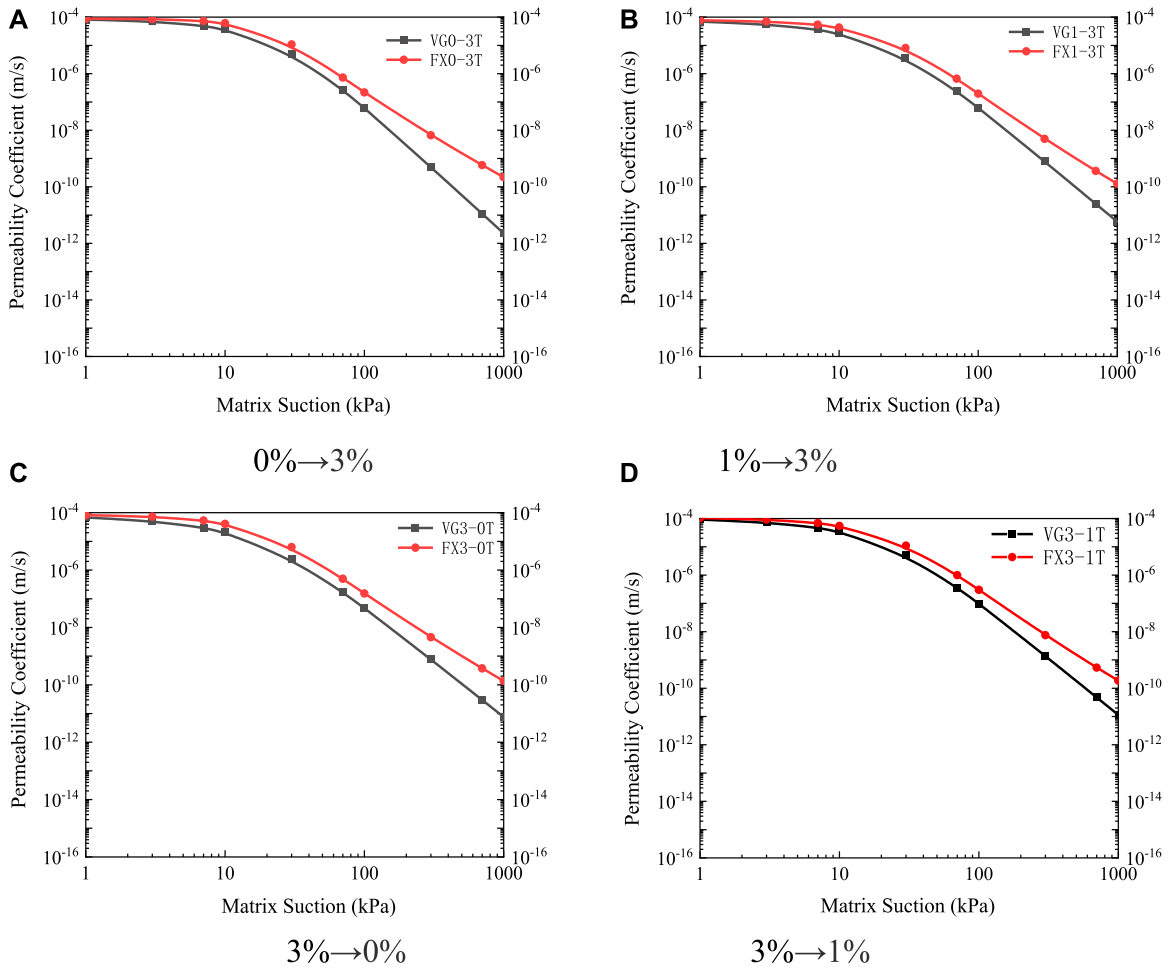


FIGURE 14
Unsaturated permeability curves under different leaching paths **(A)** 0%→3% **(B)** 1%→3% **(C)** 3%→0% **(D)** 3%→1%.

the effective area of the internal pore size of the soil become smaller, and the unsaturated permeability characteristics also become weaker.

## 5.3 Unsaturated permeation characteristics at different leaching solution concentrations

The unsaturated permeability curves at different leaching solution concentrations are shown in Figure 13. The analysis shows that when the matric suction was small, the unsaturated permeability coefficient function was mainly influenced by the saturated permeability coefficient; the unsaturated permeability coefficient of pure water was the largest, the unsaturated permeability coefficient was consistent with the saturated permeability coefficient, and the unsaturated permeability coefficient of 2% $(NH_4)_2SO_4$ and 5% $(NH_4)_2SO_4$ was smaller than that of 3% $(NH_4)_2SO_4$. With the increase in matric suction, the unsaturated permeability coefficient of different concentrations also changed, and with the increase in concentration, the unsaturated permeability coefficient decreased.

In the case of pure water, the unsaturated permeability coefficient of ionic rare earths was the largest; there was less particle decomposition, less seepage pore blockage, and a larger internal effective pore size. When the matric suction was small, most of the inside of the soil consisted of capillary water, and the unsaturated permeation characteristics of ionic rare earths could be analyzed according to the "valve model." The water inside the soil began to be composed of membrane water; the migration law of water in the water film was significantly different from the migration law of capillary water, and the migration efficiency of the membrane water was closely related to the thickness of the water film on the surface of soil particles. The exchange reaction between $NH^{4+}$ and rare earth ions on the surface of soil particles affected the thickness of membrane water on the surface of soil particles. Under different leaching solution concentrations, with the increase of concentration, the ions exchanged with each other, thereby reducing the thickness of the water film on the surface of soil particles and the permeability characteristic of membrane water in unsaturated soil. The higher the concentration of the leaching solution, the more intense the reaction, the more severe the damage to the water film on the surface of the soil particles, and the lower the unsaturated permeability coefficient.

### 5.4 Unsaturated permeation characteristics under different leaching paths

The unsaturated permeability curves under different leaching paths are shown in Figure 14. It can be seen that the different leaching paths had an effect on the function of the unsaturated permeability coefficient of ionic rare earths. For the path of "first high concentration followed by low concentration," because of the diffusion force, the internal repulsion of the soil particles was generated from the inside to the outside, which promoted the crushing of the soil particles, blocked the seepage channel, and reduced the unsaturated permeability coefficient. For the path of "first light concentration followed by high concentration," the diffusion force from the outside to the inside was generated inside the soil particles, therefore promoting the condensation of fine soil particles, widening the seepage channel, and increasing the unsaturated permeability coefficient.

The unsaturated permeability characteristics of ionic rare earths were closely related to the seepage channels in the soil. The infiltration of unsaturated soil capillary water was proportional to the effective area of the seepage pore size. Combined with the saturated seepage law and the soil-water characteristic curve, under the leaching path of "0%→3%," the seepage channel was the largest, therefore the unsaturated permeability coefficient was also the largest. Under the leaching path of "3%→0%," its seepage channel was the smallest, therefore the unsaturated permeability coefficient was also the smallest. For the leaching paths of "1%→3%" and "3%→1%," the seepage channel changed marginally, so the difference between the unsaturated permeability coefficient under these two working conditions was small.

## 6 Conclusion

(1) The type of leaching solution has a certain influence on the permeability characteristics of ionic rare earths, and the saturated permeability coefficients of the ore body are pure water, 3% $(NH_4)_2SO_4$, 3% $MgSO_4$ in descending order under different leaching conditions. When the concentration of the leaching solution increases from 2% to 5%, the saturation permeability coefficient increases and then decreases.

(2) According to the analysis of soil-water characteristic curves, under the conditions of different types of leaching solutions, the water-holding performance of the ore body under pure water conditions was the best, followed by the $MgSO_4$ working conditions, while the $(NH_4)_2SO_4$ working conditions was the worst. As the concentration of the leaching solution increased, the water content of the ore body decreased, and the water-holding capacity also decreased.

(3) The seepage law is related to the leaching path, and the permeability coefficient increased when the concentration was high, followed by a low concentration. When the concentration was first low and then high, the permeability coefficient decreased. Therefore, in the *in situ* leaching process of ionic rare earth ore, the liquid injection method of "high concentration followed by low concentration" can be used to improve the permeability of the soil and further obtain a higher rare earth leaching rate.

(4) Based on the unsaturated permeability function model, the unsaturated permeability coefficient function curve of the ore body under different leaching conditions can be obtained. The unsaturated permeability coefficient predicted by the Fredlund and Xing model is more realistic than the one obtained by the Van Genuchten model. The unsaturated permeability coefficient predicted by the model can provide a more objective and accurate assessment basis for calculating rare earth leaching rates.

## Data availability statement

The raw data supporting the conclusion of this article will be made available by the authors, without undue reservation.

## Author contributions

Conceptualization, ZG and LL; methodology, ZG; validation, KZ and LL; writing—original draft preparation, ZG and LL; writing—review and editing, ZG, LL, and KZ; supervision, ZG, WZ, and XW; project administration, ZG; funding acquisition, ZG and XW. All authors contributed to the article and approved the submitted version.

## Funding

The research was supported by the National Natural Science Foundation of China (Grants Nos. 52004106, 52174113) and the Natural Science Foundation of Jiangxi Province (Grant No. 20224BAB214035).

## Conflict of interest

The authors declare that the research was conducted in the absence of any commercial or financial relationships that could be construed as a potential conflict of interest.

## Publisher's note



## References

Chi, R. A., and Liu, X. M. (2019). Prospect and development of weathered crust elution-deposited rare Earth ore. *J. J. Chin. Soc. Rare Earths* 37 (02), 129–140. doi:10.11785/S1000-4343.20190201

Chiu, C. F., Yan, W. M., and Yuen, Ka-veng. (2012). Estimation of water retention curve of granular soils from particle-size distribution—A bayesian probabilistic approach. *J. Can. Geotechnical J.* 49 (9), 1024–1035. doi:10.1139/t2012-062

Deng, G. Q., and Yang, Y. M. (2016). A Review of the mining technologies of ion-absorbed rare Earth mineral. *J. Chin. Rare Earths.* 37 (03), 129–133. doi:10.16533/J.cnki.15-1099/tf.201603023

Fredlund, D. G., and Pham, H. Q. (2006). "A volume-mass constitutive model for unsaturated soils in terms of two independent stress state variables," in Proceedings of the A. Fourth International Conference on Unsaturated Soils, Lisbon, Portugal, June 2006.

Fredlund, D. G., and Xing, A. (1994). *Erratum*: Equations for the soil-water characteristic curve. *J. Can. geotechnical J.* 31 (4), 1026–1532. doi:10.1139/t94-120

Gao, L. X., Luan, M. T., Yang, Q., and Wang, D. L. (2008). Experimental study of permeability of unsaturated remoulded clays. *J. Rock Soil Mech.* 2008 (08), 2267–2270+2276. doi:10.16285/j.rsm.2008.08.050

Guo, Z. Q., Jin, J. F., Qin, Y. H., Wang, X. J., Zhong, W., and Zhao, K. (2017). Experimental research on one-dimensional horizontal infiltration rules of ion-adsorption rare Earth. *J. Nonferrous Metals Sci. Eng.* 8 (02), 102–106. doi:10.13264/j.cnki.ysjskx.2017.02.017

Guo, Z. Q., Lai, Y. M., Jin, J. F., Zhou, J. R., Zhao, K., and Sun, Z. (2020). Effect of particle size and grain composition on two-dimensional infiltration process of weathered crust elution-deposited rare Earth ores. *J. Trans. Nonferrous Metals Soc. China.* 30 (6), 1647–1661. doi:10.1016/S1003-6326(20)65327-4

Guo, Z. Q., Zhou, J. R., Zhou, K. F., Jin, J. F., Wang, X. J., and Zhao, K. (2021). Soil–water characteristics of weathered crust elution-deposited rare Earth ores. *J. Trans. Nonferrous Metals Soc. China* 31 (05), 1452–1464. doi:10.1016/S1003-6326(21)65589-9

He, Z. Y., Zhang, Z. Y., Chi, R. N., Xu, Z. G., Yu, J. X., Wu, M., et al. (2017). Leaching hydrodynamics of weathered elution-deposited rare Earth ore with ammonium salts solution. *J. J. Rare Earths* 35 (8), 824–830. doi:10.1016/s1002-0721(17)60982-7

Ilankoon, I. M. S. K., Tang, Y., Ghorbani, Y., Northey, S., Yellishetty, M., Deng, X. Y., et al. (2018). The current state and future directions of percolation leaching in the Chinese mining industry: Challenges and opportunities. *J. Mineng.* 125, 206–222. doi:10.1016/j.mineng.2018.06.006

Jin, J. F., Tao, W., Qiu, C., and Guo, Z. Q. (2015). Experimental research on one-dimensional vertical infiltration rule of ionic rare Earth and the effects of maximum particle size. *J. Nonferrous Metals Sci. Eng.* 6 (06), 125–131. doi:10.13264/j.cnki.ysjskx.2015.06.023

Liu, C. F., Zhou, F., Wu, X. Y., Feng, J., and Chi, R. A. (2021). Development and prospect in seepage and mass transfer process of weathered crust elution-deposited rare Earth ore. *J. Chin. Rare Earths.* 42 (01), 111–121. doi:10.16533/j.cnki.15-1099/tf.20210044

Long, P., Wang, G. S., Tian, J., Hu, S. L., and Luo, S. H. (2019). Simulation of one-dimensional column leaching of weathered crust elution-deposited rare Earth ore. *J. Trans. Nonferrous Metals Soc. China* 29 (3), 625–633. doi:10.1016/S1003-6326(19)64972-1

Ma, T. T., Wei, C. F., Xia, X. L., and Chen, P. (2016). Constitutive model of unsaturated soils considering the effect of intergranular physicochemical forces. *J. J. Eng. Mech.* 142(11). doi:10.1061/(asce)em.1943-7889.0001146

Nie, W. R., Zhang, R., He, Z. Y., Zhou, J., Wu, M., Xu, Z. G., et al. (2020). Research progress on leaching technology and theory of weathered crust elution-deposited rare Earth ore. *J. Hydromet.* 193, 105295. doi:10.1016/j.hydromet.2020.105295

Pham, H. Q. (2005). *A volume-mass constitutive model for unsaturated soils.* Saskatoon, Canada: D. The University of Saskatchewan.

Rajkai, K., Sandor, Kabos., Martinus, Th., and Van, Genuchten. (1996). Per-Erik, Jansson. Estimation of water-retention characteristics from the bulk density and particle-size distribution of Swedish soils. *J. Soil Sci.* 161 (12), 832–845. doi:10.1097/00010694-199612000-00003

Van, Genuchten. M. T. (1980). A closed form equation for predicting the hydraulic conductivity of unsaturated soils. *J. Soil Sci. Soc. Am. J.* 44 (5), 892–898. doi:10.2136/sssaj1980.03615995004400050002x

Wang, X. J., Li, Y. X., Huang, G. L., Fang, S. Y., Zhong, W., and Liao, S. Y. (2017). Research of permeability and porosity in ion-type rare Earth leaching process. *J. Chin. Rare Earths.* 38 (5), 47–55. doi:10.16533/j.cnki.15-1099/tf.201705007

Wu, A. X., Yin, S. H., and Li, J. F. (2005). Influential factors of permeability rule of leaching solution in ion-absorbed rare Earth deposits with *in-situ* leaching. *J. J. Central South Univ.* 36 (3), 506–510. doi:10.3969/j.issn.1672-7207.2005.03.031

Yin, S. H., Chen, X., and Jiang, L. C. (2015). Effect of ore particle size on solution capillary seepage in ore heaps. *J. Chin. J. Eng.* 37 (5), 561–567. doi:10.13374/j.issn2095-9389.2015.05.004

Yin, S. H., Qi, Y., Xie, F. F., Chen, X., and Wang, L. M. (2018). Permeability characteristic of weathered crust elution deposited rare Earth ores under different pore structures. *J. Chin. J. Nonferrous Metals.* 28 (5), 1043–1049. doi:10.19476/j.ysxb.1004.0609.2018.05

Zhai, Q., Rahardjo, H., Satyanaga, A., and Dai, G. (2019). Estimation of unsaturated shear strength from soil–water characteristic curve. *J. Acta Geotech.* 14 (6), 1977–1990. doi:10.1007/s11440-019-00785-y

Zhang, Z. Y., He, Z. Y., Yu, J. X., Xu, Z. G., and Chi, R. A. (2016). Novel solution injection technology for *in-situ* leaching of weathered crust elution-deposited rare Earth ores. *J. Hydromet.* 164, 248–256. doi:10.1016/j.hydromet.2016.06.015

Zhou, F., Liu, Q., Feng, J., Su, J. X., Liu, X., and Chi, R. A. (2019). Role of initial moisture content on the leaching process of weathered crust elution-deposited rare Earth ores. *J. Seppur* 217, 24–30. doi:10.1016/j.seppur.2019.02.010

frontiers | Frontiers in Earth Science

TYPE Original Research
PUBLISHED 14 July 2023
DOI 10.3389/feart.2023.1085200



OPEN ACCESS

EDITED BY
Miao Li,
Charles Sturt University, Australia

REVIEWED BY
Yang Xiao,
Xi'an University of Science and Technology, China
Yinan Guo,
China University of Mining and Technology, China

*CORRESPONDENCE
Zhen Liu,
17865811672@163.com
Biao Kong,
kongbiao8807@163.com

RECEIVED 31 October 2022
ACCEPTED 03 July 2023
PUBLISHED 14 July 2023

CITATION
Yin J, Liu Z, Yu K, Kong B, Mou X, Zhang X and Ma W (2023), A study on the simulation of psychological and behavioral dynamics in the unsafe state of coal mine workers.
*Front. Earth Sci.* 11:1085200.
doi: 10.3389/feart.2023.1085200



# A study on the simulation of psychological and behavioral dynamics in the unsafe state of coal mine workers

Jueli Yin[1,2], Zhen Liu[1,2]*, Kai Yu[3], Biao Kong[3]*, Xiaowei Mou[3], Xiaolong Zhang[4] and Wanli Ma[3]

[1]College of Finance and Economics, Shandong University of Science and Technology, Taian, China, [2]College of Economics and Management, Shandong University of Science and Technology, Qingdao, China, [3]College of Safety and Environmental Engineering, Shandong University of Science and Technology, Qingdao, China, [4]Qingdao No.1 Municipal Engineering Co., Ltd., Qingdao, China

The coal mine production safety hazards are large, and the situation is difficult, and coal mine workers are affected psychologically, producing unsafe psychological states and triggering unsafe behavior. This paper firstly studies the interactive influence process of the unsafe psychological state of coal mine workers and reveals the emergence process of unsafe psychology and behavior of coal mine workers. According to the characteristics of qualitative simulation of safety behavior, safety psychology and unsafe state of coal mine personnel, 23 simulation schemes are designed, and simulation analysis is carried out using QSIM simulation software platform. According to the simulation results of 23 schemes, the dynamic emergence process of safety behavior, safety psychology, and unsafe state of coal mine workers was sorted out from the aspects of different states and the intensity of different management measures, and the law of the effect of coal mine workers' safety psychology on safety behavior and safety state was obtained , revealing the interactive influence of coal mine workers' psychology on the unsafe state and the internal evolution mechanism of the emergent process. It is of great theoretical and practical significance for coal mine safety management to study the interaction of hazardous psychological states of coal mine workers and the dynamic generation mechanism of the emergence process of unsafe behaviors.

KEYWORDS

**coal mine workers', unsafe state, simulation calculation, experiment, safety behavior**

## Highlights

(1) Analyze and get the influencing factors of unsafe state of coal mine personnel.
(2) Study and reveal the interactive emergence process of unsafe states of coal mine personnel.
(3) Realize the simulation analysis of the unsafe state of 23 kinds of coal mine personnel.

## 1 Introduction

The report "National Energy Development Strategy 2030–2050" proposes that by 2050, the annual production of coal energy in China will be controlled at 3 billion tons, which

indicates that the proportion of coal in our energy consumption structure will not change significantly in the future period (Li et al., 2015; Peng et al., 2018). There are many hidden dangers and problems in coal mine production, and the situation is severe. Although China has successively issued relevant laws, regulations, and rules on coal mine safety production, increased the safety supervision of coal mine production, and achieved some phased safety production results, the safety problems of coal mine production in China have not been fundamentally solved (He and Song, 2012; Dong et al., 2021a; Yin et al., 2023). Because 95% of China's coal mining is an underground operation, the natural occurrence conditions of coal seams are poor, the mechanization level of coal production is low, the equipment is backward, the safety management lags behind, the coal mine safety production faces the threat of coal and rock power disasters and coal spontaneous combustion disasters, the occurrence rate and the death toll of coal mine safety accidents are still large (Tong et al., 2019a; Tong et al., 2019b; Liu et al., 2020).

The transformation and development of the coal mining industry structure, the psychology of coal mine workers are affected by many factors, and the unsafe psychological state is complex and variable (Margolis, 2010; Considine et al., 2017). At present, China's energy structure transformation needs to be more urgent, on the one hand, coal enterprises have to "remove production capacity" to realize the transformation of energy structure as soon as possible (Zhang et al., 2018; Dong et al., 2021a; Chi et al., 2021), on the other hand, due to the domestic and international situation and other influences, coal enterprises bear the responsibility of energy underwriting (Han et al., 2018; Zhou et al., 2020). Under the pressure of two aspects, the coal production and supply as well as demand are tense, which further exacerbates the tension of safe production in the coal industry, and the psychological state of coal mine workers will also change accordingly (Qing-gui et al., 2012; Yang et al., 2022a). The "psychological-behavioral research" of coal miners is an essential part of the international mining occupational health and safety research (Yu et al., 2022). Compared with the current research progress of occupational health and safety management in various industries (Zhu et al., 2022), there is still a big gap in coal-rich countries (the United States and Australia). The number of coal mine production safety accidents and deaths in the coal industry in developed countries are lower than that in China (Wang et al., 2013; Wang et al., 2016; Zhang et al., 2022).

Using simulation technology can easily and flexibly reproduce the scene of the accident, which can effectively save economic costs. Due to the rapid development of computer technology, the ability of scholars to establish simulation systems has gradually increased. To some extent, it provides technical and theoretical support for describing human behavior characteristics (Qiao et al., 2018; Cao et al., 2019; You et al., 2019; Chen et al., 2022). Based on the existing research results in psychology and physiology, the combination of the generation and action mechanism of human emotions, related scholars have constructed a human behavior model, creating a new direction of human behavior simulation research (Reynolds, 1987; Yang et al., 2022b). At the same time (Reynolds, 1987; Tu and Terzopoulos, 1994; Zhang et al., 2017), used the law of individuals imitating each other in group psychology simulates human behavior (Musse and Thalmann, 1997; Thalmann et al., 2000). Conducted a simulation study of human group behavior through the psychological law of group spiritual unity in group psychology. Used emergence theory, CGP modeling method and Netlogo simulation platform to simulate and analyze the influencing factors of unsafe behavior dynamically, The research results confirm that the necessary means to reduce the emergence degree of hazardous behavior is to control the attributes of the factors most closely related to employee behavior. Yu et al. (2019a) used the fishbone diagram to analyze the influencing factors of unsafe behavior from five aspects, and established a system dynamics model of unsafe behavior intervention, and proposed a joint intervention strategy for unsafe behavior. Structural equation models are hypothetical models that construct models and causal relationships based on theoretical literature or past empirical laws. By collecting variable data, a theoretical simulation framework is constructed to determine the reasoning and accuracy of these design relationships. Design formula models can calculate the relationships between hidden variable structures by observing variables. The QSIM algorithm is derived and simulated based on the unsafe psychological state model of coal mine workers according to preset rules, in order to fully reproduce the inference process of state evolution. This algorithm considers the unsafe psychological state of coal mine workers as a complex system. Starting from the initial situation of the system, rules are derived as constraints to reasonably deduce its continuous state changes, and the states of each stage are integrated in sequence to transform into visible state trends. Benjamin Kuipers of the University of Texas proposed a QSIM algorithm based on qualitative differential equations and constraints, gradually moving qualitative simulation from theory to application (Kuipers, 1986). Leitch R proposed that QSIM can use constraint equations to further screen newly generated states, filtering out most of the non compliant subsequent states (Leitch et al., 1991).

Chen et al. (2010) analyzed the causes of typical major accidents in coal mines from 2005 to 2010, established a causal model of human errors in mine accidents, and based on this, from research and development, management, law enforcement three perspectives put forward new ideas of safety management in line with China actual situation. Introduced HFACS (Human Factors Analysis Classification System) in the related research on miners' unsafe behavior, established a multi-level influencing factor model and SD (System Dynamics) simulation model. It can be seen that the security state of the organization has the greatest impact on the unsafe behavior of miners. Used 3D simulation technology to simulate the accident consequences that may be caused by miners' unsafe behavior, and established an unsafe behavior warning system to strengthen workers' safety awareness.

Based on this, the unsafe behavior of coal mine workers depends on their physiological and psychological state. The unsafe psychological state of coal mine workers is a key link to producing unsafe behavior, when an unsafe physiological and psychological state occurs, the probability of causing unsafe behavior increases in the production process, which has a serious impact on the safety production of coal mine enterprises and working groups. Therefore, it is the primary purpose of this research to study the interactive influencing factors of the unsafe mental state of coal mine workers, based on the literature search and qualitative analysis of the unsafe psychological state of coal mine

workers, the interactive factors analysis, model establishment, and calculation of the human factors, environment and behavior of the unsafe psychological state of coal mine workers are carried out, and the interaction factors affecting the unsafe psychological state of coal mine workers are studied. Secondly, according to the interaction factors involved in the dangerous psychological state of coal mine workers obtained from the previous research, simulation calculations are carried out to qualitatively describe the influence of the interaction factors that cause coal mine workers' psychological state on the unsafe psychological state. Thirdly, through the experimental test of coal mine workers' psychology on unsafe state, further statistical verification is carried out to analyze the development and evolution process of coal mine workers' unsafe psychology.

## 2 The interactive influence of unsafe psychological state of coal mine workers

The first characteristic of coal mine workers' work is the special working environment. Specifically, the working space is narrow, the working environment is dark, the environmental humidity is high, the scope of personnel activities is limited, and the workplace of workers is not fixed, etc. The second characteristic of the work of coal mine workers is that the working conditions are difficult. The main reasons include the remoteness of the work route and the long working time of each well. Long-term high-intensity work is easy to lead to fatigue and distraction. The third characteristic of the work of coal mine workers is that the underground production process is complex. The fourth characteristic of the work of coal mine workers is that the underground natural disasters are serious, and the coal mine working environment is poor, similar to gas, mine water penetration and other natural disasters that occur frequently.

The proposal of influencing factors mainly revolves around the actual production of miners underground. Through statistical analysis, literature review, on-site research, questionnaire survey, personnel interviews, and expert consultation methods, we deeply understand the psychological and behavioral reality of coal mine workers from various aspects such as their ideology, work, life, individual quality, and human biological rhythm. We analyze the causes and processes of unsafe psychology, and grasp the overall characteristics of coal mine workers, Analyze the specific manifestations of the unsafe psychological state of coal mine underground personnel, in order to determine the influencing factors of the unsafe psychological state of coal mine employees.

According to the working characteristics and psychological characteristics of coal mine workers, the identification indexes of unsafe psychological state of coal mine workers are determined, which mainly include: 1) Dangerous psychology: Paralytic psychology, shortcut psychology, fluke psychology, reverse psychology, adventure psychology; 2) Psychological characteristics: Personality, temperament, and emotions; 3) Personality tendency, including safety attitude, is the unique value judgment and psychological tendency of coal mine workers to work safety in the process of production and operation. Generally, safety attitude will affect the degree of coal mine workers' compliance with safety rules and regulations, as well as safety motivation and safety needs. 4) Safety stress, including psychological stress regulation and emotional control ability. Statistical analysis of data, the psychological survey model of coal mine workers is obtained as shown in Figure 1.

As can be seen from Figure 1, according to the model, the influencing factors of employees' mental health status are divided into two categories: job requirements and job resources. Excessive job requirements can lead to negative psychological states, and adequate work resources can alleviate the negative effects of job requirements on psychological states, thereby effectively promoting mental health. Employees with higher personal psychological resources can also play a similar job resource role. The psychological state of employees further affects their usual job satisfaction and loyalty to the organization. According to the model, if employees are expected to have a higher level of mental health, as well as higher satisfaction and loyalty to the organization, they can work more actively and create more excellent value for the organization.

The questionnaire survey in this article was first conducted on a small scale. 220 questionnaires were distributed and collected at Jining No. 2 Coal Mine of Yankuang Energy Group Co., Ltd. Based on feedback from respondents, the psychological survey scale for coal mine employees was modified to form an initial survey scale, which is divided into the measurement scale for basic information and psychological identification indicators of respondents. Due to the fact that the essence of the psychological safety questionnaire lies in the psychological measurement scale, which provides the corresponding degree of psychological feelings expressed by each question. The survey involved male participants. During the survey, a total of 615 questionnaires were distributed and 550 valid questionnaires were collected.

The survey mainly involves personnel from coal mining enterprises, departments, mining areas, and underground personnel. The types of work involved include coal mining, excavation, mechanical and electrical, transportation, ventilation, and safety supervision personnel. The working environment of different types of work varies, and the differences in the environment above and below the mine can cause different psychological pressures on coal mine workers. In addition, there are significant cultural differences between different types of work, and the level of education not only affects the unsafe psychological behavior of miners, but also increases the difficulty of on-site safety management in mines.

According to factor analysis, four dimensions of safety psychology, psychological characteristics, personality tendency and psychological pressure are determined to identify the unsafe psychological state of coal mine workers. The four dimensions of safety psychology, psychological characteristics, personality tendency and psychological stress are taken as the four latent variables of the model, and the corresponding indicators of each dimension are taken as the observed variables. Based on this, the original structural equation model of the identification index value of an unsafe psychological state of coal workers is generated. The construction and analysis of the structural equation model can be completed according to Amos software. AMOS is a powerful structural equation (SEM) modeling tool that extends traditional multivariate analysis methods including regression, factor analysis, correlation analysis, and variance analysis. In the AMOS environment, models can be specified, estimated, evaluated, and set under an intuitive path map to display the relationships between

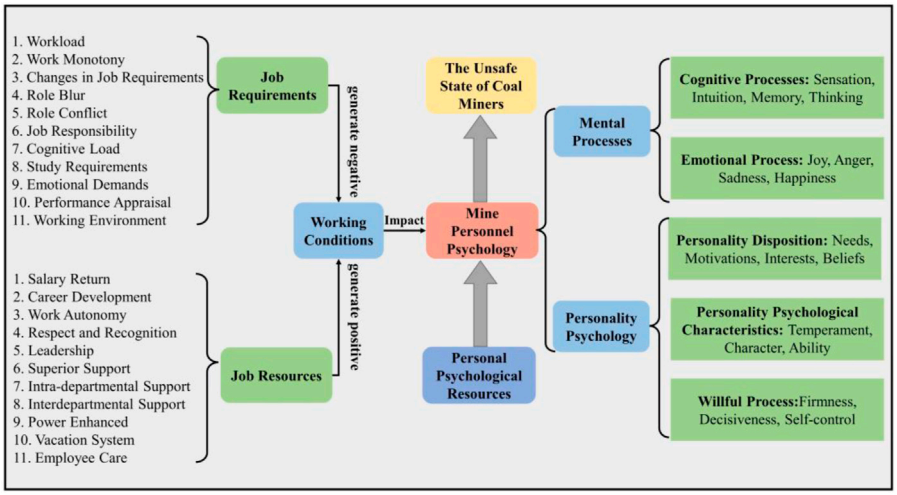


FIGURE 1
Psychological survey model of coal mine workers.

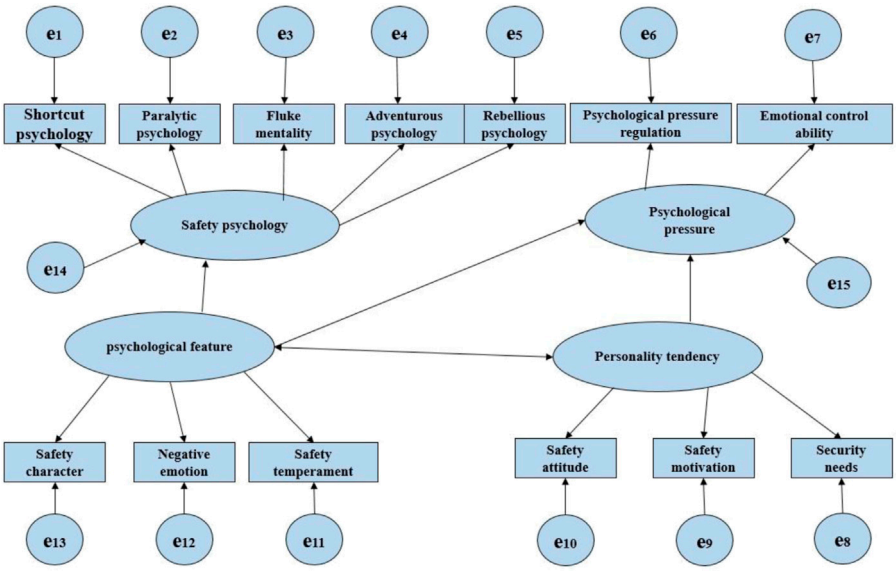


FIGURE 2
Revised structural equation model.

assumed variables, facilitating the establishment of behavioral attitude models that can truly reflect complex relationships. The original structural equation model is tested to verify the five basic assumptions proposed. After testing, the initial structural equation model is modified after deleting the wrong path. The modified structural equation model is shown in Figure 2.

Before conducting molecular analysis, it is necessary to first check whether factor indicators are suitable for factor analysis. Common test methods include KMO test and Bartlett spherical test. The result of the KMO test is between 0 and 1. The closer the KMO statistic is to 1, the higher the correlation between the factors is proven. It is generally believed that a value of KMO greater than 0.5 indicates that the indicator factor is suitable for factor analysis.

As shown in Figure 2, using SPSS software, confirmatory factor analysis was carried out on each variable, the deleted and merged indicators are divided into 4 principal components: safety psychology, personality tendency, psychological characteristics and psychological pressure. These 4 principal components explain 82.936% of the variance accumulatively, which can meet the statistical requirements. The reliability test shows that the Cronbach's alpha coefficient of each dimension index is between 0.7 and 0.9, and the identification index has good reliability, which verifies the rationality of the index division. Personality tendencies have a significant positive impact on

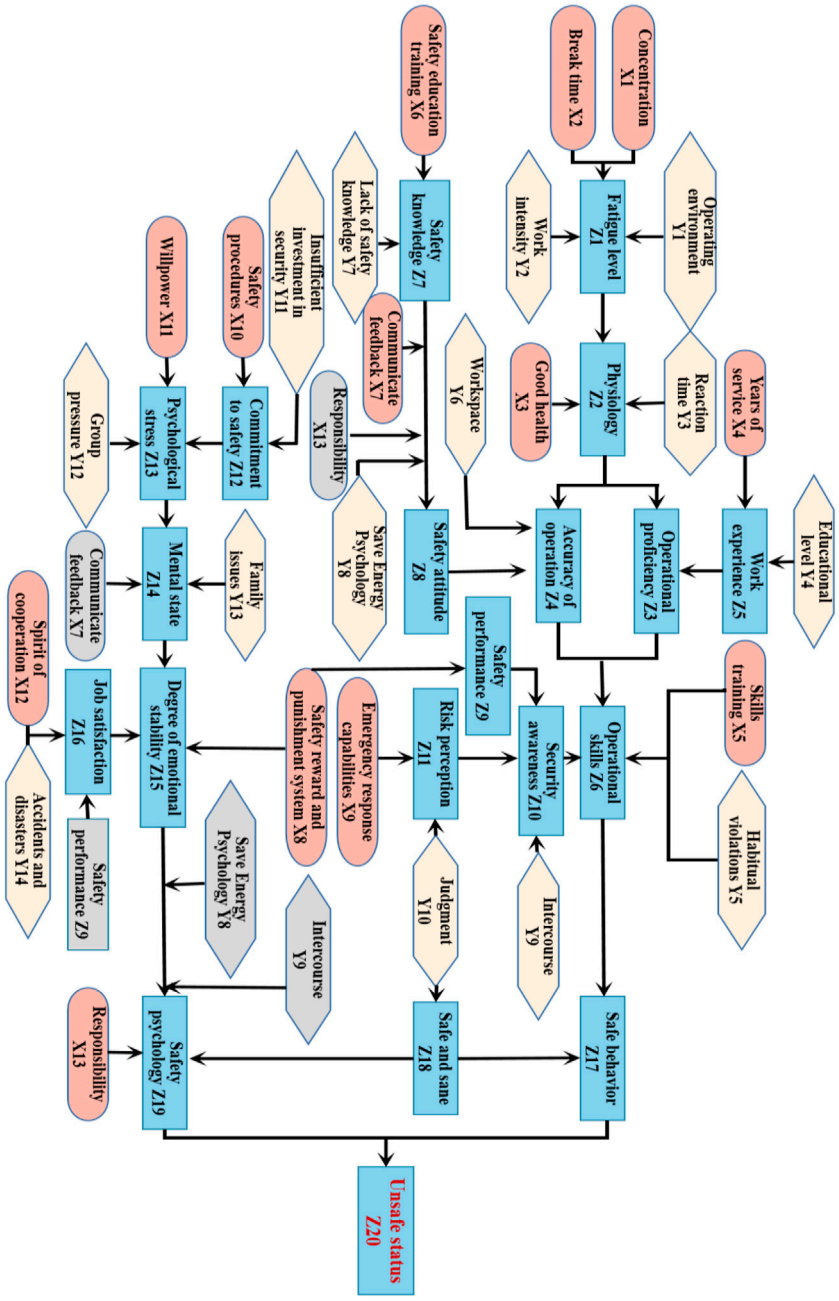


FIGURE 3
QSIM model of unsafe status of coal miners.

psychological stress; psychological characteristics have a significant positive impact on safety psychology; psychological characteristics have a significant positive impact on psychological stress.

## 3 Simulation research on the influence of coal mine personnel psychology on unsafe state

Based on the research on the influence and emergence mechanism of coal mine workers' psychology on their unsafe state, the QSIM model to simulate the unsafe state of coal miners was constructed, and the mapping relationship and laws between psychology and unsafe state was explored (Yu et al., 2019b; Cao et al., 2019; Xu et al., 2023). QSIM directly uses the relevant parameters of the device as state variables to describe the physical structure, derives the constraint relationship between the parameters from physical and mathematical laws, and treats the change of the parameters over time as a qualitative state sequence. Starting from the initial state, first generate all possible subsequent states, and then eliminate the impossible states through qualitative constraints. Repeat this process until no new states are generated

**TABLE 1 Simulation scheme table.**

| Programme | Manage variables X | | | | | | | | | | | | | Disturbance variable Y | System state variables Z | | Remarks initial state |
|---|---|---|---|---|---|---|---|---|---|---|---|---|---|---|---|---|---|
| | $X_1$ | $X_2$ | $X_3$ | $X_4$ | $X_5$ | $X_6$ | $X_7$ | $X_8$ | $X_9$ | $X_{10}$ | $X_{11}$ | $X_{12}$ | $X_{13}$ | $Y_1$-$Y_{14}$ | $Z_1$-$Z_{19}$ | $Z_{20}$ | |
| 1 | 0 | 0 | 0 | 0 | 0 | 0 | 0 | 0 | 0 | 0 | 0 | 0 | 0 | 1 | <3, →> | <3, →> | common |
| 2 | 1 | 1 | 1 | 1 | 1 | 1 | 1 | 1 | 1 | 1 | 1 | 1 | 1 | 1 | | | |
| 3 | 2 | 2 | 2 | 2 | 2 | 2 | 2 | 2 | 2 | 2 | 2 | 2 | 2 | 1 | | | |
| 4 | 0 | 0 | 0 | 0 | 0 | 0 | 0 | 1 | 1 | 1 | 1 | 1 | 1 | 1 | | | |
| 5 | 0 | 0 | 0 | 0 | 0 | 0 | 0 | 2 | 2 | 2 | 2 | 2 | 2 | 1 | | | |
| 6 | 1 | 1 | 1 | 1 | 1 | 1 | 1 | 0 | 0 | 0 | 0 | 0 | 0 | 1 | | | |
| 7 | 1 | 1 | 1 | 1 | 1 | 1 | 1 | 2 | 2 | 2 | 2 | 2 | 2 | 1 | | | |
| 8 | 2 | 2 | 2 | 2 | 2 | 2 | 2 | 0 | 0 | 0 | 0 | 0 | 0 | 1 | | | |
| 9 | 2 | 2 | 2 | 2 | 2 | 2 | 2 | 1 | 1 | 1 | 1 | 1 | 1 | 1 | | | |
| 10 | 1 | 1 | 1 | 1 | 1 | 1 | 1 | 1 | 1 | 1 | 1 | 1 | 1 | 1 | <2, →> | <4, →> | low |
| 11 | 2 | 2 | 2 | 2 | 2 | 2 | 2 | 2 | 2 | 2 | 2 | 2 | 2 | 1 | | | |
| 12 | 1 | 1 | 1 | 1 | 1 | 1 | 1 | 2 | 2 | 2 | 2 | 2 | 2 | 1 | | | |
| 13 | 2 | 2 | 2 | 2 | 2 | 2 | 2 | 1 | 1 | 1 | 1 | 1 | 1 | 1 | | | |
| 14 | 0 | 0 | 0 | 0 | 0 | 0 | 0 | 0 | 0 | 0 | 0 | 0 | 0 | 1 | <4, →> | <2, →> | high |
| 15 | 1 | 1 | 1 | 1 | 1 | 1 | 1 | 1 | 1 | 1 | 1 | 1 | 1 | 1 | | | |
| 16 | 2 | 2 | 2 | 2 | 2 | 2 | 2 | 2 | 2 | 2 | 2 | 2 | 2 | 1 | | | |
| 17 | 0 | 0 | 0 | 0 | 0 | 0 | 0 | 1 | 1 | 1 | 1 | 1 | 1 | 1 | | | |
| 18 | 0 | 0 | 0 | 0 | 0 | 0 | 0 | 2 | 2 | 2 | 2 | 2 | 2 | 1 | | | |
| 19 | 1 | 1 | 1 | 1 | 1 | 1 | 1 | 0 | 0 | 0 | 0 | 0 | 0 | 1 | | | |
| 20 | 1 | 1 | 1 | 1 | 1 | 1 | 1 | 2 | 2 | 2 | 2 | 2 | 2 | 1 | | | |
| 21 | 2 | 2 | 2 | 2 | 2 | 2 | 2 | 0 | 0 | 0 | 0 | 0 | 0 | 1 | | | |
| 22 | 2 | 2 | 2 | 2 | 2 | 2 | 2 | 1 | 1 | 1 | 1 | 1 | 1 | 1 | | | |
| 23 | 0 | 0 | 0 | 0 | 0 | 0 | 0 | 0 | 0 | 0 | 0 | 0 | 0 | 1 | <5, →> | <1, →> | very high |

(Shen and Leitch, 1993; Engler and Soultanis, 2005). Among them, the elements of QSIM model come from the index system constructed above.

According to the influencing factors and index system of unsafe state studied above, combined with the characteristics of QSIM modeling, the QSIM model of the unsafe state of coal mine personnel is constructed from the aspects of physiology and psychology. The rectangular block diagram in the model represents the system state variables, that is, the important indicators of the unsafe state of coal miners that need to be studied, and is expressed in two tuples $Z_i = \langle qval_{zi}, qdir_i \rangle$. Among them, $qval_{zi} = \{1, 2, 3, 4, 5\}$, the corresponding qualitative meanings are "very low", "low", "general", "high" and "very high"; $qdir_i = \{\downarrow, \searrow, \rightarrow, \nearrow, \uparrow\}$ means "strong reduction", "weak reduction", "unchanged", "weak addition" and "imposed" respectively. The rounded rectangle represents management variables, which usually refers to positive action measures in the management and other aspects; the hexagon is an interference variable, which has a negative effect on the system state variable, usually refers to the external environment and other interference factors; the management and interference variables are expressed in a tuple ($X_i = \langle qval_{xi} \rangle$ and $Y_i = \langle qval_{yi} \rangle$) respectively, among them, the corresponding qualitative meanings of $qval_{xi} = \{0, 1, 2\}$, $qval_{yi} = \{0, 1, 2\}$ are "no effect", "low intensity" and "high intensity". In order to reduce the intersection of connecting lines, this paper sets shadow variables, that is, the variables shown on the gray background.

Integrate and build QSIM model of unsafe state of coal mine personnel, as shown in Figure 3.

Based on the analysis of the relationship between the important influencing factors of the unsafe state of coal miners, the model describes the causal effect of each factor, including 20 system state variables, 13 management variables, 14 interference variables and

4 shadow variables. Based on this model, this paper will design a variety of simulation schemes, and explore the influence law of coal miners' psychology on their unsafe state by analyzing the simulation results.

The initial states of the management variables, interference variables and system state variables of the QSIM model (Figure 3) of the unsafe state of coal mine personnel are different, and the initial conditions of the unsafe state represented are different. In order to facilitate the analysis of the evolution process of the hazardous state of coal miners in the face of interference and intervention measures, as well as the influence law of psychology on the unsafe state, the initial state of each factor in the hazardous state model of coal mine personnel was analyzed, and different initial values of model variables according to different situations was set. Combined with the unsafe state model of coal mine personnel, and comprehensively considering the various state combinations (management, interference and system state variables) that coal mine personnel may appear in safety production, 23 simulation schemes (Table 1) are finally designed, in which each scheme represents the initial state under a typical situation.

All schemes are to analyze the impact of psychological factors on the unsafe state of coal mine personnel. Among them, scheme 1 mainly analyzes the situation that no countermeasures are taken in the face of interference in the initial state of "general"; scheme 2 is to analyze the decision-making equivalent to the interference intensity under the same initial state; scheme 3 is to analyze the situation of taking high-intensity countermeasures in the face of interference under the same initial state; scheme 4–9 mainly analyzes the situation of strengthening or weakening physiological and psychological measures respectively in the initial state of "general". Schemes 10 and 11 analyze the situation that when the initial state of each factor of coal mine personnel is "low" (qualitative value is 2), countermeasures with the same intensity and high intensity as the interference intensity are taken; schemes 12 and 13 analyze the situation of strengthening or weakening physiological and psychological measures respectively when the initial state is "low". Scheme 14–16 analyzes the situation that when the initial state is "high", no countermeasures are taken in the face of interference, countermeasures equivalent to the interference intensity and Countermeasures higher than the interference intensity are taken; scheme 17–22 analyzes the situation of strengthening or weakening physiological and psychological measures respectively when the initial state is "high". Scheme 23 analyzes the situation that no countermeasures are taken in the face of interference when the initial state is "very high".

## 4 Qualitative simulation and result analysis

The simulation results of the initial state are shown in Figure 4, $Z_1$–$Z_{19}$ are concentrated at the "very low" (qualitative value is 1) level, while $Z_{20}$ is concentrated at the "very high" (qualitative value is 5) level. This shows that in the face of external interference, without taking control measures, that is, when X=0, Y=1, Z=< 3, →>, all elements of coal mine personnel will eventually develop in the direction of "very low" (qualitative value is 1). Under the comprehensive action of various factors, the unsafe state level of coal mine personnel is "very high".

The evolution trend of safe behavior ($Z_{17}$), safe psychology ($Z_{19}$) and unsafe state ($Z_{20}$) is shown in Figures 5–7.

Figure 5 shows the changing trend of safety behavior ($Z_{17}$), it can be seen intuitively that safety behavior changes to "declining" from the 4th stage under the condition of external interference without any intervention measures, indicating that safety behavior of coal mine personnel begins to decline at this time. In stage 6, the safety behavior ($Z_{17}$) is "weakened" ("↘") the trend decreases to "low" (qualitative value is 2); until the 14th stage, the safety behavior ($Z_{17}$) continues to be "weakened" ("↘") the trend of decreased to "very low" (qualitative value is 1), and in the 18th stage, the change direction changed to "strong reduction" ("↓"), indicating that the safety behavior of coal miners will continue to accelerate and deteriorate.

Figure 6 shows the trend of safety psychology ($Z_{19}$), it can be seen intuitively that safety psychology changes to "declining" ("↘") from the 3rd stage under the condition of external interference without intervention measures, it shows that their safety psychology begins to decline at this time. In the 15th stage, safety psychology ($Z_{19}$) is "weakened" ("↘") the trend of decreases to "low" (qualitative value is 2); until the 13th stage, the safety psychology ($Z_{19}$) continues to be "weak" ("↘") the trend of decreased to "very low" (qualitative value is 1), and in the 17th stage, the change direction changed to "strong reduction" ("↓"), indicating that the safety psychology of coal miners will continue to accelerate and deteriorate.

Figure 7 for unsafe condition ($Z_{20}$) change trend, can visually see unsafe condition under the condition of the interference is not intervention, from the 4th state, change direction into a "weak plus" ("↗"), showed that coal mine personnel unsafe condition under the action of the psychological and behavior, began to rise. In the 6th stage, "weak plus" ("↗"). The trend rises to "high" (qualitative value is 4); until the 15th stage, continuing with "weak addition" ("↗") the trend rose to "very high" (qualitative value is 5), and in the 18th stage, the change direction changed to "imposed" ("↑"), indicating that the unsafe state of coal miners is still high and will continue to accelerate the deterioration.

Through in-depth comparative analysis of the change trends of safe behavior ($Z_{17}$), safe psychology ($Z_{19}$) and unsafe state ($Z_{20}$) (Figures 5–7), Figure 8, comparative analysis of the change trends of safe behavior ($Z_{17}$), safe psychology ($Z_{19}$) and unsafe state ($Z_{20}$) can be obtained.

It is not difficult to see from Figure 8 that at the initial stage of change, safety behavior ($Z_{17}$) lags behind Safety Psychology ($Z_{19}$), in contrast at the middle and later stages of change, unsafe state ($Z_{20}$) lags behind safety behavior ($Z_{17}$). This shows that when subjected to external interference, psychology changes first, followed by changes in safe behavior, and finally form a comprehensive effect, that is, changes in an unsafe state. For the potential relationship between safe behavior ($Z_{17}$), safe psychology ($Z_{19}$) and unsafe state ($Z_{20}$), this paper will verify and deeply analyze it in the subsequent simulation scheme.

The representative results of simulation analysis of scheme 2-scheme 3 are as follows: Scheme 2–the state of each element is general. In the face of interference, take control countermeasures equivalent to the interference intensity, that is, X=1, Y=1, Z=< 3, → >. The simulation results of scheme 2 are shown in Figure 9.

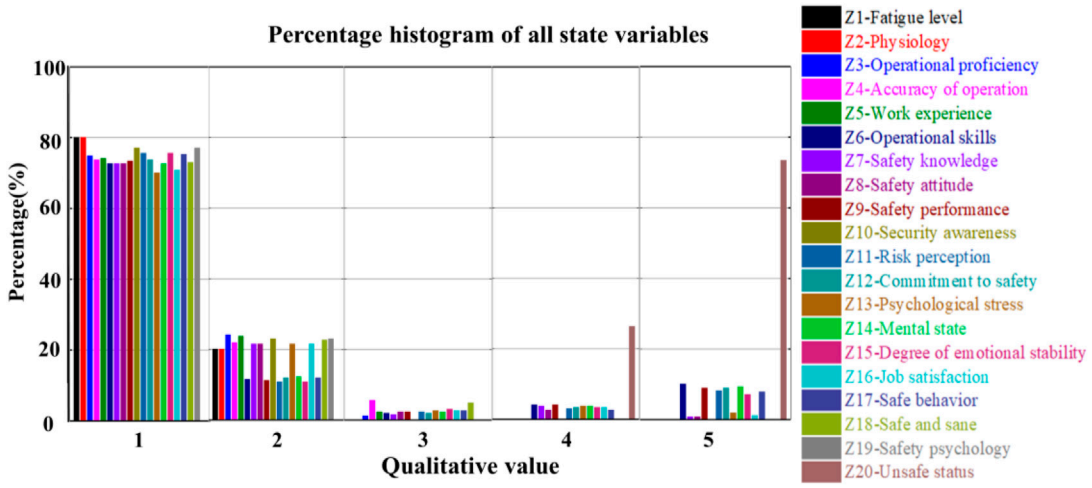


FIGURE 4
Simulation results of the initial state.

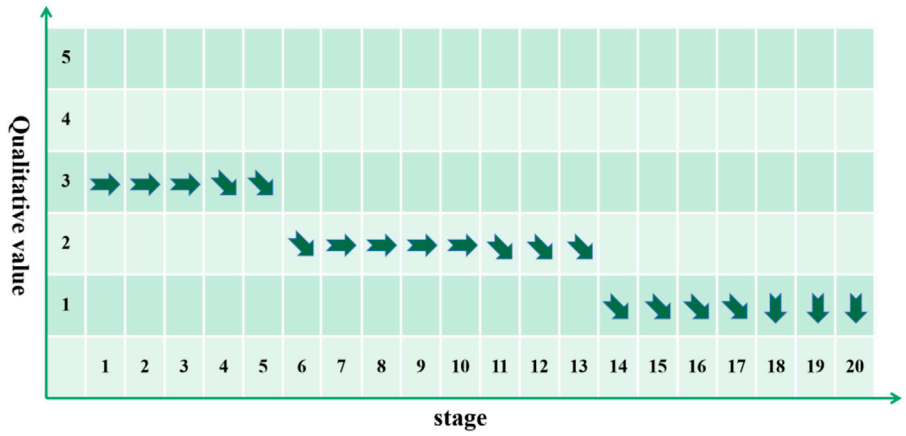


FIGURE 5
Trend of security behavior change in the initial state.

$Z_1$–$Z_{20}$ are concentrated in the "general" (qualitative value is 3) level. Through simulation and result summary and analysis, the simulation results of scheme 3 are shown in Figure 10. $Z_1$– $Z_{19}$ are concentrated at the "very high" (qualitative value is 5) level, while $Z_{20}$ is concentrated at the "very low" level. This shows that in the face of external interference, when high-intensity control measures are taken, all elements will develop in the "very high" direction, and the unsafe state will develop in the "very low" direction.

The simulation results of scheme 4 are shown in Figure 11. Scheme 4 is to analyze the impact of psychological factors on the unsafe state of coal mine personnel by enhancing or weakening physiological and psychological measures in the face of interference when the initial state is "average". The results show that $Z_1$- $Z_{18}$ are concentrated at the "low" (qualitative value of 2), while $Z_{19}$ is at the "high" (qualitative value of 4), and $Z_{20}$ is concentrated at the "general" level. This shows that in the face of external interference, when equivalent control measures are taken in terms of psychology, all elements will develop in the direction of "low", safety psychology may develop in the direction of "high", and unsafe state will develop in the direction of "general".

In scenarios 12–13, the status of each element is at "low" level, and in the face of disturbances, different intensity of control measures are taken for psychological. The simulation results for scenario 12 are shown in Figure 12, where $Z_1$–$Z_{16}$, $Z_{18}$, and $Z_{20}$ are concentrated at the "fair" (qualitative value of 3) level, while $Z_{17}$ is at the "low" (qualitative value of 2) level and $Z_{19}$ is at the "high" (qualitative value of 4) level. This indicates that in the initial state of "low" level, in the face of external interference, in the physiological aspects to take equivalent control measures, the psychological aspects of high-intensity measures, and the elements will develop in the "general" direction, safety behavior may be to the "low" direction, safety psychological development to the "high" direction,

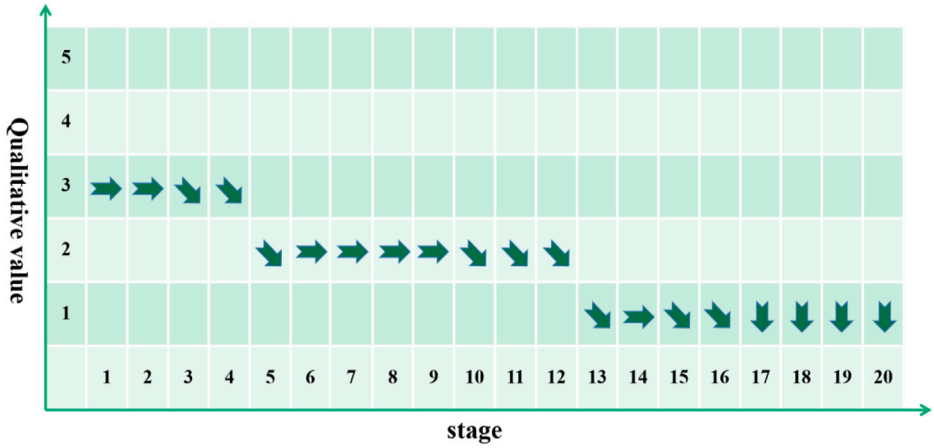


FIGURE 6
Trend of safety psychology in the initial state.

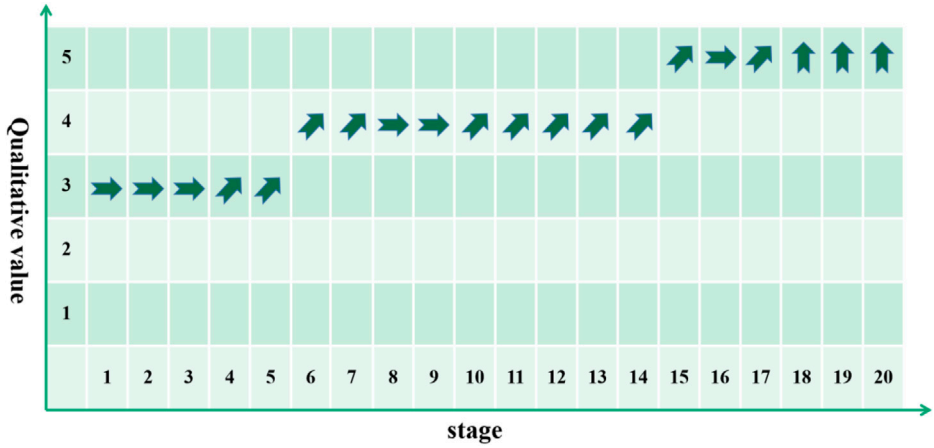


FIGURE 7
Trend of unsafe state change in initial state.

the coal mine personnel unsafe state will develop to the "general" level.

The comparative analysis of the trends of safe behavior ($Z_{17}$), safe psychology ($Z_{19}$), and unsafe state ($Z_{20}$) is shown in Figure 13.

From Figure 13, it can be obtained that in the process of unsafe state change of coal miners, safe behavior ($Z_{17}$), safe psychology ($Z_{19}$) and unsafe state ($Z_{20}$) start to change at stage 3, stage 6 and stage 7, respectively, which shows that the latest response in this case is safe behavior ($Z_{17}$), followed by safe psychology ($Z_{19}$) and finally unsafe state ($Z_{20}$).

The simulation results of scheme 13 are shown in Figure 14. $Z_1$–$Z_{16}$, $Z_{18}$, $Z_{20}$ are concentrated at the "general" (qualitative value of 3), while $Z_{17}$ is at the "high" (qualitative value of 4) level, and $Z_{19}$ is at the "low" (qualitative value of 2) level. This shows that when the initial state is "low", in the face of external interference, when high-intensity control measures are taken in the physiological aspect and equivalent interference measures are taken in the psychological aspect, and the most elements will develop in the "general" direction, safety behavior may develop in the "high" direction, and safety psychology will develop in the "low" direction. Under the action of the two, the unsafe state of coal mine personnel will develop in the "general" level.

The comparative analysis of the trends of safe behavior ($Z_{17}$), safe psychology ($Z_{19}$), and unsafe state ($Z_{20}$) is shown in Figure 15.

From Figure 15, it is easy to see that in the process of coal miners unsafe state change, safe behavior ($Z_{17}$), safe psychology ($Z_{19}$) and unsafe state ($Z_{20}$) start to change at stage 7, stage 8 and stage 9 respectively, which shows that in this case, the latest response is safe behavior ($Z_{17}$), and followed by safe psychology ($Z_{19}$) and finally unsafe state ($Z_{20}$).

The simulation results for scheme 17 are shown in Figure 16, analyzes the impact of psychological factors on the unsafe state of

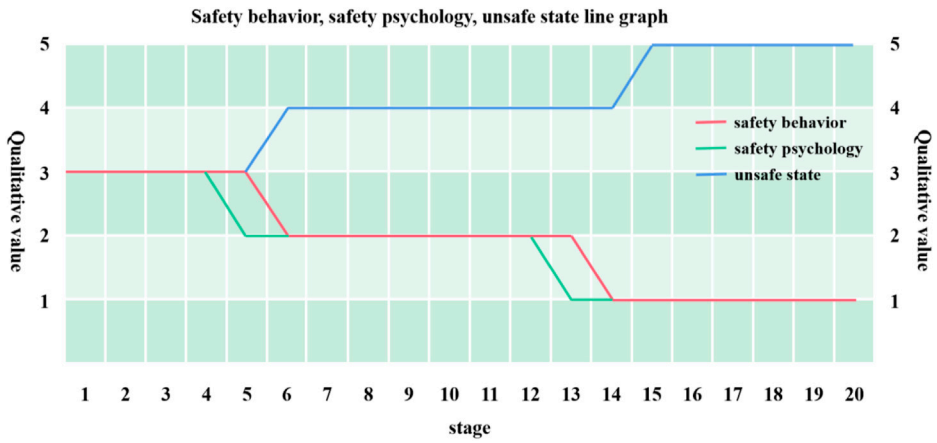


FIGURE 8
Comparison chart of the initial state of the change trend.

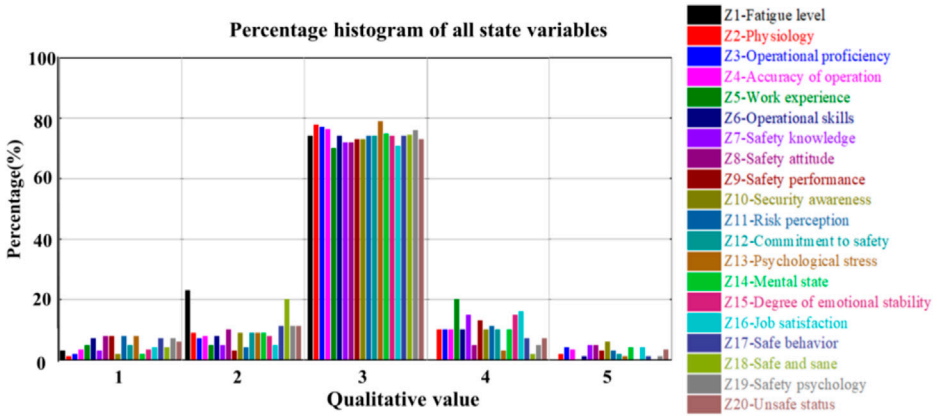


FIGURE 9
Simulation results of Scenario 2. Scheme 3—The state of each element is general. In the face of interference, take high-intensity control countermeasures, that is, X = 2, Y = 1, Z =< 3, → >. Through simulation and analysis, the simulation results of scheme 3 are shown in Figure 10. $Z_1$–$Z_{19}$ are concentrated at the "very high" (qualitative value is 5) level, while $Z_{20}$ is concentrated at the "very low" level. This shows that in the face of external interference, when high-intensity control measures are taken, all elements will develop in the "very high" direction, and the unsafe state will develop in the "very low" direction.

coal mine personnel. When the initial state is "high", in the face of interference, physiological and psychological measures are strengthened or weakened. The results show that $Z_1$–$Z_{18}$ are concentrated in the "low" (qualitative value of 2) level, while $Z_{19}$ is concentrated in the "high" (qualitative value of 4) level and $Z_{20}$ is concentrated in the "average" (qualitative value of 3) level. This indicates that in the face of external disturbances, when psychological control measures are taken, the elements will develop in the direction of "low", the security psychology may develop in the direction of "high", and the insecurity will develop in the direction of "average".

The comparative analysis of the trends of safe behavior ($Z_{17}$), safe psychology ($Z_{19}$), and unsafe state ($Z_{20}$) is shown in figure.

It can be seen from Figure 17 that in the process of changing the unsafe state of coal miners, the first response is safety psychology ($Z_{19}$), followed by safety behavior ($Z_{17}$), and finally the unsafe state ($Z_{20}$).

Scenario 23–the state of each element is at the "very high" level and no control measures are taken in the face of disturbances, i.e., X=0, Y=1, Z=<5, →>. The simulation results for scenario 23 are shown in Figure 18, where $Z_1$-$Z_{19}$ are concentrated at the "very low" (qualitative value of 1) level, while $Z_{20}$ is concentrated at the "very high" (qualitative value of 5) level. This indicates that the system state is at a "very high" level, and when no control measures are taken in the face of external disturbances, i.e., X=0, Y=1, Z=<5, →>, all elements of the coal mine personnel will eventually develop in the

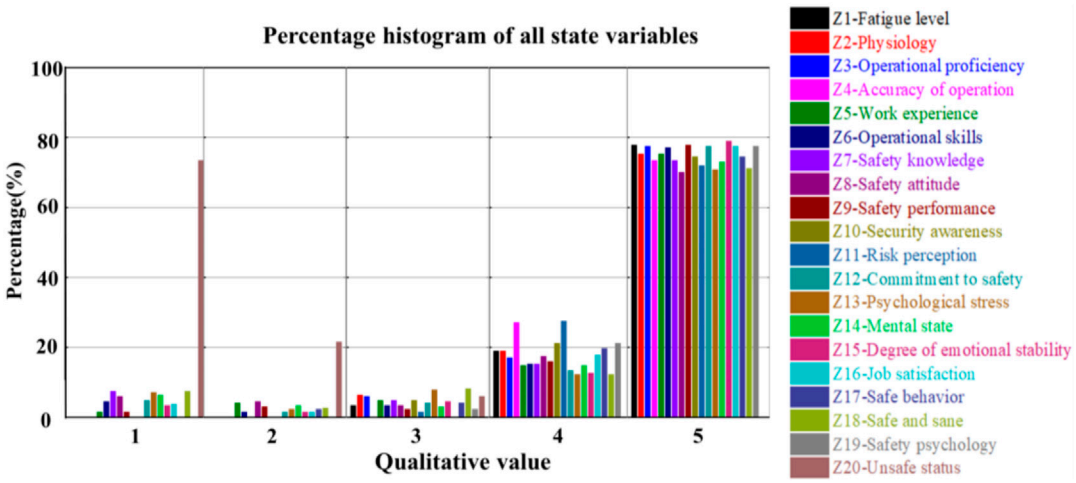


FIGURE 10
Simulation results of scheme 3.

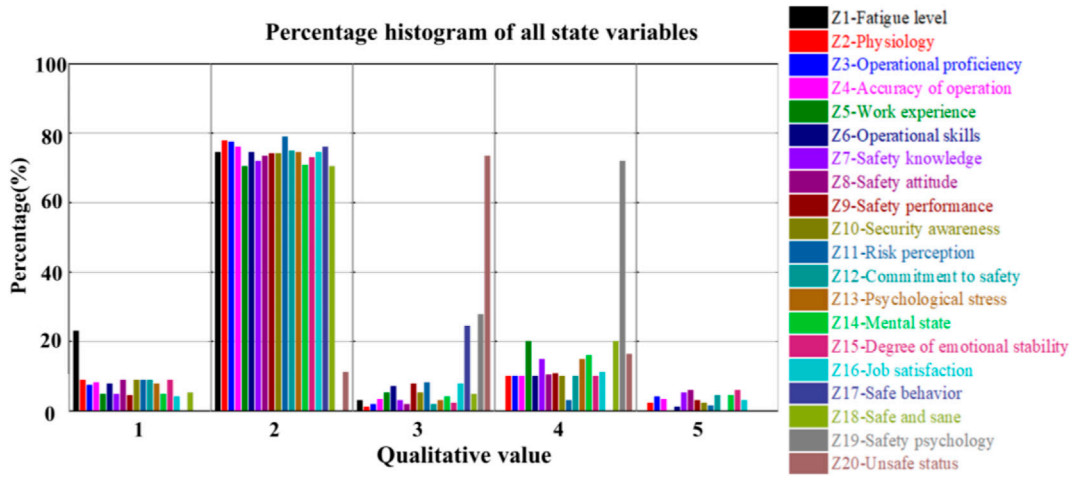


FIGURE 11
Simulation results of scheme 4.

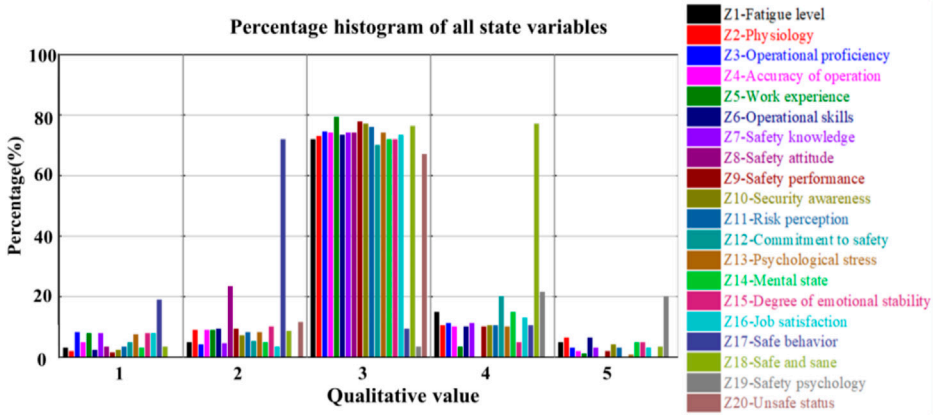


FIGURE 12
Simulation results of scenario 12.

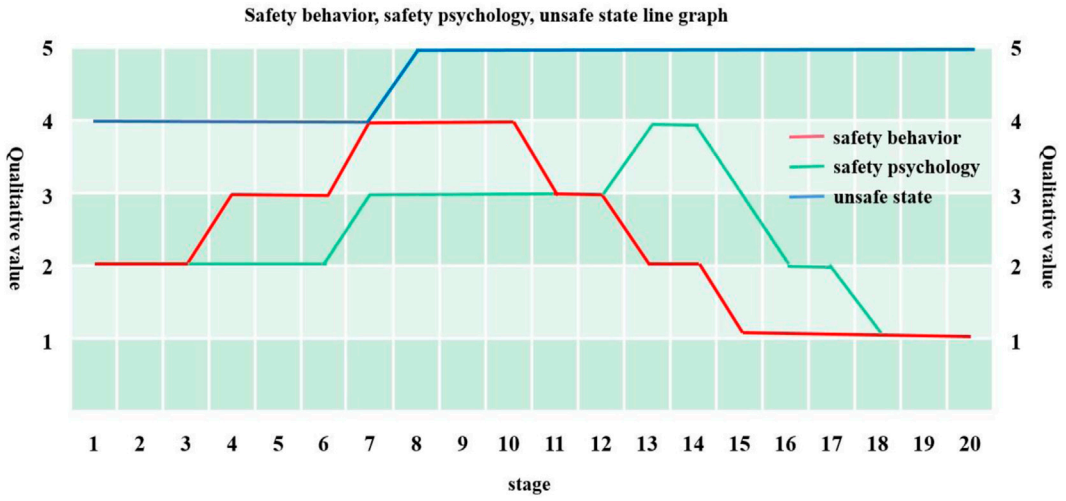


FIGURE 13
Comparison of the trend of scenario 12.

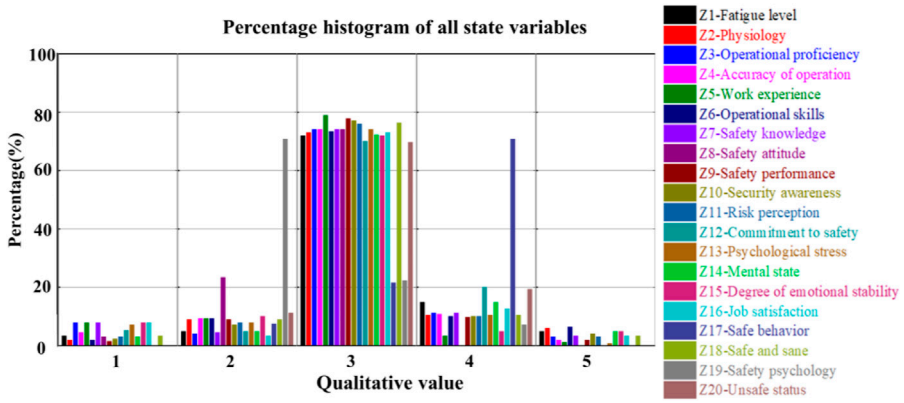


FIGURE 14
Simulation results of scheme 13.

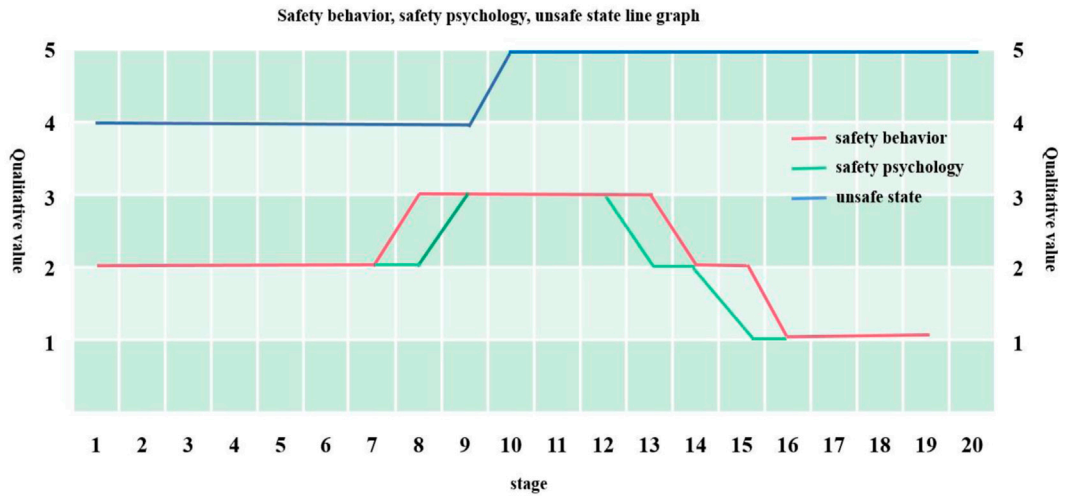


FIGURE 15
Comparison of the trend of change for scenario 13.

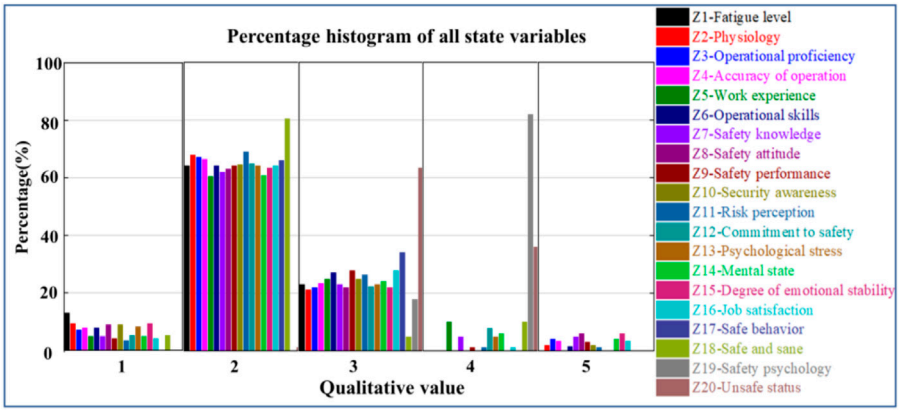


FIGURE 16
Simulation results of scheme 17.

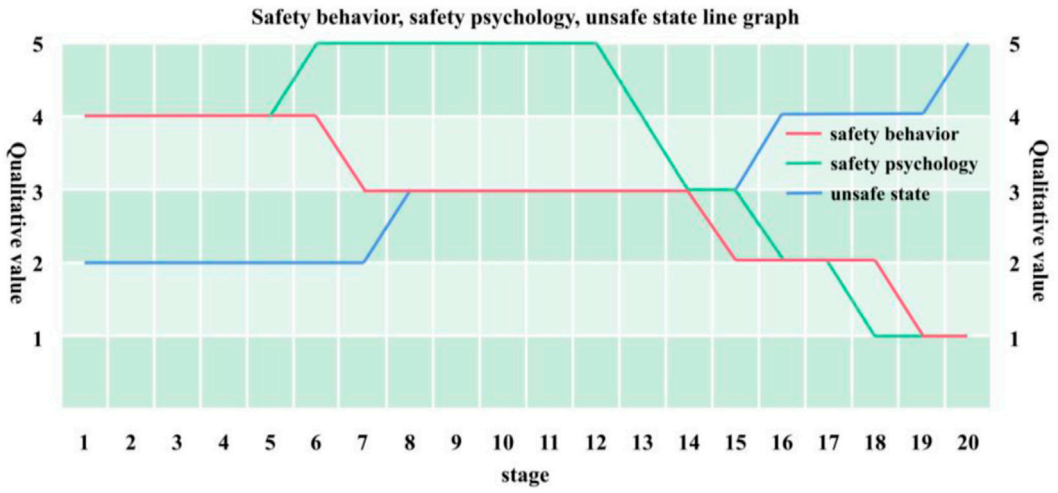


FIGURE 17
Comparison of the trend of scenario 17.

direction of "very low" (qualitative value of 1). Under the combined effect of all elements, the level of unsafe condition of coal mine personnel is "very high".

Based on the above analysis, the entire process of the simulation with the highest degree of agreement with the initial state simulation results (the 1000th simulation of this program) was selected, and the evolution trends of safety behavior ($Z_{17}$), safety psychology ($Z_{19}$) and unsafe state ($Z_{20}$) were analyzed, and their change trend graphs were made respectively, as shown in Figure 19.

Figure 19A shows the trend of safe behavior ($Z_{17}$), Figure 19B shows the trend of safe psychology ($Z_{19}$), and Figure 19C shows the trend of unsafe state ($Z_{20}$). The trend of the change in safety behavior in Scenario 23 can be seen visually that the direction of change in safety behavior changes to "weakly diminishing" ("↘") from stage 4 onwards when it is subject to external interference and no interventions are taken, indicating that the safety behavior of coal miners begins to show a downward trend at this time. In stage 6, the safety behavior ($Z_{17}$) is "weakened" ("↘"), the trend of decreases to "high" (qualitative value is 4). Until the 14th stage, the safety behavior ($Z_{17}$) continues to be "weakened" ("↘"). The trend of decreased to the "general" (qualitative value is 3), and in the 18th stage, the change direction changed to "strong reduction" ("↓"), and in the 20th stage, it fell to the "very low" level, indicating that the safety behavior of coal miners will continue to accelerate the deterioration.

Figure 20 shows that at the initial stage of change, safety behavior ($Z_{17}$) lags behind Safety Psychology ($Z_{19}$), while at the middle and later stages of change, unsafe state ($Z_{20}$) lags behind Safety Psychology ($Z_{19}$). This suggests that when subjected to external disturbances, psychological changes take the lead and affect changes in safety behavior, ultimately contributing to changes in the insecure state.

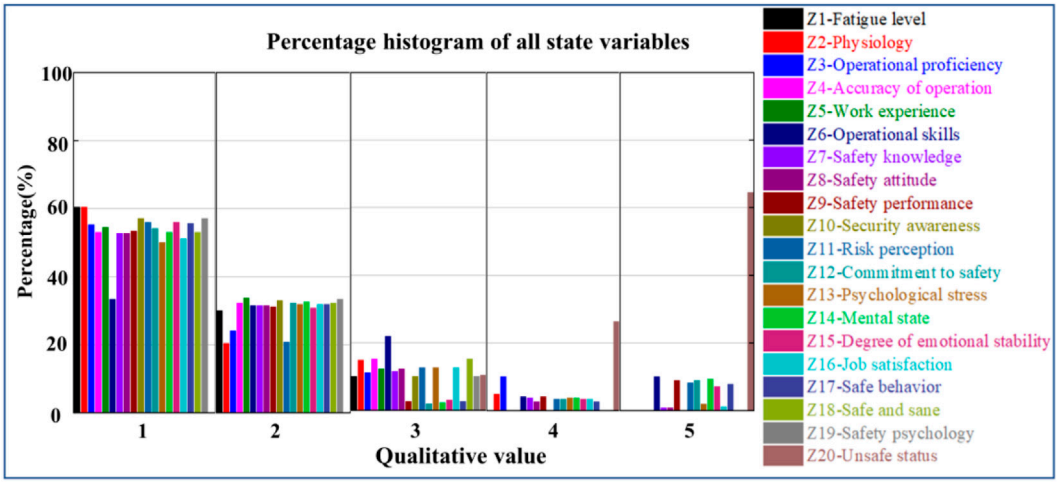


FIGURE 18
Simulation results of scenario 23.

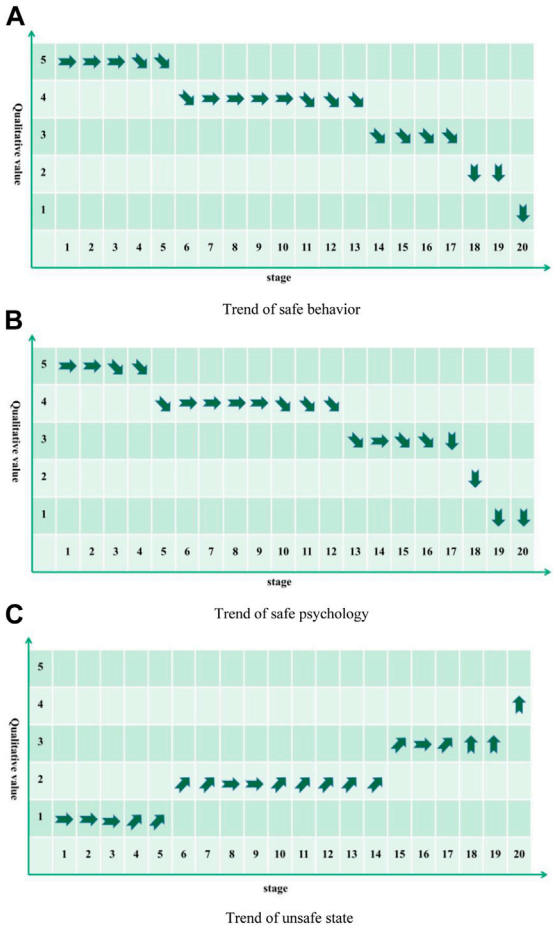


FIGURE 19
Trend of security changes for program 23.

In summary, analyzing the simulation results of the 23 scenarios, the following laws regarding the unsafe psychology and state of coal mine personnel can be derived.

① When coal mine personnel in daily production, subject to variety of external interference, regardless of their initial safety state, no safety management, no targeted management measures, coal mine personnel's safety behavior, safety psychology will develop to a "very low" level, unsafe state will develop to a "very high" level.

② When subjected to variety of external interference, if the intensity of the control measures taken and the intensity of interference is comparable or insufficient, the safety behavior of coal miners, such as the safety psychology will fluctuate, specifically in the form of first better and then back down to the original state, and finally to a lower direction; while the unsafe state is the opposite, first to a low direction and then up to the original state, and finally to a higher direction, when the intervention measures and the intensity of interference is comparable, the process contains a game.

③ If the intensity of the management measures taken is significantly higher than the intensity of the disturbance suffered, the safety behavior, safety psychology and unsafe state of the coal miners will improve significantly, but as the evolution progresses, the level of behavior, psychology and state will develop in a negative direction.

④ When the initial level of the system is different, without taking management measures or equivalent to the interference intensity, the higher the initial level of safety psychology, behavior and state, the slower its change to the negative direction.

⑤ In the face of external interference, enhance the psychological interventions, coal miners' safety psychology will develop in the direction of "high" or "very high", the trend and intensity of the

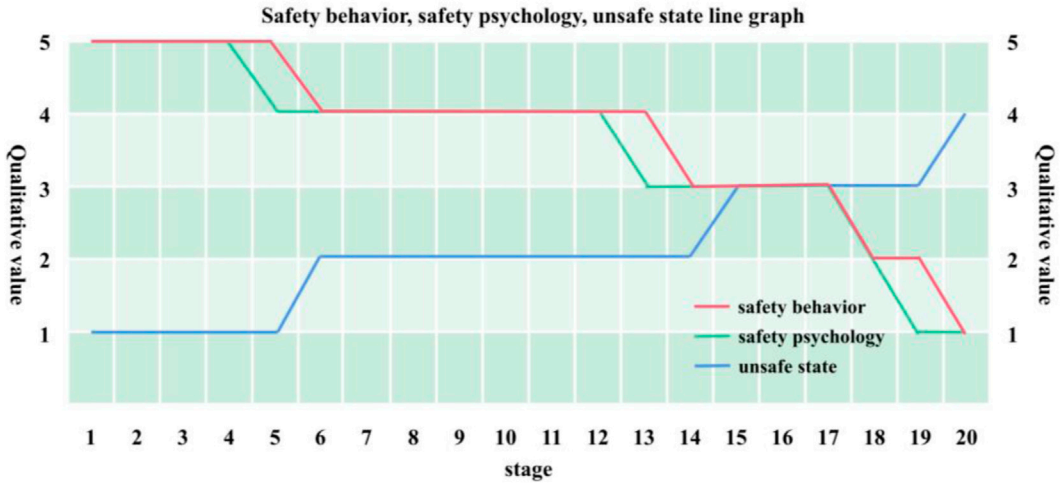


FIGURE 20
Comparison of the trend of scenario 23.

unsafe state is basically the same as the safety psychology, but will lag behind the changes in safety psychology.

⑥ In the face of external disturbances and enhanced physiological interventions, the safety behavior of coal miners will develop in the direction of "high" or "very high", and the intensity of change in the unsafe state will be slightly lower than that of unsafe behavior, but the trend of change is basically the same as that of safe behavior, and will lag behind the change in safe behavior.

⑦ In the face of external disturbances, only one aspect of the measures, regardless of the intensity, will eventually develop in a negative direction in terms of safety behavior, safety psychology and insecurity, and the rate of development will be higher than in the case of comprehensive interventions.

## 5 Conclusion

The influence relationship between the indicators of unsafe psychological state identification of coal mine workers was analyzed, and hypotheses were formulated and verified. Personality tendency had a significant positive effect on psychological stress; psychological characteristics had a significant positive effect on safety psychology; and psychological characteristics had a significant positive effect on psychological stress. According to the results of hypothesis verification, the structural equation model for coal mine workers' unsafe state identification was constructed, and the fitted indicators were tested to be within a reasonable range.

The QSIM model of coal mine personnel unsafe state was constructed, and the model focused on the analysis of the relationship between the important influencing factors of coal mine personnel unsafe state, including 20 system state variables, 13 management variables, 14 interference variables and 4 shadow variables. Based on the simulation results of the 23 scenarios, the change process of coal mine personnel's safety behavior, safety psychology and unsafe state were sorted out in terms of different states and the intensity of different management measures, and the law of the role of safety psychology on safety behavior and safety state was explored.

It is obtained that comprehensive high-intensity measures can keep the safety psychology and state of coal mine personnel at the "very high" or "high" level for a long time, but there will still be a downward trend in the end ("↘" Or "↓"), and may even fall to a "very low" level; when taking psychological management measures, the safety psychology and state of coal mine personnel will still rise, but it cannot reach the "very high" level; When the management measures are equivalent to the external interference, the change trend has fluctuations, which is the result of the game between various factors, which lays a research foundation for the study of the dynamic game evolution process of coal miners' psychology on unsafe state.

To further improve coal mine safety production management, further research can be conducted from the following three aspects: The factors affecting the unsafe status of coal mine workers are easily affected by the surrounding environment, especially changes in the international situation and national policy guidance, which also have a disturbing impact on the unsafe status of coal mine workers. The next step can be to conduct empirical research based on this research, establish a group emergence model, and continuously revise and improve the emergence mechanism of unsafe states among coal mine employees. The experimental tests on the unsafe psychology and behavior of different coal mine groups can be conducted, and provide corresponding safety management measures.

## Data availability statement

The original contributions presented in the study are included in the article/supplementary material, further inquiries can be directed to the corresponding authors.

## Author contributions

All authors contributed to the study conception and design. Material preparation, data collection and analysis were performed by ZL, WM, BK, KY, XM, and XZ. The first draft of the manuscript was written by JY and all authors commented on previous versions of the manuscript. All authors contributed to the article and approved the submitted version.

## Funding

This research was jointly supported by the Open Project Funding of the Qingdao West Coast New Area Industry and Information Technology Bureau Science and Technology Benefiting People Project (2021-109).

## Conflict of interest

Author XZ was employed by Qingdao No.1 Municipal Engineering Co., Ltd.

The remaining authors declare that the research was conducted in the absence of any commercial or financial relationships that could be construed as a potential conflict of interest.

## Publisher's note

All claims expressed in this article are solely those of the authors and do not necessarily represent those of their affiliated organizations, or those of the publisher, the editors and the reviewers. Any product that may be evaluated in this article, or claim that may be made by its manufacturer, is not guaranteed or endorsed by the publisher.

## References

Engler, A., and Soultanis, N. (2005). Droop control in LV-Grids[C]. *Int. Conf. Future Power Syst. Amsterdam* 11, 142–147. doi:10.1109/FPS.2005.204224

Cao, Q., Yu, K., Zhou, L., Wang, L., and Li, C. (2019). In-depth research on qualitative simulation of coal miners' group safety behaviors. *Saf. Sci.* 113, 210–232. doi:10.1016/j.ssci.2018.11.012

Chen, J., Cao, Q., Liu, Y., Takahashi, H., and Tokonami, S. (2010). An investigation on radon and thoron response of alpha-track detectors used in the Winnipeg case-control study. *J. Shandong Univ. Sci. Technol.* 29, 83–86. doi:10.1093/rpd/ncp177

Chen, K., Zhang, Q., Tao, Y., Luo, K., and Chen, Q. (2022). The slope safety, heavy metal leaching, and pollutant diffusion prediction properties under the influence of unclassified cemented paste backfill in an open pit. *Int. J. Environ. Res. Public Health* 19 (19), 12772. doi:10.3390/ijerph191912772

Chi, J., Wang, B., Zhang, H., Kang, J., Lu, T., Huang, Y., et al. (2021). Regional coal power overcapacity assessment in China from 2020 to 2025. *J. Clean. Prod.* 303, 127020. doi:10.1016/j.jclepro.2021.127020

Considine, R., Tynan, R., James, C., Wiggers, J., Lewin, T., Inder, K., et al. (2017). The contribution of individual, social and work characteristics to employee mental health in a coal mining industry population. *PLoS One* 12, e0168445. doi:10.1371/journal.pone.0168445

Dong, C., Qi, Y., and Nemet, G. (2021a). A government approach to address coal overcapacity in China. *J. Clean. Prod.* 278, 123417. doi:10.1016/j.jclepro.2020.123417

Dong, S., Wang, H., Guo, X., and Zhou, Z. (2021b). Characteristics of water hazards in China's coal mines: A review. *Mine Water Environ.* 40, 325–333. doi:10.1007/s10230-021-00770-6

Han, S., Chen, H., Long, R., and Cui, X. (2018). Peak coal in China: A literature review. *Resour. Conservation Recycl.* 129, 293–306. doi:10.1016/j.resconrec.2016.08.012

He, X., and Song, L. (2012). Status and future tasks of coal mining safety in China. *Saf. Sci.* 50, 894–898. doi:10.1016/j.ssci.2011.08.012

Kuipers, B. J. (1986). Qualitative simulation. *Artifical Intell.* 29, 289–338. doi:10.1016/0004-3702(86)90073-1

Leitch, R., Freitag, H., Struss, P., and Tornielle, G. (1991). *Artist: A methodological approach to specifying model based diagnostic systems*. Milan Applications Conference.

Li, B.-B., Liang, Q.-M., and Wang, J. C. (2015). A comparative study on prediction methods for China's medium- and long-term coal demand. *Energy* 93, 1671–1683. doi:10.1016/j.energy.2015.10.039

Liu, Q., Liu, J., Gao, J., Wang, J., and Han, J. (2020). An empirical study of early warning model on the number of coal mine accidents in China. *Saf. Sci.* 123, 104559. doi:10.1016/j.ssci.2019.104559

Ma, J., and Dai, H. (2017). A methodology to construct warning index system for coal mine safety based on collaborative management. *Saf. Sci.* 93, 86–95. doi:10.1016/j.ssci.2016.11.012

Margolis, K. A. (2010). Underground coal mining injury: A look at how age and experience relate to days lost from work following an injury. *Saf. Sci.* 48, 417–421. doi:10.1016/j.ssci.2009.12.015

Musse, S. R., and Thalmann, D. (1997). A model of human crowd behavior: Group inter-relationship and collision detection analysis. *Eurographics*, 39–51. doi:10.1007/978-3-7091-6874-5_3

Peng, B., Guo, D., Qiao, H., Yang, Q., Zhang, B., Hayat, T., et al. (2018). Bibliometric and visualized analysis of China's coal research 2000–2015. *J. Clean. Prod.* 197, 1177–1189. doi:10.1016/j.jclepro.2018.06.283

Qiao, W., Liu, Q., Li, X., Luo, X., and Wan, Y. (2018). Using data mining techniques to analyze the influencing factor of unsafe behaviors in Chinese underground coal mines. *Resour. Policy* 59, 210–216. doi:10.1016/j.resourpol.2018.07.003

Qing-gui, C., Kai, L., Ye-jiao, L., Qi-hua, S., and Jian, Z. (2012). Risk management and workers' safety behavior control in coal mine. *Saf. Sci.* 50, 909–913. doi:10.1016/j.ssci.2011.08.005

Reynolds, C. W. (1987). Flocks, herds and schools: A distributed behavioral model. *ACM SIGGRAPH Comput. Graph.* 21, 25–34. doi:10.1145/37402.37406

Shen, Q., and Leitch, R. (1993). Fuzzy qualitative simulation. *IEEE Trans. Syst. Man Cybern.* 23 (4), 1038–1061. doi:10.1109/21.247887

Thalmann, D., Musse, S. R., and Kallmann, M. (2000). *From individual human agents to crowds*. informatik/informatique.

Tong, R., Yang, Y., Ma, X., Zhang, Y., Li, S., and Yang, H. (2019a). Risk assessment of miners' unsafe behaviors: A case study of gas explosion accidents in coal mine, China. *Int. J. Environ. Res. public health* 16 (10), 1765. doi:10.3390/ijerph16101765

Tong, R., Zhang, Y., Yang, Y., Jia, Q., Ma, X., and Shao, G. (2019b). Evaluating targeted intervention on coal miners' unsafe behavior. *Int. J. Environ. Res. public health* 16 (3), 422. doi:10.3390/ijerph16030422

Tu, X., and Terzopoulos, D. (1994). Artificial fishes: Physics, locomotion, perception, behavior. *ACM SIGGRAPH Comput. Graph.* 28.

Wang, J., Feng, L., and Tverberg, G. E. (2013). An analysis of China's coal supply and its impact on China's future economic growth. *Energy Policy* 57, 542–551. doi:10.1016/j.enpol.2013.02.034

Wang, Z., Zhu, Y., Zhu, Y., and Shi, Y. (2016). Energy structure change and carbon emission trends in China. *Energy* 115, 369–377. doi:10.1016/j.energy.2016.08.066

Xu, Q., Peng, S., Xu, J., Jiao, F., Cheng, L., Jia, L., et al. (2023). Study on time effect of acidified pulverized coal micro components and discussion on mathematical correlation of influencing factors. *Fuel* 342, 127842–127849. doi:10.1016/j.fuel.2023.127842

Yang, L., Wang, X., Zhu, J., and Qin, Z. (2022a). Influencing factors, formation mechanism, and pre-control methods of coal miners' unsafe behavior: A systematic literature review. *Front. Public Health* 10, 792015–792019. doi:10.3389/fpubh.2022.792015

Yang, L., Wang, X., Zhu, J., Sun, L., and Qin, Z. (2022b). Comprehensive evaluation of deep coal miners' unsafe behavior based on HFACS-CM-SEM-SD. *Int. J. Environ. Res. public health* 19 (17), 10762–10829. doi:10.3390/ijerph191710762

Yin, S., Shi, L., Liu, Z., Lu, W., Pan, X., Zhuang, Z., et al. (2023). Study on the variation laws and fractal characteristics of acoustic emission during coal spontaneous combustion. *Processes* 11 (3), 1–18. doi:10.3390/pr11030786

You, M., Li, S., Li, D., and Xia, Q. (2019). Study on the influencing factors of miners' unsafe behavior propagation. *Front. Psychol.* 10, 2467. doi:10.3389/fpsyg.2019.02467

Yu, K., Cao, Q., Xie, C., Qu, N., and Zhou, L. (2019a). Analysis of intervention strategies for coal miners' unsafe behaviors based on analytic network process and system dynamics. *Saf. Sci.* 118, 145–157. doi:10.1016/j.ssci.2019.05.002

Yu, K., Wu, L., and Zhou, L. (2022). Research on the mixed education mode for the safety engineering major during the coronavirus (COVID-19) epidemic. *Int. J. Environ. Res. Public Health* 19 (4), 1967. doi:10.3390/ijerph19041967

Yu, K., Zhou, L., Cao, Q., and Li, Z. (2019b). Evolutionary game research on symmetry of workers' behavior in coal mine enterprises. *Symmetry-Basel* 11 (2), 156–212. doi:10.3390/sym11020156

Zhang, J., Li, X., and Pan, L. (2022). Policy effect on clean coal-fired power development in China. *Energies* 15, 897. doi:10.3390/en15030897

Zhang, Y.-P., Li, J.-Z., Wang, X. J., Feng, G.-R., Zhang, B.-S., Wang, T.-R., et al. (2017). Relationship research between subjective well-being and unsafe behavior of coal miners. *EURASIA J. Math. Sci. Technol. Educ.* 13. doi:10.12973/ejmste/79046

Zhang, Y., Nie, R., Shi, R., and Zhang, M. (2018). Measuring the capacity utilization of the coal sector and its decoupling with economic growth in China's supply-side reform. *Resour. Conservation Recycl.* 129, 314–325. doi:10.1016/j.resconrec.2016.09.022

Zhou, A., Hu, J., and Wang, K. (2020). Carbon emission assessment and control measures for coal mining in China. *Environ. Earth Sci.* 79, 461. doi:10.1007/s12665-020-09189-8

Zhu, J., Wang, X., Yang, L., Qin, Z., Geng, J., and Zhang, X. (2022). Research on the construction of a comprehensive evaluation model of psychological factors in coal mine workers' safety: Investigation and analysis of 1,500 miners in east China. *Front. Public Health* 10, 849733. doi:10.3389/fpubh.2022.849733

frontiers | Frontiers in Earth Science

TYPE Original Research
PUBLISHED 20 July 2023
DOI 10.3389/feart.2023.1214182



OPEN ACCESS

EDITED BY
Miao Li,
Charles Sturt University, Australia

REVIEWED BY
Shuai Cao,
University of Science and Technology Beijing, China
Yue Xiao,
Wuhan University of Technology, China

*CORRESPONDENCE
Changlong Wang,
baistuwong@139.com

RECEIVED 29 April 2023
ACCEPTED 10 July 2023
PUBLISHED 20 July 2023

CITATION
Yuan D, Liang X, Gao Y, Ping H, Wang C, Ma J, Zheng Y, Jing J, Qi Y, Zhai Y and Liu F (2023), High-temperature modification of steel slag using composite modifier containing silicon calcium slag, fly ash, and reservoir sediment.
*Front. Earth Sci.* 11:1214182.
doi: 10.3389/feart.2023.1214182



# High-temperature modification of steel slag using composite modifier containing silicon calcium slag, fly ash, and reservoir sediment

Dongxia Yuan[1], Xiaoying Liang[1], Ying Gao[1], Haoyan Ping[1], Changlong Wang[1]*, Jintao Ma[1], Yongchao Zheng[2], Jianlin Jing[1], Yang Qi[2], Yuxin Zhai[3] and Feng Liu[4]

[1]Collaborative Innovation Center for Intelligent Regulation and Integrated Management of Water Resources Jointly Built by Provinces and Ministries, School of Civil Engineering, Hebei University of Engineering, Handan, China, [2]State Key Laboratory of Solid Waste Reuse for Building Materials, Beijing Building Materials Academy of Science Research, Beijing, China, [3]China Railway Construction Group Co., LTD., Beijing, China, [4]China Railway Construction Group Construction Development Co., Ltd., Beijing, China

Steel slag (SS) is a kind of industrial solid waste, and its accumulation brings certain harm to the ecological environment. In order to promote the building material utilization of SS, high-temperature modification (HTM) of SS is performed using a composite modifier (CMSFR) containing silicon calcium slag (SCS), fly ash (FA), and reservoir sediment (RS). Then, the authors investigated the effect of CMSFR on the cementitious properties and volume soundness of SS mixture after HTM (SMHTM). After that, the mineral composition and microstructure of SMHTM were investigated through X-ray fluorescence analysis (XRF), X-ray diffraction (XRD), scanning electronic microscopy (SEM), energy dispersive spectrometry (EDS), and particle size analysis. It was found that the free CaO (f-CaO) content obviously decreased, and the cementitious properties improved in SMHTM. When the CMSFR content was 20% (SCS: FA: RS = 9:7:4), and the modification temperature (MT) was 1,250°C, the mass fraction of f-CaO in SMHTM dropped from 4.81% to 1.90%, down by 60.5%; the 28-day activity index of SMHTM increased to 85.4%, 14.3% higher than that of raw SS, which meets the technical requirement of Steel slag powder used for cement and concrete (GB/T 20491-2017): the activity index of grade I SS powder must be greater than or equal to 80%. As the mass fraction of CMSFR grew from 10% to 30%, new mineral phases formed in SMHTM, including diopside ($CMS_2$), ceylonite ($MgFe_2O_4$), gehlenite ($C_2AS$), tricalcium aluminate ($C_3A$), and magnetite ($Fe_3O_4$). The HTM with CMSFR promotes the decomposition of RO phase (a continuous solid solution composed of divalent metal oxides like FeO, MgO, MnO, and CaO) in raw SS, turning the FeO in that phase into $Fe_3O_4$. The above results indicate that the SMHTM mixed with CMSFR can be applied harmless in cement and concrete, making low-energy fine grinding of SS a possibility.

KEYWORDS

**Steel slag (SS), composite modifier, high-temperature modification (HTM), free CaO (f-CaO), cementitious activity**

# 1 Introduction

In order to promote the building material utilization of steel slag (SS), high-temperature modification (HTM) was studied to overcome the shortcomings of low cementitious activity and poor volume soundness of SS, providing reference for the design and production of high-performance SS based cementitious materials. SS is a waste product generated by steel-making industry. Typical SS consists of slag-making materials such as smelting fluxes like limestone, dolomite, and iron ore. These materials are added to modify the properties of steel, as well as the impurities separated from two mutually non-fusing liquid phase furnace materials melted at high temperature. The SS emission is roughly 12–20% of crude steel output (Shi, 2004; Guo et al., 2009; Dhoble and Ahmed, 2018). In China, the annual production of SS is about 80 million tons, and the cumulative storage amounts to around 500 million tons. However, fewer than 30% of SS has been utilized comprehensively (Alanyali et al., 2009; Li et al., 2011; Wang et al., 2018). The accumulation of huge amount of SS pollutes the environment, occupies wide stretches of land, and seriously wastes resources. SS contains some cementitious minerals, it can be used as some raw materials for cement concrete; In addition, there is also a high content of FeO and a certain amount of free CaO (f-CaO) and free MgO (f-MgO) in the SS. FeO cannot be directly separated through magnetic separation and easy to cause SS cement strength reduction. The presence of f-CaO and f-MgO makes the SS difficult to be used as a building materials due to its poor soundness. Thus, the main problems of SS in the process of building materials application can be summarized as the following four aspects: 1) The proportion of iron oxides is large and difficult to separate; 2) Lack of active mineral phase and poor hydration activity; 3) The content of free calcium oxide and magnesium oxide is high, and their stability is poor; 4) It cannot be mixed into cement in a larger proportion for application.

In terms of chemical composition, SS mainly consists of $SiO_2$, CaO, MgO, and $Fe_2O_3$, plus a small amount of $Al_2O_3$, MnO, and $P_2O_5$ (Figure 1) (Shi, 2002; Peng and Huang, 2010; Roslan et al., 2016). The main minerals in SS include $C_2S$ ($2CaO{\cdot}SiO_2$), $C_3S$ ($3CaO{\cdot}SiO_2$), $C_4AF$ ($4CaO{\cdot}Al_2O_3{\cdot}Fe_2O_3$), $C_2F$ ($2CaO{\cdot}Fe_2O_3$), $C_{12}A_7$ ($12CaO{\cdot}7Al_2O_3$), $C_3A$ ($3CaO{\cdot}Al_2O_3$), RO phase (a continuous solid solution composed of divalent metal oxides like FeO, MgO, MnO, and CaO), Fe, $Fe_2O_3{\cdot}SiO_2$, $Fe_3O_4$, and f-CaO (Waligora et al., 2010; Liu et al., 2014; Yan et al., 2014; Yüksel, 2017; Humbert and Castro-Gomes, 2019; Liu W. H. et al., 2020). Overall, the chemical and mineral compositions of SS are similar to those of cement. At present, SS is mainly utilized in subgrade engineering (Aldeeky and Hattamleh, 2017; Gu et al., 2018; Wang et al., 2020), mine filling (Li et al., 2021; Zhang et al., 2021; Zhao D. Q. et al., 2022), and asphalt concrete aggregate production (Hasita et al., 2020a; Hasita et al., 2020b; Jiao et al., 2020). The $C_2S$ and $C_3S$ in SS can react with water to generate many hydration products, such as $Ca(OH)_2$, C-S-A-H gel ($CaO{\cdot}Al_2O_3{\cdot}4SiO_2{\cdot}5H_2O$), C-A-H crystal ($CaO{\cdot}Al_2O_3{\cdot}10H_2O$), and C-S-H gel ($3CaO{\cdot}2SiO_2{\cdot}3H_2O$). Therefore, SS provides a promising auxiliary cementitious material, which could reduce resource waste and protect the environment (Palankar et al., 2016; Mo et al., 2017; Zhuang and Wang, 2021).

Many researchers have explored the potential of SS as an auxiliary cementitious material. Luxán et al. (2020), Li et al. (2011), and Shi (2004) investigated the mineralogical features and microstructure of SS. Qian et al. (2002), Natali Murri et al. (2013), Kriskova et al. (2012), and Wang et al. (2011) modified the hydraulic activity of SS by various means, such as changing the mineral compositions, water quenching, autoclave treatment, and long-

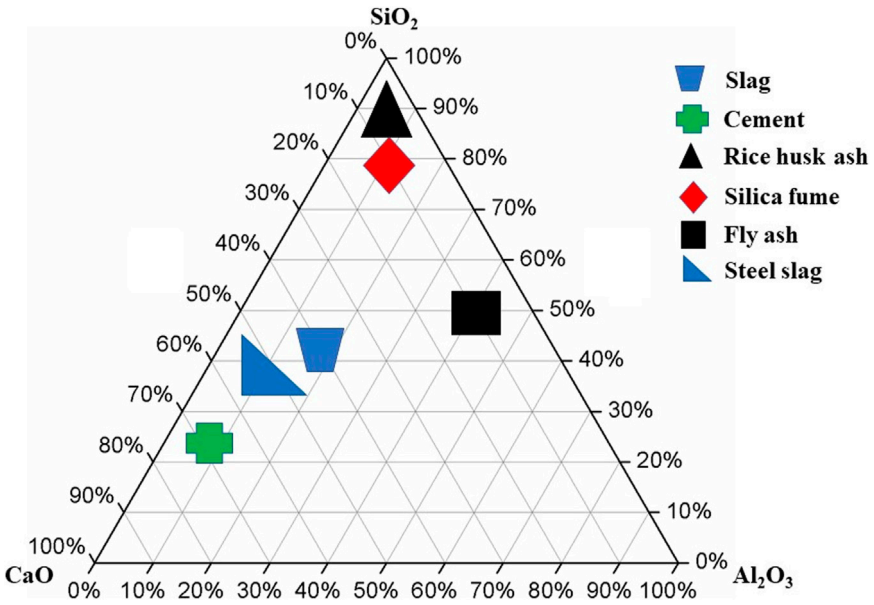


FIGURE 1
Chemical compositions of SS (Shi, 2002).

time milling in ethanol suspension. Additionally, some researchers tried to prepare composite cementitious materials out of SS and cement. These studies have primarily examined the physical and mechanical properties (Monshi and Asgarani, 1999; Shi and Hu, 2003; Adolfsson et al., 2011; Mo et al., 2016), volume expansion (Kourounis et al., 2007), volume soundness (Xue et al., 2006; Anastasiou et al., 2014; Khan et al., 2016; Wang et al., 2017; Saly et al., 2018; Saxena and Tembhurkar, 2018), durability and transportation properties (permeability to chloride ions, and resistance to sulfate attack) (Wang et al., 2013), microstructure (Zhang et al., 2011; Iacobescu et al., 2015; Dai et al., 2022), and hydration products (Zhang et al., 2011; Iacobescu et al., 2015; Rashad, 2019; Dai et al., 2022).

Despite its cementitious properties, SS has not been widely added to cement as an auxiliary cementitious material (Liu J. Z. et al., 2020). The main reasons for the limited application include the soundness problem (the presence of f-CaO and f-MgO in SS may cause volume expansion) (Kourounis et al., 2007; Wu et al., 2007; Guo et al., 2009), poor grindability (RO phase exists in SS), and heavy metal leaching (the presence of Pb, Ba, Cd, Cr, Zn, As, Ni and V) (Tossavainen et al., 2007; Guo et al., 2009; Li et al., 2011; Zhang et al., 2011). SS contains 5%–10% f-CaO, which features high formation temperature, intact crystallization, and solid fusion of some impurities. It takes a long time for f-CaO to complete hydration. Through the reaction of water, the volume of f-CaO would expand by 97.8%. That is why SS has a poor volume soundness (Zhang et al., 2012; Biskri et al., 2017; Tu et al., 2019). What is worse, SS has a content of $C_2S$ and $C_3S$, only 50%–70% of that in cement clinker (CC). Because of the excessively high formation temperature, the mineral phases form dense and large crystals, which weaken the cementitious performance (Kourounis et al., 2007; Cao et al., 2019; Zhao Y. L. et al., 2022).

In order to promote the application of SS in cement and concrete (Li et al., 2011), several backend modification techniques have been developed to improve its cementitious properties and address the soundness issue. These modification techniques include mechanical activation (Guo and Pan, 2018; Wang et al., 2018; Wang et al., 2019; Guo and Xiong, 2020), thermal activation (Li et al., 2011; Kriskova et al., 2013; Li et al., 2019), and chemical activation (Salman et al., 2015; Huo et al., 2020; Huo et al., 2021). However, these technologies usually require additional energy and chemical activators, and their modification effect varies with the chemical and mineral components of SS. SS is different from Portland CC, granulated blast furnace slag (GBFS) and pozzolanic materials, but its mineral composition is more similar to CC. The direction of modified SS mixture (MSM) can be close to CC, GBFS and pozzolanic materials. However, the potential hydraulic properties of GBFS is mainly related to the large amount of vitreous bodies formed by water quenching of GBFS and the easy dissolution of the fractal structure in an alkaline environment, while MSM cannot obtain a large amount of glass body with the actual cooling method of SS (such as hot splashing method, hot sealing method, etc.) even though its chemical composition is close to that of GBFS. The potential hydraulic hardness of pozzolanic materials is mainly related to their active amorphous substances and spherical aluminum silicate glass bodies, while high-temperature molten SS contains more iron and has a high density, which limits its ability to obtain pozzolanic activity; The hydraulic properties of CC mainly come from about 75% of the total silicate minerals, which seems to be easier to achieve from the cooling mode and mineral composition of SS. It can be seen from the formation process of SS that the heat enthalpy of liquid SS discharged during converter steelmaking reaches 1,670 $MJ{\cdot}t^{-1}$. If the waste heat can be fully utilized to MSM, a large amount of waste heat can be recovered, the composition of SS can be stabilized, and the hydration activity of SS can be improved, realize the purpose of energy saving and waste utilization. Some researchers have experimented with the addition of conditioning components to the steelmaking process in the converter to reform the SS close to the CC at the time of discharge, but due to the high requirements of the steelmaking process on the composition control of the slag and finished steel, the impact on the quality of the molten steel is not allowed, so the feasibility of in-furnace reforming is not strong, and it is easier to achieve high-temperature reforming by mixing the conditioning components at the time of discharge. The method of SS mixture after high-temperature modification (SMHTM) is easier to achieve.

In this study, the authors simulate the on-line MSM outside the furnace. The regulating direction is CC, and the regulating components are silica-alumina and calcium materials, from the perspective of resource conservation and development of green building materials, following the goal of "treating waste with waste". This study choose reservoir sediment (RS), fly ash (FA), and silicon calcium slag (SCS) to form a composite modifier (CMSFR), and the three wastes corresponding to the adjustment of Si, Al and Ca elements in SS. The composition and structure of SS were modified by this multi-component composite modifier. In this way, the secondary phase reaction was controlled, and the content of cementitious phase ($C_3S$, $C_2S$, and $C_3A$) and glass phase in SS was increased. The CMSFR helps to stabilize the unsoundness components in SS, and enhance the cementitious properties of SS, providing a reference for harmless application of SS and silicon-aluminum based solid waste in cement and concrete.

# 2 Materials and methods

## 2.1 Experimental materials

(1) SS. This study uses converter SS without going through heat stewing from China Shougang Group Qian'an Steel Co., LTD. The SS meets the requirements in *Steel slag powder used for cement and concrete* (GB/T 20491-2017). According to Mason's (1944) formula $CaO/(SiO_2+P_2O_5)$, the alkalinity of the SS is calculated as 2.79, its pH value is 12.1. Thus, the SS is highly alkaline. The f-CaO content in raw SS is 6.01%. The particle size analysis of the raw SS shows that 81.57% of the SS particles are distributed between 0.3 mm and 9.5 mm. Hence, the raw SS must be crushed before being ground. After processing, the specific surface area (SSA) of SS powder is 420 $m^2\ kg^{-1}$. The activity indexes of raw SS for 7 days and 28 days are measured to be 63.4% and 71.1%, respectively, according to Steel slag powder used for cement and concrete (GB/T 20491-2017).

The raw SS powder is used as blank samples for comparative analysis with SMHTM, and marked as S0. The main minerals of raw SS include RO phase, $C_3S$, and $C_2S$ (Figure 2A). In addition, the

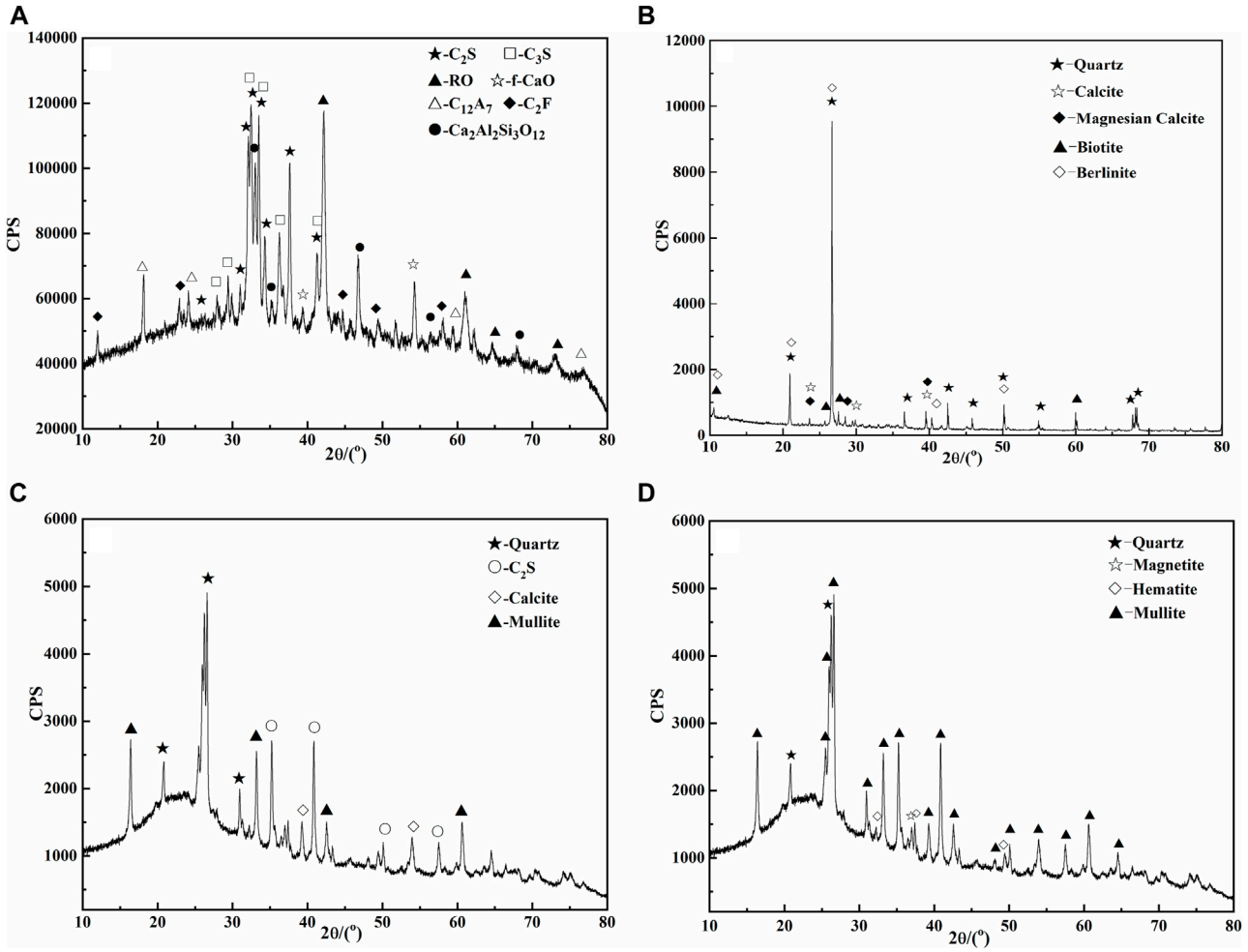


FIGURE 2
XRD patterns of raw materials. **(A)**-SS; **(B)**- RS; **(C)**- SCS; **(D)**-FA.

heavy metal leaching toxicity of SS meets the requirements of Identification standards for hazardous wastes-Identification for extraction toxicity (GB 5085.3-2007) (Table 2).

(2) RS. The RS was taken from Yuecheng Reservoir in Handan, Hebei Province, China. The RS is fine particles with a small amount of water grass and other impurities. The surface color is gray. The water content is about 70%. After precipitation and dewatering, the RS was placed in a cool indoor place for air drying. Then, it was dried in a drying box (105°C). After that, the RS was crushed to less than 2 mm by roller pressing, and blended well. The blended sample was further dried at 105°C for 24 h. The dried sample was ground to −0.074 mm by an agate grinder, and sealed for further use.

According to the results of X-ray fluorescence analysis (XRF) (Table 1), the RS mainly encompasses inorganic substances and a small amount of organic matter (14.43%). The inorganic substances include $Al_2O_3$ (14.32%), $SiO_2$ (51.41%), $Na_2O+K_2O$ (2.58%), CaO+MgO (7.54%), and $Fe_2O_3$+FeO (7.30%). Therefore, the pyrolyzed RS must perform well in gas production. The heavy metal contents (Cu, Zn, Pb, and Cd) in RS are lower than the limits in Identification standards for hazardous wastes-Identification for extraction toxicity (GB 5085.3-2007) (Table 2). As shown in Figure 2B, the main minerals in RS are berlinite, biotite, magnesium calcite, calcite, and quartz.

(3) SCS. The SCS was obtained from Inner Mongolia Power Generation Co., LTD., China Datang Group. The SCS is the waste produced by extracting aluminum from FA through limestone sintering. In the raw SCS, the water content is as high as 34.6%. Table 1 lists the chemical composition of the dried SCS. The alkali content ($Na_2O+0.658K_2O$) of 4.08% suggest that SCS is not suitable to be directly used as cement mixture and clinker. The main minerals of SCS include quartz, calcite, mullite, and $C_2S$ (Figure 2C). The leaching toxicity of heavy metals in SCS meets the requirements of Identification standards for hazardous wastes-Identification for extraction toxicity (GB 5085.3-2007) (Table 2).

(4) FA. The FA was obtained from Inner Mongolia Power Generation Co., LTD., China Datang Group. Table 1 presents the main chemical composition of FA. Owing to the

**TABLE 1 Chemical composition of raw materials (wt%).**

| Materials | $SiO_2$ | $Al_2O_3$ | CaO | MgO | $Fe_2O_3$ | FeO | $Na_2O$ | $K_2O$ | $SO_3$ | $P_2O_5$ | LOI |
|---|---|---|---|---|---|---|---|---|---|---|---|
| SS | 11.11 | 4.89 | 35.89 | 8.33 | 23.58 | 6.32 | 0.48 | 0.13 | 0.26 | 1.74 | 2.72 |
| RS | 51.41 | 14.32 | 5.18 | 2.36 | 5.29 | 2.01 | 0.58 | 2.12 | 0.46 | 1.84 | 14.43 |
| SCS | 25.15 | 8.63 | 46.87 | 2.58 | 2.49 | 1.29 | 3.40 | 1.04 | 0.38 | — | 7.42 |
| FA | 42.22 | 40.89 | 4.73 | 0.77 | 3.77 | 0.11 | 0.26 | 0.53 | 0.59 | 0.28 | 3.95 |
| Cement | 22.50 | 4.86 | 66.30 | 0.83 | 3.43 | 0.21 | 0.24 | 0.31 | — | 0.02 | 0.12 |

**TABLE 2 Leaching toxicity test results of raw materials ($mg·L^{-1}$).**

| Materials | Cu | Pb | Zn | Ni | Cd | Cr | As | Hg |
|---|---|---|---|---|---|---|---|---|
| SS | 7.813 | 0.06 | 22.19 | 0.0166 | 0.2151 | 0.587 | 0.0022 | — |
| RS | 26.161 | 0.16 | 37.71 | 0.0110 | 0.0908 | 0.172 | 0.1116 | 0.00224 |
| SCS | 1.682 | 0.07 | 18.46 | 0.0246 | 0.1361 | 1.354 | 0.3791 | 0.02480 |
| FA | 0.923 | 0.03 | 15.32 | 0.0125 | 0.0624 | 0.0573 | 0.2581 | — |
| Limit value | 100 | 5 | 100 | 5 | 1 | 5 | 5 | 0.1 |

high content of Si and Al, the FA can be used as a Si-Al modifier. According to Fly ash used for cement and concrete (GB/T 1596-2017), a comprehensive analysis of the fineness, water demand ratio, loss, water content, and $SO_3$ mass fraction of FA shows that the FA used in the study belongs to Class C. The main mineral phases of FA are quartz, mullite, magnetite, and hematite, as shown in Figure 2D. The heavy metal leaching toxicity of FA meets the requirements in Identification standards for hazardous wastes-Identification for extraction toxicity (GB 5085.3-2007) (Table 2).

(5) P·O 52.5 Portland cement. The cement is P·O 52.5 Portland cement produced by Jidong cement factory of BBMG Group, China. Whose chemical composition is displayed in Table 1. The initial and final setting time is 118 min and 190 min, respectively, which meet the requirements of Common Portland cement (GB 175-2007).

## 2.2 Experimental method

Based on the analysis of raw material characteristics, HTM of SS was carried out according to Figure 3. The cementitious properties and volume soundness of the MSM were investigated, and the reasons for the improvement of cementitious properties and soundness in SMHTM were analyzed in combination with the phase composition and structure. The following experimental methods were used in the study.

(1) HTM test. Raw SS was obtained after drying, crushing, and ball milling, reaching a SSA of about 420 $m^2 kg^{-1}$. The three materials, namely, SCS, FA, and RS, were dried to constant weight. Then the SCS, FA and RS in CMFSR were mixed well in proportion and put into the ball mill and ground until the SSA was 440 $m^2 kg^{-1}$. Based on the research on modifiers used for MSM by Zhang et al. (2012); Zhao et al. (2012), as well as the existing research foundation of the research group (Wang et al., 2022), according to the ratio of Ca, Si, and Al elements in SS, SCS, FA, and RS in Table 1, the ratio of SCS, FA, and RS in CMFSR is determined as 7:9:4. The pretreated SS powder was mixed with CMSFR in proportion. Table 3 illustrates the experimental scheme. The mixture was added an appropriate amount of water-based binder, and then evenly placed in a mold. Under a pressure of ≤30 MPa, the mixture was pressed into a φ 5 cm×3 cm cake. After that, the cake was relocated to a corundum crucible, and placed in a CD-1700X muffle oven for HTM. The modification temperature (MT) was set to 1,200°C, 1,250°C, and 1,300°C, and the heating rate was set to 10°C·$min^{-1}$. The temperature was held for 25 min after reaching each preset level. Then, the cake was taken out, and air cooled with a blower. Figure 3 shows the flow of SMHTM in laboratory.

(2) Volume soundness test. The volume soundness test was conducted using the standards method in Test method for stability of steel slag (GB/T 24175-2009). The raw SS and MSM were finely ground in a ball mill and passed through a 200 mesh sieve to obtain a sample with a particle size less than 0.074 mm. The f-CaO content in the raw SS and MSM was determined by ethylene diamine tetra acetic acid (EDTA) complex metric titration. The sample of 0.8 g was placed in a 250 mL conical flask, 20 mL of 200 g $L^{-1}$ ethylene glycol solution was added and sealed with a cap, and the sample was kept at a constant temperature of 90°C for 3 min in a water bath. The solution was filtered through quantitative filter paper, and the filtrate was placed in a 250 mL conical flask with a little calcium indicator, and the calcium glycol in the solution to be measured was titrated with EDTA standard solution.

(3) Heavy metal leaching test. SPLP was conducted to test the leaching behavior of heavy metals in raw materials, thus confirming the environmental safety. The methods of

leaching toxicity of heavy metals used the requirements of Identification standards for hazardous wastes-Identification for extraction toxicity (GB 5085.3-2007). During SPLP, the leach liquor was prepared by adding 60%/40% (mass fraction) of sulfuric acid/nitric acid and diluting appropriately with deionized water, in order to adjust the pH to 4.20 ± 0.05 (Wang et al., 2023a; Zhang et al., 2023). The leach liquor and solidified powder (0.075 mm) were mixed according to the ratio of 20:1, and shaken for 18 h in a gyrate shaker. Then, the screened mixture (0.45 μm) was put into Prodigy 7 Inductively coupled plasma emission spectrometer (ICP-OES) to analyze the concentration of Cr, Ni, Cu, Cd, Pb, Zn, As, and Hg (Wang et al., 2023b).

(4) Mortar test of SS. The mortar test mainly investigates the cementitious activity of SS. Mortar blocks were prepared according to Method of testing cements-Determination of strength (GB/T17671-2021), using a 40 mm×40 mm×160 mm standard test mold. For the SS powder ground from mortar blocks, the SSA is 420 $m^2$ $kg^{-1}$, the water-cement ratio (W/C) is 0.5, and the cement-sand ratio (C/S) is 1:3. The mixing was carried out using a cement mortar mixer. Specifically, 1,350 g standard sand (C/S of 1:3) was added after 30 s low-speed stirring. When the stirring reached 60 s, the stirring mode was switched to 30 s high-speed stirring, 90 s stoppage, and 60 s high-speed stirring again. The mixed mortar paste was poured into the 40 mm×40 mm×160 mm standard test mold. Then, the test mold was placed on a vibration table for vibro-molding. After that, the mortar paste was cured for 24 h under the standard conditions (temperature: 20 ± 1°C; relative humidity≥90%). Next, the test mold was removed, and the mortar block was relocated to a BWJ-III automated cement curing system at the temperature of 20 ± 1°C. The strength of the mortar block was measured at the specified age. Compressive strength (CS): The average value of six CS measurements obtained from a group of three 40 mm × 40 mm × 160 mm is the test result. When one of the six measured values exceeds 10% of the average of the six, the result is rejected and the average of the remaining five is the result. When the five measured values exceed their average values by 10%, the group results are invalidated. When two or more of the six measured values exceed the average value by 10%, the results of this group are invalidated. Flexural strength (FS): a group of 40 mm × 40 mm × 160 mm flexural results of the average as the test results. When one of the three strength values exceeds the average value of 10%, should be removed and then take the average value as the test results of FS; when two of the three strength values exceed the average value of 10%, the remaining one as the result of FS.

(5) SS activity index. The activity index of raw SS and SMHTM was determined according to Steel slag powder used for cement and concrete (GB/T 20491-2017):

$$A = \frac{R_t}{R_0} \times 100 \quad (1)$$

Where, A is the activity index of SS powder (%); $R_t$ is the strength of the SS mortar block at the specified age (MPa); $R_0$ is the strength of the pure cement mortar block at the specified age (MPa).

(6) SS paste test. The SS paste samples were prepared according to Test methods for water requirement of normal consistency, setting time and soundness of Portland cement (GB/T 1346-2011). Firstly, the stirring blade and stirring pot in the mixer were wiped clean with a wet mop. The SMHTM and water were added in proportion to the stirring pot. Then, the mixture was stirred at a low speed for 120 s, stopped for 15 s, and then stirred at a high speed for 120 s. The stirred paste was poured into a standard test mold of 20 mm × 20 mm × 20 mm for vibro-molding. After that, the paste was cured for 24 h under the standard conditions (temperature: 20 ± 1°C; relative humidity≥90%). Next, the test mold was removed, and the paste sample was kept in a GB/T 17671-40A standard cement curing box. The standard curing continued until the preset age. The mechanical properties of the sample were measured at that age. After the SS paste test, the central part of the sample was taken, and soaked in anhydrous ethanol solution to stop hydration. Finally, the sample was dried for testing the composition and structure of the hydration products.

## 2.3 Property characterization

The particle size was analyzed with a Malvern 2000 laser particle size analyzer (range: 0.02–2,000.00 μm), with ethanol as dispersant. The particle size distribution was measured according to Particle size analysis-laser diffraction methods (GB/T 19077.1-2008). The SSA was measured by an SSA-3200 dynamic method SSA analyzer. The CS of samples at different ages was tested in reference to Method of testing cements-Determination of strength (GB/T 17671-2021). The mechanical properties of the samples were tested by a YES-300 digital hydraulic pressure testing machine (loading rate: (2.0 ± 0.5) kN/s; maximum load: 300 kN). The X-ray diffraction (XRD) was performed using a Rigaku D/MAX-RC 12 kW rotating anode diffractometer (Cu target; working current: 150 mA; working voltage: 40 kV; wavelength: 1.5406 nm). In addition, the scanning electronic microscopy (SEM) was implemented using an AMRAY1820 scanning electron microscope (resolution: 6nm; maximum magnification: 300,000 times; maximum acceleration voltage: 30 kV).

# 3 Results and discussion

## 3.1 Volume soundness of SMHTM

The HTM can promote the thermal-chemical reactions between f-CaO and $SiO_2$, $Al_2O_3$ in mineral admixtures. The reactions reduce the content of f-CaO, and increase the content of cement mineral phases in the SS. As a result, the air-cooled SS exhibits better cementitious activity and volume soundness. Using multi-component Si-Al solid waste, this paper prepares a CMSFR rich in Si-Al minerals, and reduces the f-CaO content in raw SS through the following high-temperature chemical equations:

$$CaO + C_2S \rightarrow C_3S \quad (2)$$

$$2CaO + SiO_2 \rightarrow C_2S \quad (3)$$

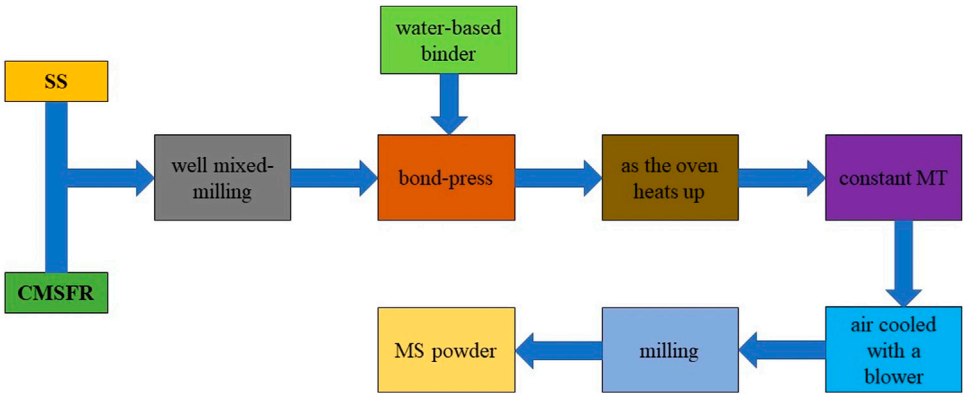


FIGURE 3
Flow of SMHTM test.

**TABLE 3 Experiment scheme design of MSM.**

| Number | Mass fraction of mixture/% | | Temperature (°C) |
|---|---|---|---|
| | S0 | CMSFR | |
| S1 | 90 | 10 | 1,200 |
| S2 | 80 | 20 | |
| S3 | 70 | 30 | |
| S4 | 90 | 10 | 1,250 |
| S5 | 80 | 20 | |
| S6 | 70 | 30 | |
| S7 | 90 | 10 | 1,300 |
| S8 | 80 | 20 | |
| S9 | 70 | 30 | |

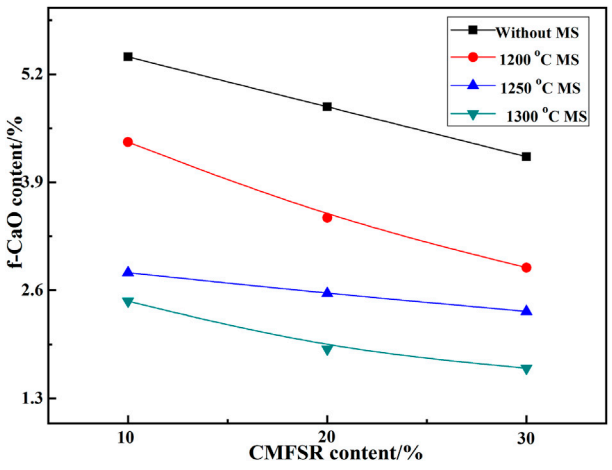


FIGURE 4
Variation law of f-CaO content in SMHTM.

$$3CaO + Al_2O_3 \rightarrow C_3A \quad (4)$$

$$2CaO + Al_2O_3 + SiO_2 \rightarrow C_2AS \quad (5)$$

$$CaO + MgO + 2SiO_2 \rightarrow CMS_2 \quad (6)$$

Figure 4 illustrates the changes in f-CaO content in SMHTM as a function of CMSFR content and MT. The raw SS of S0 and 10%–30% CMSFR mixed powder were selected as the comparison samples. As can be seen from Figure 4, the composite modifier CMSFR reduced the f-CaO content in the SS. The f-CaO content was greatly affected by MT and CMSFR content. The CMSFR content boosts MT, and suppresses f-CaO content in SMHTM.

At the CMSFR content of 10%, f-CaO content decreased from 4.38%, 2.81%–2.47%, as MT increased from 1,200°C, 1,250°C to 1,300°C. The f-CaO contents were 19.04%, 48.06%, and 54.34% smaller than those of the raw SS and CMSFR mixture, respectively. Similarly, at the CMSFR content of 20%, f-CaO content changed from 3.47%, 2.56%–1.90%, as MT rose from 1,200°C, 1,250°C to 1,300°C. The f-CaO contents were 28.48%, 46.78%, and 60.50% smaller than those of the raw SS and CMSFR mixture, respectively. At the CMSFR content of 30%, f-CaO content changed from 2.87%, 2.35%–1.66%, as MT rose from 1,200°C, 1,250°C to 1,300°C. The f-CaO contents were 31.83%, 44.18%, and 60.57% smaller than those of the raw SS and CMSFR mixture, respectively. Overall, when the MT was higher than 1,250°C and the CMSFR content was 10%–30%, the f-CaO content in the SMHTM remained below 3%, which meets the requirements in Steel slag powder used for cement and concrete (GB/T20491-2017).

The soundness of SS mainly comes from the volume expansion following f-CaO hydration. The SMHTM obtained with CMSFR can largely eliminate the volume unsoundness caused by f-CaO. Besides, SMHTM can be directly used in cement concrete, eliminating the need for aging treatment. The HTM boosts the thermochemical reactions between f-CaO and $SiO_2$, $Al_2O_3$, and other components in CMSFR, thereby reducing the f-CaO content in SS. However, after smelting at 1,650°C, the raw SS features dense structure, coarse grains, and solid melt RO phase. In this case, f-CaO cannot completely react with the chemical composition of CMSFR in SMHTM, resulting in incomplete removal of f-CaO.

**TABLE 4** Properties and activity index of mortar samples with cement, S0 and SMHTM.

| Group | Mortar fluidity/mm | Autoclave soundness | FS/MPa | | CS/MPa | | Activity index/% | |
|---|---|---|---|---|---|---|---|---|
| | | | 7d | 28d | 7d | 28d | 7d | 28d |
| C0 | 212 | qualified | 7.8 | 9.5 | 42.9 | 57.5 | 100.0 | 100.0 |
| S0M | 155 | unqualified | 5.1 | 7.2 | 27.2 | 40.9 | 63.4 | 71.1 |
| SMHTM1 | 177 | qualified | 5.3 | 7.7 | 28.5 | 45.3 | 66.4 | 78.8 |
| SMHTM2 | 188 | qualified | 5.7 | 8.3 | 30.9 | 46.1 | 72.0 | 82.2 |
| SMHTM3 | 183 | qualified | 5.2 | 7.5 | 28.0 | 43.9 | 65.4 | 76.3 |
| SMHTM4 | 207 | qualified | 5.8 | 8.4 | 31.2 | 47.8 | 72.7 | 83.1 |
| SMHTM5 | 218 | qualified | 6.1 | 8.5 | 31.4 | 49.1 | 73.2 | 85.4 |
| SMHTM6 | 197 | qualified | 5.6 | 8.2 | 30.8 | 46.7 | 71.8 | 81.2 |
| SMHTM7 | 221 | qualified | 6.3 | 8.5 | 31.5 | 49.6 | 73.4 | 86.3 |
| SMHTM8 | 227 | qualified | 6.4 | 8.6 | 31.9 | 50.9 | 74.4 | 88.6 |
| SMHTM9 | 215 | qualified | 6.2 | 8.4 | 31.6 | 48.0 | 73.7 | 83.5 |

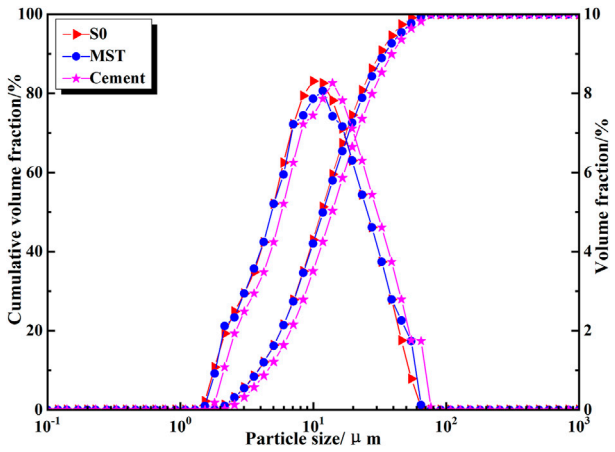


FIGURE 5
Particle distribution of S0, SMHTM and cement.

## 3.2 Cementitious properties of SMHTM

### 3.2.1 SMHTM activity

To investigate the cementitious properties of SMHTM, both the SMHTM and S0 particles were separately used as substitute for 30% (mass fraction) of P·O 52.5 cement. After mixing evenly, the properties and activity of each mortar sample were tested. The test results are recorded in Table 4, where C0 represents the mortar sample prepared with P·O 52.5 cement; S0M and SMHTM1 ~ SMHTM9 are the mortar samples prepared with 30% S0 and SMHTM, respectively. Figure 5 compares the particle size of S0, SMHTM powder, and cement. It can be observed that cement had a slightly lower particle content of 0.1–15 μm than S0 and SMHTM powder. As for the particle size >15 μm, cement had a higher particle content than SS powder, but the lead is very small.

As shown in Table 4, the mortar fluidity was small among S0M, SM 1 and SMHTM2, which may be attributed to the limited adaptability of S0 to the test cement. The mortar fluidity of the other samples was large. Thus, these SMHTM powders adapt well to the test cement.

It can be also seen from Table 4 that the mortar mixed with S0 had a low early strength. For this sample, the 7-day CS was 27.2 MPa, and 7-day activity index was 63.4%, a sign of improved later strength; the 28-day CS and activity index were 40.9 MPa, and 71.1%, respectively. For sample S0M, the 7-day FS and CS were 34.6% and 36.6% lower than those of pure cement mortar sample C0, respectively.

The CS and FS of mortars with SMHTM powders were better than those of S0M. Specifically, the 7-day FS increased by 2.0%–25.5%, and the 28-day FS increased by 4.2%–19.4%. Among all samples, SMHTM8 sample reached a 7-day FS of 6.4 MPa, and a 28-day FS of 8.6 MPa, which were 25.5% and 19.4% higher than those of sample S0M, respectively. The CS of mortar samples SMHTM1~SMHTM9, which were mixed with SMHTM powders, were 2.9%–17.3% and 7.3%–24.4% higher at 7 days and 28 days than those of S0M, respectively.

When CMSFR content was between 10% and 30%, the activity index of SS powder increased with MT. At the MT of 1,200°C and the CMSFR content of 10%–30%, the 28-day activity index of SMHTM powder increased by 5.2%–11.1% from the level of S0. At the CMSFR content of 20%, the 28-day activity index of SMHTM powder peaked at 82.2%. At the MT of 1,250°C and the CMSFR content of 10% and 20%, the 28-day activity index of SMHTM powder was 12.0% and 14.3% higher than that of S0 powder, respectively, and the activity index of SMHTM meets the requirement of Steel slag powder used for cement and concrete (GB/T 20491-2017): the activity index of grade I SS powder must be greater than or equal to 80%.

When the MT rose to 1,300°C and CMSFR content stood at 10% and 20%, the 28-day activity index of SMHTM powder were 86.3% and 88.6%, respectively, 15.2% and 17.5% higher than those of raw

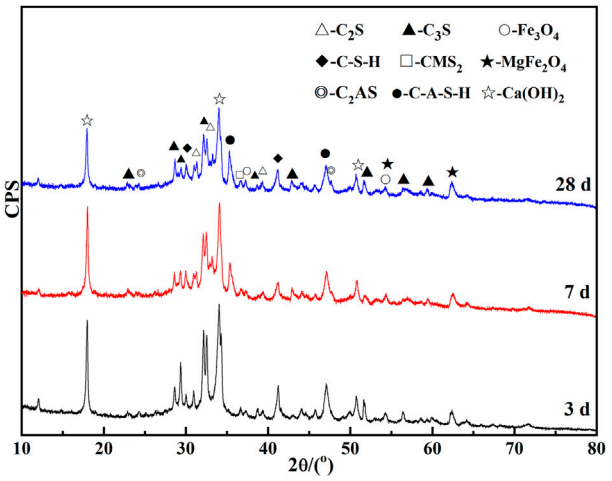


FIGURE 6
XRD patterns of SMHTM5 paste.

SS powder. Nevertheless, when CMSFR content grew to 30%, the cementitious activity of MSM at 1,250°C and 1,300°C were weaker than that of MSM at the CMSFR content of 20%. As shown in Table 4, adding 15%–25% CMSFR can effectively improve the cementitious properties of the system, when the MT is controlled at ≥ 1,250°C.

The FS and CS of SMHTM samples were lower than those of pure cement, which can be attributed to the reduced presence of cementitious phases $C_3S$, $C_2S$, and $C_3A$ than P·O 52.5 cement. The HTM with CMSFR lays the basis for enhancing the cementitious activity of SS. The cementitious properties of the system can be effectively improved by preparing CMSFR out of cheap Si-Al waste, and improving the Ca/Si ratio of the system.

### 3.2.2 Composition and structure of hydration products of SMHTM

Figure 6 shows the XRD patterns of paste samples at different ages. These samples were prepared by SMHTM5, which was produced at the CMSFR content of 20% and the MT of 1,250°C. It can be found that, after 3 days, 7 days, and 28 days of hydration, the main products of the SMHTM5 paste samples include $Ca(OH)_2$, $C_2S$, $C_3S$, unformed C-S-H gel, C-A-S-H, diopside ($CaO{\cdot}MgO{\cdot}2SiO_2$, $CMS_2$), ceylonite ($MgO{\cdot}Fe_2O_3$, $MgFe_2O_4$), gehlenite ($2CaO{\cdot}Al_2O_3{\cdot}SiO_2$, $C_2AS$), and $Fe_3O_4$. Among them, $Ca(OH)_2$, C-S-H gel, and C-A-S-H are hydration products. The presence of $C_2S$ and $C_3S$ indicates that the SMHTM5 paste system is not completely hydrated (Singh and Vashistha, 2021). Similar to CC, the active minerals $C_3S$ and $C_2S$ in SMHTM are hydrated to form $Ca(OH)_2$ and C-S-H gel (Eq. 7):

$$\mathbf{C_2S/C_3S + H_2O \rightarrow C - S - H + Ca(OH)_2} \quad (7)$$

$$\mathbf{(CaO)_m(SiO_2)_n(Al_2O_3)_k + Ca(OH)_2 + H_2O \rightarrow C - A - S - H} \quad (8)$$

In addition, the steamed bread peak in the range of 25–40° (Figure 6) indicates the presence of amorphous vitreous body ($(CaO)_m$ $(SiO_2)_n(Al_2O_3)_k$) in SMHTM. The vitreous body exhibits certain pozzolanic activity (Wilson et al., 2018; Mejdi et al., 2019) (see Eq. 8). $Ca(OH)_2$, a hydration product of $C_2S$ and $C_3S$ in SMHTM, will be consumed by the glass phase, and the mineral content of $C_2S$ and $C_3S$ in MSM will affect the hydration rate, thereby altering the activity index of SMHTM and the CS of mortar samples. $C_2AS$ minerals, mostly existing in the form of vitreous body, can react in an alkaline environment. The $C_2AS$ in the product is the residue of the reaction (8). In fact, Eq. 8 also explains the appearance of C-A-S-H crystals in the hydration products. With the extension of curing age, the $Ca(OH)_2$ generated by hydration of $C_2S$ and $C_3S$ reacted with amorphous vitreous continuously, which weakens the intensity of $Ca(OH)_2$ diffraction.

Figure 7 shows the SEM images of SMHTM5 paste samples cured for 3 days, 7 days and 28 days. From Figures 7A, B, it can be found that large plate-like hydration product $Ca(OH)_2$ crystals and loose honeycomb-like C-S-H gel appeared in the SMHTM5 paste sample at 3 days. Some $Ca(OH)_2$ crystals are embedded in C-S-H gel. The str uctures were not highly compact or cementitious.

From Figures 7C, D, it can be found that, after 7-day curing, lots of thick C-S-H gel with thin two ends appeared in the middle, obeying a radiating distribution. Many 5–15 μm pores emerged in the upper right of Figure 7C. In addition, plate-like $Ca(OH)_2$ crystals are seen in some parts of the visual range.

From Figures 7E, F, the C-S-H gel has a dense structure with sporadic pores at the age of 28 days. The number of pores has a significant decrease. There are 5–10 μm plate-like $Ca(OH)_2$ crystals in the middle, which are much smaller than those in Figures 7A, B. The development law of hydration products in Figure 8 is basically consistent with the law of XRD in Figure 7.

## 3.3 Phase and structure of SMHTM

### 3.3.1 Phase composition of SMHTM

The phase composition of SMHTM was analyzed with the CMSFR content of 10%–30%, and the MT of 1,200°C–1,300°C (see Figure 8). Figure 8A presents the XRD patterns of MSM samples (SMHTM1, SMHTM4 and SMHTM7) at different MTs, when the CMSFR content was fixed at 10%. Figure 8B displays the XRD patterns of MSM samples (SMHTM4, SMHTM5 and SMHTM6) at the MT of 1,250°C and CMSFR content of 10%–30%.

The XRD pattern (Figure 2A) of the raw SS is referred for comparative analysis. In Figure 2A, the mineral compositions were RO phase, $C_3S$, $C_2S$, $C_2F$, f-CaO, $C_{12}A_7$, and $Ca_2Al_2Si_3O_{12}$. The diffraction peaks of $C_3S$ and $C_2S$ were broad. After SMHTM was mixed with 10% CMSFR, the diffraction peaks of f-CaO became invisible (Figure 8). At the MT of 1,250°C, the diffraction peaks of $C_3S$ and $C_2S$ were significantly enhanced and sharpened. Therefore, the HTM promotes the formation of cementitious mineral phases. In cement production, 1,250 °C is the commonly used temperature to regulate the formation of $C_3S$ in the cementitious phase.

Comparing the curves of SMHTM1, SMHTM4 and SMHTM7 in Figure 8, it was learned that the $C_3S$ of the cementitious phase was mainly concentrated in SMHTM4 (1,250°C), the diffraction peak of the $C_3S$ mineral phase was relatively weak in SMHTM1 (1,200°C), and the $C_3S$ diffraction peak was strong in SMHTM5. The air cooling (Figure 3) could effectively inhibit the decomposition of $C_3S$ at a low temperature.

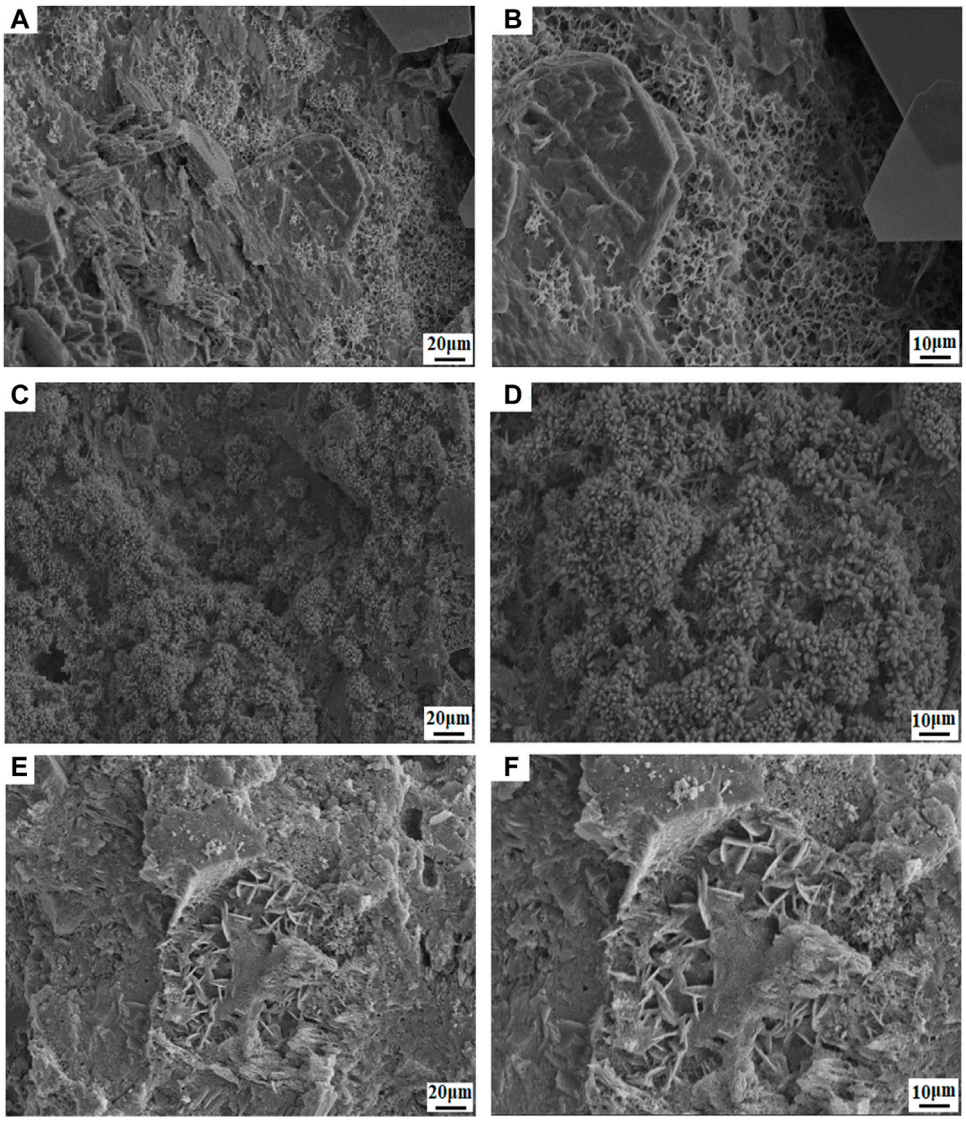


FIGURE 7
SEM images of SMHTM5 paste. **(A, B)**-3 days; **(C, D)**-7 days; **(E, F)**-28 days.

It can also be seen from Figure 8 that the diffraction peak of RO phase in the STM was significantly weaker than that of the raw SS (Figure 2A). The solid-melt of the RO phase separates at high temperatures and undergoes thermochemical reactions with minerals in the CMSFR, turning the FeO in RO phase into $MgFe_2O_4$ and $Fe_3O_4$. That is why the diffraction peak of $Fe_3O_4$ appears in Figure 8, and widens with the growing temperature. There is no diffraction peak in the XRD pattern, because minerals other than $C_2S$ in the raw materials of CMSFR, namely, $SiO_2$, $3Al_2O_3{\cdot}2SiO_2$, $CaCO_3$, $CaMg(CO_3)_2$, $K(Mg,Fe)_3$, $AlSi_3O(F,OH)$, and $AlPO_4$ participate in the modification reaction at a high temperature.

As shown in Figure 8B, when the CMSFR content changed with the MT fixed to 1,250°C, the mineral phase composition in SMHTM varied significantly, mainly in the Si-Al-based mineral phase. When the content of CMSFR was 10%, the Si-Al-based minerals $C_3S$, $C_2S$, $CMS_2$, $C_2AS$ and $C_3A$ were formed, in which $C_3S$, $C_2S$, $C_3A$, and $C_2AS$ are cementitious phase. SMHTM had much more cementitious phase than the raw SS. The formation of $CMS_2$, $C_2AS$, $C_3A$ mineral phases is mainly due to the addition of CMSFR, and the decomposition of Al-containing components ($C_{12}A_7$ ($12CaO{\cdot}7Al_2O_3$), $Ca_2Al_2Si_3O_{12}$) in the raw SS, which lowers the Ca/Si ratio in the system. After that, the liquid phase in the system increased under a high temperature, which promotes diffusion and crystal formation, as well as the formation of new mineral phases.

The analysis above indicates that, at the CMSFR content of 10–30% and the MT of 1,250°C, the content of cementitious phase was significantly increased in SMHTM, but the content of $C_3S$, $C_2S$ and $C_3A$ in the cementitious phase was lower than that in P·O 52.5 cement. As a result, the CS of the mortar sample obtained through the cementitious activity test on SS being

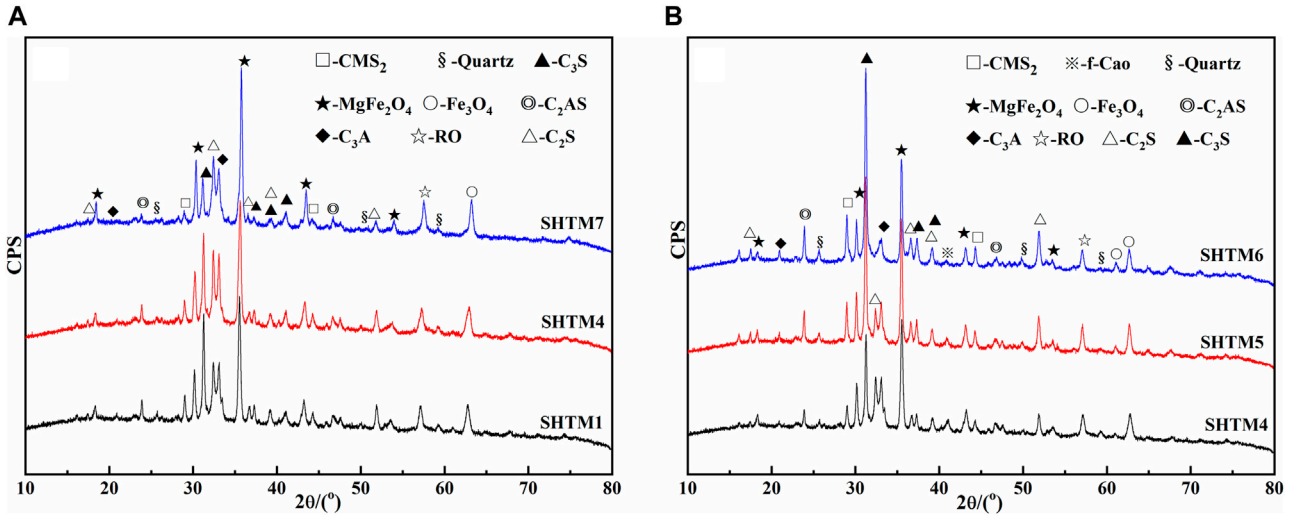


FIGURE 8
XRD patterns of MSM. **(A)** Different MT; **(B)** Different content of CMSFR.

inferior to that of the cement mortar sample. In our experiment, the CMSFR was prepared from FA, SCS, and RS. The HTM greatly elevates the content of $C_3S$ and $C_2S$ in the SMHTM, and produces new cementitious phases $C_3A$ and $C_2AS$, offsetting the adverse effect of f-CaO on the volume soundness of the raw SS. The reduction of RO phase content makes SS much more grindability. Combined with the XRD analysis on the mineral composition of the SMHTM, it is verified that the chemical reactions (Eqs 2–6) and (9) mainly occur during the SMHTM (Wang et al., 2022).

$$\mathbf{MgO + Fe_2O_3 \rightarrow MgFe_2O_4} \quad (9)$$

### 3.3.2 Microstructure of SMHTM

To further illustrate the role of CMSFR as a modifier, the authors analyzed the microstructure of SMHTM1, SMHTM5, and SMHTM9 at the MT of 1,200°C–1,300°C and the CMSFR content of 10%–30%, using SEM-EDS (see Figure 9).

From Figures 9A, 10, $C_2AS$ (point 1) is the main matrix in SMHTM1 (10% CMSFR; 1,200°C) with the mineral particles being smooth. Most of them were triangular, and hexagonal, with small number were of prismatic minerals. The numerous produced minerals did not exhibit a specific distribution.

From Figures 9C, D, it was found that the $C_2S$ with better crystallization grew concentratedly (point 2) on SMHTM5 (20% CMSFR; 1,250°C). The elliptical $C_2S$ particles could reach more than 10 μm in size, and get closely combining with each other. The mineral particles had a smooth surface, clear boundaries, large SSA, and excellent cementitious activity. From Figures 9E, 10, it was found that $MgFe_2O_4$ is the main matrix in SMHTM (30% CMSFR; 1,300°C) (point 3). The csytral structure was quite regular, and relatively complete. The large crystal grains formed a tetrahedral stacking structure. The boundaries between them were quite obvious.

Figures 9G–I provides the EDS images of SMHTM at different MTs. Combining Figures 9A, B, it can be seen that the mineral surface in MSM was smooth, with no obvious boundaries. The proportion of Ca, Si and Al in the particles at point 1 was close to that of $C_2AS$. As a glass phase in SMHTM, $C_2AS$ has low hydration activity under the excitation of alkaline solution. This again explains the lower activity index of SMHTM1 at 7 days and 28 days (66.4% and 78.8%).

The mineral crystal shape at point 2 in Figure 9D was well developed, obeying an elliptical grain distribution. The Ca/Si ratio was similar to that of $C_2S$ (see Figure 9H). Due to air cooling, $C_2S$ can stabilize in the β-$C_2S$ type, and witness a rise in hydration reactivity. That is why the activity indices of SMHTM5 samples at 7 days and 28 days were higher than those of SMHTM1.

The Ca/Si ratio at point 3 in Figure 9F was close to that of $MgFe_2O_4$ (see Figure 9I). The SS mixed with CMSFR produced a large amount of $C_3S$ at 1,300°C. With the MgO from the RO phase gradually converting into $MgFe_2O_4$ as the temperature increases. The addition of CMSFR improves the Ca/Si ratio in the system. Under a high temperature, the amount of liquid phase increased, which facilitates diffusion and crystal production, and promotes the formation of $C_3S$. At the same time, the conditions were mature for the reaction of MgO and iron oxides to generate $MgFe_2O_4$. However, $MgFe_2O_4$ exists as an inert mineral in SMHTM, i.e., it does not undergo hydration reaction, resulting in a lower hydration rate of the material than Portland cement. Furthermore, the cementitious activity and activity index of SMHTM9 were lower than those of cement.

The combined analysis of the above studies shows that the results achieved in this study for MSM are better than those already reported by Zhang et al. (2012) and Zhao et al. (2012). In this study, the f-CaO content of raw SS obviously decreased, and the cementitious properties improved in SMHTM. When the CMSFR content was 20% (SCS: FA: RS = 9:7:4), and the MT was 1,250°C,

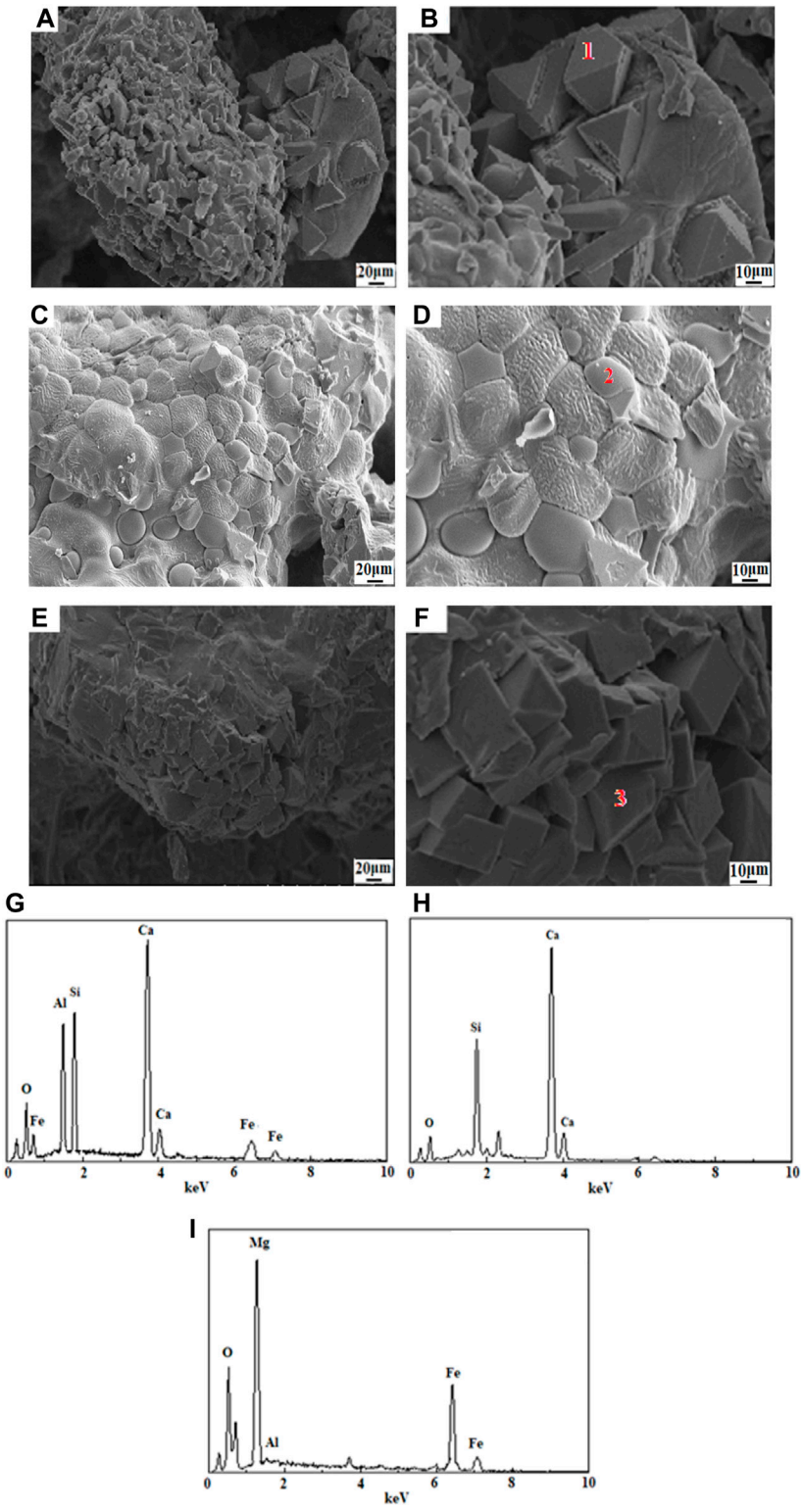


FIGURE 9
SEM-EDS images of SMHTM. **(A, B)**-SMHTM1; **(C, (D)**-SMHTM5; **(E, F)**-SMHTM9; **(G)**-Point 1; **(H)** -Point 2; **(I)** -Point 3.

the mass fraction of f-CaO in SMHTM dropped from 4.81% to 1.90%, down by 60.5%; the 28-day activity index of SMHTM increased to 85.4%, 14.3% higher than that of raw SS, which meets the technical requirement of Steel slag powder used for cement and concrete (GB/T 20491-2017): the activity index of grade I SS powder must be greater than or equal to 80%. However,


FIGURE 10
Cakes for HTM test.

in a study by Zhang et al. (2012) using iron ore tailings as a remodeling agent for reconstituted SS, when the treatment temperature was 1,250°C to 1,300°C and the iron ore tailing dosage was 10%–20%, the 28 days activity index of MSM increased from 76.4% to 83.4%, an increase of only 7.0%. According to Zhang et al. (2012) reported, the activity index of SMHTM at 1,300°C was 83.4%. However, in the author's study with 20% CMSFR added, the activity index of SMHTM at 1,250°C can reach 85.4%, and the activity index can reach 88.6% at 1,300°C, indicating that the energy consumption in Zhang's study is higher than that in the author's study. Similarly, the study of Zhao et al. (2012) used electric arc furnace (EAFSS) and FA as modifiers and the activity index of MSM was 85% when MT was 1,350°C. The energy consumption in his study was higher than that in this paper. From a comprehensive comparison perspective, the study in this paper is superior to the research of Zhang et al. (2012) and Zhao et al. (2012). The authors' study used SCS, FA and RS as modifiers, the presence of 14.43% organic matter in RS (Wang et al., 2022), and the residual carbon in FA can be effective in reducing MT.

## 4 Conclusion

Drawing on the idea of treating waste with waste, this paper prepares a composite modifier called CMSFR to improve the chemical and mineral composition of SS. The HTM with CMSFR improves the content of cementitious phase ($C_3S$, $C_2S$, $C_3A$) and glass phase in SS, and provides a reference for the harmless applications of SS and coal-based solid waste in cement concrete. The main conclusions are as follows.

(1) SCS, FA and RS are cheap modification materials to realize HTM of SS. They can improve the cementitious activity of SS, and effectively reduce the content of f-CaO in SS. At the CMSFR content of 10%–30%, the 28-day activity index of raw SS increased by 17.5%, and the f-CaO content in SMHTM was minimized at 1.66%, meeting the requirement (f-CaO content≤3%) in Steel slag powder used for cement and concrete (GB/T20491-2017).

(2) The HTM changes the mineral composition of the raw SS, producing new cement phases like $C_3A$, $C_2AS$, and $CMS_2$, $MgFe_2O_4$, and $Fe_3O_4$. In addition, the f-CaO content decreased in the raw SS, while the content of $C_3S$ and $C_2S$ increased. The decomposition of $C_{12}A_7$ and $Ca_2Al_2Si_3O_{12}$ in raw SS promoted the formation of $C_3A$. During the HTM, the RO phase was decomposed, and the FeO in that phase was converted into $Fe_3O_4$. The minerals other than $C_2S$ in the raw materials of CMSFR participated in the HTM reactions.

(3) At the MT of 1,200°C, the addition of 10% of CMSFR to the MSM produced $C_2AS$ minerals in the shape of equilateral triangles, hexagons and a small number of prisms as the matrix. At the MT of 1,250°C, the addition of 20% of CMSFR to the MSM produced elliptical $C_2S$ particles with good crystallinity; the size of these particles could reach more than 10 μm. At the MT of 1,300°C, the addition of 30% of CMSFR to the MSM generated $MgFe_2O_4$ minerals in the form of stacked regular tetrahedrons.

## Data availability statement

The raw data supporting the conclusion of this article will be made available by the authors, without undue reservation.

## Author contributions

DY proposes method and writes manuscript; CW proposes and participates in design research and reviews paper; XL, YG, HP, JM, YZ, JJ, YQ, YZ, and FL participate in design research and reviews paper. All authors contributed to the article and approved the submitted version.

## Funding

The authors gratefully acknowledge financial support by the National Key Research and Development Program of China (No. 2021YFC1910605), the Natural Science Foundation of Hebei Province (E2020402079), State Key Laboratory of Solid Waste Resource Utilization and Energy Conservation (SWR-2023-007), Science and Technology Research and Development Plan of China Railway Construction Group Co., Ltd. (No. 22-11b, 22-14b), Handan Science and Technology Research and Development Program (21422111260). The funder was not involved in the study design, collection, analysis, interpretation of data, the writing of this article or the decision to submit it for publication.

## Conflict of interest

YZ and FL were employed by China Railway Construction Group Co., Ltd.

The remaining authors declare that the research was conducted in the absence of any commercial or financial relationships that could be construed as a potential conflict of interest.

## Publisher's note



## References

Adolfsson, D., Robinson, R., Engström, F., and Björkman, B. (2011). Influence of mineralogy on the hydraulic properties of ladle slag. *Cem. Concr. Res.* 41 (8), 865–871. doi:10.1016/j.cemconres.2011.04.003

Alanyali, H., Çöl, M., Yilmaz, M., and Karagöz, Ş. (2009). Concrete produced by steel-making slag (basic oxygen furnace) addition in Portland cement. *Int. J. Appl. Ceram. Tec.* 6 (6), 736–748. doi:10.1111/j.1744-7402.2008.02317.x

Aldeeky, H., and Hattamleh, O. A. (2017). Experimental study on the utilization of fine steel slag on stabilizing high plastic subgrade soil. *Adv. Civ. Eng.* 2017, 1–11. doi:10.1155/2017/9230279

Anastasiou, E., Filikas, K. G., and Stefanidou, M. (2014). Utilization of fine recycled aggregates in concrete with fly ash and steel slag. *Constr. Build. Mater.* 50, 154–161. doi:10.1016/j.conbuildmat.2013.09.037

Biskri, Y., Achoura, D., Chelghoum, N., and Mouret, M. (2017). Mechanical and durability characteristics of High Performance Concrete containing steel slag and crystalized slag as aggregates. *Constr. Build. Mater.* 150, 167–178. doi:10.1016/j.conbuildmat.2017.05.083

Cao, L., Shen, W. G., Huang, J. Q., Yang, Y., Zhang, D., Huang, X. Q., et al. (2019). Process to utilize crushed steel slag in cement industry directly: Multi-phased clinker sintering technology. *J. Clean. Prod.* 217, 520–529. doi:10.1016/j.jclepro.2019.01.260

Dai, S., Zhu, H. J., Zhang, D. R., Liu, Z. Q., Cheng, S. Y., and Zhao, J. X. (2022). Insights to compressive strength, impermeability and microstructure of micro-expansion steel slag cement under constraint conditions. *Constr. Build. Mater.* 326, 126540. doi:10.1016/j.conbuildmat.2022.126540

Dhoble, Y., and Ahmed, S. (2018). Review on the innovative uses of steel slag for waste minimization. *J. Mater. Cycles. Waste.* 20, 1373–1382. doi:10.1007/s10163-018-0711-z

Gu, X. Y., Yu, B., Dong, Q., and Deng, Y. F. (2018). Application of secondary steel slag in subgrade: Performance evaluation and enhancement. *J. Clean. Prod.* 181, 102–108. doi:10.1016/j.jclepro.2018.01.172

Guo, J., Bao, Y., and Wang, M. (2009). Steel slag in China: Treatment, recycling, and management. *Waste Manage* 78, 318–330. doi:10.1016/j.wasman.2018.04.045

Guo, X. L., and Pan, X. J. (2018). Mechanical properties and mechanisms of fiber reinforced fly ash–steel slag based geopolymer mortar. *Constr. Build. Mater.* 179, 633–641. doi:10.1016/j.conbuildmat.2018.05.198

Guo, X. L., and Xiong, G. Y. (2020). Resistance of fiber-reinforced fly ash-steel slag based geopolymer mortar to sulfate attack and drying-wetting cycles. *Constr. Build. Mater.* 269, 121326. doi:10.1016/j.conbuildmat.2020.121326

Hasita, S., Rachan, R., Suddeepong, A., Horpibulsuk, S., Arulrajah, A., Mohammadinia, A., et al. (2020a). Performance improvement of asphalt concretes using steel slag as a replacement material. *J. Mater. Civ. Eng.* 32 (8), 04020227. doi:10.1061/(ASCE)MT.1943-5533.0003306

Hasita, S., Suddeepong, A., Horpibulsuk, S., Samingthong, W., Arulrajah, A., and Chinkulkijniwat, A. (2020b). Properties of asphalt concrete using aggregates composed of limestone and steel slag blends. *J. Mater. Civ. Eng.* 32 (7), 06020007. doi:10.1061/(ASCE)MT.1943-5533.0003148

Humbert, P. S., and Castro-Gomes, J. (2019). $CO_2$ activated steel slag-based materials: A review. *J. Clean. Prod.* 208, 448–457. doi:10.1016/j.jclepro.2018.10.058

Huo, B. B., Li, B. L., Chen, C., and Zhang, Y. M. (2021). Surface etching and early age hydration mechanisms of steel slag powder with formic acid. *Constr. Build. Mater.* 280, 122500. doi:10.1016/j.conbuildmat.2021.122500

Huo, B. B., Li, B. L., Huang, S. Y., Chen, C., Zhang, Y. M., and Banthia, N. (2020). Hydration and soundness properties of phosphoric acid modified steel slag powder. *Constr. Build. Mater.* 254, 119319. doi:10.1016/j.conbuildmat.2020.119319

Iacobescu, R. I., Angelopoulos, G. N., Jones, P. T., Blanpain, B., and Pontikes, Y. (2015). Ladle metallurgy stainless steel slag as a raw material in ordinary Portland cement production: A possibility for industrial symbiosis. *J. Clean. Prod.* 112, 872–881. doi:10.1016/j.jclepro.2015.06.006

Jiao, W. X., Sha, A. M., Liu, Z. Z., Li, W., Jiang, W., Qin, W., et al. (2020). Study on thermal properties of steel slag asphalt concrete for snow-melting pavement. *J. Clean. Prod.* 277, 123574. doi:10.1016/j.jclepro.2020.123574

Khan, M. S. H., Castel, A., Akbarnezhad, A., Foster, S., and Smith, M. (2016). Utilisation of steel furnace slag coarse aggregate in a low calcium fly ash geopolymer concrete. *Cem. Concr. Res.* 89, 220–229. doi:10.1016/j.cemconres.2016.09.001

Kourounis, S., Tsivilis, S., Tsakiridis, P. E., Papadimitriou, G. D., and Tsibouki, Z. (2007). Properties and hydration of blended cements with steelmaking slag. *Cem. Concr. Res.* 37 (6), 815–822. doi:10.1016/j.cemconres.2007.03.008

Kriskova, L., Pontikes, Y., Cizer, Ö., Mertens, G., Veulemans, W., Geysen, D., et al. (2012). Effect of mechanical activation on the hydraulic properties of stainless steel slags. *Cem. Concr. Res.* 42 (6), 778–788. doi:10.1016/j.cemconres.2012.02.016

Kriskova, L., Pontikes, Y., Pandelaers, L., Cizer, Ö., Jones, P. T., Balen, K. V., et al. (2013). Effect of high cooling rates on the mineralogy and hydraulic properties of stainless steel slags. *Metall. Mater. Trans. B* 44 (5), 1173–1184. doi:10.1007/s11663-013-9894-9

Li, B. L., Wang, Y. H., Liang, Y., and Zhang, Y. M. (2019). Sulfate resistance and hydration products of steam cured steel slag blended cement mortar under dry–wet cycle. *J. Sustain. Cem-based.* 8 (6), 353–366. doi:10.1080/21650373.2018.1564709

Li, X. L., Li, K. X., Sun, Q., Liu, L., Yang, J. L., and Xue, H. W. (2021). Preparation of cemented oil shale residue–steel slag–ground granulated blast furnace slag backfill and its environmental impact. *Materials* 14 (8), 2052–2073. doi:10.3390/ma14082052

Li, X., Yu, J., Wei, X., and Zhang, S. (2011). Structural characteristics and hydration kinetics of modified steel slag. *Cem. Concr. Comp.* 41 (3), 324–329. doi:10.1016/j.cemconres.2010.11.018

Liu, J. Z., Yu, B., and Wang, Q. (2020). Application of steel slag in cement treated aggregate base course. *J. Clean. Prod.* 269, 121733. doi:10.1016/j.jclepro.2020.121733

Liu, S. J., Hu, Q. Q., Zhao, F. Q., and Chu, X. M. (2014). Utilization of steel slag, iron tailings and fly ash as aggregates to prepare a polymer-modified waterproof mortar with a core–shell styrene–acrylic copolymer as the modifier. *Constr. Build. Mater.* 72, 15–22. doi:10.1016/j.conbuildmat.2014.09.016

Liu, W. H., Li, H., Zhu, H. M., and Xu, P. J. (2020). The interfacial adhesion performance and mechanism of a modified asphalt–steel slag aggregate. *Materials* 13 (5), 1180–1192. doi:10.3390/ma13051180

Luxán, M. P., Sotolongo, R., Dorrego, F., and Herrero, E. (2020). Characteristics of the slags produced in the fusion of scrap steel by electric arc furnace. *Cem. Concr. Res.* 30 (4), 517–519. doi:10.1016/S0008-8846(99)00253-7

Mason, B. (1944). The constitution of some basic open-hearth slags. *J. Iron Steel Inst.* 1 (1), 69–80.

Mejdi, M., Wilson, W., Saillio, M., Chaussadent, T., Divet, T., and Tagnit-Hamou, A. (2019). Investigating the pozzolanic reaction of post-consumption glass powder and the role of portlandite in the formation of sodium-rich C-S-H. *Cem. Concr. Res.* 123, 105790. doi:10.1016/j.cemconres.2019.105790

Mo, L. W., Zhang, F., Deng, M., Jin, F., Al-Tabbaa, A., and Wang, A. G. (2017). Accelerated carbonation and performance of concrete made with steel slag as binding materials and aggregates. *Cem. Concr. Comp.* 83, 138–145. doi:10.1016/j.cemconcomp.2017.07.018

Mo, L. W., Zhang, F., and Deng, M. (2016). Mechanical performance and microstructure of the calcium carbonate binders produced by carbonating steel slag paste under $CO_2$ curing. *Cem. Concr. Res.* 88, 217–226. doi:10.1016/j.cemconres.2016.05.013

Monshi, A., and Asgarani, M. K. (1999). Producing Portland cement from iron and steel slags and limestone. *Cem. Concr. Res.* 29 (9), 1373–1377. doi:10.1016/S0008-8846(99)00028-9

Murri, A. N., Rickard, W. D. A., Bignozzi, M. C., and Riessen, A. van. (2013). High temperature behaviour of ambient cured alkali-activated materials based on ladle slag. *Cem. Concr. Res.* 43 (1), 51–61. doi:10.1016/j.cemconres.2012.09.011

Palankar, N., Shankar, A. U. R., and Mithun, B. M. (2016). Durability studies on eco-friendly concrete mixes incorporating steel slag as coarse aggregates. *J. Clean. Prod.* 129, 437–448. doi:10.1016/j.jclepro.2016.04.033

Peng, C., and Huang, L. (2010). Carbon steel slag as cementitious material for self-consolidating concrete. *J. Zhejiang Univ-sc. A* 11 (7), 488–494. doi:10.1631/jzus.A0900635

Qian, G. R., Sun, D. D., Tay, J. H., Lai, Z. Y., and Xu, G. L. (2002). Autoclave properties of kirschsteinite-based steel slag. *Cem. Concr. Res.* 32 (9), 1377–1382. doi:10.1016/S0008-8846(02)00790-1

Rashad, A. M. (2019). A synopsis manual about recycling steel slag as a cementitious material. *J. Mater. Res. Technol.* 8 (5), 4940–4955. doi:10.1016/j.jmrt.2019.06.038

Roslan, H., Ismail, M., Abdul-Majid, Z., Ghoreishiamiri, S., and Muhammad, B. (2016). Performance of steel slag and steel sludge in concrete. *Constr. Build. Mater.* 104, 16–24. doi:10.1016/j.conbuildmat.2015.12.008

Salman, M., Cizer, Ö., Pontikes, Y., Snellings, R., Vandewalle, L., Blanpain, B., et al. (2015). Cementitious binders from activated stainless steel refining slag and the effect of alkali solutions. *J. Hazard. Mater.* 286, 211–219. doi:10.1016/j.jhazmat.2014.12.046

Saly, F., Guo, L. P., Ma, R., Gu, C. P., and Sun, W. (2018). Properties of steel slag and stainless-steel slag as cement replacement materials: A comparative study. *J. Wuhan. Univ. Technol.* 33 (6), 1444–1451. doi:10.1007/s11595-018-1989-3

Saxena, S., and Tembhurkar, A. R. (2018). Impact of use of steel slag as coarse aggregate and wastewater on fresh and hardened properties of concrete. *Constr. Build. Mater* 165, 126–137. doi:10.1016/j.conbuildmat.2018.01.030

Shi, C. J., and Hu, S. F. (2003). Cementitious properties of ladle slag fines under autoclave curing conditions. *Cem. Concr. Res.* 33 (11), 1851–1856. doi:10.1016/S0008-8846(03)00211-4

Shi, C. J. (2004). Steel slag—Its production, processing, characteristics, and cementitious properties. *J. Mater. Civ. Eng.* 16, 230–236. doi:10.1061/(ASCE)0899-1561(2004)16:3(230)

Shi, C. (2004). Steel slag-its production, processing, characteristics and cementitious properties. *J. Mater. Civ. Eng.* 16 (3), 230–236. doi:10.1002/chin.200522249

Shi, J. (2002). Characteristics and cementitious properties of ladle slag fines from steel production. *Cem. Concr. Res.* 2 (3), 459–462. doi:10.1016/S0008-8846(01)00707-4

Singh, S. K., and Vashistha, P. J. (2021). Development of newer composite cement through mechano-chemical activation of steel slag. *Constr. Build. Mater.* 268, 121147. doi:10.1016/j.conbuildmat.2020.121147

Tossavainen, M., Engsteom, F., Yang, Q., Menad, N., Larsson, M. L., and Bjorkman, B. (2007). Characteristics of steel slag under different cooling conditions. *Waste Manage* 27 (10), 1335–1344. doi:10.1016/j.wasman.2006.08.002

Tu, T. A., Huan, T. G., Huynh, N. N. T., and Son, N. K. (2019). Characterization of carbonated steelmaking slag and its potential application in construction. *Vie. J. Sci. Technol.* 57 (3A), 61–68. doi:10.15625/2525-2518/57/3A/14078

Wu, S. P., Xue, Y. J., Ye, Q. S., and Chen, Y. C. (2007). Utilization of steel slag as aggregates for stone mastic asphalt (SMA) mixtures. *Build. Enviorn.* 42 (7), 2580–2585. doi:10.1016/j.buildenv.2006.06.008

Waligora, J., Bulteel, D., Degrugilliers, P., Damidot, D., Potdevin, J. L., and Measson, M. (2010). Chemical and mineralogical characterizations of ld converter steel slags: A multi-analytical techniques approach. *Mater. Charact.* 61 (1), 39–48. doi:10.1016/j.matchar.2009.10.004

Wang, C. L., Jing, J. L., Qi, Y., Zhou, Y. X., Zhang, K. F., Zheng, Y. C., et al. (2023a). Basic characteristics and environmental impact of iron ore tailings. *Front. Earth Sci.* 11, 1181984. doi:10.3389/feart.2023.1181984

Wang, C. L., Qi, Y., Jing, J. L., Ma, J. T., Zhou, Y. X., Ping, H. Y., et al. (2023b). Properties and microstructure of total tailings cemented paste backfill material containing mining and metallurgical solid waste. *Front. Earth Sci.* 11, 1181952. doi:10.3389/feart.2023.1181952

Wang, C. L., Zhao, G. F., Wang, Y. B., Zhang, S. H., Zheng, Y. C., Huo, Z. K., et al. (2022). Study on the high-temperature modified steel slag using reservoir sediment and carbide slag. *Mater. Rep.* 36 (9), 21040178. doi:10.11896/cldb.21040178

Wang, C. L., Zhao, G. F., Zheng, Y. C., Zhang, K. F., Ye, P. F., and Cui, X. W. (2019). Study on the preparation of high performance concrete using steel slag and iron ore tailings. *J. New Electr. Sys.* 22 (4), 217–223. doi:10.14447/jnmes.v22i4.a07

Wang, Q., Wang, D. Q., and Zhuang, S. Y. (2017). The soundness of steel slag with different free CaO and MgO contents. *Constr. Build. Mater.* 151, 138–146. doi:10.1016/j.conbuildmat.2017.06.077

Wang, Q., Yan, P. Y., and Feng, J. W. (2011). A discussion on improving hydration activity of steel slag by altering its mineral compositions. *J. Hazard. Mater.* 186 (2-3), 1070–1075. doi:10.1016/j.jhazmat.2010.11.109

Wang, Q., Yang, J. W., and Yan, P. Y. (2013). Cementitious properties of super-fine steel slag. *Powder Technol.* 245, 35–39. doi:10.1016/j.powtec.2013.04.016

Wang, S. G., Li, X. M., Ren, K. B., and Liu, C. H. (2020). Experimental research on steel slag stabilized soil and its application in subgrade engineering. *Geotech. Geol. Eng.* 38, 4603–4615. doi:10.1007/s10706-020-01313-6

Wang, S., Wang, C., Wang, H., Liu, Z., Qian, W., Jin, C., et al. (2018). Study on cementitious properties and hydration characteristics of steel slag. *Pol. J. Environ. Stud.* 27 (1), 357–364. doi:10.15244/PJOES/74133

Wilson, W., Sorelli, L., and Tagnit-Hamou, A. (2018). Unveiling micro-chemo-mechanical properties of C–(A)–S–H and other phases in blended-cement pastes. *Cem. Concr. Res.* 107, 317–336. doi:10.1016/j.cemconres.2018.02.010

Xue, Y. J., Wu, S. P., Hou, H. B., and Zha, J. (2006). Experimental investigation of basic oxygen furnace slag used as aggregate in asphalt mixture. *J. Hazard. Mater.* 138 (2), 261–268. doi:10.1016/j.jhazmat.2006.02.073

Yan, P. Y., Mi, G. G., and Wang, Q. (2014). A comparison of early hydration properties of cement–steel slag binder and cement–limestone powder binder. *J. Therm. Anal. Calorim.* 115 (1), 193–200. doi:10.1007/s10973-013-3360-4

Yüksel, I. (2017). A review of steel slag usage in construction industry for sustainable development. *Environ. Dev. Sustain.* 19, 369–384. doi:10.1007/s10668-016-9759-x

Zhang, H. Z., Qi, Y., Jing, J. L., Wang, C. L., Zhou, Y. X., Zhang, K. F., et al. (2023). Properties and environmental impact of building foundation pit backfilling materials containing iron and steel solid waste. *Front. Earth Sci.* 11, 1181974. doi:10.3389/feart.2023.1181974

Zhang, M. G., Li, K. Q., Ni, W., Zhang, S. Q., Liu, Z. Y., Wang, K., et al. (2021). Preparation of mine backfilling from steel slag-based non-clinker combined with ultra-fine tailing. *Constr. Build. Mater.* 320, 126248. doi:10.1016/j.conbuildmat.2021.126248

Zhang, T. S., Yu, Q. J., Wei, J. X., Li, J. X., and Zhang, P. P. (2011). Preparation of high performance blended cements and reclamation of iron concentrate from basic oxygen furnace steel slag. *Resour. Conserv. Recy.* 56 (1), 48–55. doi:10.1016/j.resconrec.2011.09.003

Zhang, Z. S., Lian, F., Liao, H. Q., Yang, Q., and Cao, W. B. (2012). Modifying the properties of steel slag by iron tailings at high temperature. *J. Univ. Sci. Technol. B* 34 (12), 1379–1384. doi:10.13374/j.issn1001-053x.2012.12.011

Zhao, D. Q., Zhang, D., Shen, W. G., Huang, J. Q., Tang, X. C., Yang, Y., et al. (2022). Investigation on industrial trial production of multi-phased clinker with crude granular steel slag. *J. Clean. Prod.* 337, 130467. doi:10.1016/j.jclepro.2022.130467

Zhao, H. J., Yu, Q. J., Wei, J. X., Li, J. X., and Zhong, G. (2012). Effect of composition and temperature on structure and early hydration activity of modified steel slag. *J. Bulid. Mater.* 15 (3), 399–405. doi:10.3969/j.issn.1007-9629.2012.03.021

Zhao, Y. L., Wu, P. Q., Qiu, J. P., Guo, Z. B., Tian, Y. S., Sun, X. G., et al. (2022). Recycling hazardous steel slag after thermal treatment to produce a binder for cemented paste backfill. *Power Eng.* 395, 652–662. doi:10.1016/j.powtec.2021.10.008

Zhuang, S. Y., and Wang, Q. (2021). Inhibition mechanisms of steel slag on the early-age hydration of cement. *Cem. Concr. Res.* 140, 106283. doi:10.1016/j.cemconres.2020.106283

# Frontiers in Earth Science

**Investigates the processes operating within the major spheres of our planet**

Advances our understanding across the earth sciences, providing a theoretical background for better use of our planet's resources and equipping us to face major environmental challenges.

---

## Discover the latest Research Topics

See more →


**Frontiers**

Avenue du Tribunal-Fédéral 34
1005 Lausanne, Switzerland
frontiersin.org

**Contact us**

+41 (0)21 510 17 00
frontiersin.org/about/contact